2017-08-01

Advancements in the Understanding of Nonlinear Optics and Their Use in Material Analysis

Shawn C. Averett
Brigham Young University

Advancements in the Understanding of Nonlinear Optics and Their Use in Material Analysis

Shawn C. Averett

A dissertation submitted to the faculty of
Brigham Young University
in partial fulfillment of the requirements for the degree of

Doctor of Philosophy

James E. Patterson, Chair
Mathew C. Asplund
Steven R. Goates
William G. Pitt
Eric T. Sevy

Department of Chemistry and Biochemistry

Brigham Young University

ABSTRACT

Advancements in the Understanding of Nonlinear Optics and Their Use in Material Analysis

Shawn C. Averett
Department of Chemistry and Biochemistry, BYU
Doctor of Philosophy

Adhesion, heterogeneous catalysis, electrochemistry, and many other important processes and properties are driven by interactions at surfaces and interfaces. Vibrational sum frequency generation spectroscopy (VSFG) is an increasingly popular analytical technique because it can provide information about the nature and physical orientation of functional groups at these surfaces and interfaces. Analysis of VSFG data can be complicated by the presence of SFG signal that is not associated with a resonant vibration. This nonresonant sum frequency generation (NR-SFG) signal can interfere with the resonant signal and influence the detected spectrum. Methods have been developed to remove NR-SFG signal; however, these methods tend to be complicated and expensive. In fact many SFG practitioners do not have the ability to remove NR-SFG signal components, and systems designed to remove NR-SFG signal contributions may not be able to do so for some materials.

We have worked to help develop a better understanding of NR-SFG. As part of this work, a better understanding of the temporal and phase behavior of NR-SFG signal has been developed, based on the behavior of NR-SFG signal from Si(111) wafers. This work calls into question some assumptions underlying nonresonant suppression methods based on time-domain detection. A new method for nondestructively testing (NDT) materials has been developed that uses nonresonant second harmonic generation, the degenerate form of SFG. This new NDT technology has the potential to detect several forms of material damage, such as aluminum sensitization, and plastic deformation of materials, which are largely invisible to current NDT technologies. Methods for extracting functional group orientation from VSFG data that contains NR-SFG contributions are also demonstrated and used to investigate how the surface of high density polyethylene changes in response to mechanical deformation. This work shows that the inability to remove NR-SFG contributions from VSFG spectra does not mean that these instruments cannot be used to make important discoveries. It simply means that NR-SFG contributions must be properly understood and accounted for during experimental design, and kept in mind during the analysis of VSFG spectra.

Keywords: surface science, sum frequency spectroscopy, nonresonant sum frequency generation, high density polyethylene, nondestructive testing

ACKNOWLEDGEMENTS

I would like to thank the BYU College of Physical and Mathematical Sciences, the BYU department of Technology Transfer, and the Office of Naval Research for funding research presented in this dissertation. During my graduate studies I received the J. Rex and Marcia A. Goates Graduate Fellowship, the Loren C. and Maurine F. Bryner Graduate Award, and the Nicholes Maw Fellowship. Their support has helped make my graduation possible, and I am deeply grateful.

I owe a great deal of gratitude to my advisor Dr. James Patterson for the many hours spent teaching me how to be a scientist. I would also like to thank my advisory committee members for useful insights and loaned equipment, as well as Ted Knighton for bringing NDT to my attention, and Dr. Alexander Curtis for teaching me how to build with optics. Additionally I need to express my appreciation to Janet Fonoimoana and Spencer Rogers for helping me to navigate the pitfalls and paperwork of their respective bailiwicks.

I am especially grateful to my wife Stacy Averett and my daughters Kathryn and Ivy Averett. Stacy's hard work, selflessness, and support made this possible; Kathryn and Ivy's cheerful willingness to chip in and do without were inspiring. I could not have done this without them.

CONTENTS

LIST OF TABLES

LIST OF FIGURES

Chapter 1: Sum Frequency Generation Overview and Brief Literature Review of Nonresonant SFG

1.1: Introduction

Bacterial survival, material durability, energy storage, and data processing are among the many processes that are driven by surface chemistry. With the ability to provide surface specific chemical identification and morphological information, sum frequency generation (SFG) spectroscopy is an immensely powerful spectroscopic tool for the investigation of these, and other important, systems. In fact, the only vibrational spectra of water or polymer surfaces were taken with SFG.[1] The SFG signal, however, can be complicated, and a failure to account for all of the signal sources can lead to inaccurate analysis and dubious conclusions. Much of the confusion concerning the treatment of SFG spectra comes from an incomplete understanding of the nonresonant component of SFG signal. Therefore, in this chapter I briefly review the commonly understood aspects of SFG theory and analysis, while going into more depth discussing the existing literature on the nonresonant component of SFG signal. An excellent in depth discussion of SFG can found in the book *Fundamentals of Sum-Frequency Spectroscopy* by Y.R. Shen.[2]

1.2: Overview of SFG

SFG occurs when two photons interact with a material leading to the emission of a single photon with energy equal to the sum of the energy of the two input photons. SFG has a very low conversion efficiency, which means that SFG requires a relatively high intensity, coherent light source for practical application. Because of the requirement for large peak power, pulsed lasers

faare generally used to provide the excitation beams in SFG systems. Most SFG systems can be classified as either broadband or scanning systems. Scanning SFG systems are generally powered by lasers with nanosecond pulses that are relatively narrow spectrally. These systems scan through a range of IR wavelengths, stopping to acquire data at each wavelength of interest. The spectral width of both excitation pulses, along with the number of scanned points, defines the resolution of these systems. Broadband SFG systems tend to be powered by lasers with femtosecond pulses.[3,4] The IR excitation beam is generally kept short in time and spectrally broad, while the visible excitation beam is often lengthened in time and narrowed in frequency to improve resolution. The envelope of IR wavelengths is tuned to include frequencies for the molecular vibrations of interest. The spectrally broad IR pulse can allow for an entire SFG spectrum to be measured at the same time. The resolution of broadband SFG systems is limited by the spectral width of the visible pulse.

SFG signal intensity is significantly increased when the first photon interaction or the emitted photon has an energy corresponding to a vibrational or electronic transition. When an infrared beam is used as the source for the first interaction, the SFG signal boost from a resonant interaction can be used to identify functional groups, much like traditional IR absorption spectroscopy. This vibrationally resonant SFG, or VSFG, can also be used to gain information about the physical orientation of these functional groups. [5-7]

The intensity of VSFG signal depends on the intensity of the excitation sources and the nature of the material. This can be mathematically modeled as

$$I_{SFG} \propto I_{Vis} I_{IR} \left| \chi^{(2)} \right|^2 \quad (1)$$

where I_{SFG} is the intensity of the VSFG signal, I_{Vis} is the intensity of the second excitation source, which is often in the visible region, I_{IR} is the intensity of vibrationally resonant excitation source, and $\chi^{(2)}$ describes the nonlinear susceptibility of the material, which takes into account the amount of material present and how strongly it interacts with the excitation beams.

The nonlinear susceptibility $\chi^{(2)}$ is mathematically modeled by a 3×3×3 tensor shown in Eq. 2. Each tensor element represents a different interaction of the excitation and signal beams with the material.

$$\chi_x = \begin{bmatrix} \chi_{xxx} & \chi_{xxy} & \chi_{xxz} \\ \chi_{xyx} & \chi_{xyy} & \chi_{xyz} \\ \chi_{xzx} & \chi_{xzy} & \chi_{xzz} \end{bmatrix} \quad \chi_y = \begin{bmatrix} \chi_{yxx} & \chi_{yxy} & \chi_{yxz} \\ \chi_{yyx} & \chi_{yyy} & \chi_{yyz} \\ \chi_{yzx} & \chi_{yzy} & \chi_{yzz} \end{bmatrix} \quad \chi_x = \begin{bmatrix} \chi_{zxx} & \chi_{zxy} & \chi_{zxz} \\ \chi_{zyx} & \chi_{zyy} & \chi_{zyz} \\ \chi_{zzx} & \chi_{zzy} & \chi_{zzz} \end{bmatrix} \tag{2}$$

The VSFG $\chi^{(2)}$ tensor elements are initially modeled using the electric dipole approximation. In an isotropic material, symmetry constraints require all of the $\chi^{(2)}$ tensor elements go to zero. For many materials, this means that VSFG signal cannot be produced in the bulk. At the surface of an azimuthally symmetric material; however, the tensor elements $\chi_{xxz}, \chi_{yyz}, \chi_{xzx}, \chi_{yzy}, \chi_{zxx}, \chi_{zyy}$, and χ_{zzz} do not go to zero. This allows the polarization combinations (SSP), (SPS), (PSS), and (PPP) to generate VSFG signal, where the first, second, and third letters denote the polarization of the signal beam, the visible excitation beam, and the IR excitation beam respectively.

Different polarization combinations can be used to find the average tilt angle of a functional group. For example, the tilt angle of a methyl group, with C_{3v} symmetry, at a surface can be found from the ratio of the χ_{yyz} and χ_{yzy} tensor elements using the relationship

$$\left|\frac{\chi_{yyz}}{\chi_{yzy}}\right| = \left|\frac{(cos^3\theta) + 0.56(sin^2\theta cos\theta)}{0.44(sin^2\theta cos\theta)}\right| \tag{3}$$

where θ is the average tilt angle.[8] Several other methods involving the comparison of orthogonal stretching modes or the use of phase-sensitive VSFG can be used to find information about the orientation of a detected functional group.[5-7] It should be noted that a sufficiently broad distribution of functional group orientations can lead to an apparent tilt angle of 39.2°, often called the VSFG magic angle.[9,10]

SFG signal that is not associated with an electronic or vibrational transition can also be produced. If present, this nonresonant signal can interfere with the resonant signal and significantly change the detected spectrum.[11,12] When a nonresonant contribution is present in SFG signal, the mathematical model from Eq. 1 becomes

$$I_{SFG} \propto I_{Vis} I_{IR} \left| \chi_{NR}^{(2)} + \chi_{R}^{(2)} \right|^2 \tag{4}$$

which can be expanded into

$$I_{SFG} \propto I_{Vis} I_{IR} \left(\left| \chi_{NR}^{(2)} \right|^2 + \left| \chi_{R}^{(2)} \right|^2 + 2 \left| \chi_{NR}^{(2)} \right| \left| \chi_{R}^{(2)} \right| cos[\phi - \delta(v)] \right) \tag{5}$$

where $\chi_{NR}^{(2)}$ is a 3×3×3 tensor modeling the nonresonant susceptibility, $\chi_{R}^{(2)}$ is a 3×3×3 tensor modeling the resonant susceptibility, ϕ accounts for the relative phase between the resonant and nonresonant signals, and $\delta(v)$ is a frequency-dependent phase term. Even a relatively small amount of nonresonant signal can make the detected signal different from the purely resonant signal.[11] This can be understood by consideration of the third term in the parentheses of Eq. 5. Here the $\left| \chi_{NR}^{(2)} \right| \left| \chi_{R}^{(2)} \right|$ component indicates that a large resonant signal can amplify the observed effect of the nonresonant signal. This means that even if the first term of Eq. 5 is small, the third term, which also has a nonresonant contribution, may not be.

The ability of a small amount of NR-SFG signal to influence VSFG spectra can have significant consequences. Many methods for determining functional group orientation rely on a comparison of spectroscopic features. Because the relative phase between two different resonant SFG responses and the nonresonant signal may be different, the effect of nonresonant signal interference with the resonant responses may also be different. For example, a peak from the methylene symmetric stretch may be made smaller by interference with nonresonant signal while the peak from an antisymmetric methylene stretch may become larger. Changes in the system being studied can alter the intensity of the nonresonant SFG signal,[11] which can make it difficult to accurately track the amount of a chemical species present at a sample surface or interface when nonresonant signal is present. These interactions between resonant and nonresonant signal components can make quantitative information unreliable when extracted from spectra with nonresonant signal present.

Nonresonant SFG signal can come from three different sources: the electric dipole (ED), the magnetic dipole (MD), and the electric quadrupole (EQ), each of which can be modeled by an independent tensor as in Eq. 6.[2]

$$\chi_{NR}^{(2)} = \chi_{ED}^{(2)} + \chi_{MD}^{(2)} + \chi_{EQ}^{(2)} \quad (6)$$

The tensor that models nonresonant signal generated from an electric dipole is subject to the same symmetry constraints as those of the electric dipole used to model resonant SFG signal, and thus does not allow nonresonant SFG signal to be generated in regions with inversion symmetry. The electric quadrupole and magnetic dipole, however, are not constrained by the same symmetry considerations, and allow for the production of nonresonant SFG signal in isotropic regions, including the bulk of a material.[2] The presence of quadrupolar or magnetic dipole nonresonant contributions in SFG signal can be a significant concern.[2] At a material surface, the

amount of nonresonant signal associated with the electric quadrupole or magnetic dipole is generally much less than the resonant signal from the same region. However, the fact that quadrupole or magnetic dipole interactions can generate nonresonant signal throughout the bulk of a material means that they can still produce significant amounts of NR-SFG.

Several different strategies have been developed to deal with nonresonant signal. These approaches either suppress nonresonant signal with specialized detection or excitation methods, or seek to avoid nonresonant signal by selecting experimental conditions where little NR-SFG is expected. Because scanning SFG systems often lack the ability to suppress nonresonant signal, researchers with nanosecond pulsed, scanning systems are often limited to working with samples that do not generate NR-SFG.

It can be difficult to predict what conditions will generate NR-SFG, which can make avoiding nonresonant signal challenging. Because of this, spectra should be inspected for signs of nonresonant contributions. The presence of derivative and unevenly broadened line shapes, or a baseline that is at a different height on either side of a spectral feature, are strong indications that a spectrum includes nonresonant signal. Figures 1.1 and 1.2 are examples of VSFG spectra with nonresonant signal contributions.

Vibrationally resonant SFG occurs when the IR input beam creates a vibrationally excited state that is then upconverted to a virtual state by interaction with the visible exaction beam. The vibrationally excited state can take several ps to dephase, which allows the effects of the IR pulse to persist after the pulse has left.[13,14] Because of this relatively slow dephasing, vibrationally resonant SFG signal can still be created by the arrival of the visible pulse for some time after the end of the IR pulse.

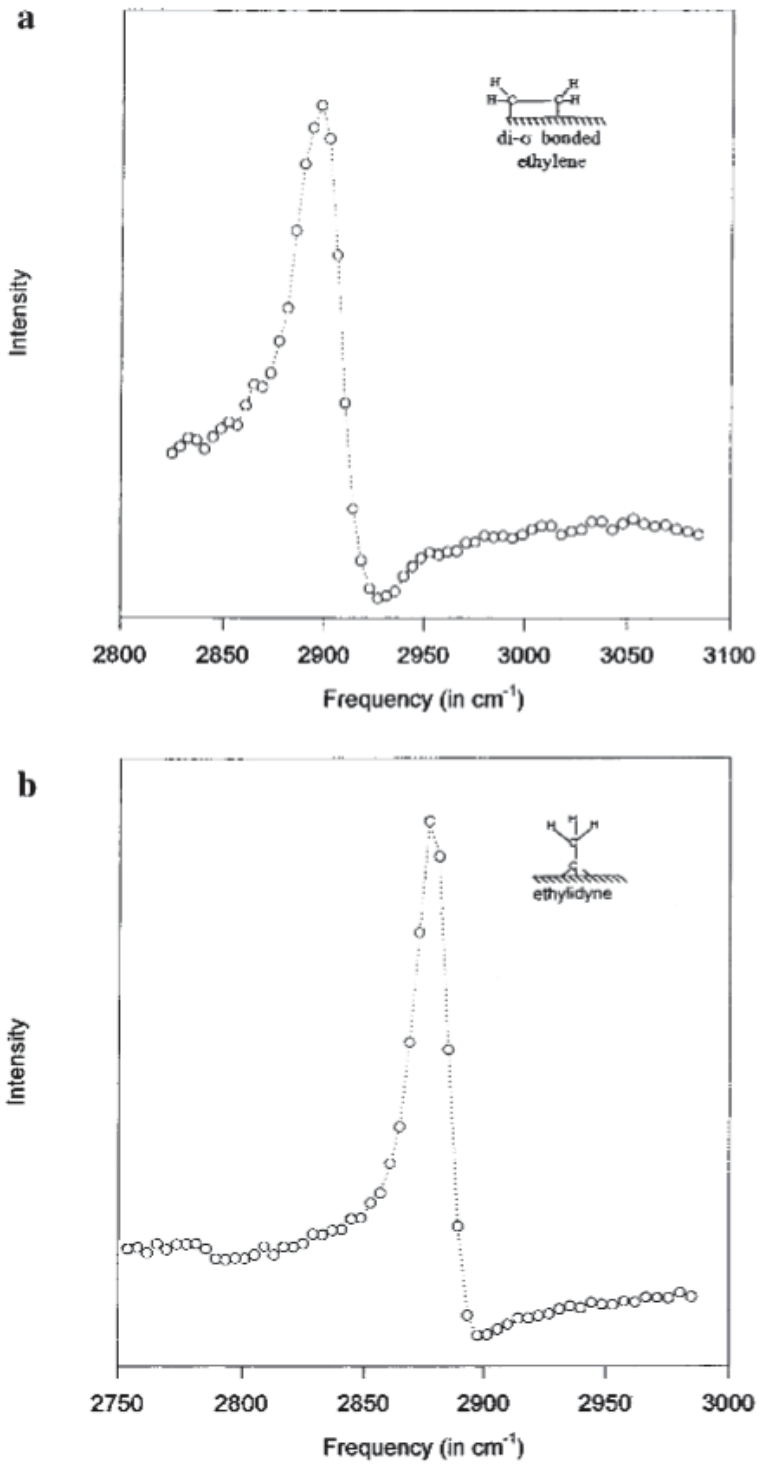

Figure 1.1. Platnum (111) substrate with saturation coverage of (a) di-cis bonded ethylene at 202 K, and (b) end on bonded ethylidyne at 300K. From Reference 25.

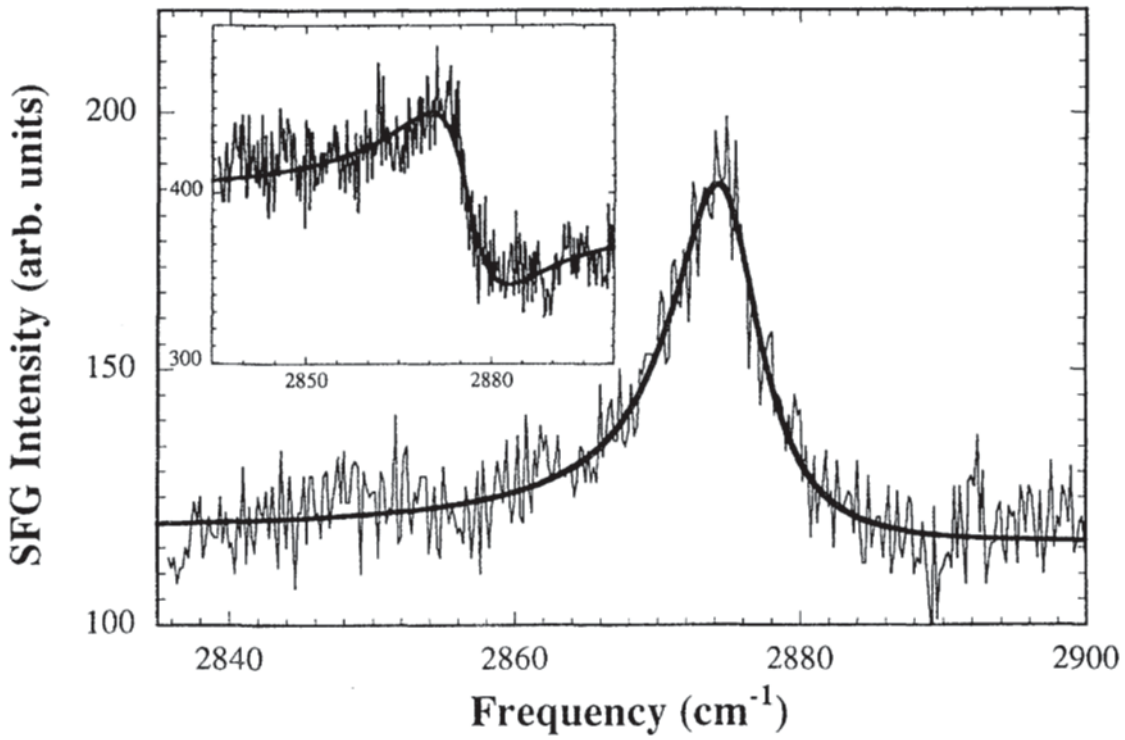

Figure 1.2. PPP polarized SFG spectra of ODT/Au(111) at azimuthal angle -37 (inset), and 7 degrees. The relative phase between the resonant and nonresonant SFG singal is different at these two azimuthal angles. The differences in the spectra are a result of the difference in the relative phases at these two angles. From reference 42.

Currently accepted SFG theory assumes that the nonresonant signal dephases rapidly, effectively decaying instantaneously with the removal of either excitation beam.[2,14] Several methods of NR-SFG suppression take advantage of this behavior to remove nonresonant signal from the detected spectrum. Nonresonant suppression based on time-delay excitation does this by delaying the pulse from the visible excitation source in time, relative to the resonant excitation pulse.[13] If the second pulse is sufficiently delayed, the nonresonant excitation will have decayed away, but some of the longer-lived, resonant excitation will still be present. While this process can remove nonresonant contributions from the detected signal, the incomplete sampling in time also alters the resonant spectrum.[15] The original resonant signal can be reconstructed[15]; however, this process is time consuming.

Nonresonant suppression accomplished by delaying the visible pulse is commonly done by increasing the delay time between the excitation pulses until nonresonant signal is no longer produced from a standard, such as a gold mirror. The presence of resonant signal can cause the nonresonant signal to persist longer than it otherwise would,[16] meaning that additional delay time may be required for full nonresonant suppression. This is particularly important when the second excitation pulse does not have a sharp leading edge. It should also be noted that the persistence of the resonant signal can be affected by the frequency of the second excitation beam.[17] This means that broadband systems using different frequencies for the visible excitation beam may produce different spectra when using the same delay time for the visible pulse.

Time-domain detection is also based on the assumption that NR-SFG cannot exist without the presence of both excitation beams. Detecting in the time-domain rather than the frequency domain, as is done with the time-delay suppression method, allows for the acquisition of phase

information along with the spectrum. VSFG can be mathematically modeled in the time domain as[18]

$$E_{SFG}^{(2)}(t;t_{IR}) \propto \int_0^\infty dt_2 \int_0^\infty dt_1 R^{(2)}(t_2,t_1)\, E_{vis}(t-\ t_2;t_{IR}) E_{IR}(t-\ t_2-\ t_1) \tag{7}$$

Here $E_{SFG}^{(2)}(t;t_{IR})$ is the SFG signal, $R^{(2)}(t_2,t_1)$ is the molecular response, E_{vis} and E_{IR} are the visible and IR laser electric fields, t_1 is the time elapsed after the IR pulse interacts with the sample, t_2 is the time elapsed after the visible pulse interacts with the sample, and t_{IR} is the time between the peak maxima of the visible and IR pulses. If the nonresonant signal dephases quickly enough to be treated as instantaneous then

$$R^{(2)}(t_2,t_1) \approx\ R^{(1)}(t_1)\delta(t_2) \tag{8}$$

which, when combined with the approximation that E_{IR} (t) ≈ $\delta(t)$ allows Eq. 7 to be simplified to

$$E_{SFG}^{(2)}(t;t_{IR}) =\ E_{vis}(t;t_{IR})R^{(1)}(t) \tag{9}$$

This allows the visible pulse to act as a temporal window, which can be used to select portions of the SFG response that are free of nonresonant signal.[18] However, if the NR-SFG signal does not dephase instantaneously, the nonresonant signal cannot be removed from Eq. 7 and is still present in the detected VSFG signal.

Phase-sensitive SFG spectroscopy can be used to deal with nonresonant SFG signal in several ways, one of which is related to time-domain SFG detection. VSFG signal is complex, with both a real and imaginary component. Phase-sensitive SFG assumes that nonresonant signal is only present in the real component of SFG signal and that the phase of the nonresonant component is either 0 or π.[1] The fixed phase of the nonresonant signal component allows it to be

identified in time and removed from the overall signal.[19] It should be noted that this assumption is called into question by some of the experimental work discussed in Chapter 3 of this text.

In addition to removing a portion of the signal in the time-domain, phase sensitive SFG also allows for a series of scans to be taken with the sample and a known standard. This data can then be mathematically analyzed to deduce the resonant signal.[1] Much like time-domain VR-SFG suppression relies on the assumed instantaneous dephasing of NR-SFG, this approach relies on the assumed phase behavior of NR-SFG signal. The math behind this method is beyond the scope of this text but can be found in Reference 1.

To summarize, because NR-SFG signal can distort VSFG data, several methods have been developed to remove nonresonant signal contributions from SFG spectra.[1,13,15,18,20] Unfortunately, these methods can be complex and expensive, and are not readily available to many of the research groups working with SFG. A thorough understanding of NR-SFG is essential for these groups so that they can effectively avoid nonresonant signal contamination, as well as recognize when nonresonant contributions are present in a spectrum.

1.3: Brief Literature Review of Nonresonant SFG/SHG

The publications discussed here were chosen because they help explain the fundamental nature of nonresonant SFG signal and what experimental conditions can affect the nonresonant response, aid in the understanding of my work presented later, or may be useful in future work that develops from the research discussed in later chapters.

Some of the literature discussed in this section deals with second harmonic generation spectroscopy, (SHG) which is a degenerate form of SFG, where the excitation photons have the same energy. In this section, nonresonant SHG is assumed to be a reliable model for most forms

of nonresonant SFG. Although SHG requires the interaction of two excitation photons with the material, many SHG systems use only one excitation beam, where both of the excitation photons come from the same beam.

1.3.1: Excitation Wavelength and Pulse Shape

VSFG systems use a visible beam as the second excitation source. He et al.[17] used a scanning SFG system to investigate the effect of different visible excitation wavelengths on resonant and nonresonant SFG. As shown in Figure 1.3, the intensity of nonresonant signal from a bare gold surface more than doubles as the visible excitation wavelength is moved from 600 nm to 475 nm with the IR excitation source held constant at 3400 nm. They proposed that this wavelength dependence was related to surface phonons, which can be created by light in the 450-500 nm range on a gold surface and are believed to enhance SFG signal.

Another interesting finding from He et al.[17] is that the dephasing time for vibrationally-resonant SFG signal also varied with time. This work, shown in Figure 1.4, was done using a Au surface coated with 1-octadecanethiol (ODT) and looked at the dephasing time for the CH_3 ν_s, ν_{as}, and ν_{Fr} vibrational modes at visible excitation wavelengths ranging from 475 nm to 800 nm. Differences of up to a ps in dephasing time were observed, which the authors ascribe to influences from the electronic structure of the Au substrate.

The temporal and frequency profile of the excitation beams can also play a role in SFG signal generation, particularly in systems using time-delay nonresonant suppression.[14] The time delay nonresonant suppression method is generally used with a broadband IR and spectrally narrow visible pulse. The wider the visible pulse used, the less spectral resolution of resonant features the system has. A visible pulse shaped in time by an etalon with a sharp leading edge, such as the

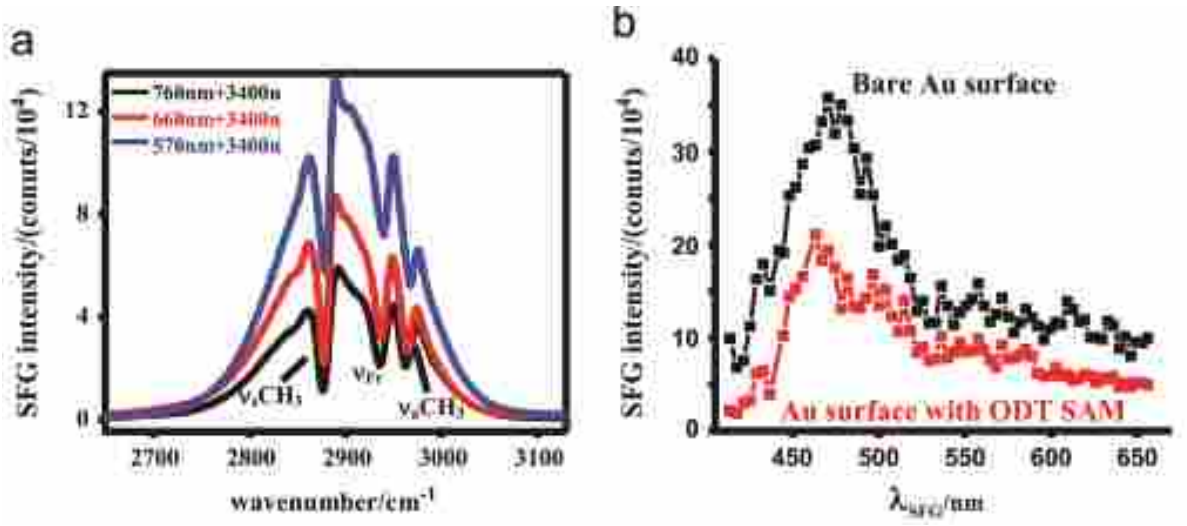

Figure 1.3. (a) SFG spectra of ODT coated Au at different visible excitation beam wavelengths, (b) peak intensity of NR-SFG signal from bare, and ODT SAM coated, Au surfaces at different visible excitation beam wavelengths. From reference 15.

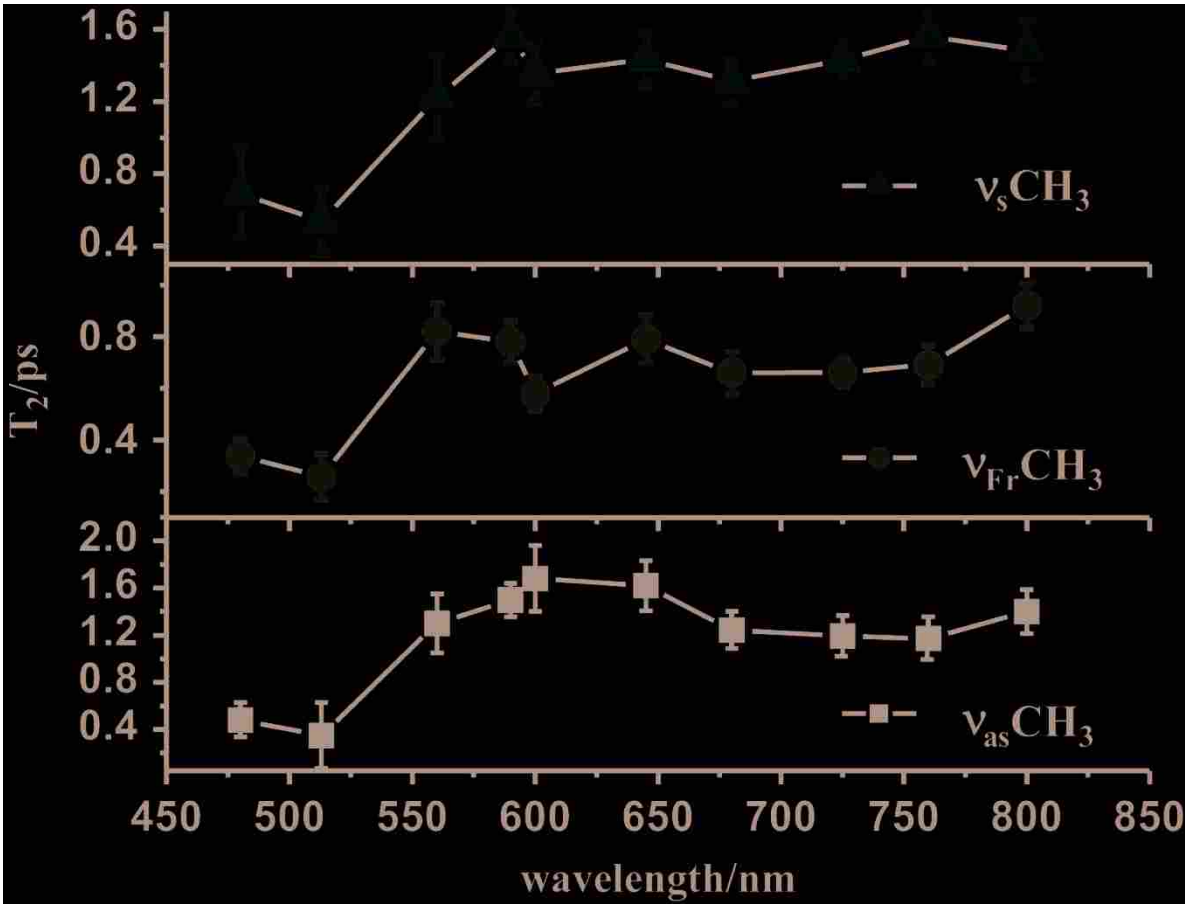

Figure 1.4. The vibrational dephasing time of the ν_s, ν_{Fr}, and ν_{as} C-H vibrational modes at different visible excitation beam wavelengths. From reference 15.

one shown in Figure 1.5, brings the visible peak closer in time to the IR pulse peak without up-converting nonresonant signal. This can allow for a more efficient suppression of nonresonant signal components and better upconversion of resonant signal components.[14]

1.3.2 Sample Charge

The charge of the sample or sample substrate has also been found to affect the amount of nonresonant signal that is generated.[2] Figure 1.6 shows an example of this work where Zhao et al. [21] studied platinum electrodes in a 0.1 M perchloric acid solution. Here the nonresonant response shows an interesting correlation to the charge of the scanned electrode. The signal intensity goes down as the potential becomes more positive until the potential reaches 0.22 V, where the nonresonant SFG signal intensity begins to climb. Changes in the amount and nature of adsorbates are also known to affect the nonresonant response. They concluded that this was not a factor in these experiments because little to no OH vibrations were detected on the electrode. Resonant VSFG intensity has also been found to be sensitive to the charge of the substrate, with different stretching modes exhibiting unique responses.[2]

The sensitivity of SFG signal to regional charge has some interesting implications for aqueous systems. For example, changing the pH of an aqueous solution containing $\beta-$lactoglobulin (BLG), bovine serum albumin (BSA), or lysozyme (LSZ) caused changes in the interfacial charge at the air/liquid interface, [22] which are shown in Figure 1.7. As the pH increased, the methyl, methylene, and aromatic VSFG signal at the left of the spectra are suppressed and the signal intensity from OH stretches, shown in the middle of the spectra,

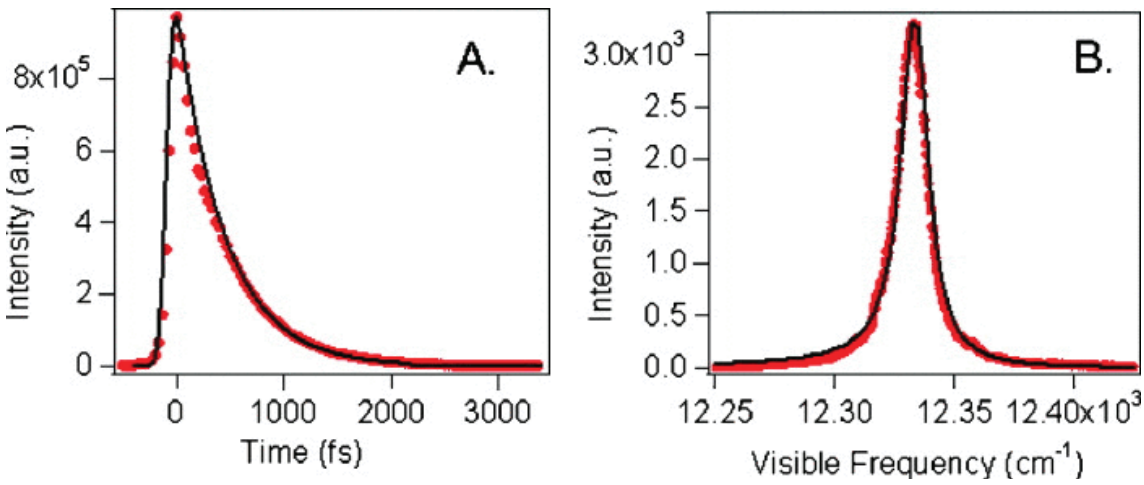

Figure 1.5. (a) Temporal profile of a narow-band visible pulse shaped by an air-space etalon, (b) spectrum of the pulse. From reference 3.

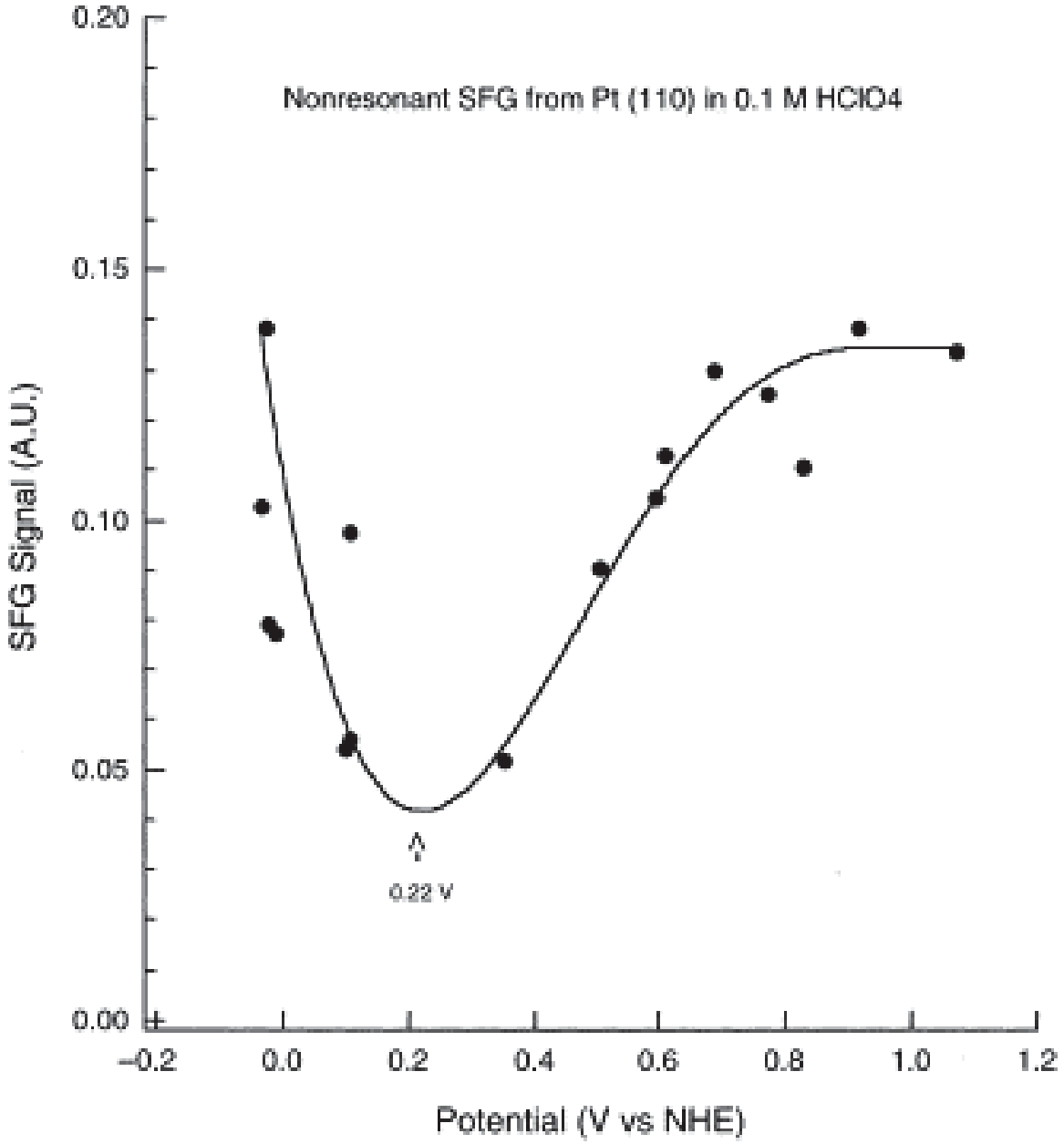

Figure 1.6. NR-SFG signal intensity as a function of the applied potential on a Pt(110) electrode in 0.1M perchloric acid. The line represents a fifth-order polynomial fit. From reference 2.

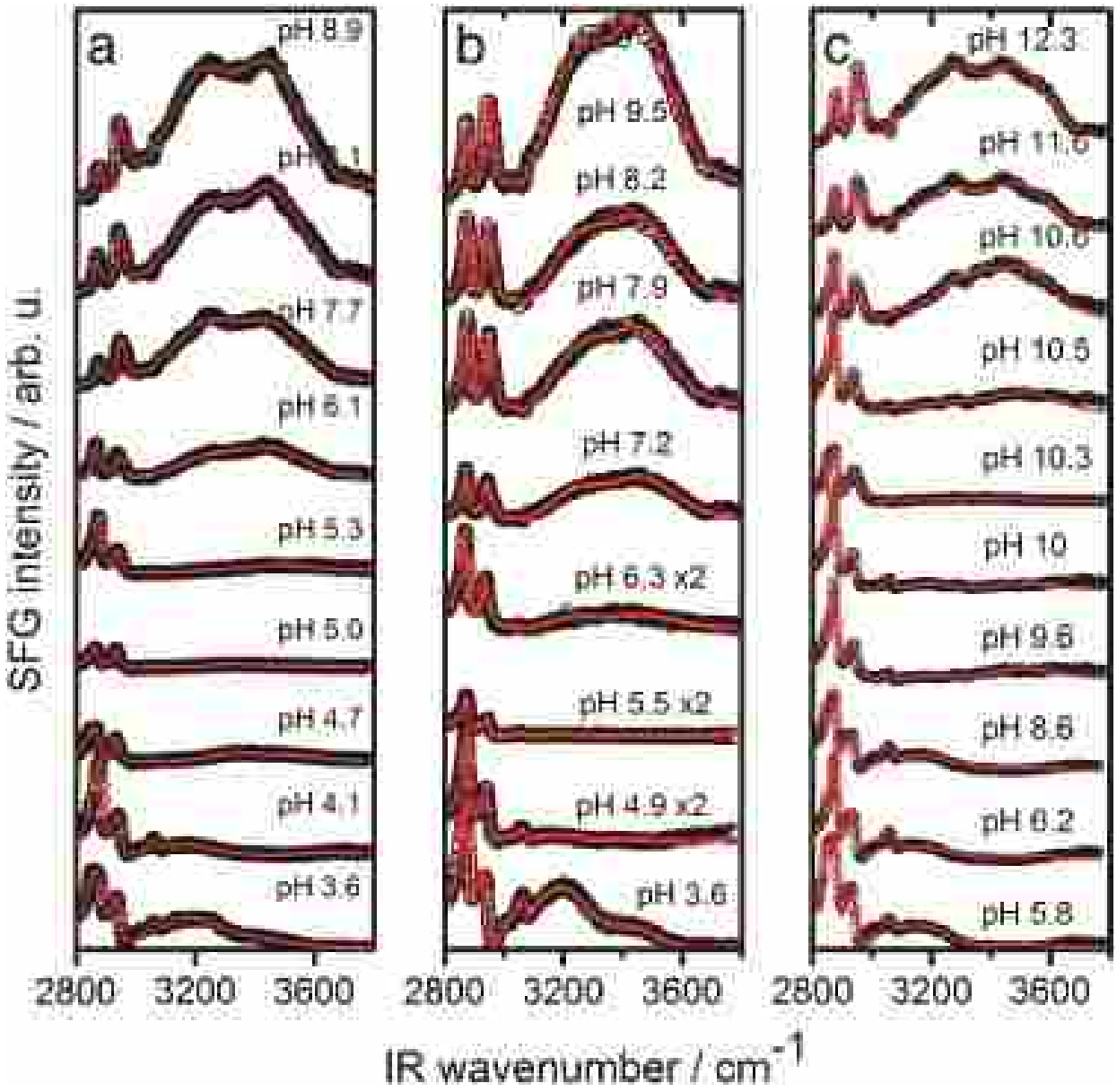

Figure 1.7. VSFG spectra of the air-water interface of (a) β-lactoglobulin (BLG), (b) bovine serum albumin (BSA), and (c) lysozyme (LSZ) proteins at different electrolyte pH levels. From reference 19.

increased significantly. It was also found that the presence of NaCl in a solution could mask an applied charge at a fused silica/water and polystyrene/water interface.[22]

Fundamental thermodynamic values, such as surface pK_a, have been determined using the sensitivity of nonresonant SHG to interfacial charge. In Figure 1.8, an acid functionalized silica surface/water interface was interrogated with nonresonant SHG at different pH levels and salt concentrations.[23] The surface charge was determined from the intensity of the SHG response, which was used along with the SHG data from different ion concentrations (shown in the inset), to calculate the pK_a for two observed acid base equilibria at the studied interface.

SFG can directly probe an interfacial potentials with the application of the $\chi^{(3)}$ method.[24] This is done by adding a third-order, nonlinear optical term to the standard, second-order SFG optical response.[25] The third-order nonlinear susceptibility can be coupled with the two excitation beam electric fields and the static electric field charge from the interfacial potential, which allows the interfacial potential to be probed.[24]

1.3.3: Quadrupole and Magnetism Contributions to Nonresonant SFG

Although often ignored, the electric quadrupole and magnetic dipole can both provide significant amounts of nonresonant SFG signal.[2] For example, the surface of liquid hexane, which has no dipole, produces nearly as much nonresonant signal as the surface of water, which has a strong dipole. The best explanation for this observed behavior is that the hexane quadrupoles are able to generate significant nonresonant SFG signal.[26]

Another possible example of quadrupole-related SFG signal comes from work done by Cremer et al.,[27] which is shown in Figure 1.1. Here SFG spectra were taken of ethylene that had absorbed onto a Pt(111) surface in two different ways. In panel **a** the molecule is adsorbed side

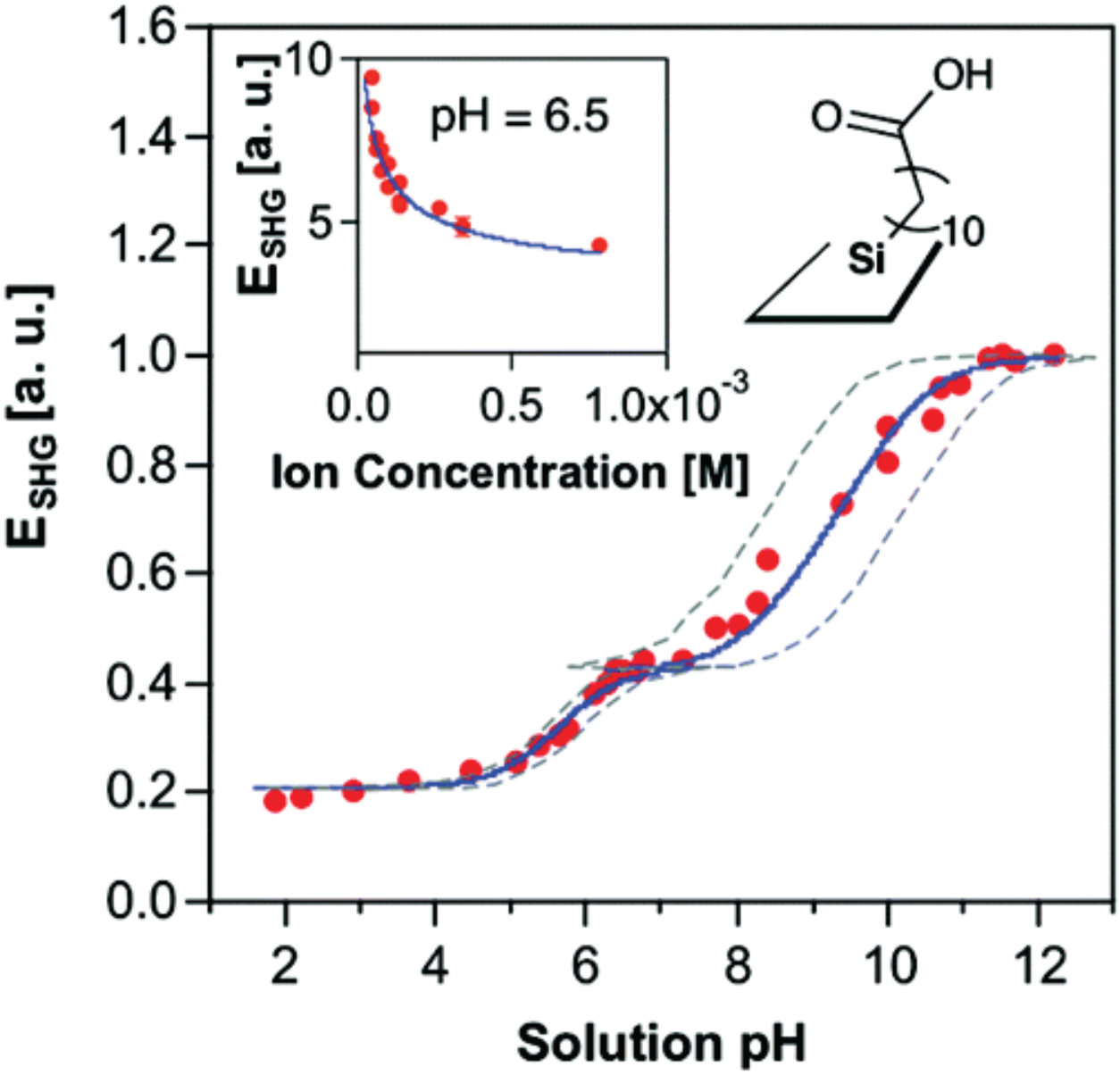

Figure 1.8. SHG electric field (E_{SHG}) as a function of pH from an acid-functionalized silica/water interface at room temperature. The solid line is the pKa fit, with the dashed lines showing 1 standard deviation from that fit. The inset shows E_{SHG} as a function of salt concentration in the bulk at a pH of 6.5. From reference 20.

on, while in panel **b** it has a head on orientation. Although not discussed in the text, both spectra display the derivative line shape associated with nonresonant and resonant signal interference. The spectrum from the side bonded ethylene in panel **a**, however, has a more Gaussian profile, a deeper dip at the right edge of the peak, and a more pronounced difference between the apparent left and right baselines. All of these features indicate a stronger nonresonant signal from the side bonded samples. This larger nonresonant signal may be caused by the adsorbed molecules enhancing the ability of the substrate to generate NR-SFG; it may be directly produced from the ethylene quadrupole, which is available to generate signal in the side-on conformation, but not end on.

The potential for nonresonant signal production from electric quadrupoles should be taken into consideration by researchers. Because SFG signal originating from electric quadrupoles does not have the same symmetry constraints as the electric dipole, SFG signal can be generated from an isotropic bulk.[2] This means that in many systems a small quadrupole susceptibility can still generate significant amounts of nonresonant signal and interfere with resonant signal from the surface of interest.

Magnetic dipoles can also generate enough nonresonant signal to be problematic. In fact, SHG has been used to investigate surface magnetism.[2] The discovery of SHG sensitivity to surface magnetism was done using a Fe(110) single crystal held between the jaws of an electromagnet, which aligned the magnetic domains in the sample.[28] SHG signal was taken with both an "up" and "down" magnetization. Both magnetic field directions were perpendicular to the plane of incidence of the SHG beams and pointed in opposite directions. Figure 1.9 shows a schematic of the experimental setup with the magnetic field in the up direction. Samples were scanned under ultra-high vacuum at three different times after sample preparation with typical

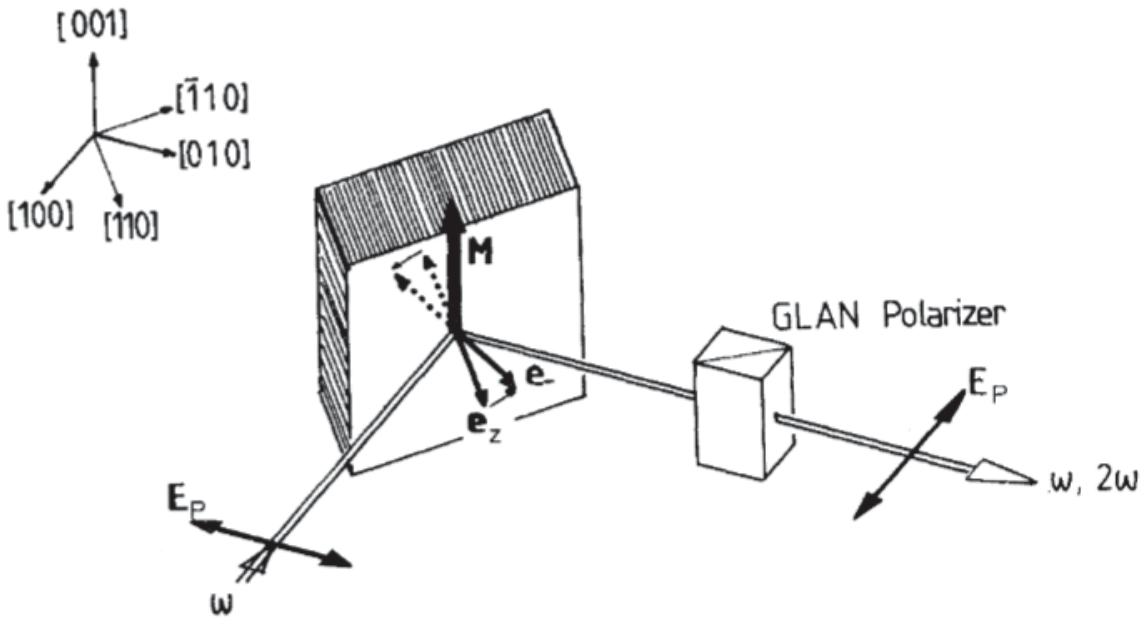

Figure 1.9. Schematic of the experimental setup with relevant crystalographic directions shown in the inset. Sample magnetization was along the 001 direction. The excitation beam and SHG signal were both P polarized. From reference 26.

results shown in Figure 1.10. SHG signal was taken from 250 shots at each time. Each shot was normalized to the expected SHG signal from a standard Fe(110) single crystal sample for Figure 1.10 with the horizontal bars showing the average of these shots. The loss of the magnetized effect over time was ascribed to the absorption of CO to the sample surface.[28]

Section 1.3.4: Surface Adsorption

Nonresonant SFG/SHG signal has often been used to track or detect the absorption of molecules onto a conducting or semiconducting substrate. Examples include tracking surface contaminants on Ag, Si, and Ge, Na adsorption onto clean Ge, O_2 adsorption onto Si(111),[2] thiocyanate onto gold electrodes,[29] CO on Pt,[30] and CO on W(110).[31] Nonresonant SFG has been shown to be sensitive to both the nature and quantity of the adsorbate.[21] Nonresonant SFG signal has also been found to increase as the work function decreases in response to the adsorption of O_2 onto a W(110) surface,[31] as is shown in Figure 1.11. Changes in the nonresonant signal have also been observed from silicon wafers and gold when coated with a polystyrene thin film,[12] and from soda lime glass in response to surface contamination (discussed in more detail in section 3.3.2).

Section 1.3.5: Surface Plasmon Enhancement of Nonresonant SFG and the Importance of Linear Optical Constants

In the late 1980s, theoretical calculations suggested that nonresonant SHG intensity should be enhanced by one or more orders of magnitude, relative to the bare reflector, when coupling with one of several forms of surface plasmons.[32] This prediction has since been experimentally confirmed.[2] Further work has shown that SHG signal enhancement from surface plasmons can

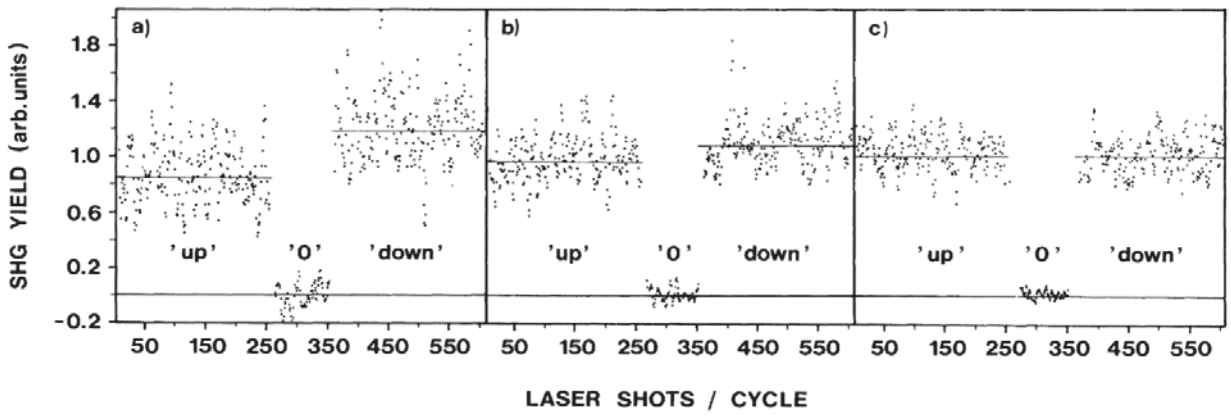

Figure 1.10. SHG signal intensity with the magnetic field pointing up (as shown in Figure 1.9) and down at (a) 45 min, (b) 60 min, and (c) 180 min after sample preparation. Solid lines represent the average of the 250 shots at each orientation. SHG signal was normalized to the expected signal level from the sample without the influence of magnetization. From reference 26.

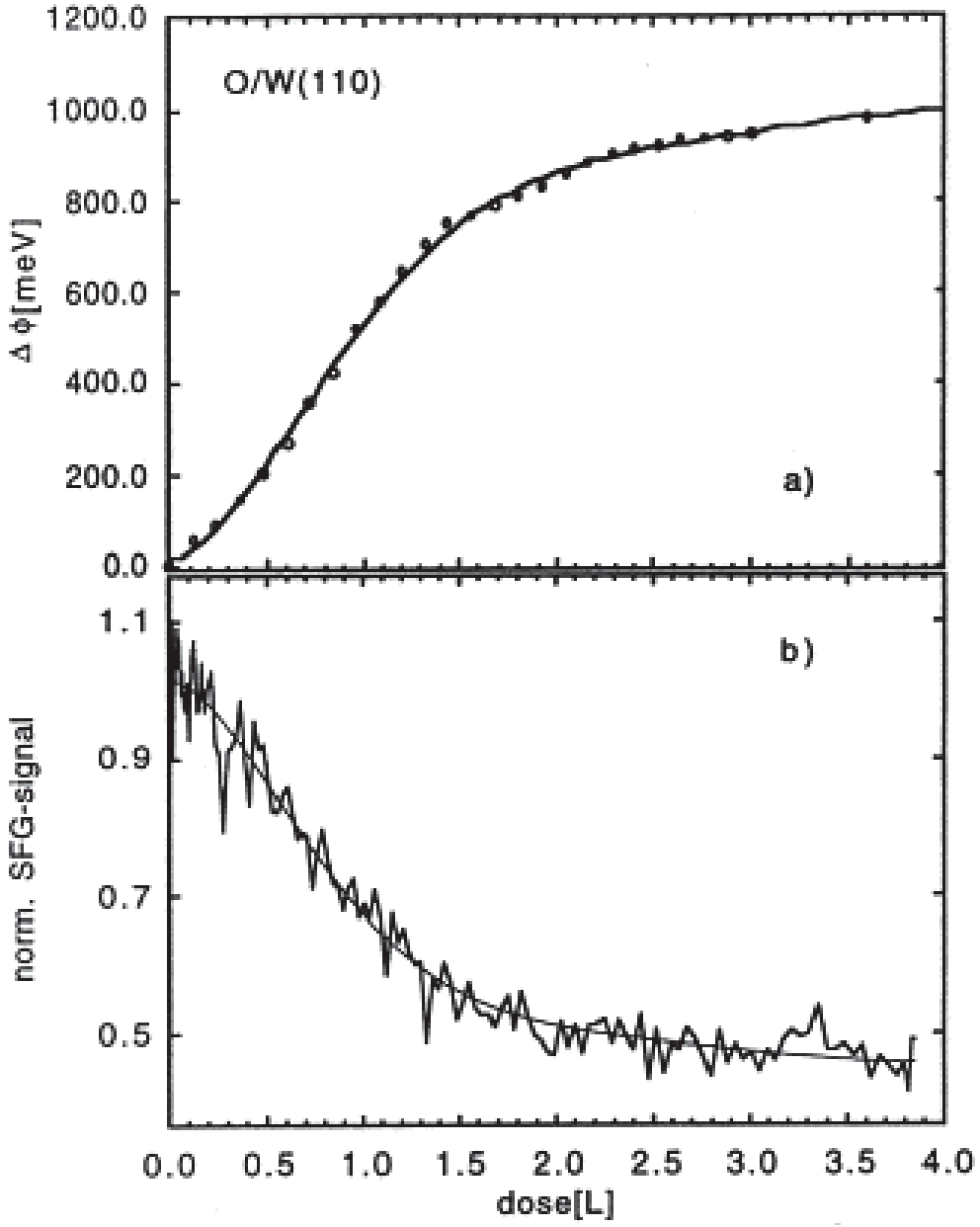

Figure 1.11. (a) NR-SFG signal intensity and (b) substrate work function during O2 adsorption onto a W(110) substrate. From reference 29.

be predicted by calculations similar to those used in surface enhanced Raman scattering (SERS).[2,33]

The coupling of nonresonant SFG with surface plasmons helps to explain the increase in nonresonant SHG signal produced from roughened conductor surfaces.[2,34,35] Further understanding can be gained by considering theoretical work for SERS, which found that only non-radiative plasmons form on a smooth surface. These non-radiative plasmons can't enhance the Raman signal,[36] and are likely to have a similar relationship with SFG. In addition to allowing for the formation of SHG enhancing plasmons, roughening a surface may also make it possible for the excitation beams to couple with surface plasmons more strongly.[32] Even without coupling to plasmons, roughening the surface may still allow for increased nonresonant signal if the processing creates asymmetry in the local field and orthogonal polarization components in that field.[37]

Another significant and often overlooked factor in the intensity of nonresonant SFG signal is the linear ability of a material to absorb and emit photons at the SFG excitation and signal wavelengths. This was well expressed by Krause et al.[35] when they wrote "Interestingly, the aluminum sample has the highest bulk susceptibility, even though silver produces the strongest SHG signal….The result that the $\chi^{(2)}$ of aluminum is larger than the $\chi^{(2)}$ of silver clearly demonstrates that the total SHG yield depends not only on surface condition and the nonlinear susceptibility but also on the linear optical constants at both the linear frequency ω and the nonlinear frequency 2ω." This means that the ability of the material to absorb and emit radiation of the SFG excitation and signal frequency can affect the amount of SFG signal generated.

1.3.6: Effects of Crystal Structure

As mentioned in the previous section, roughening a sample surface can increase the nonresonant SFG/SHG signal.[2,34,35] At a more atomic level, lattice dislocations, defects, and lattice strain also have an effect on the amount of nonresonant signal generated.[38-41] Vazquez et al.[39] showed that, in at least some cases, dislocations had a much stronger effect on the nonresonant signal than surface roughening. Their work was focused on improving the surface quality of laser waveguides with Nd:YAG as the material of interest. Standard polishing methods create dislocations just below the material surface which interfere with the smooth transmission of light. To remove the dislocations created by polishing, the crystal was bombarded by accelerated Ne and N atoms with energies as high as 2 MeV. In addition to removing the buried dislocations, the bombardment also roughened the surface**.** After bombardment, the crystal was resmoothed by immersion in an orthophosphoric acid bath, the results of which are shown in Figure 1.12 where panel **a** is after one smoothing bath, and panel **b** is after two. During this process SHG was used to track the removal of dislocations. These results are shown in Figure 1.13, where the signal drops by roughly 90% after bombardment and then increases again after each acid treatment. The authors did not speculate as to why the acid treatment caused the SHG signal level to change.

Theoretical work by Lyubchanskii et al. [40] showed that lattice dislocations do not produce SHG at all symmetry-allowed polarization combinations. The work was done using a polarization analysis of scattered second harmonic light to separate the terms of a nonlinear photoelastic tensor. Using this process, it was found that lattice strain was able to generate SHG signal at all polarization combinations. Lattice dislocations, however, were only available to generate P polarized signal with either a P or S polarized excitation beam.

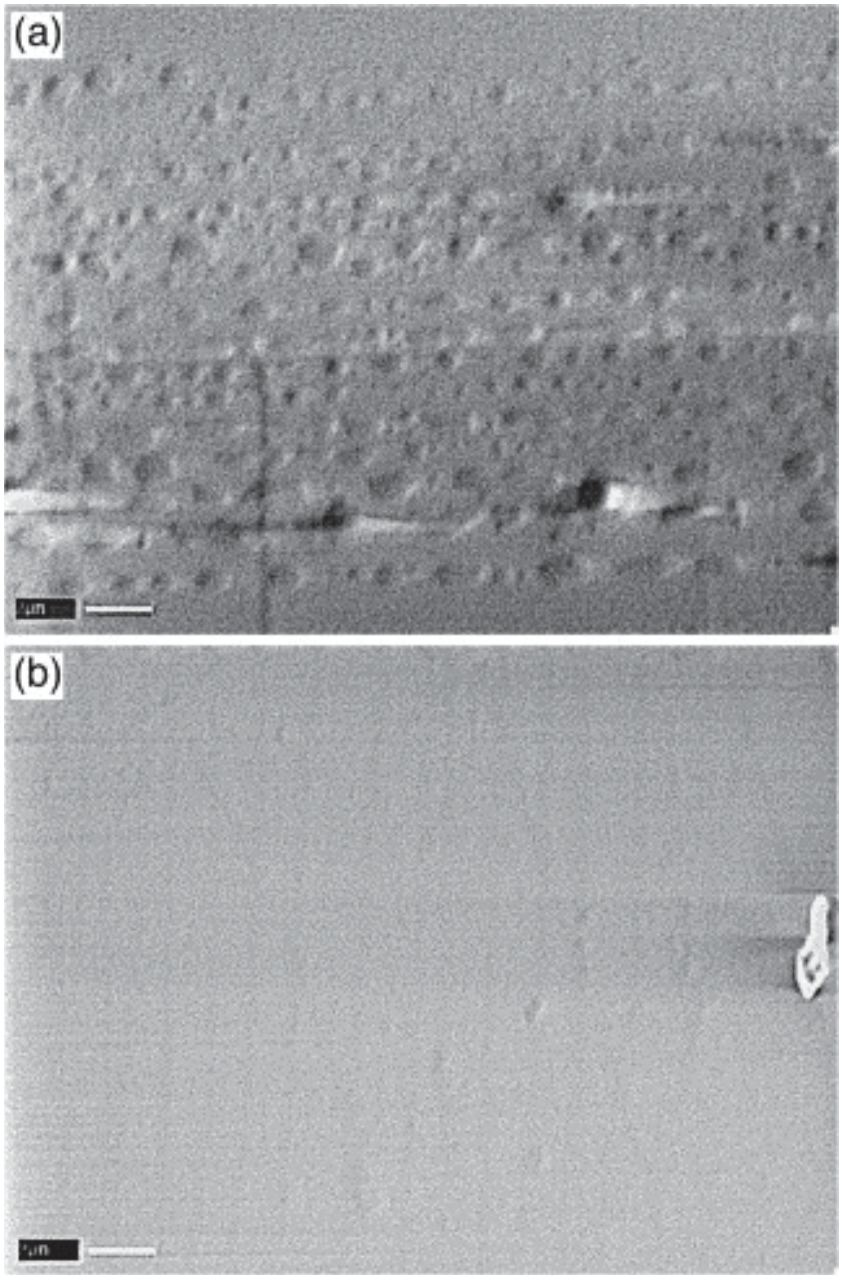

Figure 1.12. SEM images of Nd:YAG crystal face after bombardment with nitrogen ions and (a) one or (b) two orthophosporic acid baths. From reference 37.

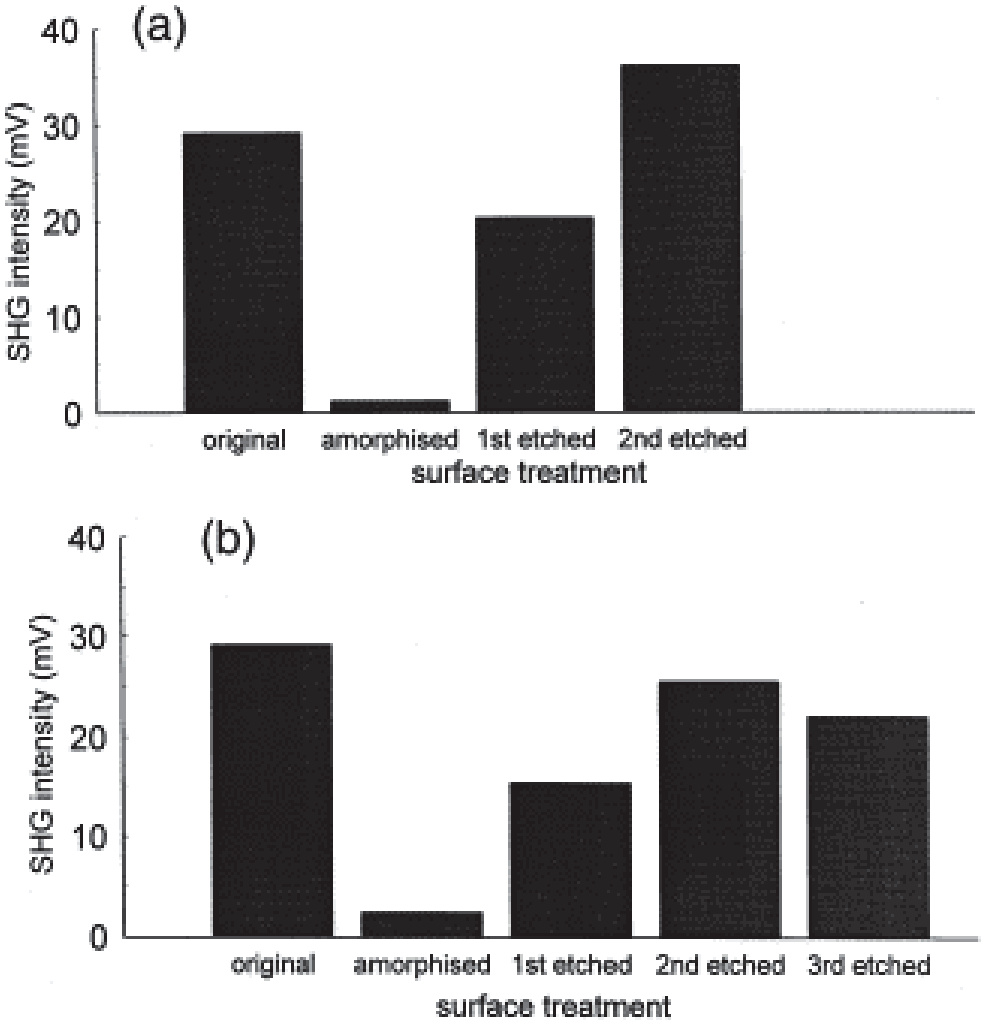

Figure 1.13. SHG signal intensity for Nd:YAG samples. Amorphisation accomplished with bombardment from (a) neon ions, and (b) nitrogen ions. From reference 37.

Differences in the morphology of crystal surfaces can also play a role in the amount of nonresonant SFG/SHG signal generated. Pt(100) and Pt (110) electrodes were found to respond differently to charging in a 0.1 M perchloric acid solution.[21] SHG was used to detect the reconstruction of Au(111) surfaces after coating with an alkyl thiol monolayer.[42] SHG was also used to detect the reconstruction of the buried GaAs surface at the ZnSe/GaAs(001) interface.[43]

Texture in polycrystalline materials and the azimuthal angle in (111) single crystals have also been shown to affect nonresonant SFG/SHG signal. Clean Al (111) surfaces were investigated with SHG and found to have different SHG responses at different azimuthal angles.[44] The nonresonant SFG response (PPP polarization) from Au(111) single crystals coated in octadecanethiol, shown in Figure 1.14, were found to oscillate as the azimuthal angle was changed with a 60° periodicity. It was also discovered that the relative phase between the resonant and nonresonant signal was different at different azimuthal angles, as is shown in Figure 1.2. These findings are similar to our own results with polystyrene coated Si(111) wafers, which are discussed in Chapter 3.

Nonresonant SHG has been used to detect texture in extruded aluminum as well as barium titanate thin films.[41,45] As with the single crystal samples discussed in the previous paragraph, these polycrystalline samples were scanned at a range of azimuthal angles. The results for extruded aluminum can be seen in Figure 1.15 and show a 90° periodicity with a 180° periodicity in maximum SHG intensity. It is particularly interesting to note that the SHG intensity pattern observed for extruded aluminum is very similar to the pattern produced by rotating the excitation beam polarization on *a*-textured barium titanate thin films, shown in Figure 1.16. Here *a*-textured growth has the c axis parallel to the substrate surface, and *c*-textured growth (shown in Figure 1.17) has the c axis perpendicular to the substrate surface. Like the *a*-textured thin film, the

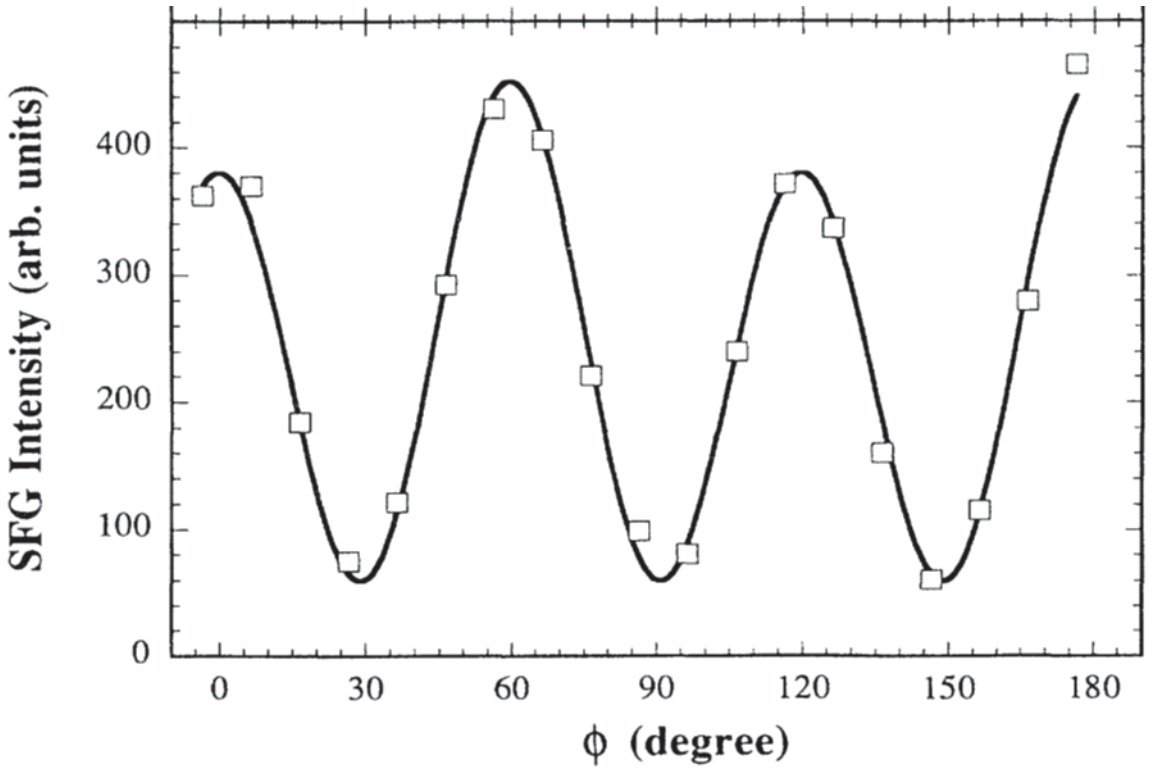

Figure 1.14. NR-SFG signal intensity from ODT/Au(111) as a function of the azimuthal angle. From reference 42.

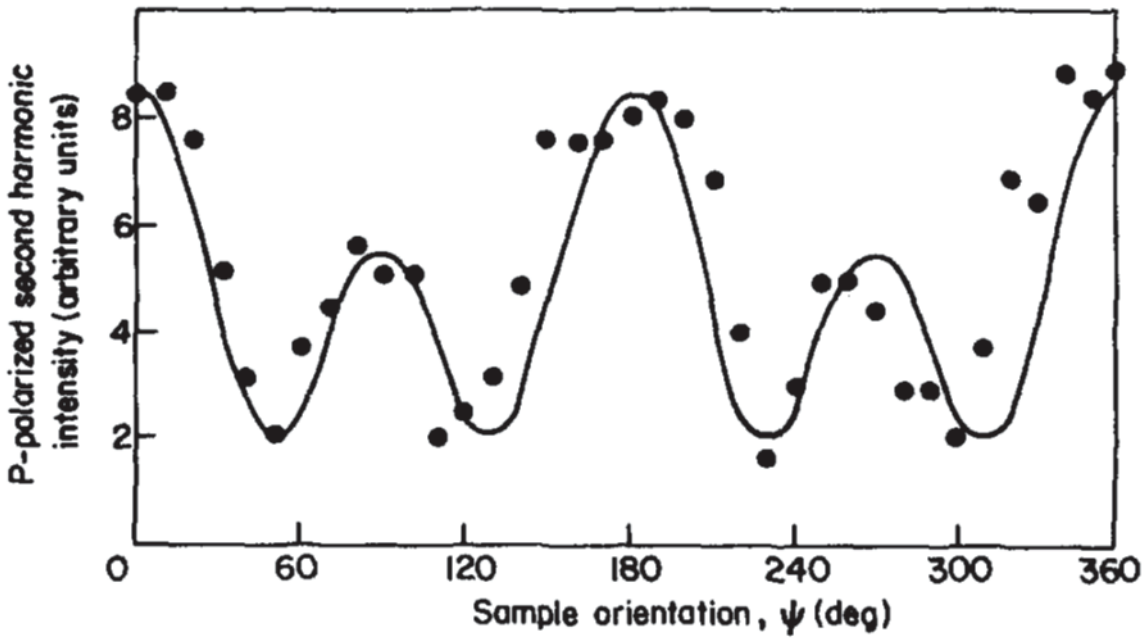

Figure 1.15. P polarized SHG signal intensity as a function of azimuthal angle from an extruded aluminum sample. From reference 44.

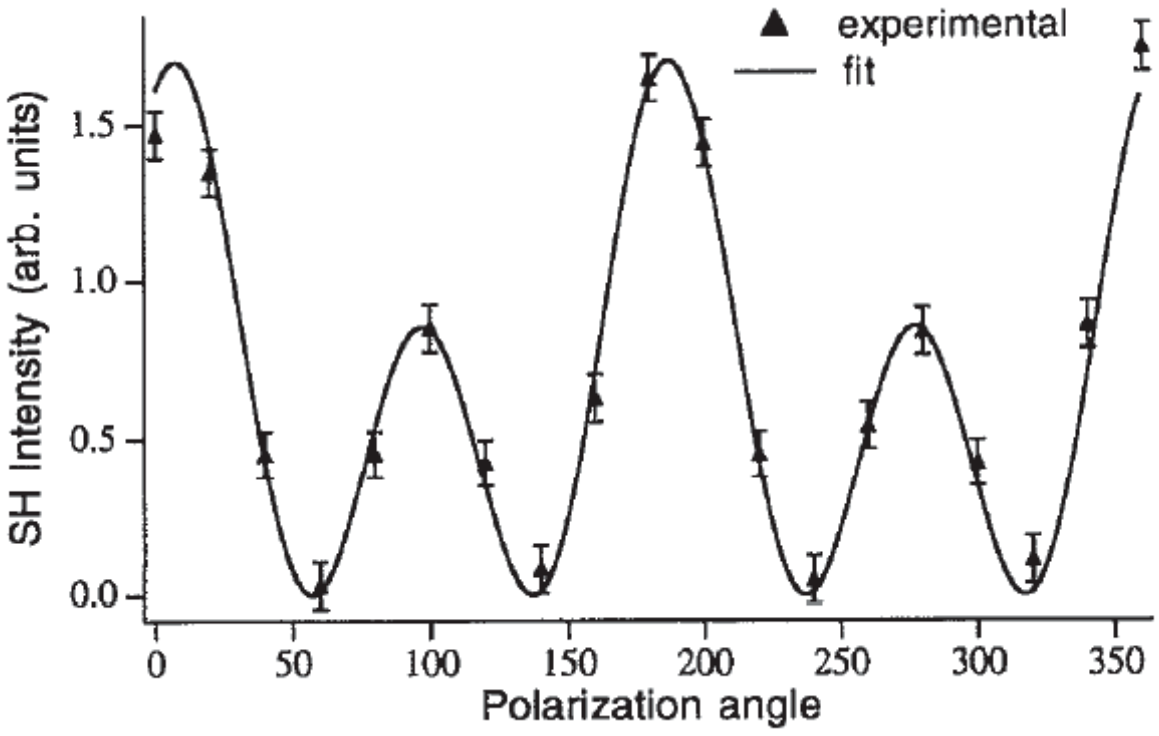

Figure 1.16. P polarized SHG signal intensity as a function of the excitation beam polarization angle from *a*-textured barium titanate thin film. From reference 39.

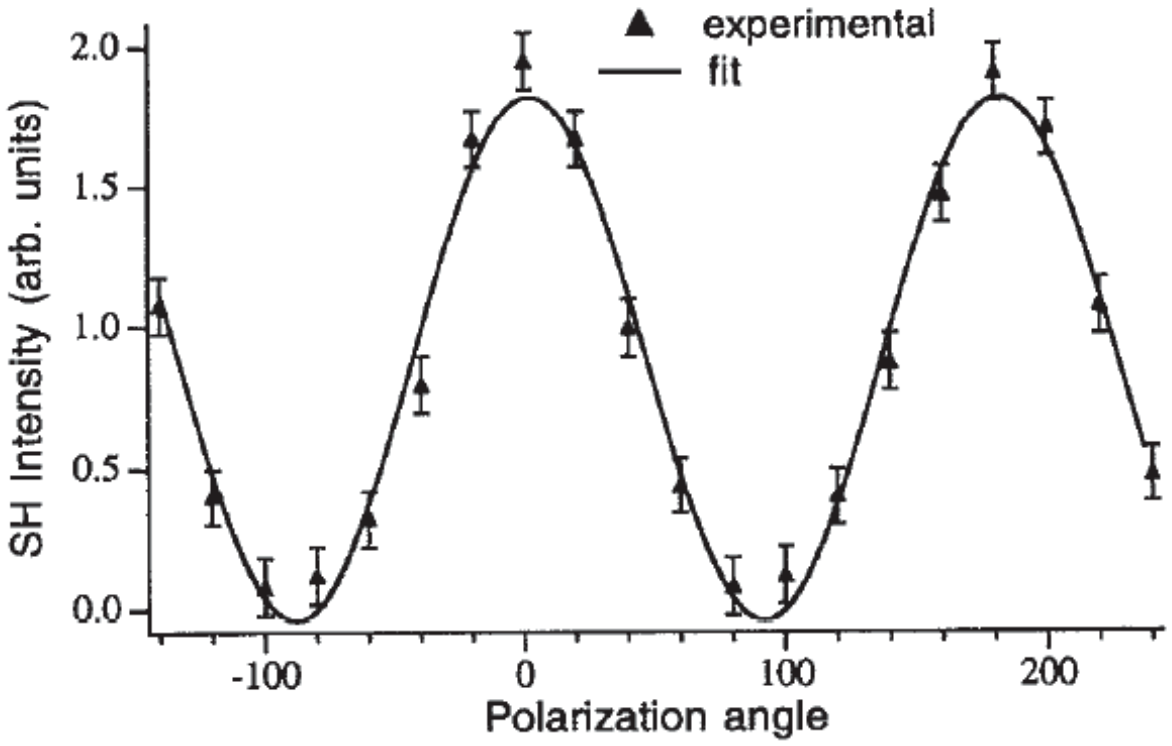

Figure 1.17. P polarized SHG signal intensity as a function of the excitation beam polarization angle from *c*-textured barium titanate thin film. From reference 39.

c-textured film also has a 90° periodicity, but the *c*-textured film does not have the alternating peak heights exhibited by both extruded aluminum and *a*-textured barium titanate thin films.

Differences in the orientation of the crystals can also produce different amounts of nonresonant SFG signal.[46] Figure 1.18 shows an example of this. Here polycrystalline copper covered with an ODT monolayer was imaged with optical microscopy (panels **a** and **c**) and SFG microscopy (panels **b** and **d**). Grain boundaries are highlighted in the SFG images with red lines. Differences in the intensity of NR-SFG signal were used to identify much smaller domains than can be seen with optical microscopy. Electron backscattering diffraction (EBSD) was used to confirm that the domains identified with nonresonant SFG correspond to different crystal facets at the surface of the copper.

1.4: Conclusion

SFG can be a powerful analytical tool with the ability to gain surface specific chemical and morphological information unavailable to any other established technique. Nonresonant SFG signal components, however, can interfere with resonant SFG signal and change the detected spectrum. A wide range of physical conditions can change the nonresonant SFG signal intensity. This means that the nonresonant signal component cannot be ignored or treated as a consistent background.

Several methods have been developed to account for nonresonant SFG signal, all of which are based on the idea that the nonresonant SFG signal dephases, and thus effectively disappears, as soon as one or more of the excitation sources is removed, while resonant signal components can persist. Time-delay methods bring in the visible excitation source after the IR source has left,

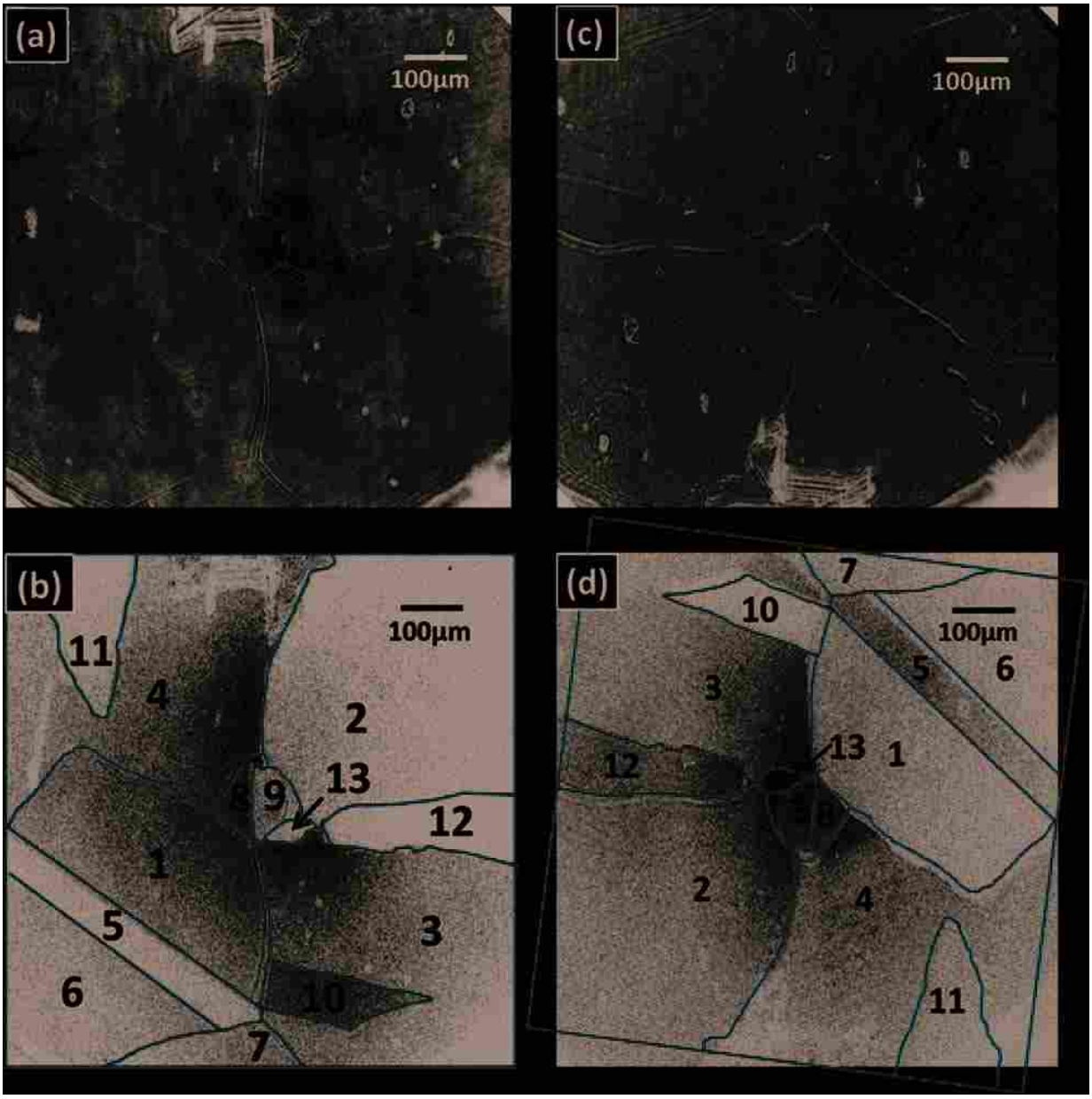

Figure 1.18. (a) Optical image and (b) unprocessed NR-SFG image of polycrystalline copper with an ODT monolayer at azimuthal angle 0°. Optical image and (c) (b) unprocessed NR-SFG image of polycrystalline copper with an ODT monolayer at azimuthal angle 180° with the grain boundaries marked in red. From reference 44.

leaving a portion of the resonant signal to be detected in the frequency-domain. Time-domain and phase-sensitive methods detect the SFG signal in time and rely on mathematical treatments as well as the assumption that nonresonant signal is locked into a given time window, to remove nonresonant components from the detected signal.

Nonresonant SFG signal has been shown to be useful in acquiring information about the morphology of crystalline materials as well as physical information, such as material charge at a surface or interface, adsorbate density, and crystalline defects. Much of my work discussed later involves either learning more about the nature of nonresonant SFG signal, using nonresonant signal to detect material damage, or developing ways to accurately analyze VSFG signal that contains nonresonant components.

1.5: References

(1) Shen, Y. R. Phase-Sensitive Sum-Frequency Spectroscopy. *Annual Review of Physical Chemistry* **2013**, *64*, 129-150.

(2) Shen, Y. R.: *Cambridge Molecular Science : Fundamentals of Sum-Frequency Spectroscopy*; Cambridge University Press: Cambridge, United Kingdom, 2016.

(3) van der Ham, E. W. M.; Vrehen, Q. H. F.; Eliel, E. R. High-resolution sum-frequency spectra using broadband laser sources. *Vibrations at Surfaces* **1996**, *368*, 96-101.

(4) Richter, L. J.; Petralli-Mallow, T. P.; Stephenson, J. C. Vibrationally resolved sum-frequency generation with broad-bandwidth infrared pulses. *Optics Letters* **1998**, *23*, 1594-1596.

(5) Khatib, R.; Backus, E. H. G.; Bonn, M.; Perez-Haro, M.-J.; Gaigeot, M.-P.; Sulpizi, M. Water orientation and hydrogen-bond structure at the fluorite/water interface. **2016**, *6*, 24287.

(6) Curtis, A. D.; Calchera, A. R.; Asplund, M. C.; Patterson, J. E. Observation of sub-surface phenyl rings in polystyrene with vibrationally resonant sum-frequency generation. **2013**, *68*, 71-81.

(7) Hirose, C.; Akamatsu, N.; Domen, K. Formulas for the Analysis of the Surface SFG Spectrum and Transformation Coefficients of Cartesian SFG Tensor Components. *Applied Spectroscopy* **1992**, *46*, 1051-1072.

(8) Guyot-Sionnest, P.; Hunt, J. H.; Shen, Y. R. Sum-frequency vibrational spectroscopy of a Langmuir film: Study of molecular orientation of a two-dimensional system. *Physical Review Letters* **1987**, *59*, 1597-1600.

(9) Wang, H.-F.; Velarde, L.; Gan, W.; Fu, L. Quantitative Sum-Frequency Generation Vibrational Spectroscopy of Molecular Surfaces and Interfaces: Lineshape, Polarization, and Orientation. *Annual Review of Physical Chemistry* **2015**, *66*, 189-216.

(10) Simpson, G. J.; Rowlen, K. L. An SHG Magic Angle: Dependence of Second Harmonic Generation Orientation Measurements on the Width of the Orientation Distribution. *Journal of the American Chemical Society* **1999**, *121*, 2635-2636.

(11) Quast, A. D.; Curtis, A. D.; Horn, B. A.; Goates, S. R.; Patterson, J. E. Role of Nonresonant Sum-Frequency Generation in the Investigation of Model Liquid Chromatography Systems. *Analytical Chemistry* **2012**, *84*, 1862-1870.

(12) Curtis, A. D.; Reynolds, S. B.; Calchera, A. R.; Patterson, J. E. Understanding the Role of Nonresonant Sum-Frequency Generation from Polystyrene Thin Films. *The Journal of Physical Chemistry Letters* **2010**, *1*, 2435-2439.

(13) Lagutchev, A.; Hambir, S. A.; Dlott, D. D. Nonresonant Background Suppression in Broadband Vibrational Sum-Frequency Generation Spectroscopy. *The Journal of Physical Chemistry C* **2007**, *111*, 13645-13647.

(14) Stiopkin, I. V.; Jayathilake, H. D.; Weeraman, C.; Benderskii, A. V. Temporal effects on spectroscopic line shapes, resolution, and sensitivity of the broad-band sum frequency generation. *The Journal of Chemical Physics* **2010**, *132*, 234503.

(15) Curtis, A. D.; Asplund, M. C.; Patterson, J. E. Use of Variable Time-Delay Sum-Frequency Generation for Improved Spectroscopic Analysis. *The Journal of Physical Chemistry C* **2011**, *115*, 19303-19310.

(16) Calchera, A. R. Obstacles And Solutions To Studying Functional Adhesives Using Vibrational Sum-Frequency Generation Spectroscopy. Brigham Young University, 2013.

(17) He, Y.; Chen, G.; Xu, M.; Liu, Y.; Wang, Z. Vibrational dephasing of self-assembling monolayer on gold surface. *18th International Conference on Dynamical Processes in Excited States of Solids* **2014**, *152*, 244-246.

(18) Laaser, J. E.; Xiong, W.; Zanni, M. T. Time-Domain SFG Spectroscopy Using Mid-IR Pulse Shaping: Practical and Intrinsic Advantages. *The Journal of Physical Chemistry B* **2011**, *115*, 2536-2546.

(19) Stiopkin, I. V.; Jayathilake, H. D.; Bordenyuk, A. N.; Benderskii, A. V. Heterodyne-Detected Vibrational Sum Frequency Generation Spectroscopy. *Journal of the American Chemical Society* **2008**, *130*, 2271-2275.

(20) Roke, S.; Kleyn, A. W.; Bonn, M. Time- vs. frequency-domain femtosecond surface sum frequency generation. **2003**, *370*, 227-232.

(21) Zheng, W. Q.; Pluchery, O.; Tadjeddine, A. SFG study of platinum electrodes in perchloric acid solutions. **2002**, *502–503*, 490-497.

(22) Engelhardt, K.; Peukert, W.; Braunschweig, B. Vibrational sum-frequency generation at protein modified air–water interfaces: Effects of molecular structure and surface charging. **2014**, *19*, 207-215.

(23) Konek, C. T.; Musorrafiti, M. J.; Al-Abadleh, H. A.; Bertin, P. A.; Nguyen, S. T.; Geiger, F. M. Interfacial Acidities, Charge Densities, Potentials, and Energies of Carboxylic Acid-Functionalized Silica/Water Interfaces Determined by Second Harmonic Generation. *Journal of the American Chemical Society* **2004**, *126*, 11754-11755.

(24) Geiger, F. M. Second Harmonic Generation, Sum Frequency Generation, and χ(3): Dissecting Environmental Interfaces with a Nonlinear Optical Swiss Army Knife. *Annual Review of Physical Chemistry* **2009**, *60*, 61-83.

(25) Zhao, X.; Subrahmanyan, S.; Eisenthal, K. B. Determination of pKa at the air/water interface by second harmonic generation. **1990**, *171*, 558-562.

(26) Electric quadrupole contribution to the nonresonant background of sum frequency generation at air/liquid interfaces. *The Journal of Chemical Physics* **2011**, *134*, 184705.

(27) Cremer, P. S.; Su, X.; Shen, Y. R.; Somorjai, G. A. Ethylene Hydrogenation on Pt(111) Monitored in Situ at High Pressures Using Sum Frequency Generation. *Journal of the American Chemical Society* **1996**, *118*, 2942-2949.

(28) Reif, J.; Zink, J. C.; Schneider, C. M.; Kirschner, J. Effects of surface magnetism on optical second harmonic generation. *Physical Review Letters* **1991**, *67*, 2878-2881.

(29) Wang, J.; Xu, M.; Huangfu, Z.; Wang, Y.; He, Y.; Guo, W.; Wang, Z. Observation of gold electrode surface response to the adsorption and oxidation of thiocyanate in acidic electrolyte with broadband sum-frequency generation spectroscopy. **2016**, *85*, 122-127.

(30) Somorgai, G.; Li, Y.: *Introduction to Surface Chemistry and Catalysis*; 2 ed.; John Wiley and Sons, Inc.: Hoboken, New Jersey, 2010.

(31) Schröder, U.; Guyot-Sionnest, P. Optical sum frequency studies of adsorption and laser-induced desorption of CO on W(110). **1999**, *421*, 53-58.

(32) Tzeng, C.-C.; Lue, J. T. Nonlinear optical generation from noble metals and aluminum films in various geometric configurations. *Physical Review A* **1989**, *39*, 191-196.

(33) Liebsch, A.: *Electronic Excitations at Metal Surfaces*; Plenum Press: New York, NY, 1997.

(34) Chen, C. K.; de Castro, A. R. B.; Shen, Y. R. Surface-Enhanced Second-Harmonic Generation. *Physical Review Letters* **1981**, *46*, 145-148.

(35) Krause, D.; Teplin, C. W.; Rogers, C. T. Optical surface second harmonic measurements of isotropic thin-film metals: Gold, silver, copper, aluminum, and tantalum. *Journal of Applied Physics* **2004**, *96*, 3626-3634.

(36) Aroca, R.: *Surface-Enhanced Vibrational Spectroscopy*; John Wiley and Sons Ltd: West Sussex, England, 2006.

(37) Canfield, B. K.; Husu, H.; Laukkanen, J.; Bai, B.; Kuittinen, M.; Turunen, J.; Kauranen, M. Local Field Asymmetry Drives Second-Harmonic Generation in Noncentrosymmetric Nanodimers. *Nano Letters* **2007**, *7*, 1251-1255.

(38) Zhang, C.; Xiao, X.; Wang, N.; Fung, K. K.; Loy, M. M. T.; Chen, Z.; Zhou, J. Defect-enhanced second-harmonic generation in (SimGen)p superlattices. *Applied Physics Letters* **1998**, *72*, 2072-2074.

(39) Vázquez, G. V.; Rams, J.; Townsend, P. D.; Hole, D. E. Improved surface quality of Nd:YAG monitored by second harmonic generation. **1999**, *167*, 171-176.

(40) Lyubchanskii, I. L.; Dadoenkova, N. N.; Lyubchanskii, M. I.; Rasing, T.; Jeong, J.-W.; Shin, S.-C. Second-harmonic generation from realistic film–substrate interfaces: The effects of strain. *Applied Physics Letters* **2000**, *76*, 1848-1850.

(41) Bihari, B.; Kumar, J.; Stauf, G. T.; Van Buskirk, P. C.; Hwang, C. S. Investigation of barium titanate thin films on MgO substrates by second-harmonic generation. *Journal of Applied Physics* **1994**, *76*, 1169-1174.

(42) Yeganeh, M. S.; Dougal, S. M.; Polizzotti, R. S.; Rabinowitz, P. Interfacial Atomic Structure of a Self-Assembled Alkyl Thiol Monolayer/Au(111): A Sum-Frequency Generation Study. *Physical Review Letters* **1995**, *74*, 1811-1814.

(43) Yeganeh, M. S.; Qi, J.; Yodh, A. G.; Tamargo, M. C. Influence of heterointerface atomic structure and defects on second-harmonic generation. *Physical Review Letters* **1992**, *69*, 3579-3582.

(44) Ying, Z. C.; Wang, J.; Andronica, G.; Yao, J. Q.; Plummer, E. W. Azimuthal and incident angle dependences in the second-harmonic generation from aluminum. *Journal of Vacuum Science & Technology A: Vacuum, Surfaces, and Films* **1993**, *11*, 2255-2259.

(45) Pedersen, K.; Keller, O. Nonlinear optical methods in the nondestructive testing of metal surfaces. **1988**, *21*, 411-414.

(46) Fang, M.; Baldelli, S. Grain Structures and Boundaries on Microcrystalline Copper Covered with an Octadecanethiol Monolayer Revealed by Sum Frequency Generation Microscopy. *The Journal of Physical Chemistry Letters* **2015**, *6*, 1454-1460.

Chapter 2:VSFG Instrument Operation

2.1: Introduction

The vibrational sum Frequency generation (VSFG) instrument used for this work was primarily built by Dr. Alexander Dean Curtis. A description of how the instrument was built, and why specific components and geometries were used, can be found in Chapter 3 of his doctoral dissertation.[1] The main purpose of this chapter is to discuss capabilities that were added or refined after Dr. Curtis published his dissertation. This chapter is also intended to act as an operator's instruction manual, with protocols for maintaining and optimizing the system, as well as troubleshooting advice for common problems.

2.2: Additions to Dr. Curtis's Instrument Design

There are three significant modifications that have been made to the VSFG instrument since Dr. Curtis described it in his dissertation.

1. A new sample mount was designed to allow the sample to rotate 360° in the plane of the sample surface.

The initial rotational mount was designed in cooperation with Dr. Angela Calchera and Therin Garrett of the BYU Precision Machining Lab. A technical drawing of the assembly is shown in Figure 2.1.

2. The sample mount was redesigned to allow a sample to be scanned and rotated while under load from a modified Instron 3345 single arm material testing machine.

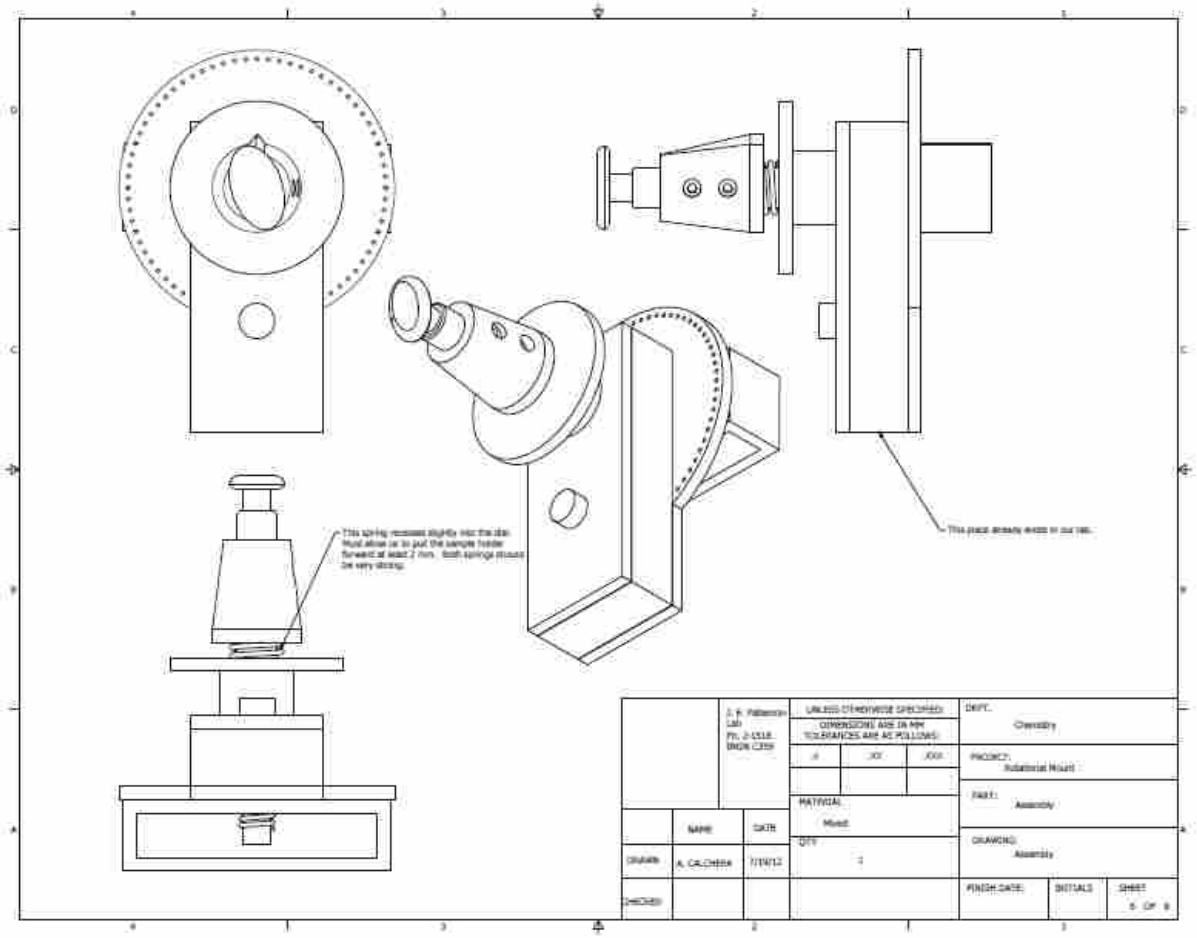

Figure 2.1. Technical drawing of the original rotational sample mount.

The redesign of the rotational mount was done in cooperation with Therin Garret and Joshua Hanson, an undergraduate research assistant. A technical drawing of the assembly is shown in Figure 2.2. This mount was designed to incorporate portions of the first rotational sample mount for standard samples. Alternatively, the components from the first rotational mount can be removed and replaced with the assembly shown in Figure 2.3. This modification will allow for samples to be scanned while under a controlled load. A schematic of the sample clamps is shown in Figure 2.4. The cable that connects the clamps to the Instron is inserted in the hole at the back of a clamp and held in place with the corresponding set screw. Full technical drawings for the latest sample mount can be found in Appendix A.

3. The collection beam path was modified to allow for S or P polarized light to be filtered out of the signal.

Polarized filtering of the collection beam is accomplished by manipulating a waveplate and a polarizing beamsplitter cube in the collection path. The polarizing beamsplitter is mounted on a 1 inch translational stage following the waveplate in the collection beam path. When positioned in the beam path, the beamsplitter will pass P polarized signal and send S polarized signal out of the detection pathway. The waveplate rotates S polarized signal to be P polarized. The stage can be manually pulled back and locked out of the beam path. Set points for the waveplate post holder base are bolted onto the optics table so that the waveplate can be easily removed and returned to the same position. To remove P polarized SFG from the signal, place both the waveplate and the cube in the signal beam path. To remove S polarized SFG from the signal, place only the cube in the signal beam path. NOTE: The polarizing beamsplitter cube can be positioned so that it does not reduce the signal level of the desired polarization; however, this requires careful adjustments and should be checked periodically.

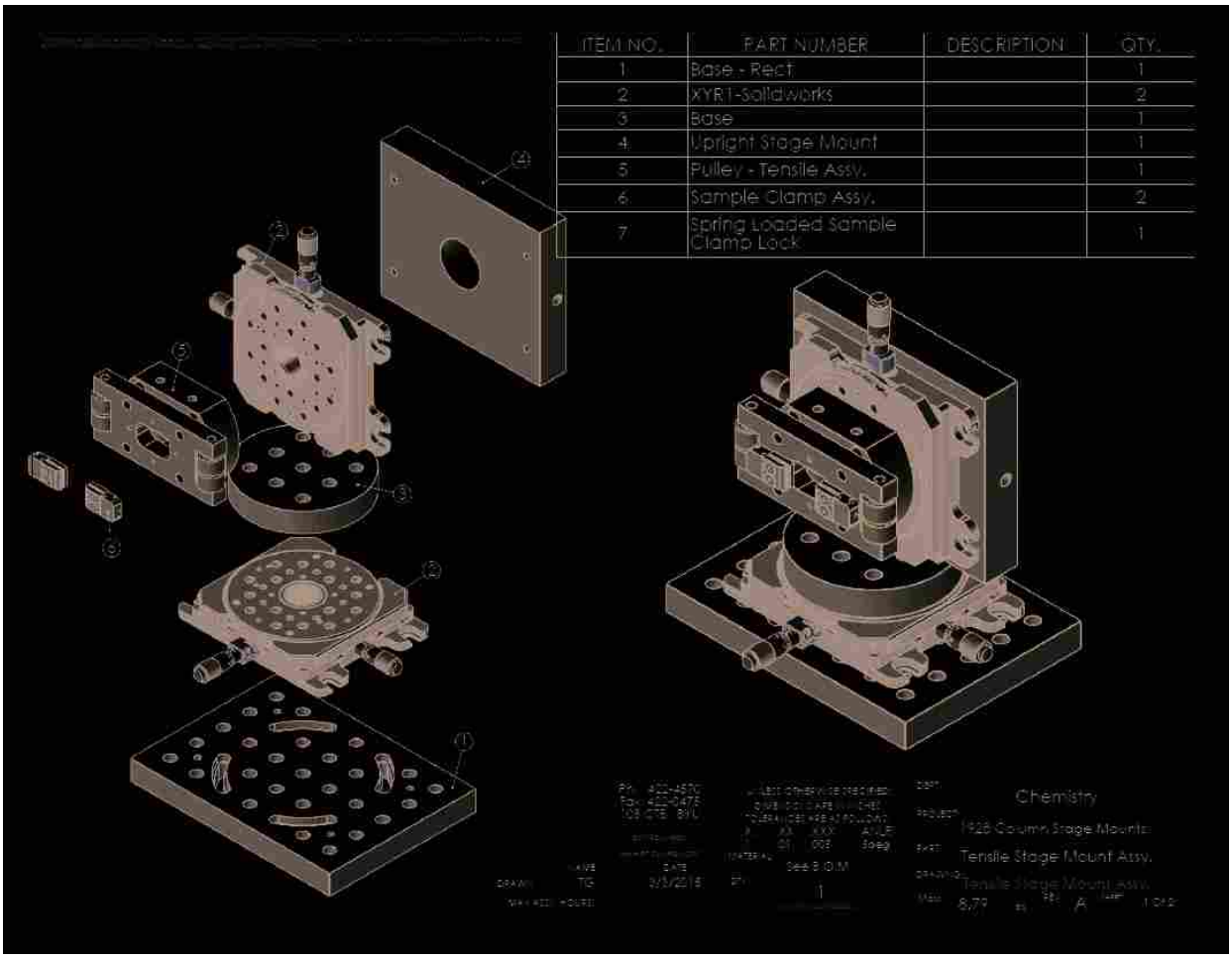

Figure 2.2. Assembly drawing of the current rotational and live-pull sample mount.

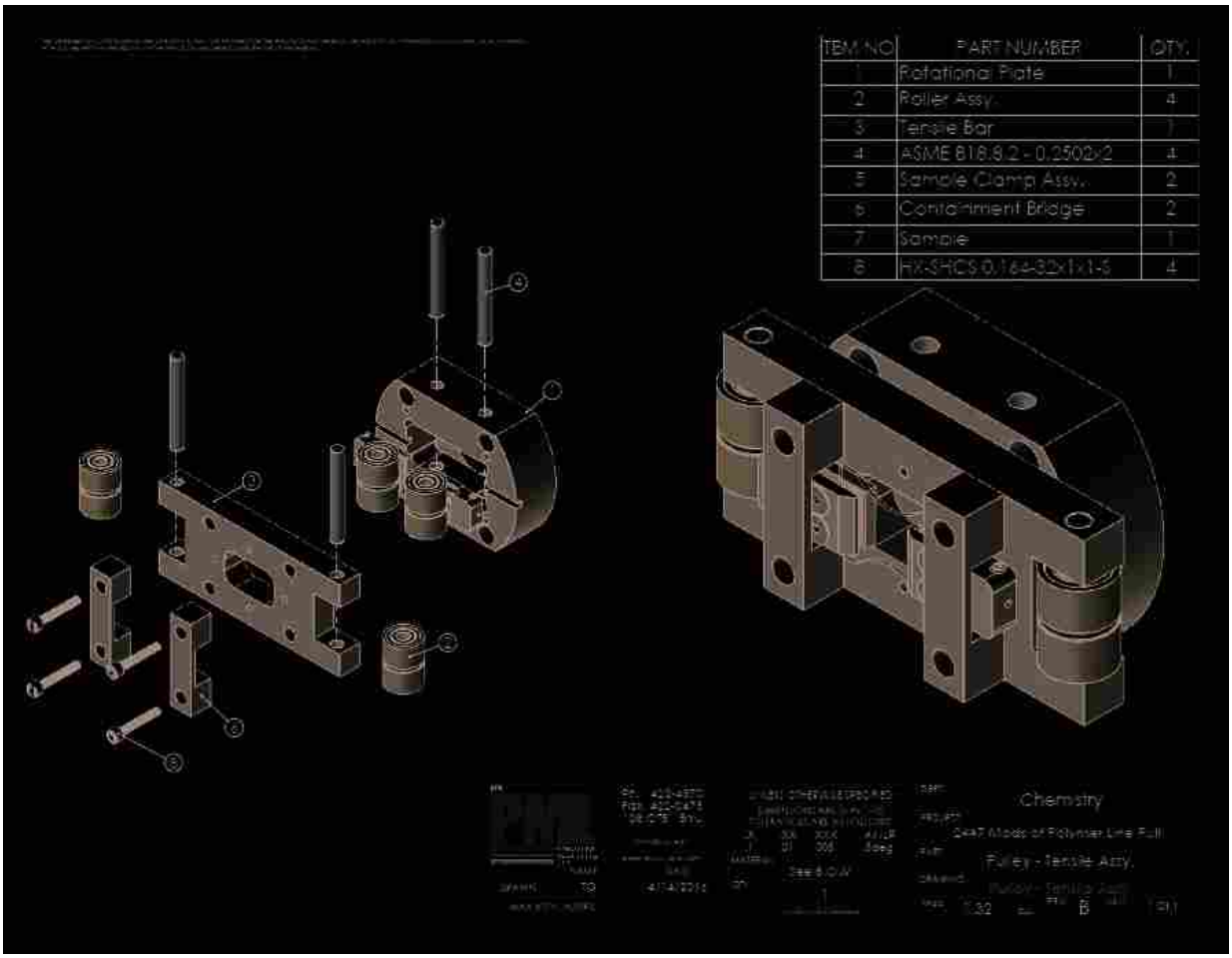

Figure 2.3. Assembly drawing of the live pull adapter for the current sample mount.

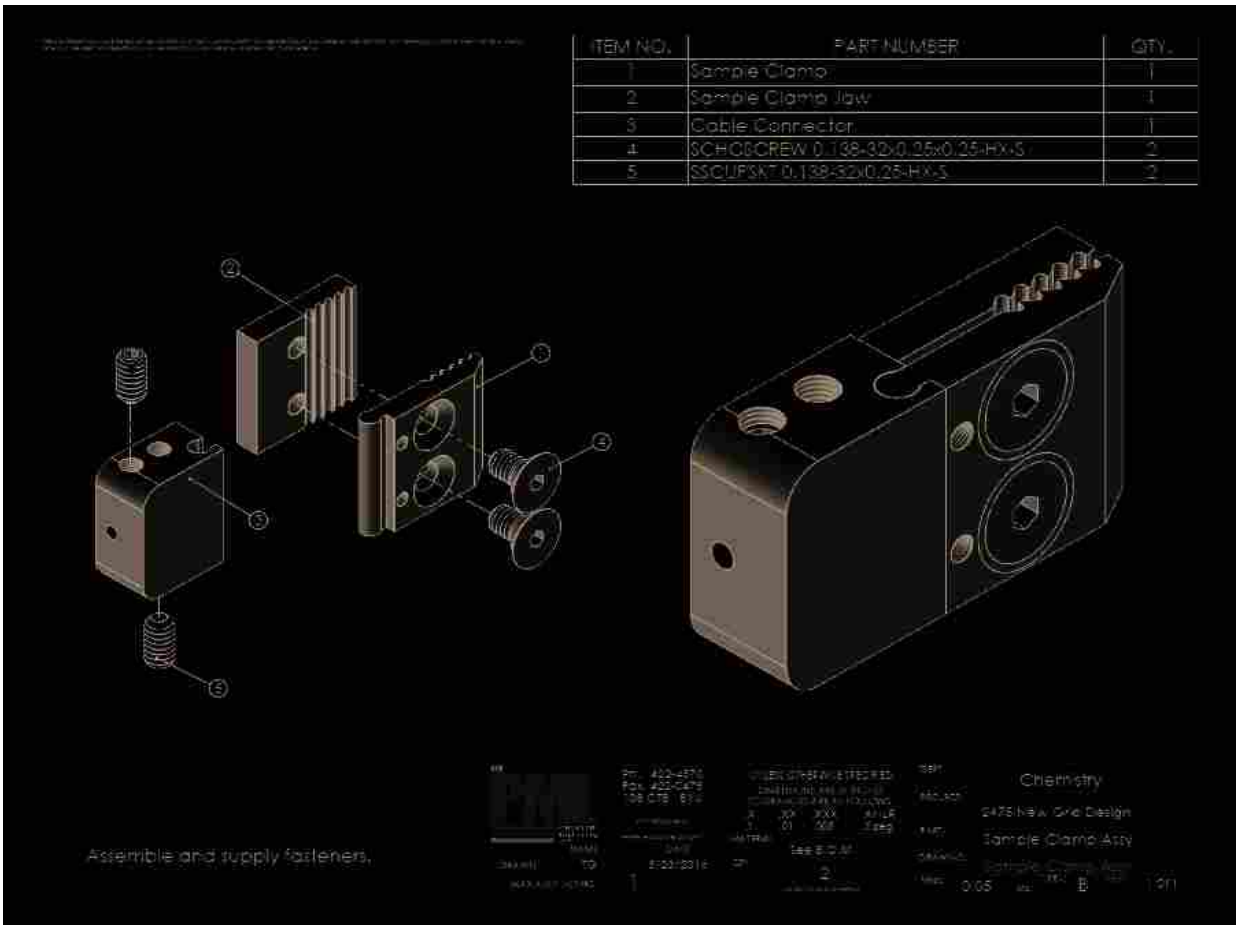

Figure 2.4. Assembly drawing of a sample clamp used with the live pull adapter for current sample mount.

2.3: Instrument Overview and Operation

2.3.1: Instrument Overview

Figure 2.5 includes a diagram and a picture of the VSFG system with the visible, infrared (IR), and signal beam paths marked in red, purple, and orange respectively. The locations of key optical elements are highlighted in yellow with an accompanying site number.

The optical elements at each point are:

1. The beam is split at this point with 70% going to the TOPAS-C and 30% following the visible beam path marked in red.
2. The TOPAS-C is an optical parametric amplifier (OPA) that uses the visible beam to produce a tunable IR pulse, which then follows the IR beam path marked in green.
3. The visible pulse is narrowed spectrally and shaped temporally by the etalons here. It is also down collimated to reduce the beam size here.
4. Most samples will be burned by the visible beam unless a neutral density filter is placed in the mount here.
5. This is a half waveplate that allows you to select either S or P polarization for the visible excitation beam. We generally use an S polarized visible beam.
6. This is a computer controlled stage which allows you to change the arrival time of the visible pulse relative to the IR pulse.
7. The visible and IR beams are focused onto the sample in this area.
8. The diverging signal beam is collimated here.

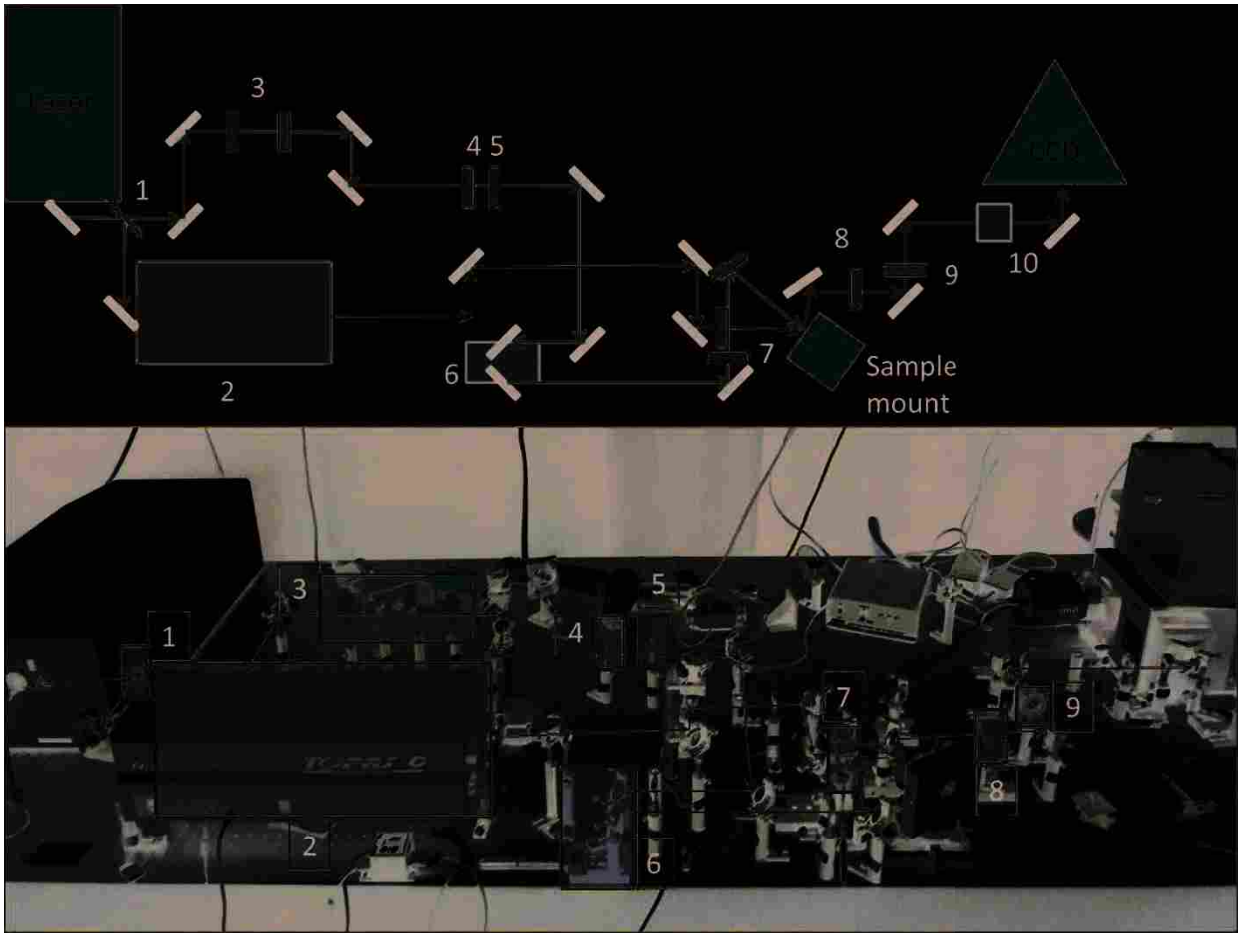

Figure 2.5. Diagram and annotated picture of the VSFG instrument. Key optical elements are highlighted in yellow. They are:

1) beam splitter, 2) OPA, 3) etalons, 4) neutral density filter, 5) half waveplate, 6) computer controlled stage, 7) Lenses to focus the visible and IR beams onto the sample, 8) collimator, and 9) half wave plate.

9. This half waveplate allows you to change the polarization of the signal beam. This may be done for filtering purposes, or to make the signal beam P polarized, which the Andor CCD is more sensitive to.
10. A polarizing cube can be placed here to filter the signal. It is not shown in the accompanying picture.

Figure 2.6 has blue arrows that indicate adjustment points and common problem areas.

a. The TOPAS-C is very sensitive to the pointing of the input visible beam. A small bump at either of these locations will generally significantly reduce the IR power.
b. Portions of these mirrors are off the table and are easily bumped. Check the beam overlap and positioning irises to make sure they are in the right place.
c. The stage and mirror here allow you to adjust the IR beam focal point and position on the sample.
d. This mirror allows you to adjust the visible beam position on the sample.
e. The collimator is on a stage which allows you to adjust the collimation. This should only need to be done if significant changes were made upstream.
f. The mirrors at points f and g allow you to adjust the signal beam path.

2.3.2: Establishing Signal

The directions for establishing signal are made with references to Figure 2.6.

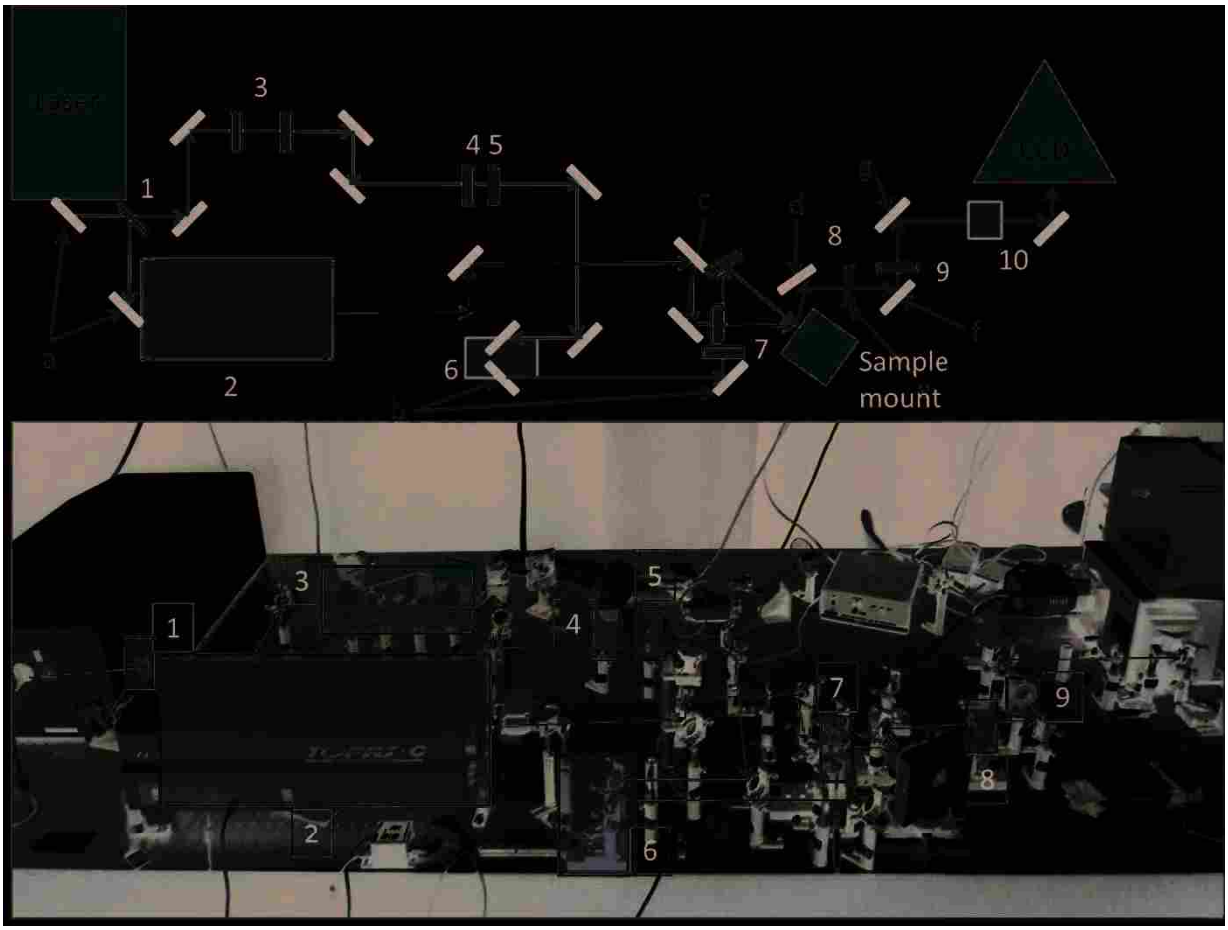

Figure 2.6. Diagram and annotated picture of the VSFG instrument. Key adjustment points are pointed out with blue arrows.

To establish signal:

1. Tune the etalons. This should not need to be done unless conditions have been changed upstream of them, but if the visible beam looks weak the etalons should be checked.
2. Tune the TOPAS-C and insure that it is generating a minimum of 6mW of power.

   Note: This should only be done by authorized personnel; the TOPAS-C is touchy and expensive to get fixed.
3. Position the excitation beams with the mirrors at locations c and d. In particular, check the IR beam as it can clip the edge of the sample mount and make sure that the visible beam is in the center of the sample mount.
4. Overlap the excitation beams spatially. *Because of chromatic aberrations this is difficult to do if you are wearing glasses.* The excitation beams can be overlapped on an IR viewer card, or a piece of cardstock covered in pencil lead. The beams can also be overlapped with a Cleartran crystal, however this method tends to overlap the beams in the bulk of the crystal not the crystal face which doesn't put them in the right position to generate signal from a sample. When overlapping the beams on a graphite covered card
    1. Make sure that the graphite layer is thick.
    2. With the visible beam blocked, look for a spark on the graphite that will indicate the location of the IR beam. You may need to frequently move the graphite covered card to keep the IR spark visible.
    3. Move the IR beam spark into the same position as the visible beam.

5. Place the yellow Cleartran crystal in the sample mount and overlap the excitation beams in time by moving the stage at point b to the point where the Cleartran glows the brightest.
6. Replace the yellow Cleartran crystal with the transparent Cleartran crystal. Check the signal beam path with a card and adjust mirrors f and g so that the beam goes through the center of the irises after mirror g.
7. Set the Andor aperture to 10μm and the acquisition time to 1s or less then optimize the signal by adjusting mirror f to give the largest detected signal on the Andor software. Note: the CCD will often be saturated before the optimal position of mirror f is reached. However, as alignment is improved the width of the saturated peak will increase. This can be used to continue optimizing the pointing with the Cleartran after the CCD has been saturated.
8. Replace the crystal with a gold mirror and optimize the signal. Start with a large Andor aperture setting (1000-1200 μm).
    1. Optimize the IR focus and beam overlap with the stage and mirror at point c.
    2. Use the motorized delay stage software to optimize the temporal overlap.
    3. Optimize the signal beam path by adjusting mirrors f and g so that the signal travels through the center of the irises after mirror g.
    4. Make fine adjustments to mirror g to optimize the signal.
9. Reduce the Andor aperture setting until 20-40 counts of signal is detected with an integration time of 1s and repeat the optimization steps 3 and 4.

For workable data acquisition you should have at least 100 counts from gold with a 1s acquisition time and a 150μm Andor slit width.

2.3.3: Daily Operations

2.3.3.1 Startup SOP for Integra-C Laser

1. Turn on the laser warning light and oscilloscope.
2. Make sure that the external beam is blocked.
3. Open the laser enclosure and turn on the oscillator.
4. Turn the key to the right until the system starts up, then when prompted press Select.
5. Recall the regen setup on the oscilloscope and make sure the cables are attached correctly (green on input 1, black on input2).
6. Wait for the system to complete its startup routine, typically around 5min.
7. Once the startup routine is completed switch the Integra to external PRF:
    1. Press Menu and choose Settings.
    2. Press Select.
    3. Choose Set Mode and press Select.
    4. Press Select again to leave the laser in PRF mode. **(NEVER CHOOSE CW MODE)**
    5. Choose Ext, and press Select.
    6. Press Select again to confirm settings.
8. Open the laser shutter and verify that the pump laser is operating properly.
9. Turn on the TEC.
10. Gradually increase the operating current to the last set point and watch for the regen pulse train on the scope. The optimal current may be slightly different from the last time the Integra was run.

11. After the system has warmed up for 15-20 min, adjust the current again to optimize the pulse train.
12. After the system has warmed up for ~50 min, optimize the current for IR power as measured after the TOPAS-C.
13. Measure the IR and Integra power then record them along with the current and voltage in the laser logbook.

2.3.3.2 Shutdown SOP for Integra-C Laser

1. Block the external beam from the laser.
2. Close the shutter.
3. Turn off the TEC.
4. Turn off the main key switch.
5. Wait approximately 5min for the shutdown routine to complete then turn off the oscillator.
6. Turn off the scope and laser warning light.

2.3.3.3 Taking SFG Data

Before taking an SFG spectrum, check the signal level by taking a 3s scan from a gold mirror with the Andor aperture at 150μm. Generally 250 counts or better is needed for most data acquisition. Close the TOPAS-C shutter and block the visible beam then replace the gold mirror with the sample.

To acquire data:

1. Save the spectrum from gold. This may be needed later to determine if differences in spectral shape and intensity are due to a material change or a change in the SFG system.
2. Check that the sample of interest is properly loaded and that the visible beam is unblocked.
3. Turn off the monitor and lights inside the laser bay.
4. Login to the SFG computer from outside the laser bay. The computer name is: lsrlabgx745.
5. Adjust the CCD settings in Andor.
6. Check that the TOPAS-C is tuned to the correct IR wavelengths.
7. Acquire a background, and then check the background for unusual and/or large features.
8. Take data.
9. Save the data and in the file name record: the date of acquisition (YearMonthDay), sample name, scan settings, signal filtering if any, and all treatment the sample had received prior to the scan.
10. Check that the spectrum has saved correctly.

2.3.4: Live-Pull Equipment Set-Up

The sample mount shown in Figure 2.7 has been designed to facilitate the scanning of a sample while it is under load from the lab's Instron material testing machine. The equipment shown in Figure 2.8 is used to connect the Instron to the sample mount.

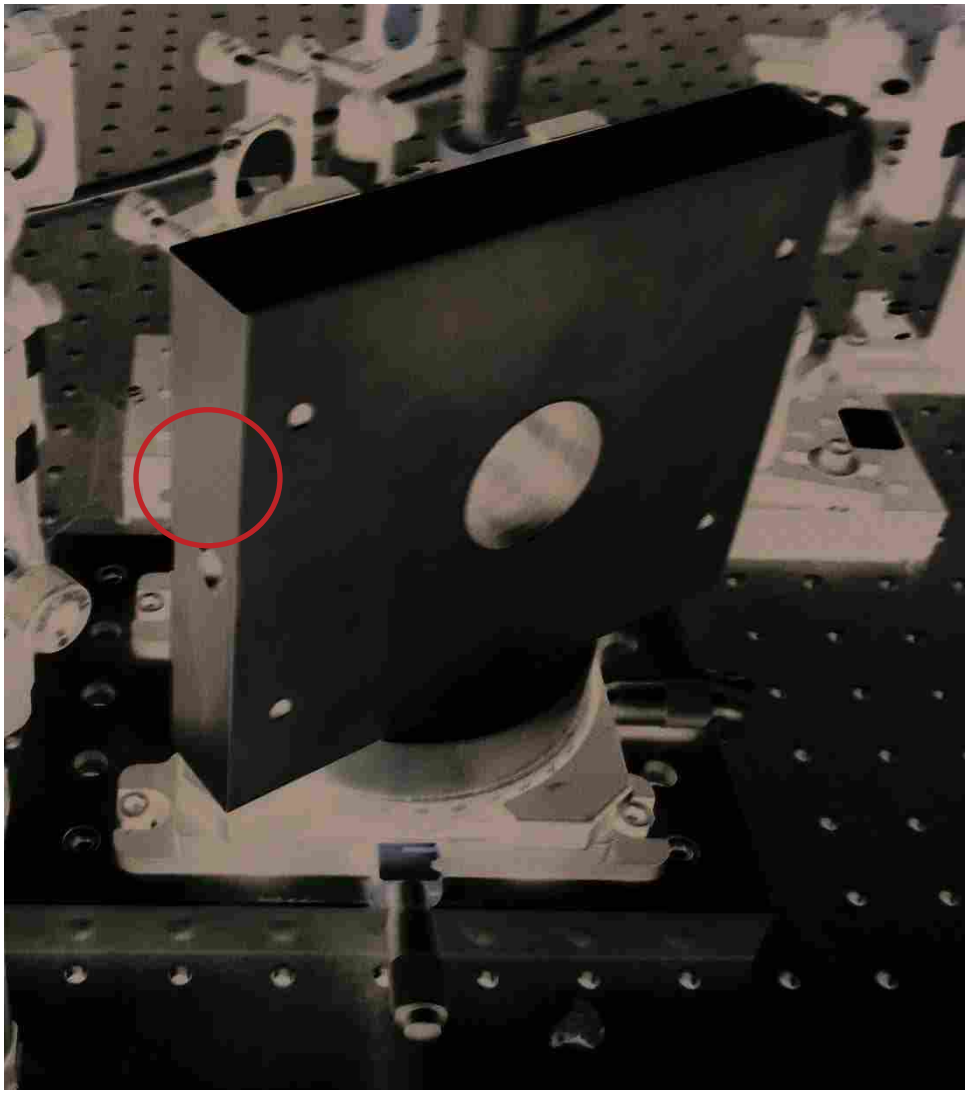

Figure 2.7. Back of the current sample mount. The connection point for the Instron is circled in red.

Figure 2.8. Adapter that allows the Instron to interface with the sample mount. The points circled in red connect to the sample mount. One of the connection points is circled in red in Figure 2.7.

To set up the live-pull equipment:

1. Unbolt and remove the sample holder and plunger from the front of the sample mount and replace it with the live pull mount face shown in Figure 2.3.
2. Replace the upper Instron clamp with the hook attachment leaving the force transducer in place.
3. Remove the lower Instron clamp and clamp housing, then bolt the base of the equipment in Figure 2.8 to the Instron where the lower clamp assembly was.
4. Position the Instron behind the sample mount and connect the rod ends circled in red in Figure 2.8 to the sample mount using the threaded holes, one of which is circled in Figure 2.7.
5. Run the cable connecting the clamps outside of the pulleys on the sample mount face shown in Figure 2.3, then back through the center of the sample mount.
6. Connect the clamps cable to a cable running down from the hook attached to the Instron force transducer and through the pulley at the top of the equipment in Figure 2.8.

2.4: Common and Potential Problems

2.4.1: The Time Delay Stage

The motorized stage, used for the VSFG visible beam time delay, tends to be temperamental. The most common problem is that the operating software either fails to identify, or loses connection with, the stage motor control box. To give yourself the best chance of the stage working, always start the stage control software before any other programs and don't try to run two stages from the same computer.

When the stage control software stops working:

1. Close all software.
2. Unplug the control cube, and leave it unplugged for at least 1 minute.
3. Repower the control cube.
4. Start the APT controller configuration software and make sure that the control cube has been identified.
5. Close the APT controller configuration software and open the APT stage control software.

2.4.2: Excitation Beam Power Loss

There are three common sources of power loss in the excitation beam that you might be able to address. The first issue to be aware of is laser power loss due to insufficient cooling. This can occur when the air flow to the cooling system is restricted, or when the room temperature is too high. If needed, the air flow can be supplement with a large external fan, and/or the instrument can be run at night when the lab is generally cooler.

The second issue is laser power loss due to moisture in the pump laser. This can be prevented by monitoring the desiccant and replacing it when indicated by the gauge on the top left. If this is the problem, your laser power will start out fine but drop off after operating for a few hours.

The third common issue is a change in the beam alignment in the TOPAS-C. This problem can be identified when the IR power drops well below previous values, and the laser power doesn't. The TOPAS-C can be realigned by following the directions on page 26 of the accompanying user manual. The system diagram on page 15 of the TOPAS-C user manual may

also be useful. **NOTE:** Only personnel authorized by Dr. Patterson should attempt to realign the TOPAS-C.

2.4.3: Light Contamination

The VSFG signal is visible light, which can make background light contamination a real problem. Light contamination is especially problematic when working with samples that produce low levels of signal, such as glass, or samples that do not have a perfectly smooth and flat surface, such as polymer dogbones. Long acquisition times are needed to obtain meaningful spectra from samples like these, which make scans very sensitive to background light. Getting low enough levels of background light in these situations often requires that the acquisition be done at night, with the collection path fully boxed. Even with these precautions, any scan that requires more than four hours total, two hours for the background and two hours for the data, will have too much noise to be useful.

The most common and problematic source of light contamination at night has come from cleaning and security staff, who enter the lab despite the warning light being on. This problem can be reduced with clear and prominent signage, and by actively intercepting nighttime staff before they get to the lab door. Maintenance staff may move or remove signage, so check to make sure all measures are still in place before starting a long acquisition.

Attempting to acquire VSFG spectra in the OH stretching region will require additional precautions, as there is a large, narrow noise source that shows up in that region of the CCD. This noise appears to come from the Integra laser itself, and travels along the visible beam path. Closing the alignment irises before and after the delay stage to the point where they just begin to

cut into the beam, closing the collection path alignment irises to the point just before they cause the signal level to drop, and narrowing the Andor aperture to 100μm can remove this noise.

When running long scans of HDPE samples you can also get light contamination from SFG signal generated on the Teflon face of the plunger that holds the sample in place. This will be a problem with samples which require long scans and are not completely opaque. This issue can be avoided by placing a sheet of glass attached to a sheet of frosted glass with double sided tape between the polymer sample and the Teflon plunger face.

2.4.4: Potential Problems in the Live-Pull

The Instron 3345 material testing machine is much better at responding to changes in the extension than it is changes in the load. This means that if you want the Instron to stop before it breaks the sample, extension (or strain) must be used for program cues, not load (or stress). Also note that the Bluehill software has two different places where the test can be programmed to end and will stop when either is reached. This can be useful, but can also ruin a test, so double check both. You should also be aware that the faster the Instron pull rate, the lower the load and extension at which a sample is likely to break. For example, it is difficult to get our high density polyethylene samples to develop a good neck at pull rates above 0.003mm/s.

There is also a potential issue in the live pull sample mount. As it currently exists, the clamps that hold the sample are not tightly constrained in any direction other than by the cables which transfer the load. This means that if a cable twists during loading, the sample face will also twist which will put the signal beam out of alignment. The VSFG instrument collection path is very sensitive to alignment, so even a very small change in the orientation of the sample face can lead to a loss of signal.

2.5: References

(1) Curtis, A. D. Refining Vibrationally-Resonant Sum Frequency Generation Spectroscopy for Studies of Interfacial Interactions. Brigham Young Univeristy, **2012**.

Chapter 3: Investigations Into the Nature of Nonresonant SFG

3.1: Introduction

Sum frequency generation spectroscopy can be a powerful tool. Vibrational SFG can give interface and surface specific information about the nature and physical orientation of functional groups. Many sample systems also produce a second, nonresonant SFG signal. Interference with the nonresonant SFG signal can significantly alter the detected, resonant SFG spectrum.[1,2] Methods have been developed to remove nonresonant interference, but these methods rely on the assumption that NR-SFG signal has a predictable phase and decays instantaneously with the removal of either excitation pulse.[3-5] Existing literature and work discussed in this chapter strongly suggest that, in at least some cases, these assumptions are wrong.

Ignoring or improperly treating NR-SFG can lead to inaccurate analysis and incorrect conclusions. Furthermore, ignoring NR-SFG signal contributions throws away valuable information that can provide unique and useful insights into the nature and dynamics of a system. This chapter is an amalgamation of research projects that were intended to add to the understanding of the nature of NR-SFG signal. The hope is that this work will help researchers better use, and account for, NR-SFG signal in their efforts. A portion of this work was published in Optics Letters volume 40 issue 21 on September 29, 2015 as "Polarization and phase characteristics of nonresonant sum-frequency generation response from a silicon (111) surface". The published text has been reformatted to align with the style of this dissertation, with figures and references from the published paper integrated into the rest of the chapter. Other than these cosmetic changes, the paper is included as published in section 3.2.

3.2 Optics Letters Publication

Polarization and phase characteristics of nonresonant sum-frequency generation response from a silicon (111) surface

Shawn C. Averett,[1] Angela R. Calchera,[1,2] James E. Patterson[1,*]

[1]*Department of Chemistry and Biochemistry, Brigham Young University, Provo, UT 84602*

[2]*Present location: Intel Corporation, Hillsboro, OR 97124*

**Corresponding author: jepatterson@chem.byu.edu*

Received 12 August 2015; revised 26 September 2015; accepted 28 September 2015; posted 29 September 2015 (Doc. ID 247760); published 19 October 2015

Silicon (111) [Si(111)] surfaces both with and without a thin film of polystyrene are investigated with sum-frequency generation (SFG) spectroscopy with S-polarized visible and P-polarized infrared inputs. On uncoated Si, the nonresonant polarization changes from S to P, with the maximum signal in each polarization component repeating every 60° of sample rotation. With polystyrene on Si(111), the resonant features go in and out of phase with the nonresonant signal every 120°. The resonant response is only S-polarized, as expected, however the nonresonant response again switches between S and P polarization. Implications for proper collection and interpretation of SFG spectra from crystalline substrates are discussed.

OCIS Codes: (190.4350) Nonlinear optics at surfaces, (300.6420) Spectroscopy, nonlinear, (300.6490) Spectroscopy, surface. http://dx.doi.org/10.1364/OL.99.099999

Vibrational sum-frequency generation (VSFG)[6,7] has become a powerful tool for investigating the molecular structure of free surfaces and buried interfaces. In this nonlinear optical technique, two laser pulses, one visible and one infrared, interact with a surface or interface, producing a nonlinear polarization that oscillates at the sum of the two input frequencies. Under the dipole approximation, the nonlinear susceptibility, $\chi^{(2)}$, is identically zero for an isotropic medium, thus no VSFG signal is produced from amorphous bulk material. A surface or interface, however, is by definition anisotropic, therefore some elements of the susceptibility tensor are nonzero; this fact provides VSFG with inherent selectivity for surfaces and interfaces of isotropic media. As we show in this Letter, however, the situation can be significantly more complicated when a thin film of amorphous polymer is supported by a crystalline substrate. Changes in the selection rules of the spectroscopy manifest in the polarization and phase of the SFG response from the substrate, and these effects must be included in the analysis and interpretation of the spectral data.

In VSFG, the frequency of the infrared pulse is tuned so as to be resonant with normal vibrational modes of molecules located at the surface or interface under investigation. One aspect of the VSFG measurement that has not received as much attention, however, is the nonresonant response. The nonlinear susceptibility that governs the VSFG process is typically written as

$$\chi^{(2)} = \chi^{(2)}_{NR} + \chi^{(2)}_{R}(\omega) = \chi^{(2)}_{NR} + \sum_{R} \frac{A_R}{\omega - \omega_R + i\Gamma_R} \tag{1}$$

where the overall susceptibility consists of a nonresonant (NR) term, typically considered to be frequency-independent, and a resonant (R) term that consists of individual elements for each discrete vibrational resonance, represented by a Lorentzian profile with amplitude A_R, central frequency ω_R, and line width Γ_R. Both the resonant and nonresonant terms are complex

functions, meaning the various contributions can interfere with each other. The measured VSFG signal can be mathematically represented as follows:

$$I_{SFG} \propto \left|\chi_{NR}^{(2)}\right|^2 + \left|\chi_R^{(2)}(\omega)\right|^2 + 2\left|\chi_{NR}^{(2)}\right|\left|\chi_R^{(2)}(\omega)\right|\cos\left[\delta(\omega)\right] \tag{2}$$

where $\delta(\omega)$ is a frequency-dependent phase. This last term in Eq. (2) accounts for the interference between the resonant and nonresonant contributions and often results in dispersive line shapes of the resonant features.

The nonresonant contribution is an important part of a VSFG measurement because of the interference and the distortions it causes; it should not be thought of simply as a "background" to the resonant response. While the source of the nonresonant signal is still an area of investigation, it is generally accepted that this contribution arises from fast electronic responses in the sample.[8,9] Interference with the nonresonant signal is also used to determine the absolute orientation of molecules relative to the surface,[10,11] which requires knowledge of the relative phase of the resonant and nonresonant responses. In this Letter, we examine the polarization and phase characteristics of the nonresonant sum-frequency response from Si(111) both with and without a thin film of polystyrene. In particular, we have observed that the polarization and phase of the nonresonant response are dependent on the orientation of the sample relative to the probe beams. Our observations serve as a caution to practitioners in the field to pay careful attention to how they treat the nonresonant response, particularly from crystalline substrates.

Our VSFG system has been described previously.[2] Briefly, a portion of the output of an amplified Ti:sapphire laser (Integra C, Quantronix) is used to pump a broadband infrared optical parametric amplifier (OPA) (TOPAS-C, Light Conversion via Quantronix). The visible upconversion beam is spectrally narrowed with two Fabry-Perot étalons. In all cases, the IR light

was P-polarized and the visible light was S-polarized. According to the selection rules for VSFG, an azimuthally symmetric surface, such as an amorphous polymer, can only generate an S-polarized output with these inputs; this combination of input and output polarizations is typically labeled SSP. The time delay between the visible and infrared pulses was set to maximize the overall VSFG signal. Introduction of a time delay between the two pulses experimentally suppresses the nonresonant response,[12] however for the spectra shown in this Letter, no such suppression was used to better observe the nonresonant response. The samples were mounted in a rotational stage that allowed for full rotation of the sample about the surface normal.

The collection path has two elements, a half-wave plate and an analyzing polarizer, that can be included or removed to isolate a specific polarization component of the VSFG signal. In all cases, the signal at the spectrometer was P-polarized for the most efficient detection. For unfiltered spectra, the analyzing polarizer was not included, but the waveplate was used to rotate the predominantly S-polarized light to P-polarization. For filtered SSP spectra, both the waveplate and polarizer were in place to isolate the S-polarized component. To isolate the P-polarized component, the waveplate was removed and the polarizer was included.

We begin with a simple sample, ~100 nm thick polystyrene (PS) on Si(111). Fig. 3.1 **a** contains SSP spectra with and without the polarizer in the collection path. (The waveplate was in place, thus the polarizer passed the light that was S-polarized at the sample.) The dominant resonant features are the ν_2 mode at 3069 cm^{-1} and the ν_{20b} mode at 3027 cm^{-1}.[13] Note that the intensity of the nonresonant signal on either side of the resonant features differs with the insertion or removal of the analyzing polarizer. A more dramatic example of this effect is seen in Fig 3.1 **b**, which shows similar SSP spectra for a polystyrene sample that was kept in ambient air

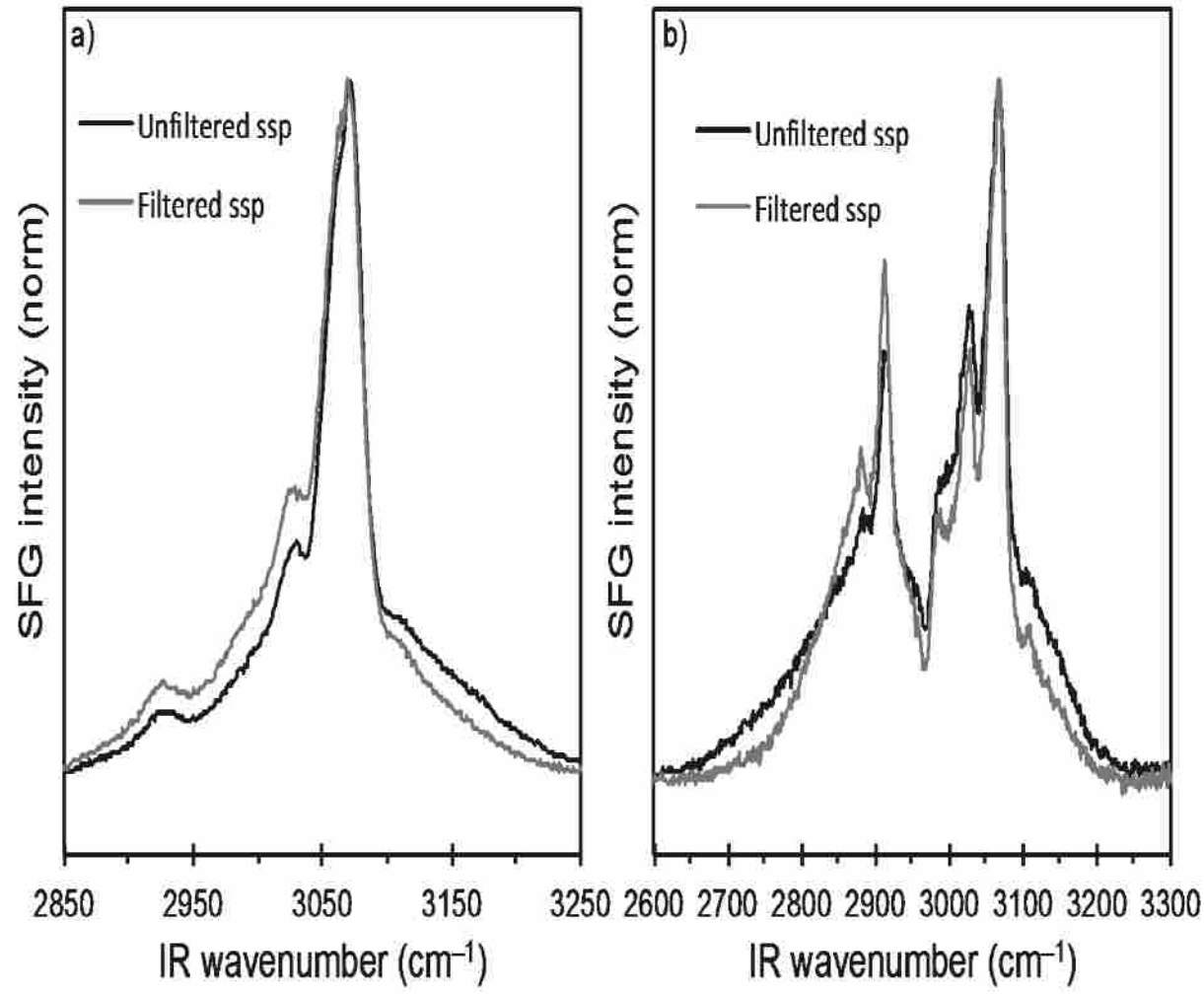

Figure 3.1. a) Unfiltered and filtered ssp VSFG spectra of polystyrene on Si(111). b) Unfiltered and filtered ssp VSFG of "dirty" PS in Si(111).

and became contaminated with organic material. Here, the IR profile was centered between the aromatic and aliphatic C–H stretch regions. Note that the nonresonant intensity again rises and falls with frequency depending on whether the polarizer was in or out of place.

The differences in the nonresonant response with the presence or absence of the polarizer suggest that some signal is present in the P-polarized component; with S-polarized visible and P-polarized IR, this combination is termed PSP. From an azimuthally symmetric surface, such as the polystyrene thin film, the PSP polarization combination is strictly forbidden (within the dipole approximation), however this is not necessarily true for the crystalline Si(111) substrate. It also appears that the SSP and PSP components of the nonresonant response interfere with each other in a frequency-dependent fashion; in both Figs. 3.1 **a** and 3.1 **b**, the interference changes from constructive to destructive along the spectrum.

These interference effects are more than a mere curiosity, but rather have significant practical consequences. One of the hallmarks of VSFG spectroscopy is the ability to determine the orientation of functional groups at surfaces and interfaces.[10,11] Such an analysis is based on the relative intensities of the various vibrational modes and how they interfere with the nonresonant response. As is clearly seen in both Figs. 3.1 **a** and 3.1 **b**, the relative intensities of the resonant features are significantly different in the filtered and unfiltered spectra, indicating that any orientations determined from the filtered and unfiltered spectra would also be different. There also appear to be some changes in the line shape with and without the polarizer. Analysis of VSFG spectra typically treats the nonresonant response as purely nonresonant, i.e. no dependence on frequency, therefore any post-processing methodology that included this assumption would not correct for these observed effects.

To further investigate the polarization characteristics of the nonresonant response, and how it depends on the substrate material, we collected SSP VSFG spectra on three uncoated substrates: polycrystalline Au, polycrystalline stainless steel (SS), and single crystal Si(111). The half-wave plate was in place for these measurements, therefore the polarizer passed the S-polarized light from the sample. Fig. 3.2 **a** shows the relative intensity with the polarizer compared to total intensity without the polarizer, in other words the fraction in the S-polarization component, for Au and SS as a function of the rotational position of the sample. As can be seen, the fraction of S-polarized light is basically unchanged with respect to the angle of the sample for the polycrystalline substrates; some variation is seen due to the sample mount and/or slight polarization impurity, but not deemed to be significant, especially when compared to the results for single crystal Si(111), shown in Fig. 3.2 **b**.

On the single crystal material, the polarization state of the nonresonant response switches back and forth between S and P polarization every 30°, with a 60° period as the sample is rotated. This appears similar to what was seen with the second harmonic generation (SHG) response of Si(111) as a function of sample angle.[14-16] It should be noted that the S- and P-polarized components were measured separately and that the waveplate was not in the optical path for the measurement of the P-polarized component, thus the two measurements do not necessarily add up to 100% at each angle. The pattern of oscillation, however, is unmistakable, as is the fact that measurement of unfiltered VSFG light from Si(111) will contain a mixture of polarization states, depending on sample orientation.

Clearly the single-crystal nature of Si(111) results in very different polarization characteristics compared to the polycrystalline Au and SS. Because we have previously seen that the presence of a PS film affects the nonresonant response,[2,17] we coated both SS and Si(111)

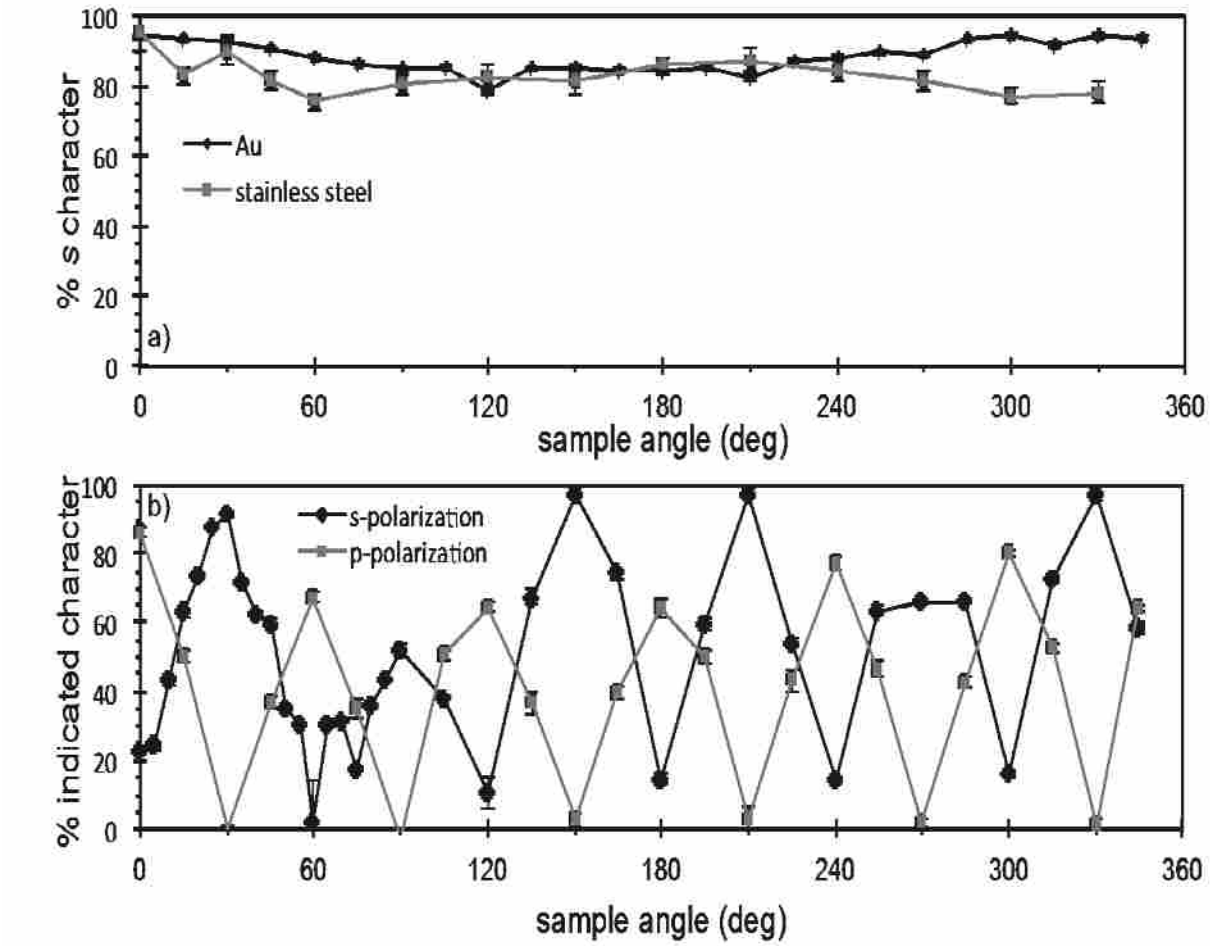

Figure 3.2. a) Percentage of S-polarization in the purely nonresonant response from Au and stainless steel as a function of sample orientation relative to plane of incidence. b) Percentage of S- and P-polarization in the purely nonresonant response from Si(111) as a function of sample orientation relative to plane of incidence.

with ~100 nm PS. The SS samples were aged for 3 weeks whereas the Si(111) samples were annealed at 120°C in a vacuum oven for 2 h, followed by cooling overnight. Fig. 3.3 **a** contains unfiltered and filtered SSP spectra of PS on SS at three rotational angles. To better isolate the resonant and nonresonant components from each other, the center frequency of the OPA was tuned to place the PS resonances on the side of the IR profile. Also included in Fig. 3.3 **a** are the corresponding filtered spectra that isolate the P-polarized component of the signal. (The waveplate was not in place for these measurements.) The results at these angles are representative of all angles used, 16 in total, showing no dependence on sample orientation. Note that the P-polarized component is completely devoid of any resonant response; the resonant response is only in the S-polarized component, as dictated by the VSFG selection rules for a thin film of amorphous polymer.

The situation is very different for PS on Si(111), as shown in Fig. 3.3 **b**. As with the spectra in Fig. 3.3 **a**, the IR profile was positioned such that the resonant features are displaced from the intensity maximum, which allows us to observe the resonant and nonresonant behavior separately. In the unfiltered spectra, the nonresonant response looks similar at each angle, but the resonant response goes in and out of phase with the nonresonant response. What is particularly striking about this pattern is that it repeats every 120°, rather than every 60° as is seen in the variation of the polarization state of the nonresonant response. Note also that the destructive interference is incomplete; at a sample rotation of 90°, the resonant features exhibit dispersive line shapes. As with the SS substrates, polarization filtering to isolate the P-polarized component removes all the resonant response, however the nonresonant polarization varies in the same manner as seen for the uncoated Si(111), as shown in Fig. 3.3 **c**.

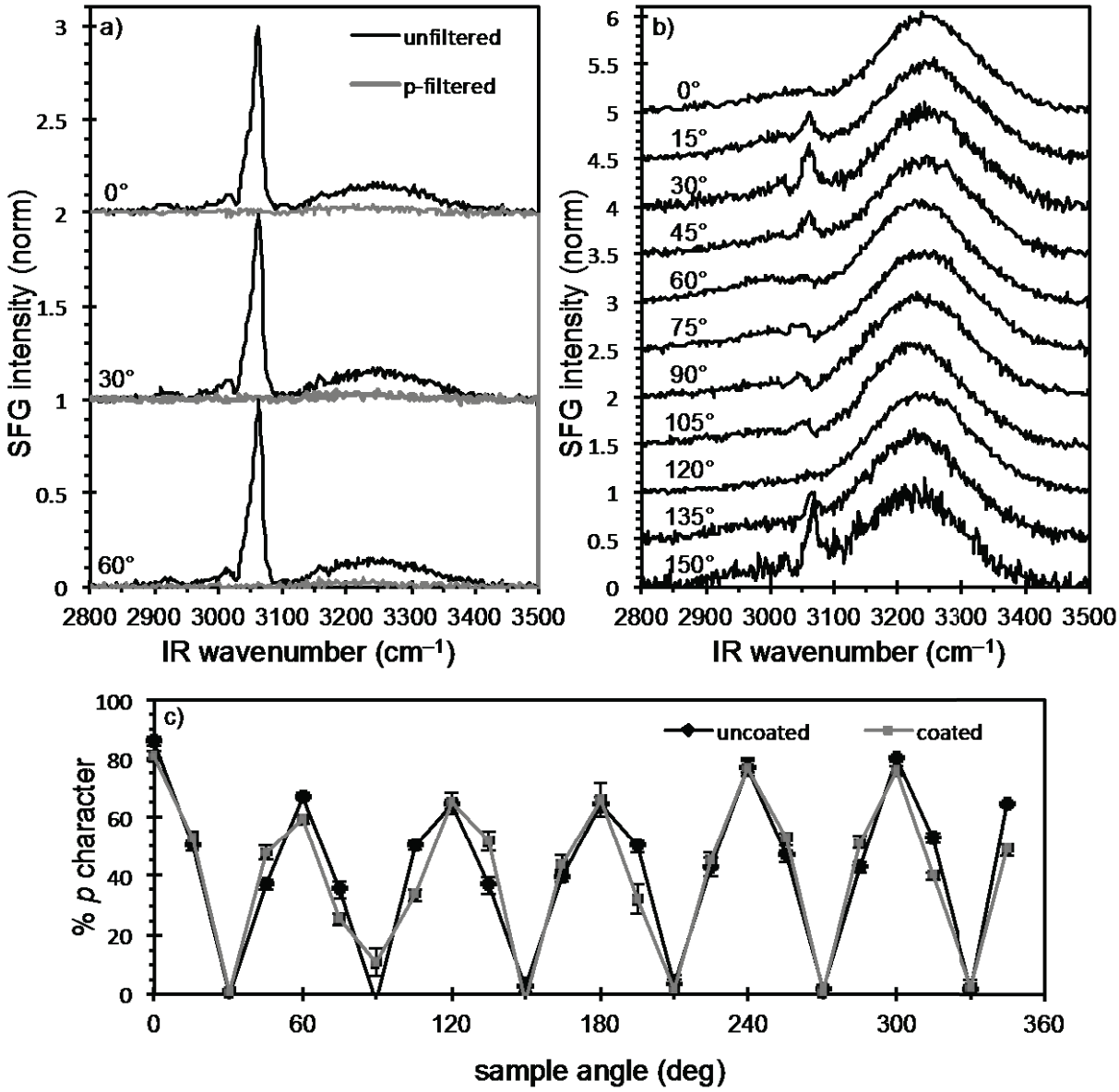

Figure 3.3. a) Unfiltered and P-filtered VSFG spectra of polystyrene on stainless steel at three sample angles relative to plane of incidence. Spectra offset for clarity. b) VSFG spectra of polystyrene on Si(111) at a series of angles relative to plane of incidence. Spectra offset for clarity. c) Percentage of p-polarization in the nonresonant response of uncoated and coated Si(111) as a function of sample angle.

These polarization and phase characteristics likely reflect underlying symmetries of the Si(111) surface, as shown in Fig. 3.4. It should also be noted that although SFG and SHG should be expected to give similar results when looking at bare Si(111), the situation can be very different with the presence of a polymer film. When detecting the response of only the crystalline substrate, either with SHG or SFG, all phase information is lost; only the first term of Eq (2) contributes to the measured signal. The presence of the polymer film, however, allows for interference, as described by the last term in Eq (2). Thus, 120° appears to be the actual periodicity of the phase and polarization characteristics of the nonresonant response from Si(111). These periodicities are consistent with the hexagonal packing of the (111) surface as seen in Figure 3.4, however several more crystalline systems need to be investigated before we can offer a detailed physical model of how the polarization and phase of the nonresonant response depend on surface structure. Preliminary measurements on Si(100), for example, seem to show no dependence on sample orientation.

The nonresonant SFG response is important because it can complicate the accurate orientation analysis of molecules at surfaces and interfaces. Because the measured signal includes interference effects, as shown in Eq. (2), and the individual components cannot generally be measured independently, improper assumptions in treating the nonresonant response can lead to erroneous results.[16] In particular, we have shown that modeling the nonresonant response with

$$\chi_{NR}^{(2)} = B_{NR} e^{i\phi} \tag{3}$$

where B_{NR} is the amplitude and ϕ represents the phase of the substrate, is problematic for thin film samples. The results in this Letter add further weight to this concern because if Eq. (3) were used to model the nonresonant response of Si(111), the phase term would need to depend on

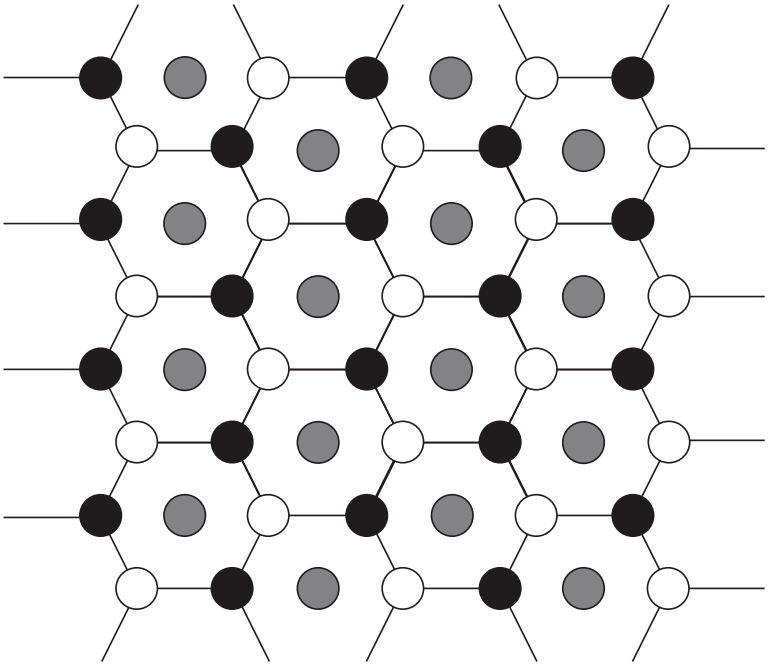

Figure 3.4. Representation of the Si(111) surface. Open circles are the top atomic layer. Black circles represent the second atomic layer, with the third atomic layer directly beneath the second. Gray circles represent the fourth atomic layer.

sample orientation, otherwise it would be uncertain if the relevant functional groups were pointing away from or into the surface.

These results also raise some concerns about other methods to post-process VSFG spectra, especially those collected with heterodyne[4] or phase sensitive detection,[18] or with time-domain SFG.[5,8] The assumption has been made that the nonresonant response is "instantaneous" and should therefore only be included in the real portion of the signal, meaning the imaginary component is purely resonant.[5] While this assumption may be valid for monolayer samples on polycrystalline substrates of the type used in the prior work, where the molecules are in the immediate proximity of the substrate, we have serious reservations about applying this approach to polymer thin films, where the surface molecules that give rise to the resonant response are spatially separated from the substrate. The fact that we see phase changes in the nonresonant response relative to the resonant response with orientation of the sample strongly suggests that the nonresonant response must be included in both the real and imaginary components of the VSFG response from a sample consisting of a polymer thin film on a single crystal substrate.

There are experimental methods for removing the nonresonant response, but only for broadband systems based on an ultrafast laser. This is done by introducing a temporal delay between the IR and visible probe pulses.[12] This time delay affects the measured resonant response because of apodization in the time domain,[3] but these effects can be corrected through additional measurements at multiple delay times.[19] For practitioners with such a system, we therefore strongly recommend experimentally suppressing the nonresonant response to measure the purely resonant response and minimize the number of assumptions that must be made in the post-processing of the data. We make this recommendation even for those using heterodyne detection. For those using narrowband, frequency-scanning systems, the nonresonant response

cannot be removed experimentally. For samples with single crystal substrates, therefore, we recommend orienting the sample to maximize the resonant response, which should enable better extraction of the resonant parameters, although multiple sample orientations should probably be probed to gain a more complete understanding of the sample.

This work also highlights another potential use of the nonresonant SFG response. Instead of being at best a background and at worst a nuisance, it may provide important structural information about a material. Further work is underway on additional materials of different symmetry, and we foresee adding nonresonant SFG to the list of optical methods to determine degree of crystallinity and even the orientation of crystalline samples. We encourage other practitioners to contribute to this effort by explicitly measuring the polarization and phase of the nonresonant response on their particular systems of interest. We also encourage the removal of the analyzing polarizer occasionally to ascertain the presence of "forbidden" contributions to the nonresonant response. As a more detailed picture emerges of how the nonresonant response relates to surface/material structure and properties, it will allow researchers to make significant use of what has often been an underutilized component of the VSFG measurement.

Acknowedgments The authors thank Alexander D. Curtis for helpful discussions in the early stage of this work and Logan Kitchen for assistance in sample preparation.

3.3: Additional Findings

3.3.1: Variations in Phase and Persistence of Nonresonant SFG

Vibrational SFG occurs when the IR input beam vibrationally excites molecules. The vibrationally excited state can persist after the IR pulse has left, effectively preserving the effects

of the IR pulse in time. Until the molecular vibrations caused by the IR beam have dephased, the system can create SFG signal with the arrival of the visible pulse.[3,12] This means that VSFG can still be created by the second, visible pulse several ps after the departure of the IR pulse. Because nonresonant SFG does not involve resonant molecular vibrations, which can preserve the effects of the IR beam, it is assumed that, unlike resonant SFG signal, nonresonant SFG signal cannot be created without the temporal overlap of both excitation pulses.[3-5,20,21] This assumption is at the heart of both time-delay, and time-domain, nonresonant SFG signal suppression methods. Time-delay nonresonant signal suppression works by delaying the arrival of the visible excitation pulse until after the first IR pulse has left.[3] The correct delay time is generally found experimentally by increasing the time between the visible pulse and IR pulse arrival until nonresonant signal is not generated from a standard sample, such as a gold mirror. Time-domain methods detect the SFG signal in the time domain and then process the data to remove the portion of the signal that is expected to have nonresonant components. [4,5] This section discusses three experimental findings that suggest that the assumption of instantaneous nonresonant decay, which is central to time-domain suppression methods, is not valid for some systems.

Figure 3.3 **b** in section 3.2 shows a polystyrene thin film on a Si(111) wafer. The relative phase between the resonant and nonresonant response changes as the azimuthal angle of the sample is changed. Differences in the relative phase between resonant and nonresonant signal components have also been observed at different azimuthal angles from an octadecanethiol (ODT) monolayer on a Au(111) substrate.[22] Interestingly a Si(100) wafers does not exhibit the same nonresonant behavior as a Si(111) wafer. Figure 3.5 shows spectra taken from a Si(100) wafer with a polystyrene thin film coating. Unlike the 120° phase periodicity seen from polystyrene coated Si(111), the VSFG spectra from this sample are almost identical at azimuthal

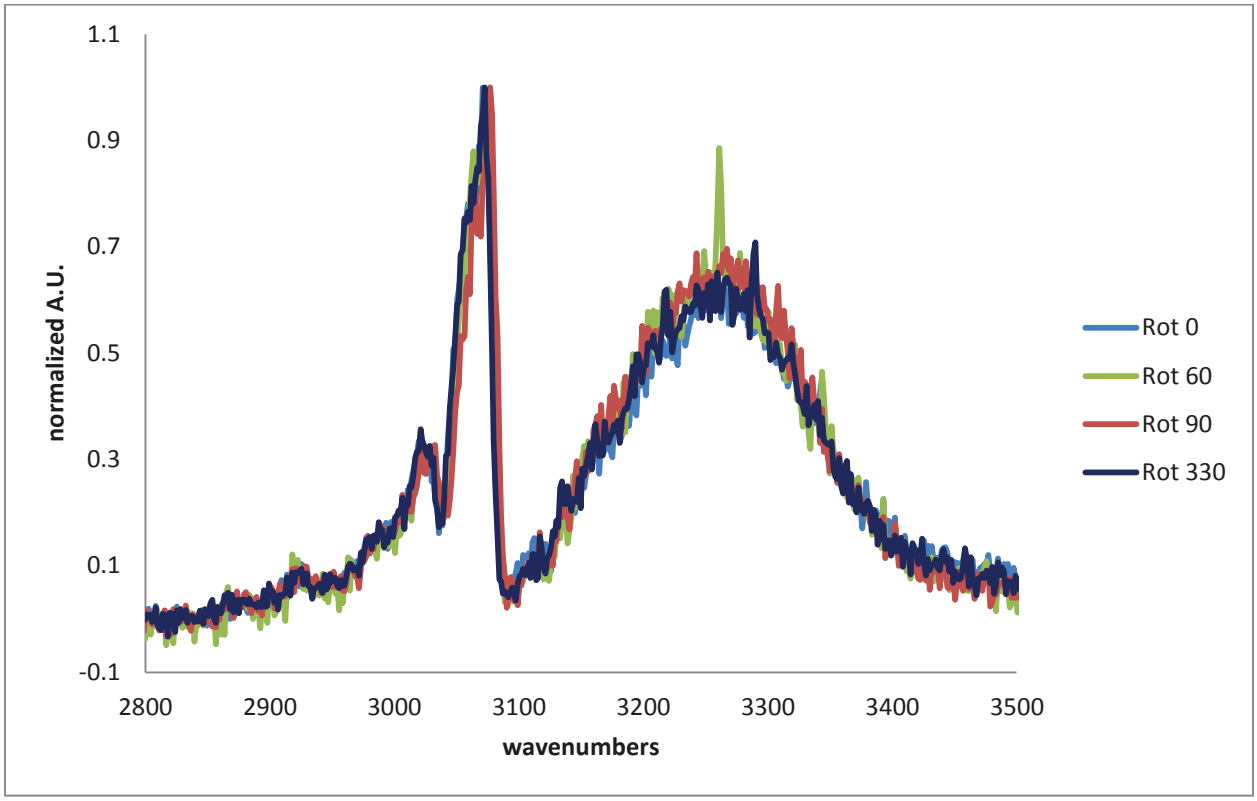

Figure 3.5. VSFG spectra of a polystyrene coated Si(100) wafer at four different azimuthal angles.

angles 0°, 60°, 90°, and 330°. The observation that the nonresonant phase of Au(111) and Si(111) vary with azimuthal angle, but the phase of nonresonant signal from Si(100) does not, suggests that the crystalline structure of the substrate is primarily responsible for the observed phase behavior.

The argument may be made that the changes in the relative phase between resonant and nonresonant signal contributions can be attributed to changes in the phase of the resonant signal. The fact that the same effect was observed from both polystyrene coated Si(111) and ODT coated Au(111), where the only similarity was the crystal structure of the substrate, argues that the changing phase comes from the substrate, and is thus a change in the phase of the nonresonant signal components. The fact that polystyrene thin films on Si(111) and Si(100) substrates did not behave the same supports the assertion that the observed azimuthal dependence of the relative resonant and nonresonant phase is caused by changes in the nonresonant phase. If the persistence and phase of nonresonant SFG signal is only dependent on the temporal properties of the excitation beams, then rotating a sample, as was done in these experiments, should not change the phase of the nonresonant signal contributions. The fact that it does strongly suggests that the phase of nonresonant signal contributions can be influenced by the material from which the nonresonant components are produced.

Commonly accepted assumptions predict that the NR-SFG temporal profile should be the same no matter what material the nonresonant signal is produced on. As is shown in Figures 3.6 and 3.7, this is not the case. Figure 3.6 comes from reference[17]. Here the authors measured the intensity of nonresonant SFG signal as a function of the delay time between the IR and visible excitation beams for Au, a polystyrene thin film on fused silica, and a bare silicon wafer. Each

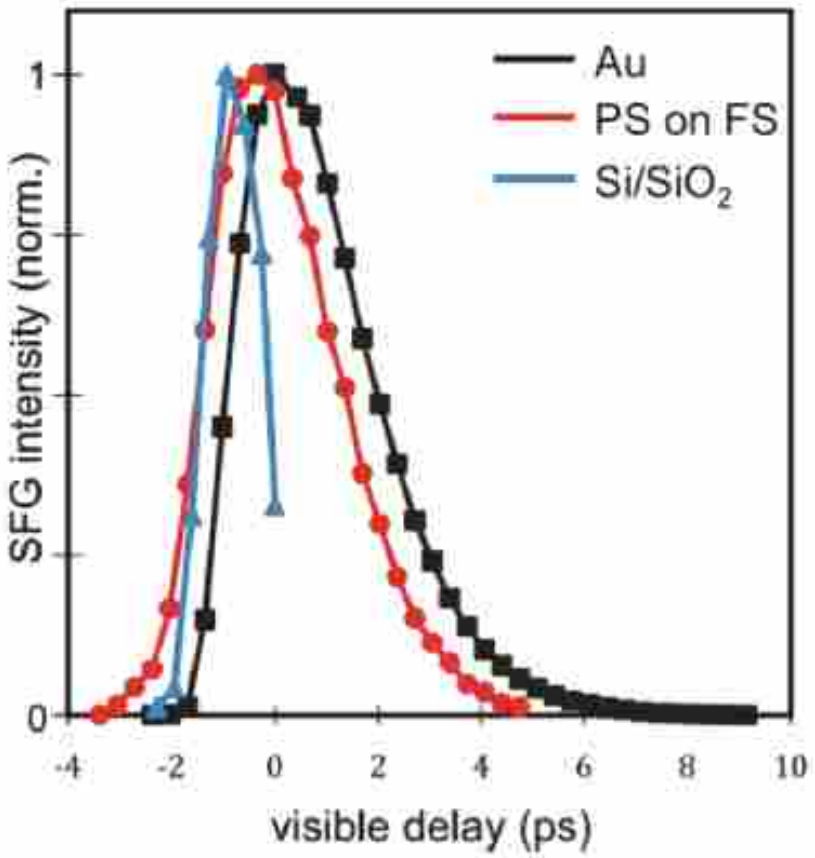

Figure 3.6. Maximum SFG signal from gold, a polystyrene thin film on fused silica, and a silicon wafer at different visible delay times. The maximum signal level from gold was chosen as time zero. From reference 17.

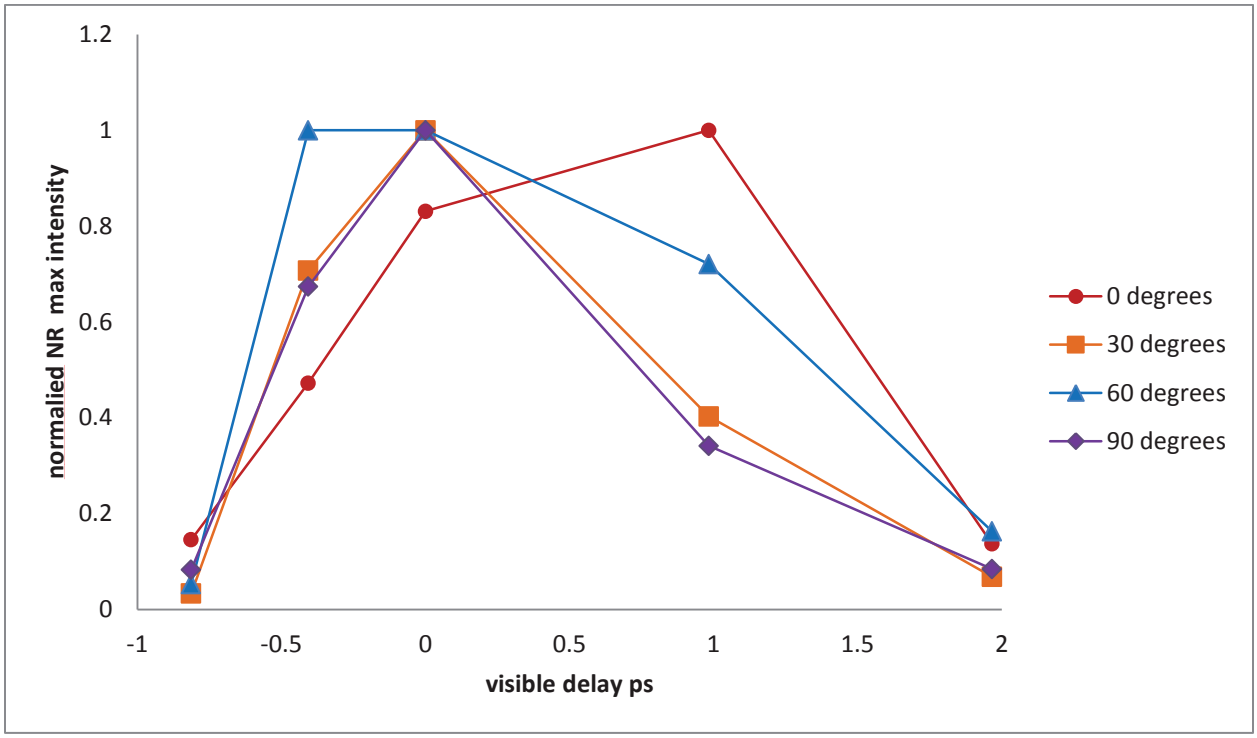

Figure 3.7. MaximumS-polarized NR-SFG signal level from a Si(111) wafer at different visible delay times. Measurements were taken at azimuthal angles of 0°, 30°, 60°, and 90°.

material exhibited a different response, both in the rate of nonresonant decay, and in the optimal delay time for maximum nonresonant signal.

Some of my related exploratory work, using an as received Si(111) wafer, is shown in Figure 3.7, here normalized, S-polarized nonresonant signal intensity is plotted vs the time delay of the visible pulse. Time zero was arbitrarily assigned, as was the 0° azimuthal angle. It is immediately apparent from Figure 3.7 that the temporal behavior of the nonresonant SFG signal is affected by the azimuthal angle of the sample. Furthermore, the optimal time delay appears to oscillate, with very similar temporal behavior at azimuthal angles 30° and 90°. This apparent 60° periodicity recalls the 60° periodicity of the relative phase between the resonant and nonresonant signal, shown in Figure 3.3 **b**. This behavior supports the assertion that the changes in the relative phase between resonant and nonresonant signal components, shown in Figure 3.3 **b**, come from changes in the temporal response of nonresonant signal components.

The temporal behavior of nonresonant SFG signal can also be affected by the presence of resonant SFG signal components. The interaction of the resonant and nonresonant signal can cause nonresonant signal components to persist longer than they otherwise would. Dr. Alexander Curtis predicted this behavior and Dr. Angela Calchera performed the experimental conformation and expanded on Dr. Curtis's theoretical work.[23] The experimental approach was based on my idea to detect nonresonant signal components by filtering P-polarized light out of the SFG signal.

Experiments were conducted using polymer thin films on a silicon wafer substrate. Resonant SFG produced by the interaction of S-polarized visible and P-polarized IR excitation beams on an azimuthally symmetric surface, such as a polymer thin film, are forbidden to be P-polarized. Nonresonant SFG produced at the polymer-substrate interface, however, does not have the same

symmetry constraints and can be either S- or P-polarized. Thus if a spectrum is changed by removing P-polarized components, nonresonant contributions were present.

Figure 3.8 shows SFG spectra from a polystyrene thin film on a Si wafer substrate with an unknown Miller index.[23] These spectra were taken using the broadband SFG system described in Chapter 2, with a visible pulse delay time that fully suppressed nonresonant SFG signal from a polycrystalline gold mirror. The spectrum shown in black had P-polarized components filtered out of the signal, whereas the red spectrum did not. Nonresonant signal components are clearly still present, despite a visible time delay that fully suppressed NR-SFG signal from gold. This means that even if nonresonant SFG signal originally exhibits the assumed phase and temporal behavior, interactions with resonant SFG signal can extend the lifetime of the nonresonant signal, making time and phase-sensitive nonresonant suppression techniques questionable.

The spectra in Figure 3.9 add further weight to the conclusions drawn from Figure 3.8. These spectra were taken from a thin film of PMMA overlaying a polystyrene thin film on a stainless steel substrate. As with the spectra in Figure 3.8, the visible pulse delay time for the spectra in Figure 3.9 was set so that the nonresonant signal from gold was fully suppressed. In Figure 3.9, however the filter was set to remove S-polarized signal, only allowing P-polarized nonresonant signal components to be detected. Panel **a** shows the raw spectra, while panel **b** shows the normalized spectra for comparison.

The observed peaks in the filtered spectrum can come from one of two sources. The first explanation for the remaining signal in the filtered spectrum is that the filtering was incomplete and some S-polarized resonant signal was detected by the CCD. If the detected spectrum had only resonant signal components, however, the relative peak heights should not have changed.

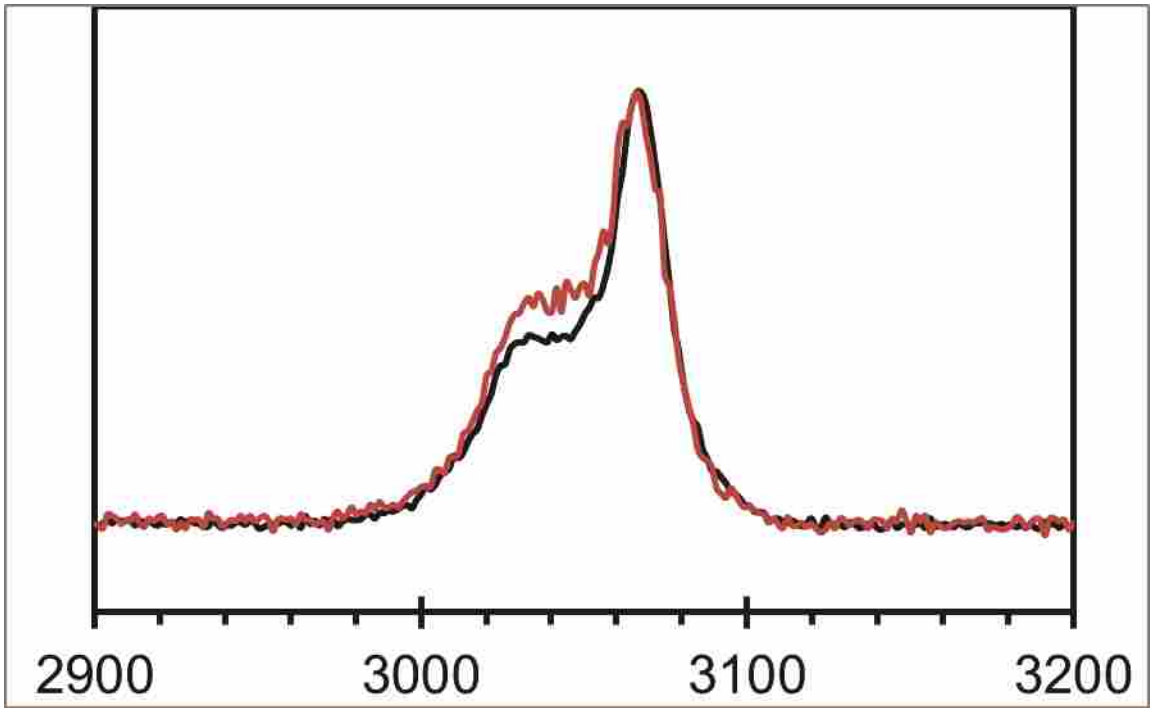

Figure 3.8. VSFG spectra from a polystyrene thin film on a polished silicon wafer. The black spectrum had P polarized signal removed, the red spectrum did not. Both spectra were taken at the same visible pulse delay time which fully suppressed NR-SFG signal from gold.

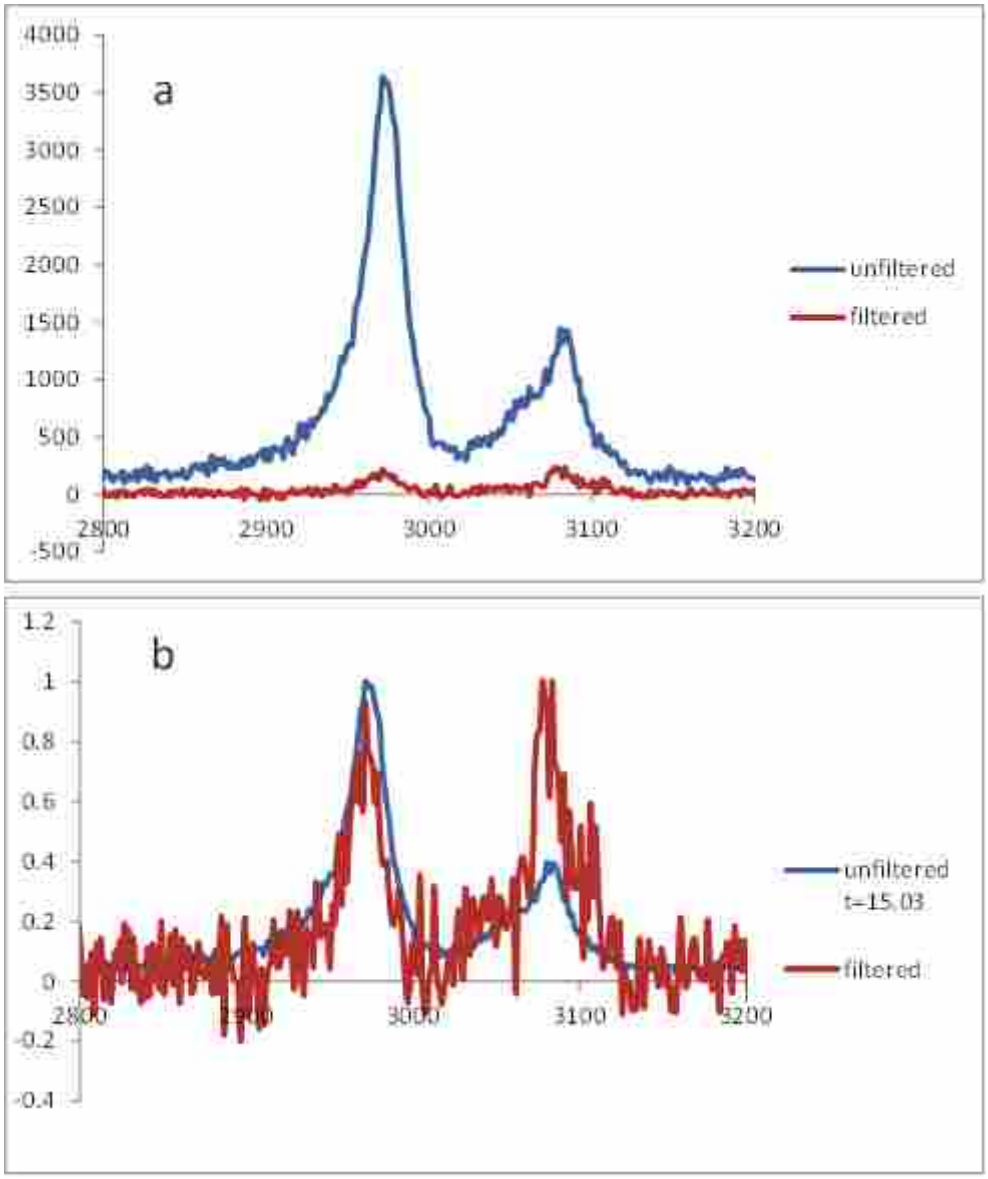

Figure 3.9. VSFG spectra of a PMMA thin film overlaying a polystyrene thin film on a stainless steel substrate. (a) The blue spectrum was not filtered and may contain both S and P polarized components. The red spectrum was filtered to remove S polarized components. (b) Shows the normalized spectra to highlight the remaining P polarized VSFG signal.

The fact that the relative peak heights did change with filtering strongly suggests that some nonresonant signal contributions were present.

Another possible explanation for the remaining signal in the filtered spectrum is that the S-polarized resonant SFG signal was filtered out and the detected signal is P-polarized nonresonant SFG. If this is the case, the appearance of a resonant-like spectrum in the nonresonant signal can be explained by interactions between the resonant and nonresonant contributions which extended the temporal lifetime of the nonresonant signal, but only at wavelengths where resonant signal contributions existed. Crucially, both explanations lead to the conclusion that nonresonant SFG signal contributions can persist longer than generally accepted theory says they can.

3.3.2: The Effects of Electron Mobility on NR-SFG Signal Intensity

The nonresonant SFG response can be thought of, and mathematically modeled, as coming from currents created at the surface of a material by interactions with the electric fields of the excitation beams.[24] Within this model, one would expect that an increase in electron mobility would lead currents to be established more easily on a material surface, and thus generate a larger nonresonant SFG response. For example, an N-doped silicon wafer, with added electrons, would be expected to exhibit a stronger nonresonant response than a P-doped silicon wafer, which has less electron density. Figure 3.10 shows NR-SFG signal from both N- and P-doped Si(111) wafers. The wafers were scanned as received from University Wafer (catalog numbers 2439 and 2331) with the factory cut flat edge parallel to the plane of incidence of the SFG beams. The predicted behavior is observed, with the N-doped Si wafer producing roughly four times as much NR-SFG signal as the P-doped analog.

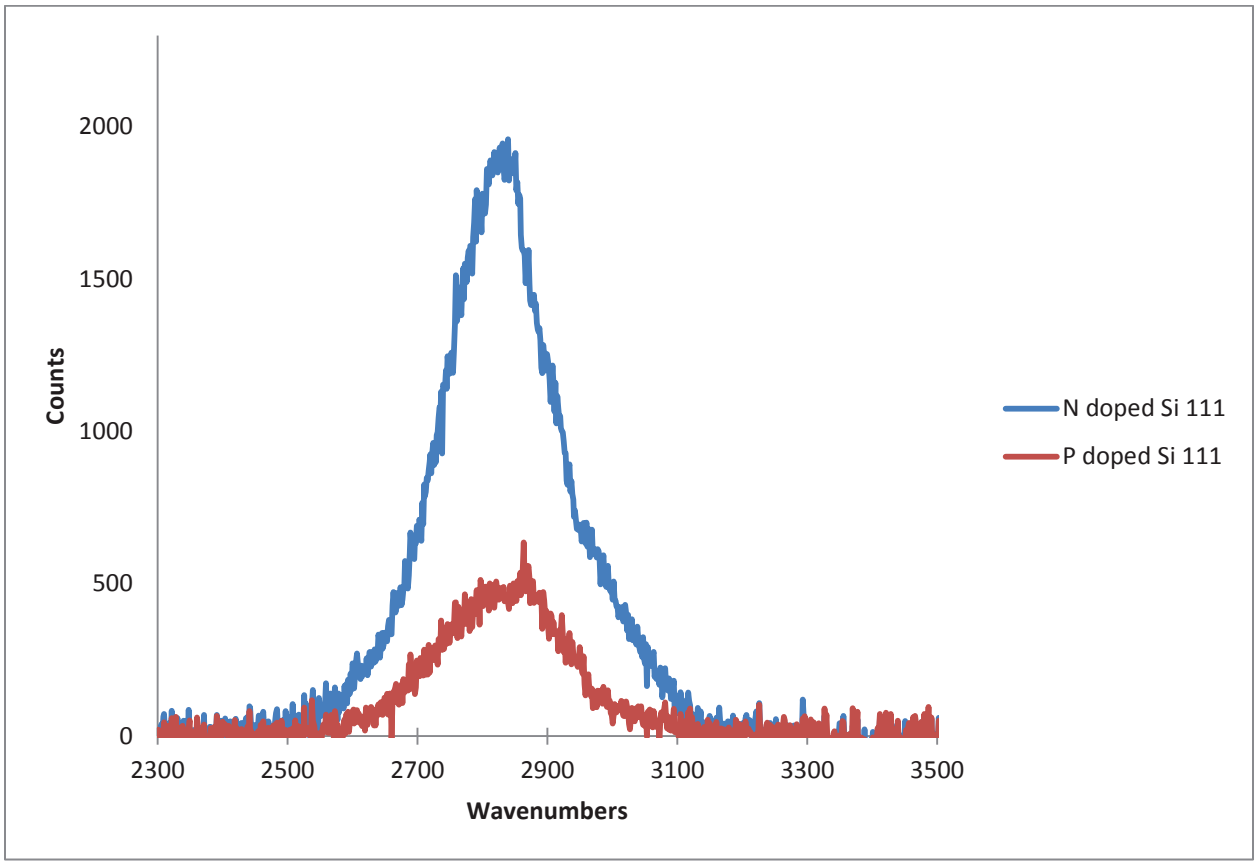

Figure 3.10. NR-SFG spectra from an N doped (blue) silicon (111) wafer and a P doped (red) silicon (111) wafer. Wafers were scanned with the factory cut flat edge parallel to the plane of incidence.

A smaller, but possibly related NR-SFG response can be observed in Figure 3.11 **a** where Eagle XG Glass has been scanned with the IR excitation beam envelop tuned to avoid any resonant interactions. The red spectrum comes from a sample that has been treated with HCl, as outlined in reference, [25] and the blue spectrum is from a sample that was not treated after receipt from the factory. The HCl treatment is expected to leach some of the existing calcium ions out of the glass and replace them with hydronium ions.[25,26] The increase in the number of valence electrons at the surface of the glass may allow the electron cloud to be more easily deformed, accounting for the small increase in NR-SFG response seen in the treated sample.

Interestingly the difference between treated and untreated glass samples becomes much more pronounced two weeks after exposure to the lab atmosphere. This effect is shown in panel **b** of Figure 3.11. Methyl stretches were detected from these samples, and hydrocarbons are known to generate NR-SFG signal,[27,28] so hydrocarbon surface contamination is probably responsible for the increase in NR-SFG signal with age. The fact that the untreated sample did not show the significant increase in nonresonant signal intensity with age exhibited by the HCl treated sample suggests that the hydrocarbons are interacting very differently with the two surfaces.

3.4: Conclusion

Small material changes such as the nature of a silicon wafer dopant, or the azimuthal orientation of the wafer, can cause significant differences in the nonresonant SFG response. These differences can manifest as differences in the strength of the nonresonant response, or as differences in the temporal behavior of nonresonant signal contributions. The presence of a resonant SFG response can also alter the temporal behavior of nonresonant SFG signal components.

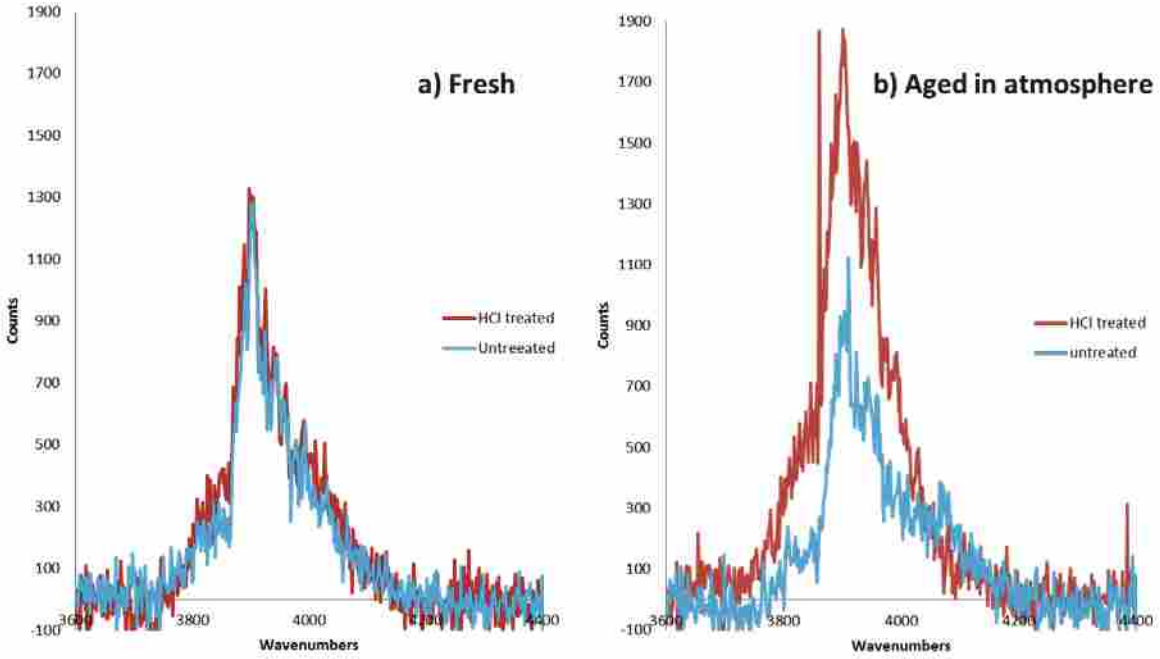

Figure 3.11. VSFG spectra of Eagle XG glass. (a) Untreated (blue) and HCl treated (red) glass samples scanned immediately after removal from a sealed container. (b) VSFG spectra of the same glass samples after two weeks of exposure to the laboratory atmosphere.

Variability in the temporal behavior of nonresonant SFG signal offers intriguing opportunities and important cautions. Developing an understanding of how material characteristics influence the temporal behavior of NR-SFG signal could lead to fascinating insights and new experimental methods. For example, relatively simple and inexpensive instruments may be able to conduct time resolved experiments by incorporating materials that have a well understood NR-SFG temporal behavior. On the cautionary side, however, nonresonant SFG temporal behavior can be more complex than is often assumed. Failure to account for the complexities of the NR-SFG temporal response may lead practitioners to erroneously assume their data is free of nonresonant contributions when it is not.

3.5: References

(1) Quast, A. D.; Curtis, A. D.; Horn, B. A.; Goates, S. R.; Patterson, J. E. Role of Nonresonant Sum-Frequency Generation in the Investigation of Model Liquid Chromatography Systems. *Analytical Chemistry* **2012**, *84*, 1862-1870.

(2) Curtis, A. D.; Reynolds, S. B.; Calchera, A. R.; Patterson, J. E. Understanding the Role of Nonresonant Sum-Frequency Generation from Polystyrene Thin Films. *The Journal of Physical Chemistry Letters* **2010**, *1*, 2435-2439.

(3) Stiopkin, I. V.; Jayathilake, H. D.; Weeraman, C.; Benderskii, A. V. Temporal effects on spectroscopic line shapes, resolution, and sensitivity of the broad-band sum frequency generation. *The Journal of Chemical Physics* **2010**, *132*, 234503.

(4) Stiopkin, I. V.; Jayathilake, H. D.; Bordenyuk, A. N.; Benderskii, A. V. Heterodyne-Detected Vibrational Sum Frequency Generation Spectroscopy. *Journal of the American Chemical Society* **2008**, *130*, 2271-2275.

(5) Laaser, J. E.; Xiong, W.; Zanni, M. T. Time-Domain SFG Spectroscopy Using Mid-IR Pulse Shaping: Practical and Intrinsic Advantages. *The Journal of Physical Chemistry B* **2011**, *115*, 2536-2546.

(6) Zhu, X. D.; Suhr, H.; Shen, Y. R. Surface vibrational spectroscopy by infrared-visible sum frequency generation. *Physical Review B* **1987**, *35*, 3047-3050.

(7) Shen, Y. R. Surface properties probed by second-harmonic and sum-frequency generation. **1989**, *337*, 519-525.

(8) Roke, S.; Kleyn, A. W.; Bonn, M. Time- vs. frequency-domain femtosecond surface sum frequency generation. **2003**, *370*, 227-232.

(9) Malyk, S.; Shalhout, F. Y.; O'Leary, L. E.; Lewis, N. S.; Benderskii, A. V. Vibrational Sum Frequency Spectroscopic Investigation of the Azimuthal Anisotropy and

Rotational Dynamics of Methyl-Terminated Silicon(111) Surfaces. *The Journal of Physical Chemistry C* **2013**, *117*, 935-944.

(10) Ward, R. N.; Davies, P. B.; Bain, C. D. Orientation of surfactants adsorbed on a hydrophobic surface. *The Journal of Physical Chemistry* **1993**, *97*, 7141-7143.

(11) Zhuang, X.; Miranda, P. B.; Kim, D.; Shen, Y. R. Mapping molecular orientation and conformation at interfaces by surface nonlinear optics. *Physical Review B* **1999**, *59*, 12632-12640.

(12) Lagutchev, A.; Hambir, S. A.; Dlott, D. D. Nonresonant Background Suppression in Broadband Vibrational Sum-Frequency Generation Spectroscopy. *The Journal of Physical Chemistry C* **2007**, *111*, 13645-13647.

(13) Curtis, A. D.; Calchera, A. R.; Asplund, M. C.; Patterson, J. E. Observation of sub-surface phenyl rings in polystyrene with vibrationally resonant sum-frequency generation. **2013**, *68*, 71-81.

(14) Guidotti, D.; Driscoll, T. A.; Gerritsen, H. J. Second harmonic generation in centro-symmetric semiconductors. **1983**, *46*, 337-340.

(15) Driscoll, T. A.; Guidotti, D. Symmetry analysis of second-harmonic generation in silicon. *Physical Review B* **1983**, *28*, 1171-1173.

(16) Sipe, J. E.; Moss, D. J.; van Driel, H. M. Phenomenological theory of optical second- and third-harmonic generation from cubic centrosymmetric crystals. *Physical Review B* **1987**, *35*, 1129-1141.

(17) Curtis, A. D.; Burt, S. R.; Calchera, A. R.; Patterson, J. E. Limitations in the Analysis of Vibrational Sum-Frequency Spectra Arising from the Nonresonant Contribution. *The Journal of Physical Chemistry C* **2011**, *115*, 11550-11559.

(18) Ji, N.; Ostroverkhov, V.; Chen, C.-Y.; Shen, Y.-R. Phase-Sensitive Sum-Frequency Vibrational Spectroscopy and Its Application to Studies of Interfacial Alkyl Chains. *Journal of the American Chemical Society* **2007**, *129*, 10056-10057.

(19) Curtis, A. D.; Asplund, M. C.; Patterson, J. E. Use of Variable Time-Delay Sum-Frequency Generation for Improved Spectroscopic Analysis. *The Journal of Physical Chemistry C* **2011**, *115*, 19303-19310.

(20) Shen, Y. R.: *Cambridge Molecular Science : Fundamentals of Sum-Frequency Spectroscopy*; Cambridge University Press: Cambridge, United Kingdom, 2016.

(21) Shen, Y. R. Phase-Sensitive Sum-Frequency Spectroscopy. *Annual Review of Physical Chemistry* **2013**, *64*, 129-150.

(22) Yeganeh, M. S.; Dougal, S. M.; Polizzotti, R. S.; Rabinowitz, P. Interfacial Atomic Structure of a Self-Assembled Alkyl Thiol Monolayer/Au(111): A Sum-Frequency Generation Study. *Physical Review Letters* **1995**, *74*, 1811-1814.

(23) Calchera, A. R. Obstacles And Solutions To Studying Functional Adhesives Using Vibrational Sum-Frequency Generation Spectroscopy. Brigham Young University, 2013.

(24) Krause, D.; Teplin, C. W.; Rogers, C. T. Optical surface second harmonic measurements of isotropic thin-film metals: Gold, silver, copper, aluminum, and tantalum. *Journal of Applied Physics* **2004**, *96*, 3626-3634.

(25) Cushman, C. V.; Zakel, J.; Sturgell, B. S.; Major, G. I.; Lunt, B. M.; Brüner, P.; Grehl, T.; Smith, N. J.; Linford, M. R. Time-of-flight secondary ion mass spectrometry of wet and dry chemically treated display glass surfaces. n/a-n/a.

(26) Bradley, L. C.; Dilworth, Z. R.; Barnette, A. L.; Hsiao, E.; Barthel, A. J.; Pantano, C. G.; Kim, S. H. Hydronium Ions in Soda-lime Silicate Glass Surfaces. **2013**, *96*, 458-463.

(27) Electric quadrupole contribution to the nonresonant background of sum frequency generation at air/liquid interfaces. *The Journal of Chemical Physics* **2011**, *134*, 184705.
(28) Somorgai, G.; Li, Y.: *Introduction to Surface Chemistry and Catalysis*; 2 ed.; John Wiley and Sons, Inc.: Hoboken, New Jersey, 2010.

Chapter 4: Nondestructive Testing With Nonlinear Optical Spectroscopy

4.1: Introduction

Failures in the oil field that occur while drilling or pumping can cost hundreds of thousands of dollars. Entire batches of manufactured products are thrown away because one sample in the batch failed a destructive test. Aircraft, bridges, rail systems, and ships suffer material failures regularly, which can lead to consequences as small as a PR problem over lost cabin pressure, or as large as the loss of hundreds of lives and millions of dollars of equipment. Mechanical failures like these are a routine part of every industry. Nondestructive testing (NDT) methods, which can detect damage without harming the sample, have been developed to help predict and avoid these costly mechanical failures. Nondestructive testing was a billion dollar a year industry in 2013 and is projected to grow to nearly seven billion dollars a year by 2020.[1,2]

Five of the most common NDT methods are: radiography, magnetic particle inspection, dye penetrant testing, ultrasonic testing, and eddy current testing.[3,4] Table 4.1 includes a brief overview of each method, including some of their limitations. One limitation shared by all of these methods is the inability to detect damage that has occurred without the formation of cracks. This is a major shortcoming because significant material damage can occur without the formation of cracks through processes such as aluminum sensitization, plastic deformation, and hydrogen embrittlement. Damage to composite materials and 3D printed metals is also difficult to detect with standard NDT technologies. We have found that second harmonic generation (SHG) is sensitive to plastic deformation in metals and sensitization in aluminum. There is also

Table 4.1. Brief description of common NDT methods and some of their limitations.

Method	How it works	Limitations
Radiography	X-rays, or other high energy radiation is used to image parts much like medical x-ray methods.	• Does not detect surface defects well. • Can be a health hazard. • Requires expensive equipment and facilities, and skilled technicians.
Magnetic Particle Inspection	Magnetic flux is generated in the tested item, which causes iron filings or other small magnetic materials to gather at surface defects	• Only detects surface defects. • Restricted to ferromagnetic materials. • Can miss defects.
Dye Penetrant Testing	A part is coated in a penetrant dye that is drawn into cracks by capillary action. Excess dye is removed ,and penetrant dye is then drawn back out of cracks with chalk. The part is then visually inspected.	• Only detects surface defects. • Surface must be clean and dry. • Cannot detect through coatings or oxidation. • Less sensitive.
Ultrasonic Testing	Much like medical ultrasound and military sonar, ultrasonic NDT methods detect sound waves that reflect off of defects in a part.	• No permanent record, depends entirely on operator skill. • Requires skilled technician. • Requires surface contact. • Surface must be clean and

		smooth. • Doesn't work with very thin materials.
Eddy Current Testing	An electric current is induced in a metal part and the resulting magnetic field is detected. Defects change the flow of the induced current and are identified by changes in the detected magnetic field.	• Sensitive to many parameters. • Only detects defects at or near the surface. • Requires skilled technician.

reason to believe that SHG will be sensitive to hydrogen embrittlement, damage in composite materials, and manufacturing defects in 3D printed metals.

4.1.1 Brief Overview of SHG

Optical SHG occurs when two photons of the same energy are combined in a material and then released as a single photon which has twice the energy of an excitation photon. This process was first experimentally observed by Brown et al. in 1965,[5] and has been used as an experimental tool for decades. SHG signal intensity has been shown to be sensitive to many different changes in the molecular and physical nature of a material. Some of these observations, and a review of sum frequency generation (SHG is a special form of sum frequency generation) are discussed in Chapter 1 of this text. SHG can be resonantly enhanced; however all of the work discussed in this chapter was done with nonresonant SHG.

Figure 4.1 **a** shows a diagram of a simple SHG system with the three key components: a high peak power excitation source, a detector (often a PMT as shown here), and a way to separate the signal light from the remaining excitation beam. Figure 4.1 **b** is a diagram of the current SHG instrument. In this instrument additional filtering of the green excitation light is accomplished with the use of a solar blind PMT and two dichroic mirrors which pass the remaining 532 nm excitation beam and reflect the 266 nm SHG signal. Separating the signal and excitation beams can also be done spatially with a counter-propagating beam geometry, or a prism in the collection line. In Figure 4.1 **b** the excitation beam has been focused onto the sample to increase the intensity at the point of interest on the sample.

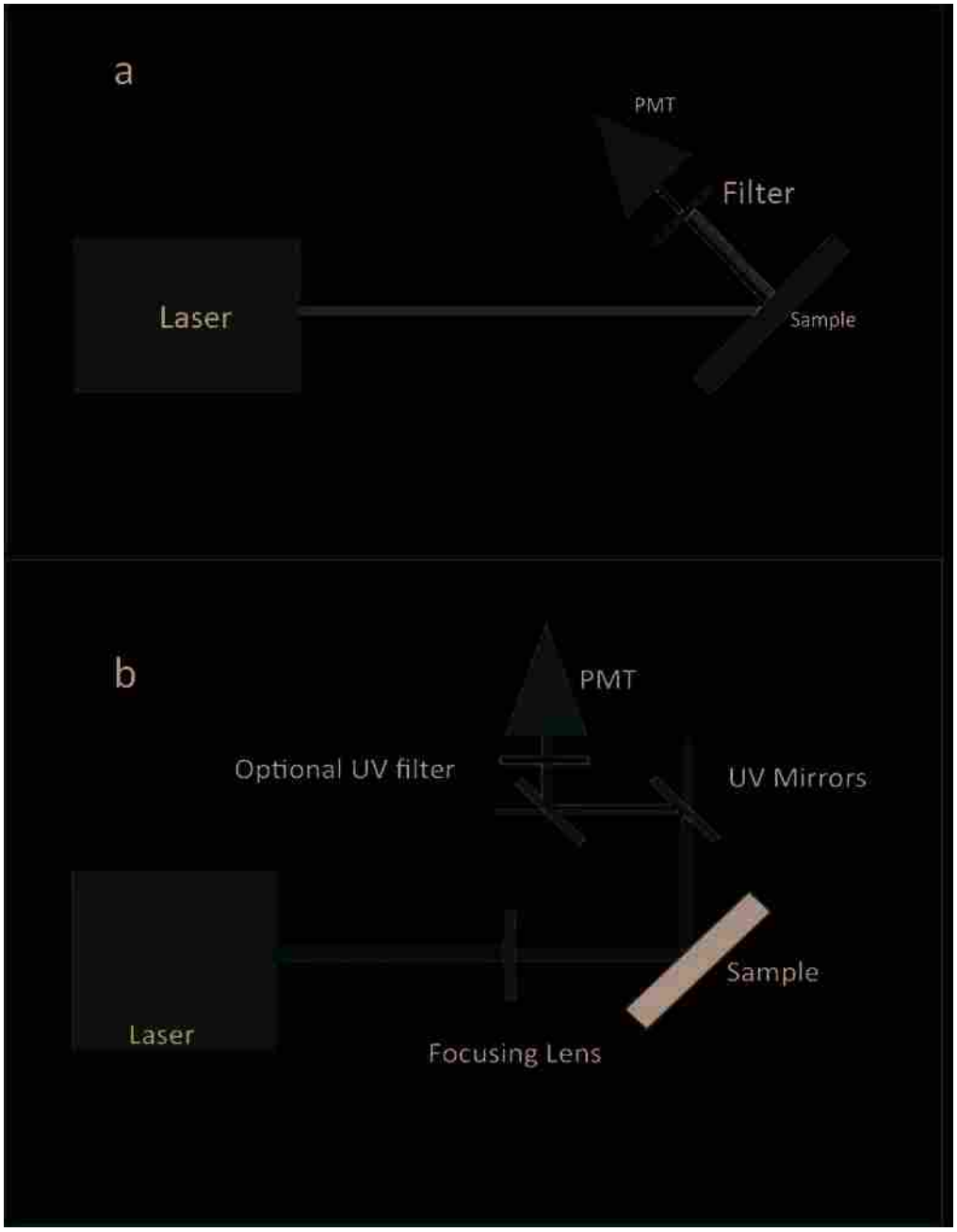

Figure 4.1. (a) Diagram of a simple SHG system. (b) Diagram of the current SHG system. In this system the UV signal is separated from the green excitation light with two dichroic mirrors, and several edge-pass filters.

4.2: SHG Detection of Mechanical Deformation in Metals

4.2.1 Overview of Tensile Testing

In order to understand how a material will behave in service it is often necessary to understand how the material responds to tensile, compression, and multiaxial forces.[6] Tensile forces can be thought of as forces acting to pull the sample apart. For example, the rope in a tug of war experiences tensile forces. This chapter discusses stainless steel and aerospace grade aluminum samples that were subjected to tensile forces using a single arm, Instron 3345 material testing machine.

During the test, the amount of force exerted on the sample is tracked as a function of how far the material gauge has been extended. To compare properties across sample types and shapes, the load and extension can be converted into engineering stress and strain. Engineering stress is defined as the load divided by the cross-sectional area of the sample. Engineering strain is defined as the extension divided by the initial length of the sample gauge.[6] Because samples narrow and extend as they are deformed under tensile load, the cross-sectional area and gauge length of the sample change throughout deformation. This means that engineering stress and strain are actually an approximation based on the initial conditions of the sample.

True stress and strain provide a more precise measurement than engineering stress and strain. True stress is defined as the load at a given point in time divided by the instantaneous cross-sectional area of the sample at that time. True strain is defined as the extension at a given point in time divided by the instantaneous gauge length of the sample at that time. True stress and stain can be difficult to measure accurately and are not reported as often as engineering stress and

strain. If the type of stress or strain measured is not specified it can generally be assumed to be engineering.

Many of the samples discussed in this chapter have a beveled waist rather than a gauge, which makes strain difficult to quantify. For this reason, tensile deformation data will be left in the raw load and extension form rather than the more common stress and strain. This does not present a problem in comparing samples, as they were precision machined to be the same, and thus should experience the same stress and strain at any given load and extension.

Material deformation can be either elastic or plastic in nature. Elastic deformation occurs when a material is stretched then relaxes back into the previous state when the load is released. Plastic deformation, on the other hand, permanently changes the material so that after the load is removed it does not completely return to the original state.[6]

Loading may cause elastic deformation in the majority of a material, while causing plastic deformation in a small region. This can be caused by the shape of the sample or the presence of defects, both of which can increase local stress. Repeated plastic deformation in these high stress areas leads to material fatigue and failure. Defects at surfaces can be particularly important, which is why the surface roughness often affects the fatigue properties of a material.[7]

Important material properties can be determined by examining a graph of the stress vs strain, or load vs. extension. An example of a load vs. extension graph for one of our 2024 Al samples is shown in Figure 4.2. The load in Newtons is graphed on the y axis, and the extension in mm is graphed on the x axis. The graph is linear initially and then begins to curve at roughly 1000 N. The linear region, inside the orange shading, is where the material is being elastically deformed. At around 1000 N the sample begins to be plastically deformed. The point where the type of

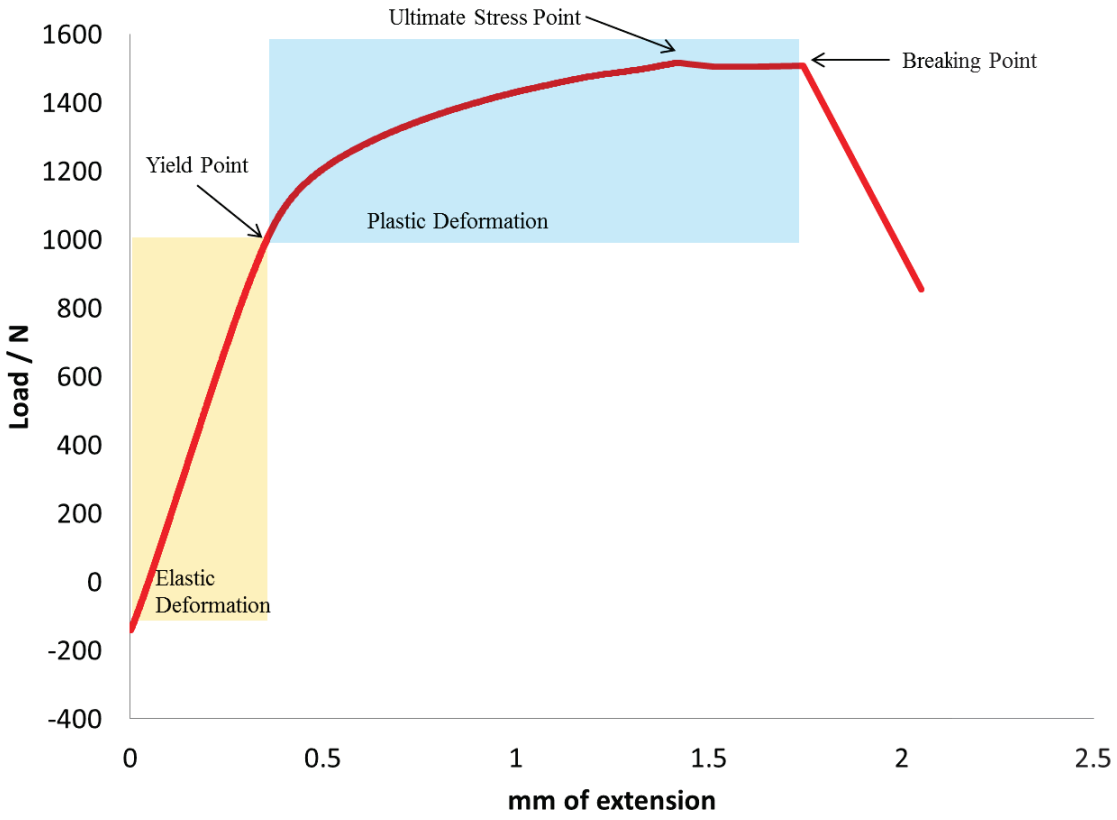

Figure 4.2. Representative load vs extension curve for a 2024 aluminum sample.

deformation transitions from elastic to plastic is called the yield point. The slope of the straight line in the elastic deformation region can be used to calculate the modulus of elasticity, also called Young's modulus, which is a measure of the stiffness of a material. A steeper slope, and larger modulus of elasticity, corresponds to a stiffer material. The point where the load drops off sharply is the material breaking point, and the highest load value on the load vs extension curve is at the ultimate stress, or in this case ultimate load, point.

4.2.2 Stainless Steel

Our use of SHG for nondestructive testing began with SFG and the plastic deformation of stainless steel. It was well known that metals tended to generate a strong nonresonant SFG signal, and that metal grains were physically changed when a polycrystalline metal experienced plastic deformation. Putting the two together, it was decided to investigate if the changes caused by plastic deformation would change the intensity of nonresonant SFG signal produced from a stainless steel surface. For this project the precision machining lab at BYU made stainless steel dogbones, as seen in Figure 4.3. These stainless steel samples were placed in an Instron 3345 single arm material testing machine and pulled to a tensile load of 2000 N, well into the plastic deformation region.

SFG scans were taken of the sample before and after loading. These scans were then averaged at each point on the x axis to create a composite response, which is shown in Figure 4.4. The blue trace is from the unpulled sample, and the red trace is from the stainless steel sample after it had been plastically deformed. The shape of the blue trace comes from the intensity profile of the IR excitation beam and does not contain chemical information about the sample. As can be seen from Figure 4.4, the intensity of the nonresonant SFG signal does contain

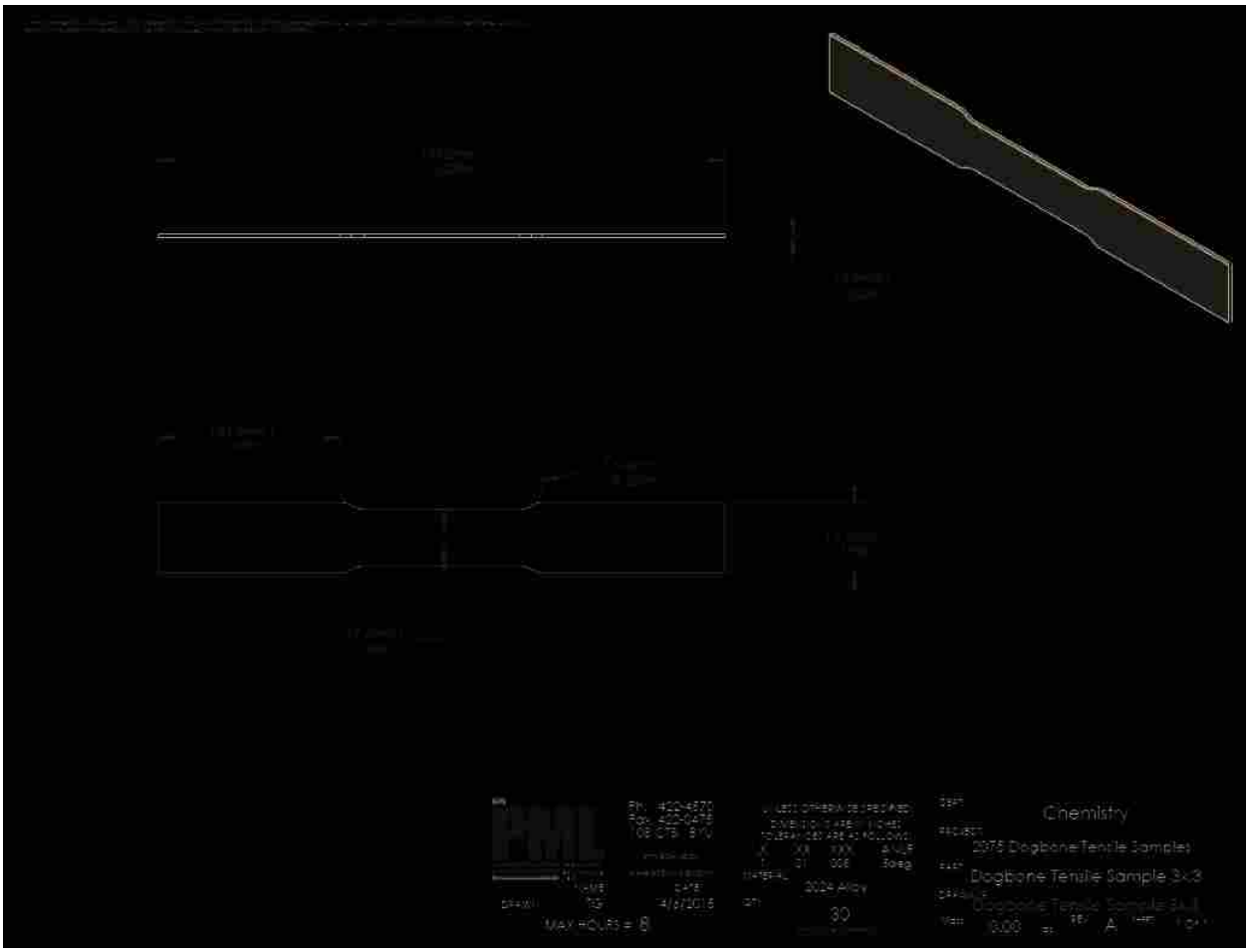

Figure 4.3. Technical drawing for stainless steel samples

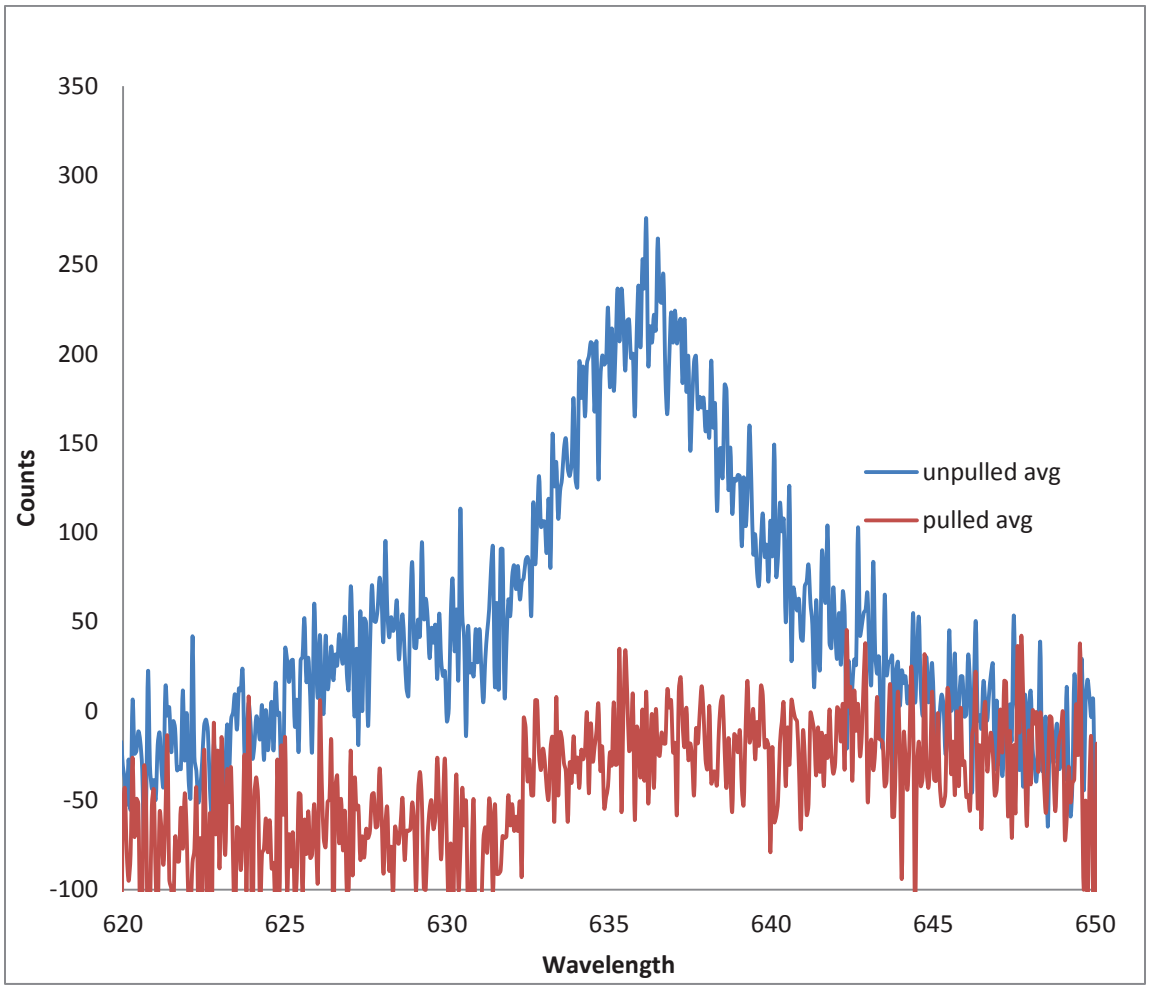

Figure 4.4. Nonresonant SFG response from a stainless steel sample before (blue), and after (red) the sample was plastically deformed with an Instron material testing machine. Each data point of this graph is the average of the corresponding value from spectra taken at three different spots on the sample.

information about the sample. In particular, the detected SFG signal produced by the stainless steel clearly decreased after the sample had been mechanically deformed.

Drs. Eric Homer and David Fullwood, faculty members in the Department of Mechanical Engineering at Brigham Young University, were consulted in an effort to better understand the material behavior that caused the observed change in nonresonant SFG signal intensity. They proposed that changes in the density of lattice dislocations at the surface of the steel, caused by the mechanical deformation, were most likely responsible for the change in SFG signal intensity. Give that lattice dislocations, defects, and strain (discussed in section 1.3.6) are known to influence the strength of nonresonant SFG/SHG signal, this seems likely. We are currently working with Dr. Fullwood's research group to experimentally investigate this explanation by comparing SHG and electron backscatter difraction.

4.2.3: 2024 Aluminum

After learning that the ability to nondestructively detect plastic deformation in metals may be of use to the aerospace industry, we shifted our focus away from stainless steel and onto 2024 aluminum, which is commonly used in aircraft. We also switched from nonresonant SFG to nonresonant SHG, which is much cheaper to produce, and should have a similar response to material changes. In addition to being less expensive, SHG testing can also be done through optical fibers, which would allow a probe to test the inside of pipes and turbines as well as other hard-to-reach areas.

Our first SHG work was conducted using a modified version of the SHG instrument built by Anthony Peterson as part of his Masters research project. This instrument was powered by the 532 nm output option from a Continuum Infinity YAG. In transitioning from stainless steel to

2024 aluminum, we also made the sample shape shorter, so that they would fit more easily in the SHG instrument, and adopted a beveled middle section, so that the part of the sample most affected by loading could be easily identified and scanned. A technical drawing for these samples is shown in Figure 4.5.

A significant problem initially was the inability to get detectable SHG signal without burning the aluminum samples. Burning the sample like this changed the SHG signal level over time, as is shown in Figure 4.6. Undergraduate researchers Dustin Broderick and Alex Farnsworth overcame this challenge by translating the sample mount during data acquisition, so that each pulse from the laser hit a new and unburned spot on the sample. Figure 4.7 **a** shows what one of these samples looked like after mechanical deformation and SHG interrogation. The marks at the end of the sample were made by the Instron clamps during mechanical deformation; the lines down the middle were made by the laser as part of the SHG scanning process. A close up of one of these lines is shown in Figure 4.7 **b,** where the burn marks from individual laser pulses can be seen.

The SHG data came as a time vs intensity trace and was processed for easier analysis by a program written by Dustin Broderick. The program set the data baseline to zero and then performed a simple integration by summing the intensity level of all the data points. After finding the integrated signal intensity at each sample spot, the program averaged all of the spots and outputted an average signal intensity for the scanned sample. Figure 4.7 **c** is an example of the data they were able to acquire using this method. The data at points 1 and 2 on the x axis correlate to two different sides of the same sample, the data at points 3 and 4 on the x axis are two sides of a second sample. This suggested that mechanical deformation in aluminum could be detected with nonlinear spectroscopy. Interestingly, however, only one side of each sample saw

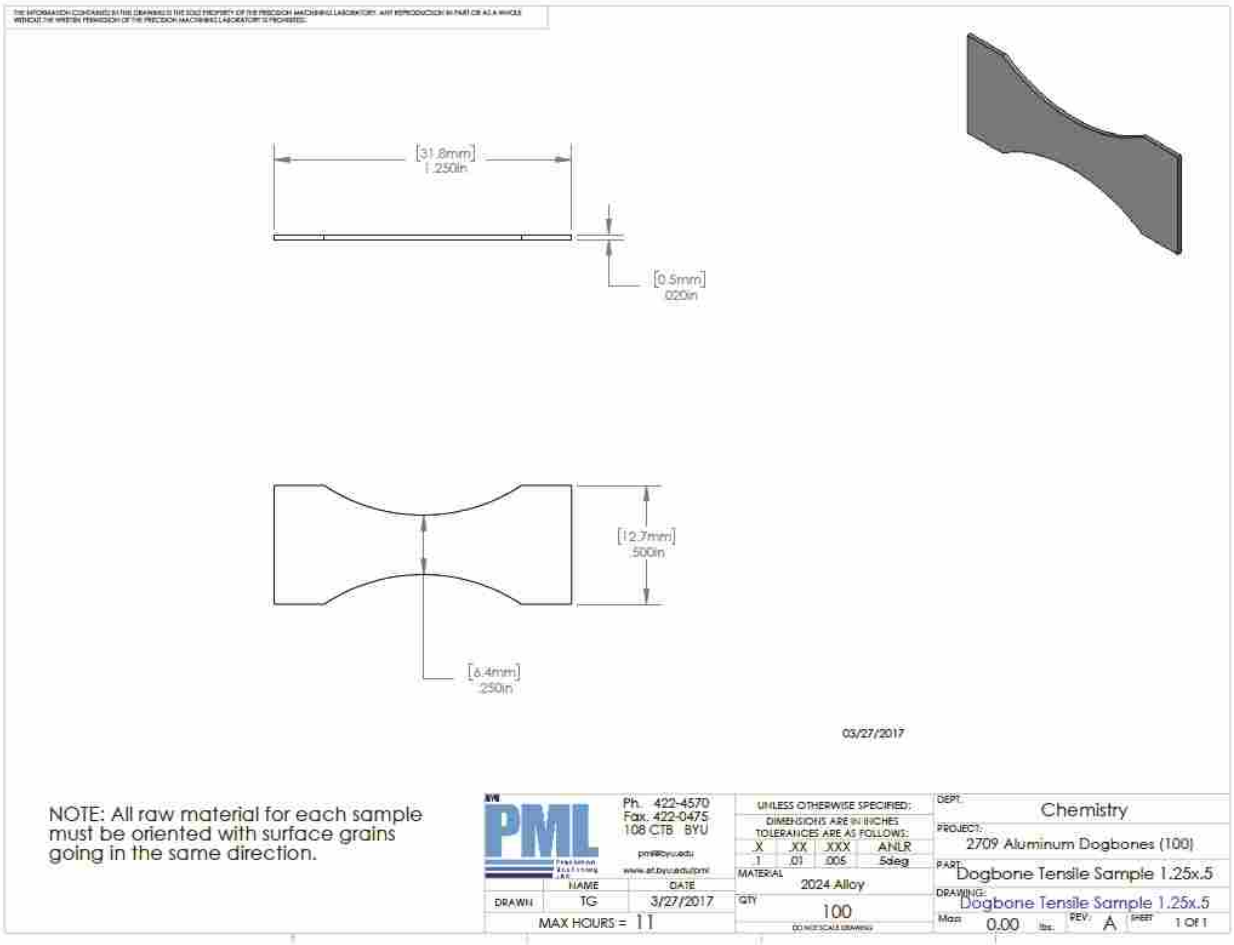

Figure 4.5. Technical drawing for the 2024 aluminum samples.

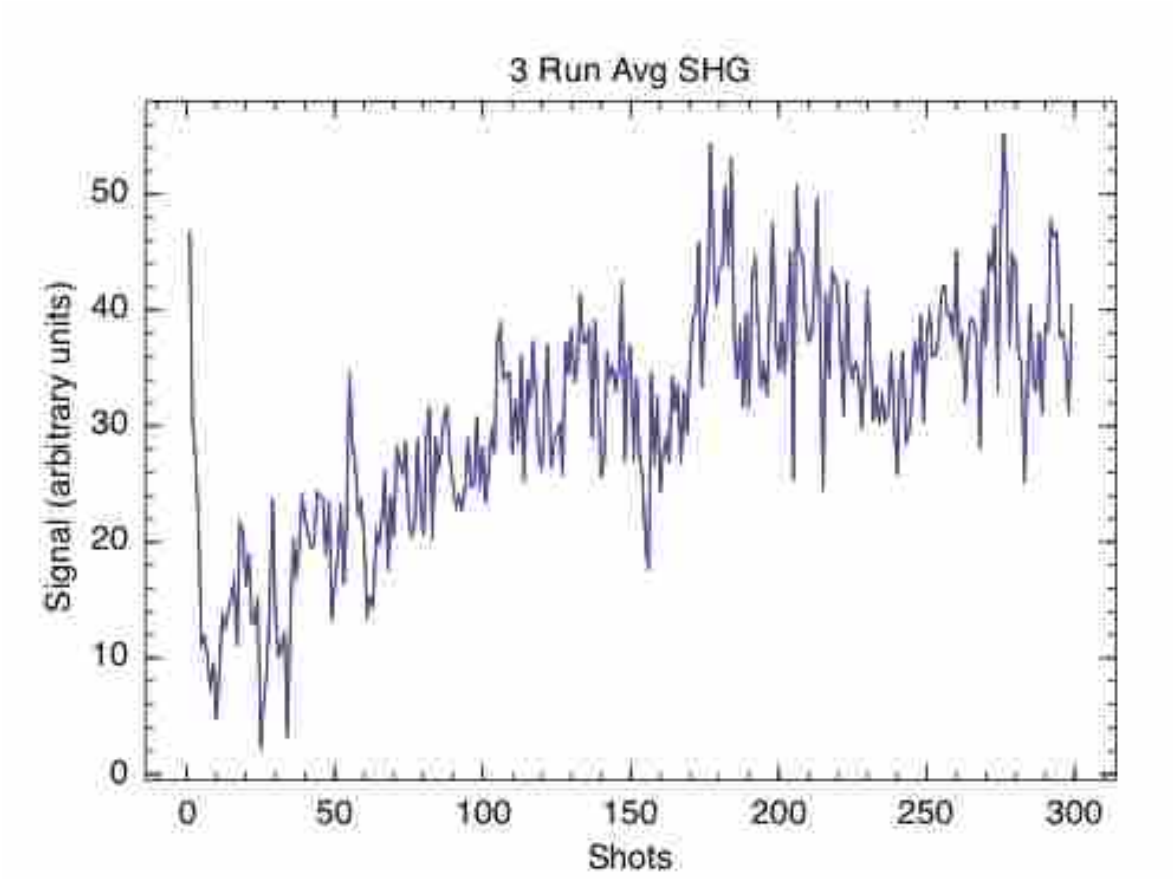

Figure 4.6. SHG signal intensity for 300 successive shots in the same sample spot. Reported data is the average of data taken from three different sample spots.

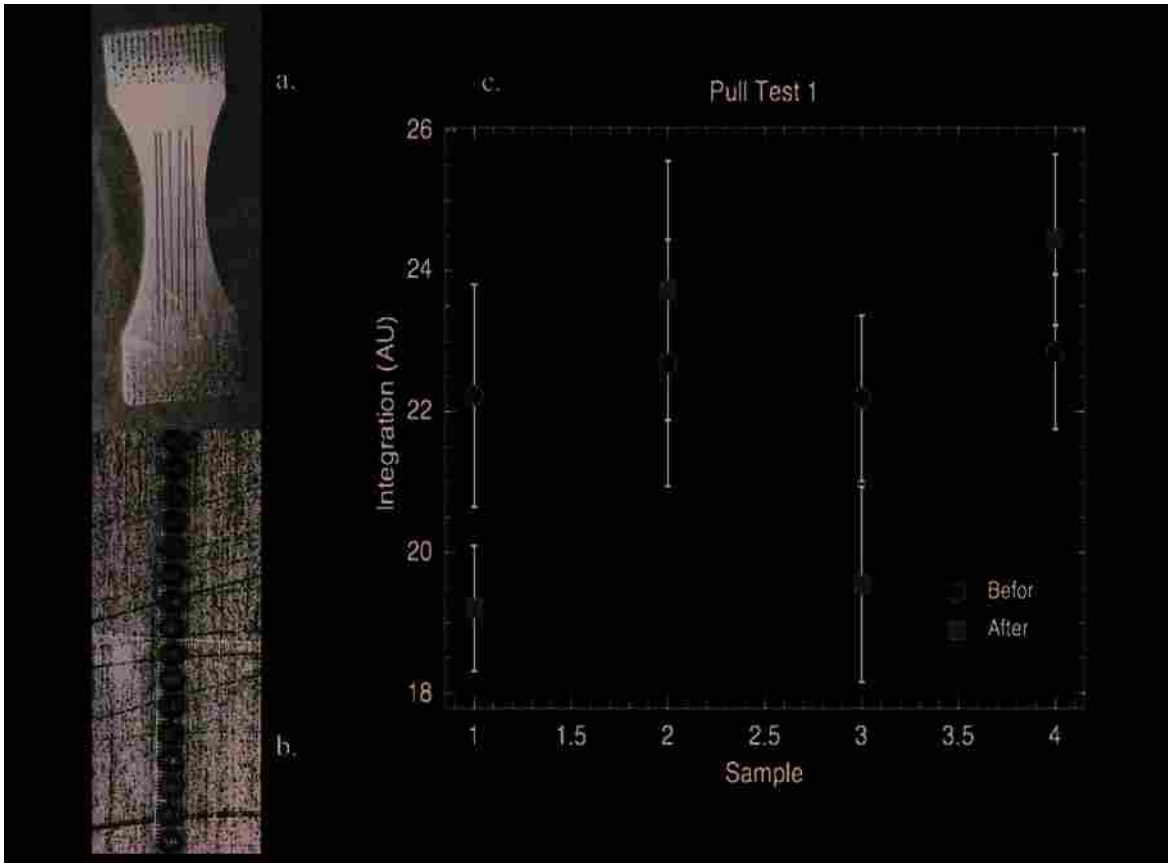

Figure 4.7. (a) Representative 2024 aluminum sample that has been burned by the Infinity laser during scanning. (b) Close of the burned spots on the sample shown in (a). (c) SHG signal intensity from 2024 aluminum samples before (blue) and after (red) mechanical deformation. The data at points one and two on the x axis are from two different sides of the same sample. The data at points three and four are from different sides of a second sample.

the signal level go down after deformation, like the stainless steel had. On the other side of both samples, the signal intensity went up. Although the error bars for the signal increases after deformation were too large for this to be a conclusive result, it strongly suggested that this was worth looking into more.

Translating the sample during scanning moved the project forward, but it had a few shortcomings. First, burning a sample while scanning isn't a nondestructive test. Second, in order to get enough data points the sample had to be scanned outside of the narrow waist section, where the mechanical deformation was expected to be most significant. The next step then was to take data without burning the sample so that analysis could be done nondestructively and in the region most affected by the mechanical deformation.

The primary obstacle to this goal was the beam profile from the YAG, which had several hot spots. An excitation beam intensity that was high enough to generate good SHG signal levels was also high enough for the hot spots in the beam to burn the sample. This problem was overcome with the excitation beam modification shown in Figure 4.8. Rather than removing the hot spots from the beam, the beam was expanded, and an iris was used to block everything but one hot spot. After the iris, the remaining excitation beam was focused onto the sample. Because we were now only dealing with one hot spot, the excitation beam intensity could be tuned to a level that allowed good SHG signal to be generated by the remaining beam, without any other beam components interacting with, and burning, the sample.

This modification allowed the data shown in Figure 4.9 to be taken without burning the samples. Unlike the data shown in Figure 4.7, these samples were only scanned on one side. The side with the best reflective surface, as determined by visual inspection, was chosen for SHG

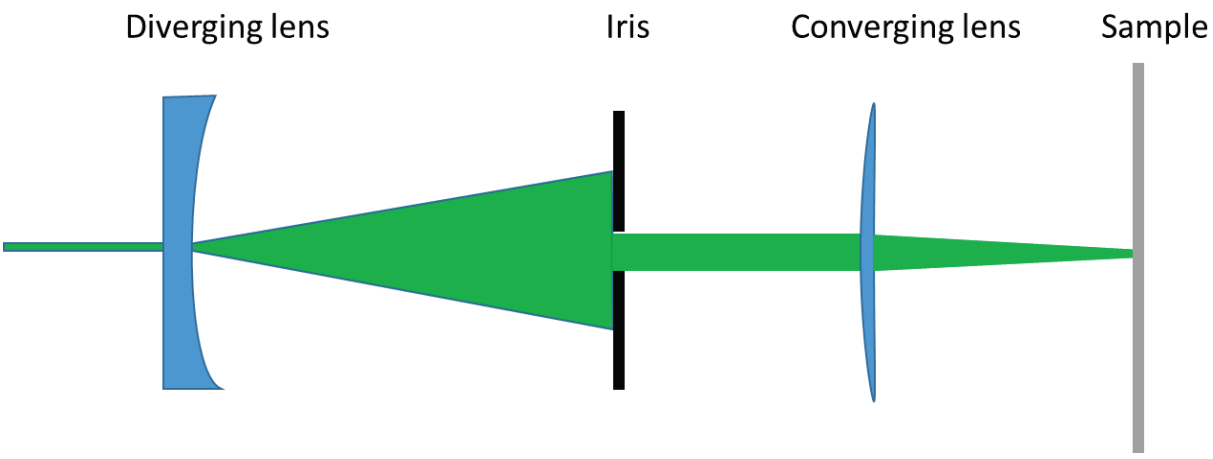

Figure 4.8. Diagram of the method used to shape the excitation beam so that SHG data could be taken without burning the sample.

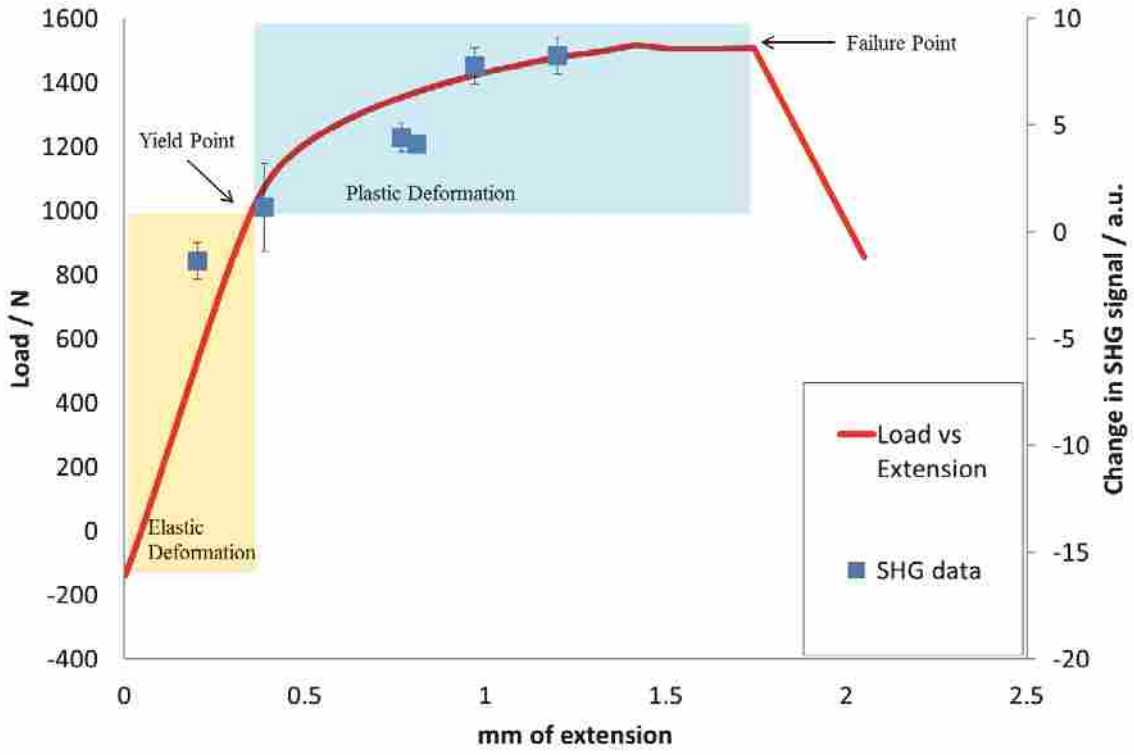

Figure 4.9. Load vs. extension curve for 2024 aluminum samples overlain with SHG data. The load vs extension curve is shown in red, with the extension on the x axis, and the load at that extension shown on the left y axis. The SHG data is shown with the blue squares with the maximum distance the sample scanned was pulled to on the x axis, and the change in the intensity of the SHG signal it produced before and after deformation shown on the y axis at the right.

scans. For easier analysis, the SHG data in Figure 4.9 is plotted along with a representative load vs. extension plot (discussed in section 4.2.1) from a 2024 aluminum sample. The extension to which the sample was pulled is plotted on the x axis with the corresponding load on the left y axis. For the SHG data, the x axis is the maximum extension to which the scanned sample was pulled, and the right y axis is the change in the SHG signal level caused by the sample deformation.

The data in Figure 4.9 argue strongly for the potential of SHG as a nondestructive testing technology. Plans were made to repeat and expand upon this work, however, the excitation beam power became so unstable that it was difficult to compare SHG data taken before and after the sample was mechanically deformed. A grant was received to purchase a Minilite II YAG laser from Continuum as a new excitation source, and work is currently underway to reproduce and expand on the results discussed in this section.

4.3: SHG Detection of Aluminum Sensitization

4.3.1: Overview of Aluminum Sensitization

Aluminum, like most metals, is composed of many small, randomly oriented crystals stuck together. The small crystal pieces are called grains, and the area in between crystals is called the grain boundary. With time and heat, Mg atoms in some Al alloys move through the crystal structure and accumulate at the grain boundaries. The high concentration of Mg at the boundaries causes a new structure, called β-phase aluminum, to form at the interface between the grains. The more β-phase Al that has formed, the more sensitized the material has become.

Sensitization can occur in the aluminum used to make superstructures in modern warships,[8] where it can weaken the material and lead to damage like that shown in Figure 4.10. Repairing the damage caused by sensitization costs the U.S. Navy over $66 million dollars a year.[9] This damage is usually repaired by cutting out the affected area and welding in new material.[10] Not only is this expensive, but the heat from the cutting and welding process can accelerate the sensitization and failure of the surrounding aluminum.

The formation of β-phase aluminum in grain boundaries is shown in Figure 4.11. These images were obtained using optical metallography by Kramer et al. [10] Figure 4.11 panel **a** shows a naval grade aluminum sample before it has been heated to encourage the formation of beta phase aluminum. Panel **b** shows the same sample after it has been heated for 24 hours at 150°C. After heat treatment, the intergranular β-phase aluminum can be seen as dark lines in the sample. The formation of β-phase aluminum makes the material more susceptible to intergranular corrosion, which can significantly weaken the metal.[10,11] A common method for measuring the amount of β-phase aluminum in a sample is to remove a portion and soak it in nitric acid. The amount of sensitization is quantified by the amount of mass lost after the nitric acid treatment.

It is possible to reverse aluminum sensitization, and return the affected material to its original characteristics. In 2011 a portable system was developed that would allow structures to be repaired in place.[10] Despite this technology, sensitization is still a costly problem for the Navy, in part because the sensitized areas can't be identified without destructive testing or visible signs of damage. To overcome this problem, several attempts have been made to develop a nondestructive technology that the navy could use to detect sensitization,[12] but so far nothing commercially feasible has been developed.

Figure 4.10. Examples of damage caused by aluminum sensitization. From reference 10.

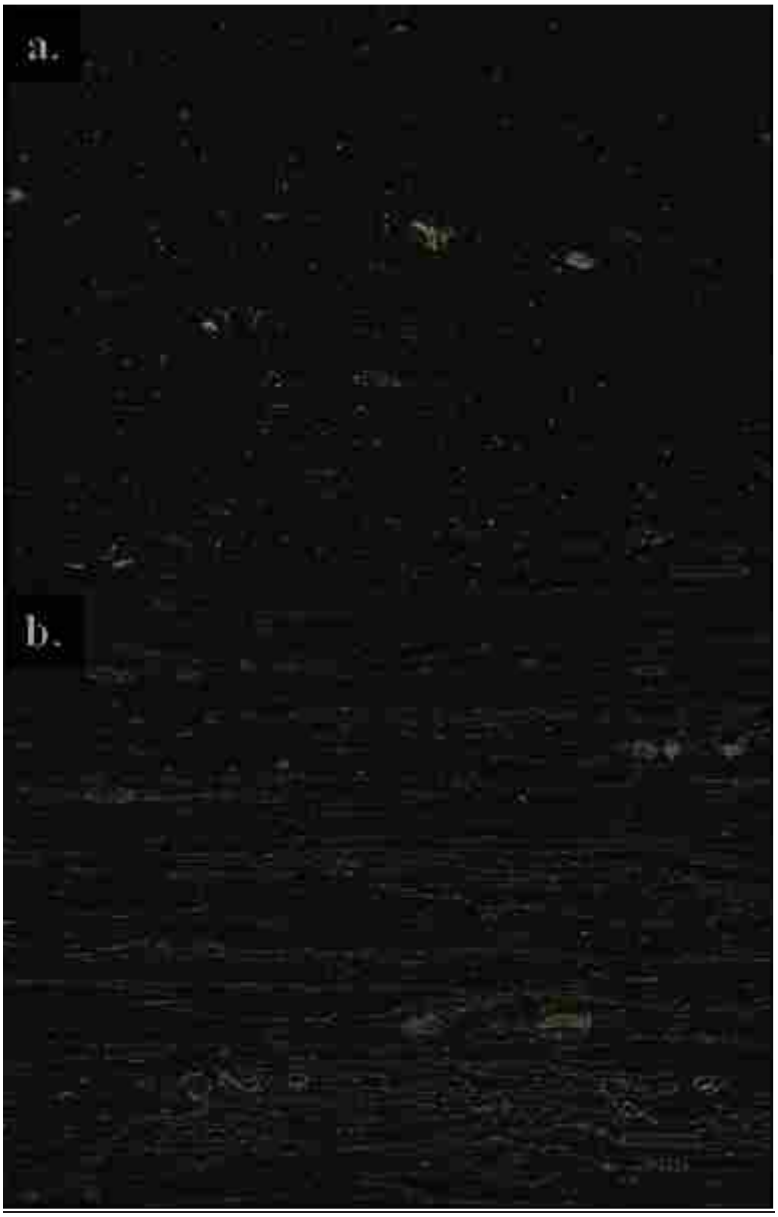

Figure 4.11. 5456 aluminum before (a), and after (b) sanitization. The sample was kept at 150° C for 24 h to develop the β-phase aluminum seen in the grain boundaries of (b). From reference 10.

4.3.2: SHG Detection of Aluminum Sensitization

A collaboration with Dr. Ronald Holtz at the Naval Research laboratory was established to investigate the sensitivity of SHG to aluminum sensitization. Dr. Holz initially provided us with three naval grade aluminum samples that we scanned with the Infinity powered SHG instrument. These data were taken using the sample translation method developed by Dustin Broderick and Alex Farnsworth. Data analysis was done using the program Dustin wrote for that purpose. Both the translational method and program are discussed in Section 4.2.3. The results of these scans are shown in Figure 4.12. The sample labeled "Sensitized" had been heat treated to increase the amount of intergranular β-phase aluminum, the sample labeled "Annealed" had been treated in a solution to remove β-phase aluminum, and the sample labeled "As Received" was untreated by Dr. Holtz.

These results were very encouraging, and when we developed the ability to scan samples without burning Dr Holtz sent us another set of samples. None of these samples had been treated to remove β-phase aluminum; instead three samples had been heated for different amounts of time, with the amount of β-phase aluminum increasing as the duration of heating increased. The sample treated for 12 days is sensitized to the point where it would be expected to fail in a warship; the sample heated for 6 days is not. As with the last set, one sample was kept as a control, and left untreated. The SHG data from these samples is shown in Figure 4.13, where the x axis shows the number of days the sample was treated, and the y axis shows the SHG signal strength, as processed by the analysis program. Although the error bars are larger on this data set, there is a clear difference in the SHG signal strength from the sample heated for 6 days, which is still structurally sound, and the sample heated for 12 days which is likely to fail.

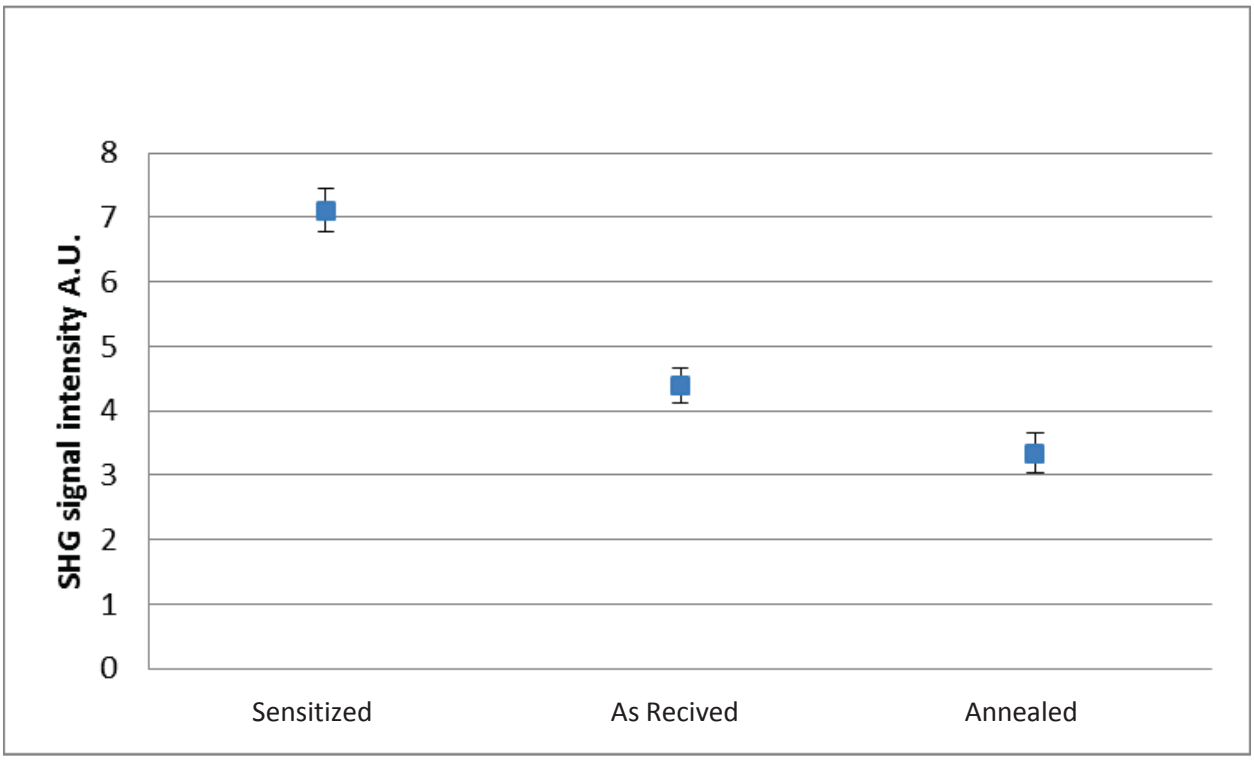

Figure 4.12. SHG signal intensity from naval grade aluminum samples that have been treated to remove β-phase aluminum (Annealed), increase β-phase aluminum (Sensitized), and left untreated (As Received).

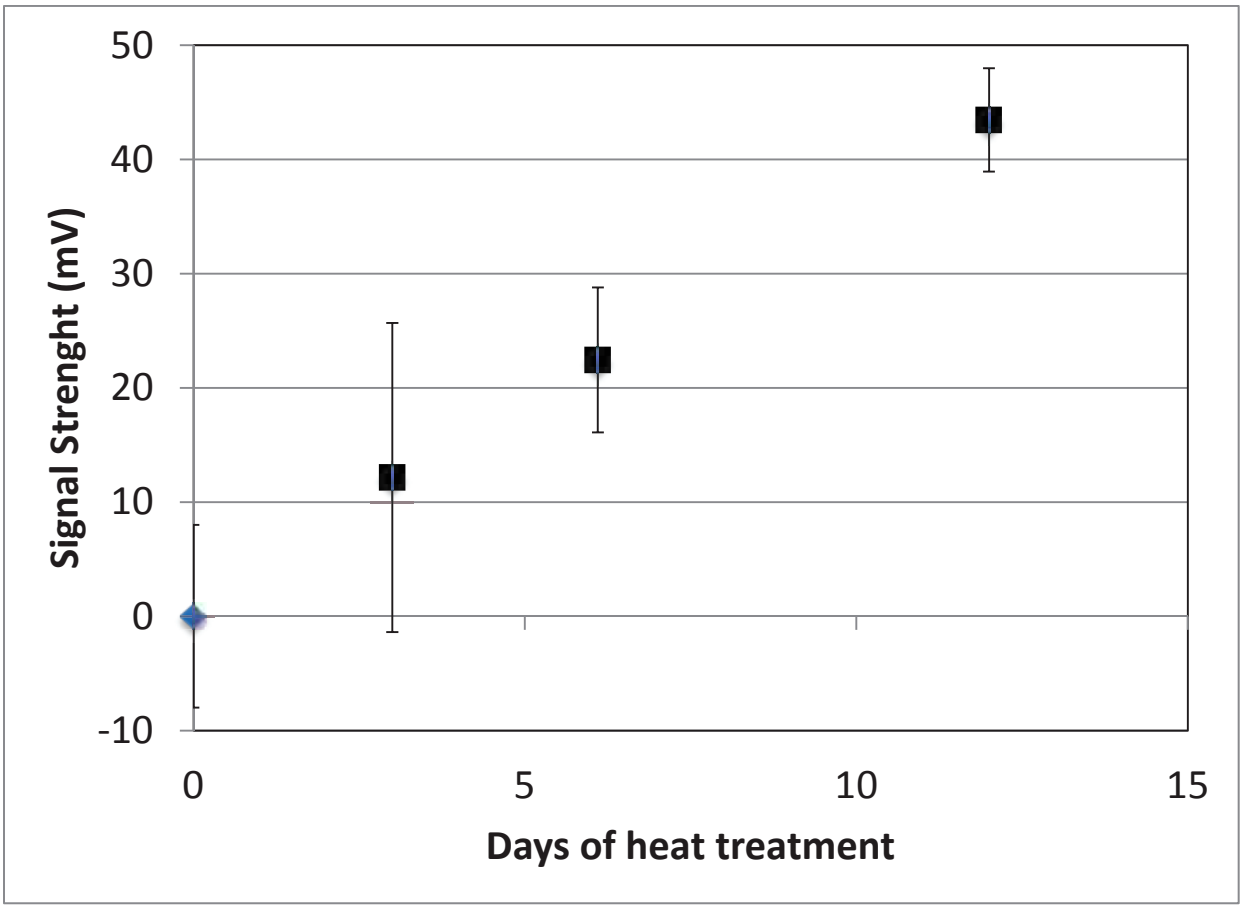

Figure 4.13. SHG intensity from naval grade aluminum samples. Samples with more days of heat treatment have higher levels of sensitization. The sample treated for twelve days has been sensitized to point that it would be expected to fail on a ship. The preceding sample, with six days of heat treatment has not been sensitized enough to fail on a ship.

Based on the strength of this work, we received funding and two new sets of sensitized aluminum samples from the Carderock Division of the Office of Naval Research (ONR). The first set of 4 samples, labeled HVH, had a recrystallized microstructure. The second set of 4 samples, labeled HVG, were from the same lot but had not been recrystallized. The HVH samples were cut from sections of material that had been measured by ONR to have a mass loss of 1.9, 28.0, 44.2, and 50.3 mg/cm^2. The HVG had come from material that the ONR measured to have a mass loss of 4.2, 24.5, 38.1 and 40.6 mg/cm^2. The HVH sample stock with a 1.9 mg/cm^2 mass loss and the HVG sample with a 4.2 mg/cm^2 mass loss both came from untreated, as-received material.

These samples were scanned with the SHG instrument powered by the Minilite II YAG laser. A new analysis program, which allowed for more flexibility in data analysis, was created by the undergraduate researcher Scott Smith. Using this analysis program, it was found that the SHG signal intensity often changed over time, even if the sample was not visibly burned. Because of this, and to account for potential variation from spot to spot on a single sample, data were collected from five different locations on each sample. To change the sample spot that was scanned, the sample was moved 2.5mm vertically with an electronically controlled stage.

Selected data from these samples are shown in Figure 4.14 where graph **a** is from the HVH samples, and graph **b** is from the HVG samples. Each data point is an average of the SHG intensity from the first laser shot at each of the five sample points scanned. The SHG data from these samples look similar to each other, but quite different from that obtained from the samples prepared by Dr. Holtz. It is especially notable that the SHG signal level goes down with increasing sensitization until going up at the most sensitized sample.

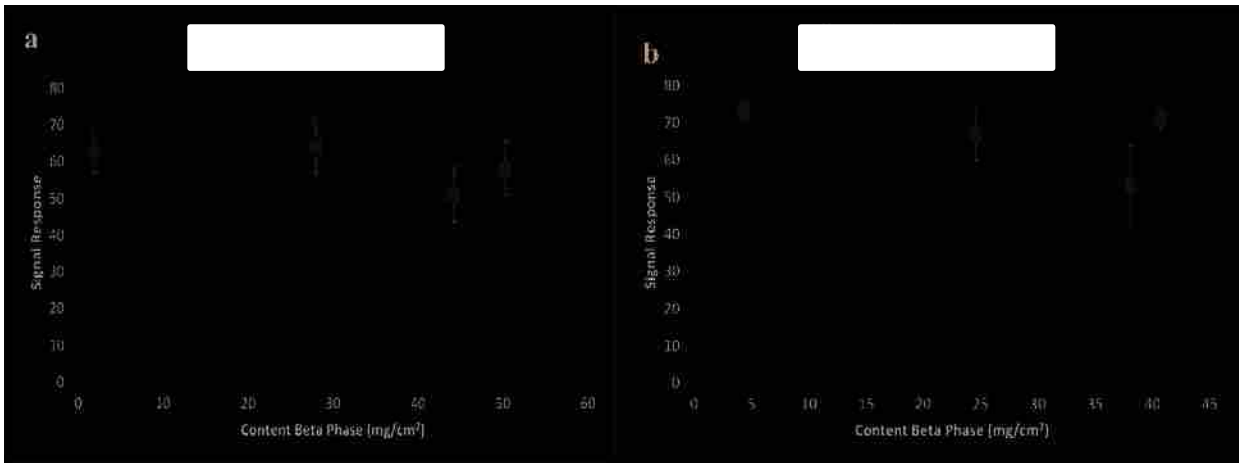

Figure 4.14. (a) SHG response from HVH naval grade aluminum samples and (b) HVG naval grade aluminum samples. The x axis shows the level of sensitization, as measured by mass loss. The y axis is the average of one laser shot from five different locations on each sample, and is reported in arbitrary units.

Work done by Pedersen et al.[13] and shown in Figure 4.15 offers a potential explanation for why the samples from ONR behaved differently than the samples from Dr. Holtz. Pederson et al.[13] scanned an extruded aluminum sample at multiple azimuthal angles before and after annealing it. Graph **a** in Figure 4.15 is from before the sample was annealed, and graph **b** is after annealing. The SHG intensity from the sample went down at almost every tested angle after the sample had been annealed. One of the explanations given for the reduction of SHG signal intensity after annealing was a reduction in the number of dislocations at the sample surface. It is possible that the amount of dislocations at the surface of the ONR samples was reduced during heat treatment. This would have reduced the overall SHG signal intensity and masked an increase in SHG signal intensity caused by sensitization. For future work, I would strongly suggest using the sensitization methods of Dr. Holtz, and/or investigating how differences in the sensitization process can affect the SHG signal. Differences in the sample surface finish, surface contaminants, and sample orientation may also have played a role in the unexpected signal decrease. However, the fact that both sample sets exhibit the same trend suggests that the heat treatment method is most likely the cause of the unexpected, initial signal drop.

4.4: Suggested Next Steps

This section is composed of materials and processes that appear to have a high demand for better nondestructive testing methods and technologies. The bulk of these subjects have come to my attention through conferences and personal interactions and as such are not easy for me to reference with literature.

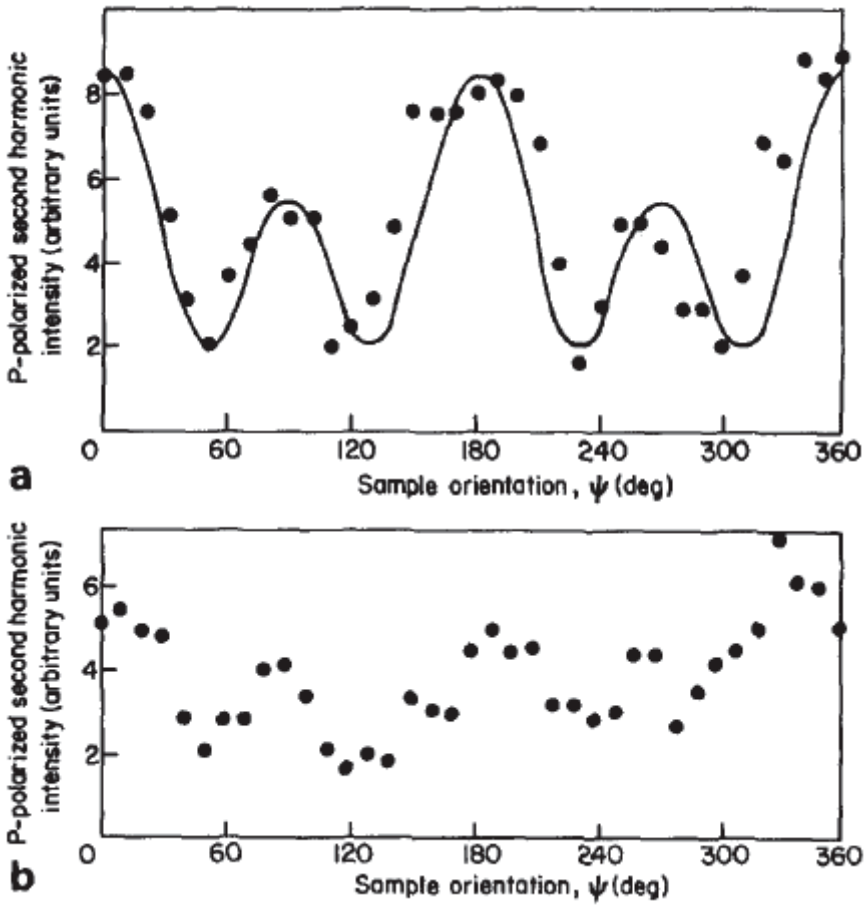

Figure 4.15. Intensity of P-polarized SHG from an extruded aluminum sample at different azimuthal orientations. (a) is before and (b) is after annealing. From reference 13.

4.4.1: Suggested Materials and Processes for SHG Based NDT Detection

4.4.1.1: Hydrogen Embrittlement

Hydrogen embrittlement affects almost all metals and alloys and often leads to sudden material failure.[14,15] The rising importance of hydrogen as a fuel source, and the increased use of high strength lightweight alloys, are making the prevention and detection of hydrogen embrittlement increasingly important.[15,16] The nondestructive testing methods for hydrogen embrittlement that I have found are based on high energy systems such as XRD and gamma radiation emision.[17] These methods tend to be expensive, both in terms of equipment and the fact that companies are legally required to pay technicians a hazard bonus when working with high energy radiation in the field. Hydrogen related damage can come in several forms; however, they all involve a chemical or phase change in the material.[14] Our work with aluminum sensitization suggests that SHG may be a good candidate to solve this problem.

4.4.1.2: Plastic Deformation in Structural Steels

Years ago, Dr. Patterson and I met with a professor from BYU's Department of Civil Engineering. He expressed an interest in SHG based NDT, primarily as a way to evaluate buildings and bridges after a major event such as an earthquake. The impact of this project may not be huge, but it is very closely related to the aerospace grade aluminum project and should be relatively easy to do. Especially since early work with stainless steel suggests that SHG detection of plastic deformation is not limited to aluminum.

4.4.1.3: Fatigue in 2024 Aluminum

Most NDT technologies are designed to detect a crack, which generally means they are designed to detect fatigue. Despite a range of methods, including some like laser shearography that claim to be able to detect sub-micron sized surface defects, better fatigue detection still seems to generate quite a bit of interest and research money. Given that SHG is known to respond to lattice strain and defects (see section 1.3.4 and 1.3.5) which precede the formation of the cracks most methods are looking for, our method should provide unrivaled early detection of metal fatigue.

4.4.1.4: Impact Damage and Delamination in Composites

Because of their outstanding strength to weight ratio, composite materials are an important structural material, with common applications including aircraft and wind mills. One of the weaknesses of composite materials is that they are particularly susceptible to impact damage, which is often found below the surface and is difficult to detect.[18,19] Several forms of material damage may occur in composite materials as a result of an impact, including delamination and cracking in the matrix.[18,19] When delamination or matrix cracking occurs, new matrix/gas interfaces are created. These interfaces may generate nonresonant SHG signal, allowing our system to detect the damage. The interfaces formed by impact may not be perfectly parallel to the material surface, and signal generated at these can be expected to follow a reflection and transmission path that is somewhat different from that of the excitation beam. Imaging sub-surface may also be challenging, although at least some of the damage should be near the surface.

Ultrasound and thermal flow are methods for nondestructively testing composite materials. Both can detect cracks in the material, but have resolution issues that SHG may be able to overcome. Delamination of matrix planes, as well as delamination between the matrix and fibers, is also difficult to detect with ultrasound and thermal flow. Additionally, ultrasound can't be used with thin parts, and temperature sensitive parts cannot be tested with thermal flow methods.

4.4.1.5: Irradiated Materials

A significant problem in using and storing radioactive materials is the damage caused to the containers and equipment used. I have contacted Dr. James Smith, who works with irradiated materials at Idaho National Laboratory, and he has expressed interest in working with us to test the use of SHG to detect radiation damage. We aren't equipped to handle irradiated materials, so we would need to send someone to INL to work on this project.

4.4.1.6: 3D Printed Metals

The field of metamaterials, developed with 3D printing technology, is poised to explode. A particularly exciting growth area is the development of 3D printed metals. These are often formed by spatially overlapping two laser beams in a metal powder. Printed metal parts can have a much higher strength to weight ratio than traditional metals and alloys. Because they use less material printed metal, parts can also be more cost effective. For example Boeing is expecting to reduce the cost of building new 787 Dreamliner aircraft by incorporating 3D printed titanium parts.[20] Defects in the material formed during the printing process significantly reduce the strength and reliability of 3D printed metals. It may be possible to follow one of the laser beams used to form a 3D metal part with an SHG interrogation beam, providing real time analysis of the

part as it is formed. Not only would this certify the part as sound, but it may also be possible to detect and remediate defects before the rest of the part is formed.

4.4.2: Potential Instrument Modifications

An apertureless scanning near-field optical microscope (ASNOM) offers insight into how an SHG based NDT system could be enhanced. An ASNOM, schematic shown in Figure 4.16, takes advantage of the SHG signal enhancement derived from a nearby electrical charge to get much better resolution than a standard SHG microscope.[21] The ASNOM achieves this high degree of resolution by using a small probe, often a silver coated fiber, to create an electrical charge near the subject's surface. The strong localized electric field enhances the SHG signal for the affected area and can allow for a resolution of ten nanometers or less.

The signal enhancing properties of a nearby charge may also be useful in nondestructive testing with SHG. In addition to enhancing the signal level, disruptions such as cracks in the material may dampen the current in the material responding to the charge, and would thus be expected to reduce the charge enhancement. This may allow SHG to also function as a very sensitive eddy flow instrument, allowing its results to be directly correlated with existing nondestructive testing techniques.

If an SHG instrument is designed for a specific metal, then using an excitation wavelength that couples into a surface plasmon should provide a large increase in signal intensity. Since the ability of SHG signal to couple with plasmons is thought to be influenced by surface defects, using an excitation wavelength that couples into a plasmon may also increase the SHG sensitivity to physical changes in a material. Comparing changes in plasmon enhanced SHG to changes in unenhanced SHG, and/or charge enhanced SHG, may also help determine if

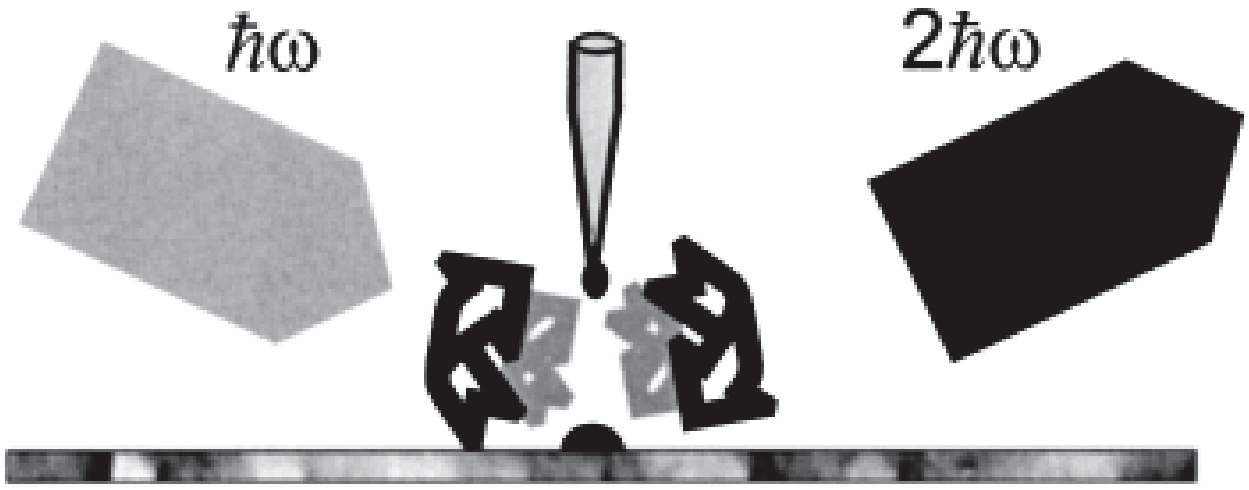

Figure 4.16. Schematic of an apertureless SHG microscope which uses an electrically charged probe to enhance sensitivity. From reference 21.

those changes are related to chemical or physical material changes. See section 1.3.5 for more information about surface plasmon SHG enhancement.

4.5: Conclusion

Because it saves lives and a great deal of money nondestructive testing is a vital and fast growing industry. Although a great deal of progress has been made in the development of nondestructive technologies, many important forms of material damage cannot be detected with commercially available equipment. There is also a great deal of interest in developing methods for earlier and more reliable detection of fatigue.

SHG has shown the potential to fill these needs. Because SHG is sensitive to changes in the metal lattice, it can detect plastic deformation in a metal, which causes changes in the metal lattice and cannot be detected with current NDT technology. Fatigue related failure also starts with material changes at the lattice level, and the ability of SHG to sense these changes may allow it to detect fatigue well before cracks form and the damage becomes visible to current NDT methods.

The inability to detect hydrogen embrittlement in metals and insensitivity to damage in composites are two of the biggest shortcomings of current NDT technologies. SHG has shown sensitivity to chemical changes such as the formation of rust on iron[22] and sensitization in naval grade aluminum. These sensitivities suggest that SHG is a very strong candidate for the detection of hydrogen embrittlement. VSFG work done with polymers and adhesives suggest that SHG may also be sensitive to damage in composite materials.

In addition to sensitivity for many forms of damage that are undetectable to current NDT, SHG evaluation can be done remotely, through coatings like paint,[22] and in hard-to-reach places

via fiber optics. The potential portability and relative affordability of SHG based NDT is also attractive, as is the fact that SHG based NDT will not give a false negative. If SHG says a material surface is unchanged, the material surface is unchanged.

A downside to SHG based NDT is the potential for false positives. Because SHG is sensitive to many different forms of material change, it may respond to a benign alteration. Careful calibration of the SHG response to the changes a particular material can undergo will help technicians determine what material changes are most likely to have caused a change in the SHG response. It is likely that unenhanced, surface plasmon enhanced, and charge enhanced SHG signal will respond differently to some types of material changes. Comparing these responses may also help determine what material changes are responsible for a change in SHG signal intensity.

4.6: References

(1) Sullivan, F. a. *the Nondestructive Testing (NDT) Industry Survey Understanding NDT Market Dynamics and Evolving End-user Preferences*2013.

(2) Non-Destructive Testing Equipment & Services Market worth $6.88 Billion by 2020. (accessed September 3 2015).

(3) Comparison of Non Destructive Tests. http://marineengineeringonline.com/tag/limitations-of-non-destructive-testing/ (accessed June 17, 2017 2017).

(4) Willcox, M.; Downes, G. A review of common nondestructive tests. *The Tube and Pipe Journal* [Online early access]. Published Online June 13, 2006, 2006. http://www.thefabricator.com/article/testingmeasuring/a-review-of-common-nondestructive-tests (accessed June 17, 2017).

(5) Brown, F.; Parks, R. E.; Sleeper, A. M. Nonlinear Optical Reflection from a Metallic Boundary. *Physical Review Letters* **1965**, *14*, 1029-1031.

(6) Davis, J. R.: *Tensile Testing*; 2 ed.; A S M International: Materials Park, OH, 2004.

(7) Walter, D. P.: *Formulas for Stress, Strain, and Structural Matrices*; 2nd ed.; John Wiley and Sons Inc.: Hobocan New Jersey, 2005.

(8) Schwarting, R.; Ebel, G.; Dorsch, T. J.: Manufacturing Techniques and Process Challenges with CG47 Class Ship Aluminum Superstructure Modernization and Repairs. American Society of Naval Engineers, 2011.

(9) Lucas, E. Personal Communication, 2015.

(10) Kramer, L.; Phillippi, M.; Tack, W. T.; Wong, C. Locally Reversing Sensitization in 5xxx Aluminum Plate. **2012**, *21*, 1025-1029.

(11) Jones, R. H.; Vetrano, J. S.; Windisch, C. F. Stress Corrosion Cracking of Al-Mg and Mg-Al Alloys. *CORROSION* **2004**, *60*, 1144-1154.

(12) Li, F.; Xiang, D.; Qin, Y.; Pond Jr, R. B.; Slusarski, K. Measurements of degree of sensitization (DoS) in aluminum alloys using EMAT ultrasound. **2011**, *51*, 561-570.

(13) Pedersen, K.; Keller, O. Nonlinear optical methods in the nondestructive testing of metal surfaces. **1988**, *21*, 411-414.

(14) Louthan, M. R. Hydrogen Embrittlement of Metals: A Primer for the Failure Analyst. **2008**, *8*, 289-307.

(15) Barnoush, A.; Vehoff, H. Recent developments in the study of hydrogen embrittlement: Hydrogen effect on dislocation nucleation. **2010**, *58*, 5274-5285.

(16) Koyama, M.; Akiyama, E.; Lee, Y.-K.; Raabe, D.; Tsuzaki, K. Overview of hydrogen embrittlement in high-Mn steels. **2017**, *42*, 12706-12723.

(17) Alex, F.; Byrne, J. G.: Nondestructive detection and measurement of hydrogen embrittlement. Google Patents, 1977.

(18) Kassapoglou, C.: *Modeling the Effect of Damage in Composite Structures Simplified Approaches*; 1 ed.; Wiley: Chichester, England, 2015.

(19) Shin, C.-S.; Liaw, S.-K.; Yang, S.-W. Post-Impact Fatigue Damage Monitoring Using Fiber Bragg Grating Sensors. *Sensors* **2014**, *14*.

(20) 3D Printing Titanium Parts Could Save Boeing Millions on Dreamliner Production. *Fortune* [Online early access]2017. http://fortune.com/2017/04/11/3d-printing-norsk-boeing-dreamliner/ (accessed June 6, 2017).

(21) Zayats, A. V.; Sandoghdar, V. Apertureless near-field optical microscopy via local second-harmonic generation. **2001**, *202*, 94-99.

(22) Ying, J.; Liu, F.; Ho, P. P.; Alfano, R. R. Nondestructive evaluation of incipient corrosion in a metal beneath paint by second-harmonic tomography. *Optics Letters* **2000**, *25*, 1189-1191.

Chapter 5: Nonresonant-Independent VSFG Analysis of Cold-Drawn High Density Polyethylene

5.1: Chapter Introduction

With roughly 300 million tons of plastic produced in a year[1], polymers are a major part of our lives. Polymers also play a significant role in composite materials and adhesives, both of which are growing in importance. Because of their immense impact and potential, polymers have been studied for decades. The molecular level behavior of polymer surfaces, however, is a noticeable hole in our current understanding. Since many properties, such as adhesion and adsorption, are influenced by the material surface this is a significant deficit.

Vibrational spectroscopy can be a powerful tool in developing a molecular level understanding of a system or material. Surface specific vibrational information can be difficult to obtain, however. In fact, Dr. Yuen-Ron Shen, speaking about sum frequency spectroscopy (SFS), states that "SFS applications to water and polymer surfaces, for example, have produced the only vibrational spectra available for such surfaces".[2] VSFG experiments with polymers however, have generally been limited to thin films, leaving a wide range of materials and processes uninvestigated. The work in this chapter was conducted with extruded polymers, and represents an effort to expand the reach of VSFG spectroscopy to a wider range of polymer-based samples and behaviors.

The bulk of this chapter comes from the first revision of a paper submitted to Macromolecules as "Orientation of the Polymer Backbone and Methylene Groups at the Surface

of Mechanically Deformed HDPE". The manuscript has been formatted to align with the style of this text, with figures and references from the submitted paper integrated into the rest of the chapter. Section 5.2.6 of this chapter does not appear in the submitted paper. Section 5.2.6.1 was considered too technically involved with the spectroscopy for the intended audience, and section 5.2.6.2 does not yet have enough data to justify publication.

5.2: Macromolecules Paper

Orientation of the Polymer Backbone and Methylene Groups at the Surface of Mechanically Deformed HDPE as Revealed by Nonlinear Vibrational Spectroscopy

*Shawn C. Averett, Steven K. Stanley[†], Joshua J. Hanson[‡], Stacey J. Smith, James E. Patterson**

Department of Chemistry and Biochemistry, Brigham Young University, Provo, UT 84602

KEYWORDS. Mechanical deformation, vibrational sum-frequency generation (VSFG), stress-induced alignment, surface structure.

ABSTRACT. High-density polyethylene (HDPE) has been extensively studied, both as a model for semicrystalline polymers and because of its own importance. During cold drawing, crystalline regions of HDPE are known to break up and align with the direction of force, however the effect of mechanical deformation on the molecular structure of the surface has not previously been explored. Vibrational sum-frequency generation (VSFG) spectroscopy was used

to investigate changes in the molecular-level structure of the surface after cold drawing. X-ray diffraction (XRD) was used to confirm that the observed surface behavior corresponds to the expected bulk response. Prior to tensile loading, there is significant isotropy in the surface structure and tilt of the methylene groups away from the surface normal. After deformation, hydrocarbon chains at the surface of visibly necked HDPE are aligned with the direction of loading, while the associated methylene groups are oriented with the local C_{2v} symmetry axis roughly parallel to the surface normal. Small amounts of unaltered material are also found at the surface of necked HDPE, with the relative amount of unchanged material decreasing as the amount of deformation increases. Aspects of the nonresonant SFG response in the transition zone between necked and undeformed polymer may give additional insight into the deformation process.

5.2.1: Introduction

Because of their strength, relatively low cost, and wide range of physical properties, polymers have become integral to our daily lives. For example, the global demand for polyethylene (PE) alone is expected to reach nearly 100 million metric tons by 2018.[3] Semicrystalline polymers in particular have found use in a wide range of applications, from food packaging to artificial joints. This is because differences in processing conditions and additives can lead to very different physical and mechanical properties of these materials. For example, plastic shopping bags and industrial water pipes are made from the same polymer, but clearly have different characteristics. The properties of these materials can also change with mechanical, thermal and other stresses, which can be an asset or a problem depending on how well the changes can be understood and predicted. For these reasons, semicrystalline polymers have been

studied for decades, with high-density polyethylene (HDPE) often used as a model system for this class of materials. Design of next-generation materials will require a better understanding of how semicrystalline polymers respond to processing conditions, as well as how they change in response to mechanical stress and other environmental conditions.

Not only are the bulk properties of polymers affected by processing and environmental conditions, but the surface structure of a semicrystalline polymer also changes in response to these same conditions. The surface properties of a material control such phenomena as adhesion, adsorption, and reactivity. For example, it is the surface of a polymer component of a medical implant that will interact with the immune system of the patient. Thus it is critical that a molecular-level understanding of the surface, and how it responds to external stresses, be developed. Unfortunately, despite the considerable amount of work that has been done on HDPE, a detailed molecular understanding of how the surface of this material responds to mechanical deformation is still lacking.

Development of this understanding requires the use of spectroscopic tools that can give detailed, molecular insight into the structure of the surface, independent of the bulk structure of the material. In this study, we utilize vibrational sum-frequency generation (VSFG) spectroscopy, a surface sensitive technique, to interrogate the surface structure of HDPE before and after mechanical deformation. This study demonstrates the usefulness of this nonlinear optical technique for probing the surface structure of industrially relevant polymers and how that structure may change in response to external stresses and environmental conditions.

5.2.2: HDPE Morphology

The morphology and behavior of polyethylene (PE) has been discussed extensively,[4-12] therefore only a brief summary of the most relevant points is provided here. Polyethylene

consists of long hydrocarbon chains that weakly interact with each other to form ordered regions in an otherwise randomly ordered material. Under the right conditions, sections of polymer chains align with each other to form plates called lamellae. A single polymer chain can fold back on itself repeatedly within a single lamella, or it can leave one lamella to become part of the amorphous region and then become part of another lamella. The ability to form lamellae is strongly influenced by branching in the polymer chains; the fewer branches that exist on the average PE chain, the easier it is for lamellae to form. High-density polyethylene (HDPE) chains are relatively unbranched, thus lamellae form quite easily in this material. Larger scale structures can also be formed as multiple lamellae interact with each other. For example, lamellae can stack on top of each other, and these stacks can then arrange in a three-dimensional structure known as a spherulite, In a spherulite the stacked lamellae radiate out from a central point, somewhat like the spines on a sea urchin. Gaps between the lamellae and their stacks are filled with amorphous polymer.

It is because of these ordered regions in the midst of amorphous, unordered material, that HDPE is classed as a semicrystalline polymer. The degree of crystallinity in a HDPE sample affects its material properties, with an increase of crystallinity leading to an increase in tensile strength, a reduction in conductivity, and an increase in optical opacity. Changes in the degree of crystallinity can be brought about during the material processing or later in the lifetime of the sample due to prevailing or changing conditions and stresses. For example, cooling time and flow-induced shear stresses during processing have a significant impact on the degree of crystallinity. Heating to temperatures near the glass transition temperature as well as mechanical loading can also change the degree of crystallinity in a given sample. For components that are exposed to a variety of environmental conditions, but where material properties need to be stable,

it is therefore important to be able to monitor these characteristics throughout the life cycle of that component. Without such monitoring, it can be difficult to be certain that the material properties have not changed in ways that may compromise performance.

Under sufficient tensile loading, deformation of the polymer sample can cause the material to neck, which is identified by a significant localized thinning of the material. Necking causes a reduction in the overall tensile strength of the material; however, the hardness is increased.[13] Changes in roughness and surface mechanical properties due to tensile loading have also been investigated.[14] These macroscopic material properties are caused by changes in the mesoscale and molecular-level structure of the polymer. In the necking region, cavities are often formed that change the appearance of the polymer from semi-translucent to an opaque white.[15] In addition, lamellae are torn away from each other and broken into smaller pieces. Amorphous polymer chains are also pulled into alignment with the direction of stress, and the remaining lamellae fragments are strung along these aligned chains in structures known as shish-kebabs.[16] In addition to changes in bulk properties, these structural changes will also manifest at the surface of the material, and the use of surface sensitive spectroscopy, such as VSFG, can improve our understanding of these dynamic processes in response to mechanical stress and other perturbations.

5.2.3: Use of VSFG for Analysis of Surface Structure

VSFG has become a well-established technique for the structural analysis of surfaces of various kinds.[17] A few aspects of VSFG and its application to polymer surfaces merit some attention here. Due to the selection rules of this nonlinear optical technique, VSFG signal can only be produced in regions of a material that lack inversion symmetry (within the dipole approximation). At first glance, the selection rules for VSFG are potentially satisfied at three

locations: within crystalline domains, at the free surface, and at the interfaces between crystalline and amorphous regions. Each of these possibilities will be considered in turn for their possible VSFG activity.

At first glance, the generally ordered nature of the polymer chains in a crystalline region could cause us to expect VSFG signal to be produced from crystalline regions throughout the sample, particularly from the necked region where stress-induced realignment has taken place. The crystalline regions of HDPE, however, have unit cells in the orthorhombic P_{nma} space group.[18] This space group is centrosymmetric, thus no VSFG signal can be generated from within crystalline regions of HDPE.

Outside these crystalline regions, it must be noted that well-ordered, all-*trans* hydrocarbon chains possess local inversion symmetry of the methylene groups, as illustrated in Figure 5.1. So long as methylene group **a** is in a similar environment to methylene group **b**, inversion symmetry exists along the polymer chain and no VSFG signal will be produced. Such is the case in the bulk of both crystalline and amorphous regions. At the surface, however, the two types of methylene groups, **a** and **b**, are in different environments; group **a** is exposed to the air and group **b** is not. This difference of environment breaks the local inversion symmetry and allows signal to be produced at the surface of the material, even from well-ordered chains and crystalline regions.

In principle, VSFG signal could also be generated throughout the bulk at the interfaces of crystalline and amorphous regions. There are two reasons, however, why this is unlikely in our measurements. First, when such interfaces are present within bulk polyethylene, there is not a

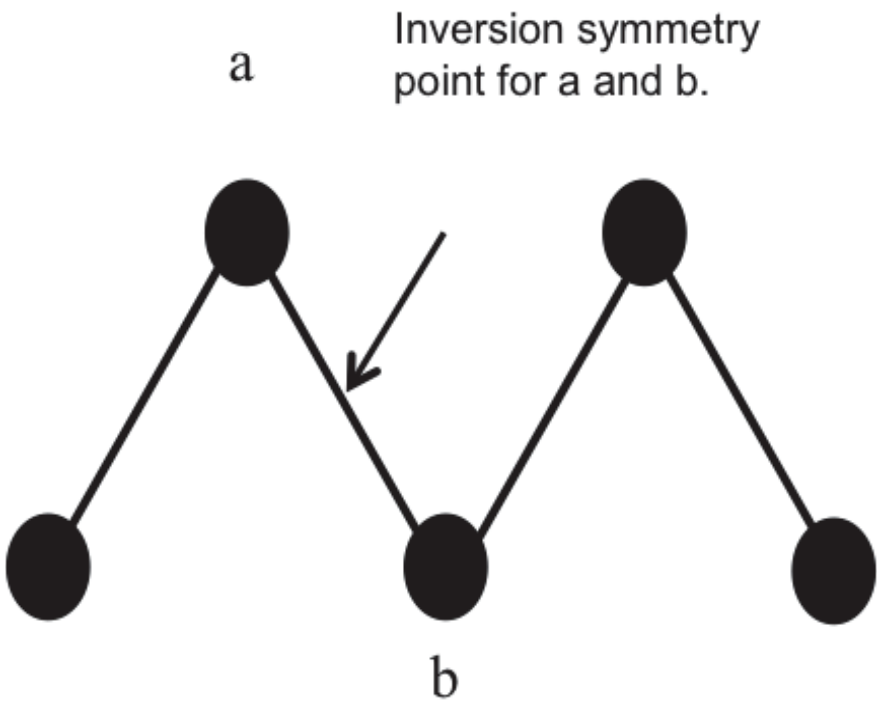

Figure 5.1. Representative section of an HDPE chain illustrating the inversion symmetry between adjacent carbon atoms **a** and **b.** This symmetry forbids VSFG signal from being produced in the bulk of a crystallite, or the ordered bulk of necked HDPE. This symmetry is broken at the surface, however.

significant discontinuity of material properties, optical index of refraction, and dielectric properties, across these boundaries. When VSFG is used to probe buried interfaces, there is typically a significant difference in one or more of these properties across the interface, as seen with solid-liquid or polymer-glass boundaries. That is not the case here, which suggests that any signal generated from amorphous/crystalline interfaces within the bulk HDPE would be significantly weaker than the signal from the free surface. In addition, the reflection geometry of our spectrometer, makes it unlikely that the measured response would be dominated by such signals, because the relevant buried interfaces would need to be oriented parallel to the free surface in order for the signal to reach the detector. Given the relatively low probability of this alignment, it seems unlikely that the measured VSFG signal would be dominated by signal from such buried interfaces. Given these considerations, the measured signal in our experiments does not come primarily from crystalline/amorphous interfaces throughout the bulk of the polymer, but rather predominately from the free surface of the HDPE sample.

Figure 5.2 shows a representative VSFG spectrum from an unperturbed HDPE sample. Clearly, there are two strong peaks in the spectrum. Before proceeding, the mode assignments of the methylene stretch modes in VSFG spectra merit some discussion. In detailed polarization studies by Lu, et al.[19] on a series of neat liquid diols, it was found that the symmetric methylene stretch occurred around 2850–2870 cm^{-1} and the antisymmetric stretch occurred around 2900–2910 cm^{-1}. Fermi resonances between the symmetric stretch and the bend were observed between 2920 and 2950 cm^{-1}. Based on these assignments, which are admittedly from a different physical system than our HDPE samples, an initial assignment would be to designate the 2863 cm^{-1} peak as the symmetric methylene stretch and the 2933 cm^{-1} peak as a Fermi resonance. For reasons that will become clear in the Results and Discussion, however, these assignments do not

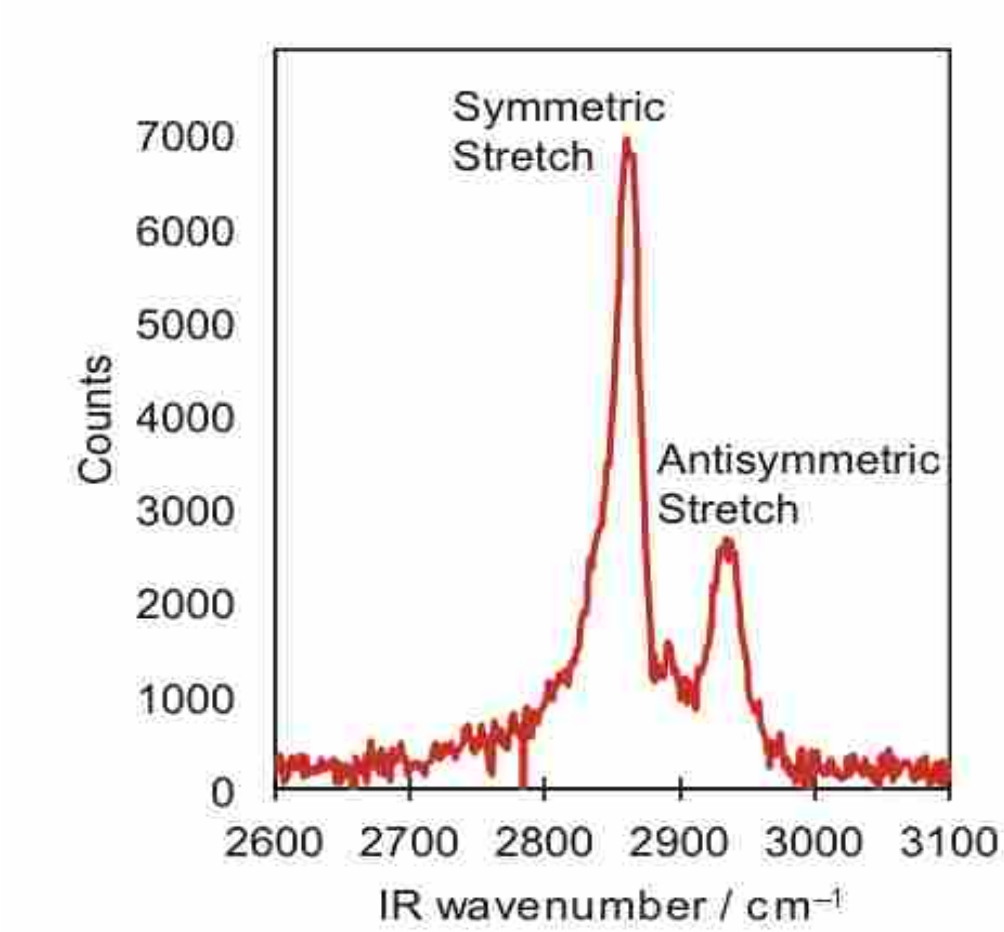

Figure 5.2. Representative VSFG spectrum of HDPE. The relative height of the symmetric stretch (2863 cm^{-1}) to the antisymmetric stretch (2933 cm^{-1}) can be used to gain information about the orientation of the methylene groups relative to the surface normal.

appear to be correct for our HDPE samples. As stated in Ref [19], the selection rules of the Fermi resonance and of the symmetric stretch must be the same, because both the symmetric stretch and the bend are of the same symmetry. In our observations, however, the higher frequency peak clearly behaves differently from the lower frequency peak as the sample is deformed and rotated with respect to the optical plane of incidence. This suggests that the two modes are of different symmetry types. We therefore assign the lower frequency peak as the symmetric methylene stretch and the higher frequency peak as the antisymmetric methylene stretch. These assignments are consistent with other VSFG studies of polyethylene.[20]

The relative intensity of the symmetric and antisymmetric signatures can be used to infer the average orientation of the methylene groups that are probed by VSFG.[21] As illustrated in Figure 5.3, the transition dipole moments of these two vibrational modes are orthogonal to each other. This means that when the polarization of the IR probe beam couples well with the symmetric stretch, there is poor coupling to the antisymmetric stretch, and vice versa. The IR probe beam is P-polarized, thus the maximum coupling to the symmetric stretch will occur when the methylene groups are oriented vertically at the surface, i.e. the methylene C_{2v} symmetry axis is parallel to the surface normal. This orientation of the methylene groups will also lead to a very weak antisymmetric stretch response. As the tilt angle increases, so does the intensity of the antisymmetric stretch, while the symmetric stretch signal decreases. These relations will form the basis of the orientation analysis presented later in this paper. More complete discussions of orientation analysis of VSFG spectra are available in the literature.[21-23]

In this paper, VSFG is used as the primary spectroscopic tool to gain information about how the orientation of methylene groups and polymer chains at the surface of HDPE samples is affected by mechanical deformation, specifically cold drawing at a low strain rate. X-ray

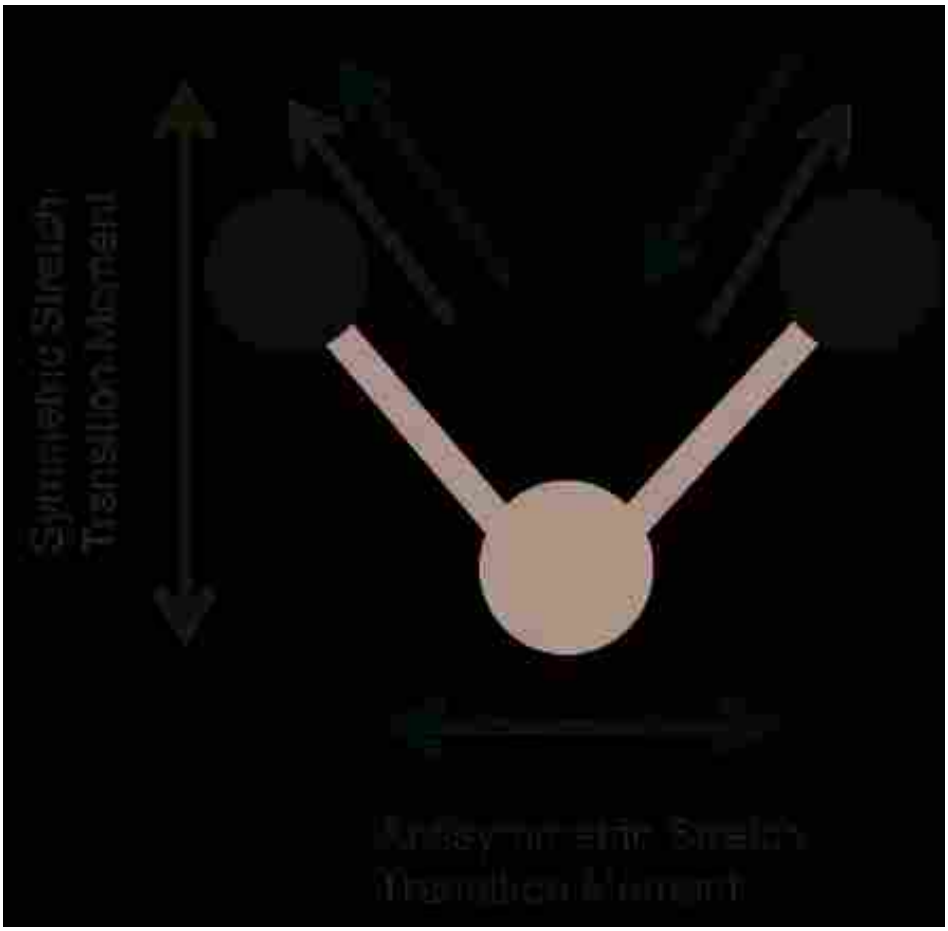

Figure 5.3. The transition moment of the methylene symmetric stretch is perpendicular to that of the antisymmetric stretch. This means that as one vibrational mode interacts more strongly with the polarized infrared excitation beam, the other mode interacts more weakly.

diffraction (XRD) measurements are used to corroborate the bulk behavior of cold drawn HDPE with the VSFG results. Prior to deformation, there is considerable variation in the surface orientation of the methylene groups. Once necking occurs, however, the samples consistently exhibit an orientation where the polymer chains are aligned with the direction of the pull and the methylene groups are oriented normal to the surface. These results show the power of VSFG to identify structural changes in response to mechanical deformation, such as stress-induced realignment and the resultant reorientation of surface methylene groups, in a noninvasive and nondestructive fashion.

5.2.4: Methods

5.2.4.1: HDPE Sample Preparation

High-density polyethylene (HDPE) samples were extruded using 12,000 MW pellets (Sigma Aldrich). To create the flat surface needed for our VSFG instrument, the samples were heated after extrusion for two hours at 140°C while pressed between glass plates. Standardized spacers were placed between the glass plates to maintain a consistent sample thickness of 0.8 mm. After this smoothing process, the samples were punched from the polymer slab using a custom built die. Figure 5.4 shows the shape of the punched samples. The hourglass shape, similar to what has been used in earlier studies,[14] was used to ensure localization of the tensile stress at the waist of the sample. The HDPE samples were mechanically deformed using a single-arm mechanical testing apparatus (Instron, model 3345) at a constant strain rate of 0.003 mm/s. Once the desired maximum extension was reached, the samples were held at a constant extension overnight prior to probing with the VSFG system.

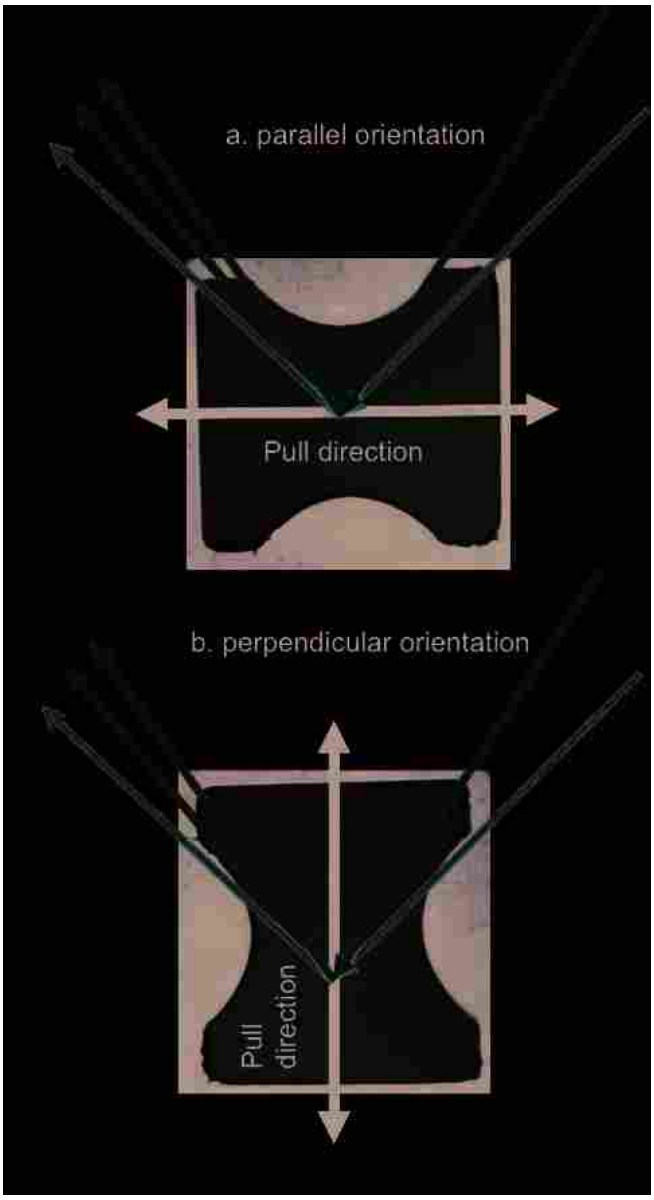

Figure 5.4. a) Illustration of the parallel orientation of the sample. In this orientation the direction of tensile load is in the plane of incidence of the VSFG beams; the plane of incidence comes out of the page. b) Illustration of the perpendicular orientation of the sample. In this orientation the direction of load is perpendicular to the plane of incidence.

5.2.4.2: X-Ray Characterization

HDPE samples, both pulled and unpulled, where characterized using a single crystal X-ray diffraction (XRD) instrument equipped with a MACH3 kappa goniometer coupled to a Bruker Apex II CCD detector and a Bruker-Nonius FR591 rotating anode X-ray source producing Cu K_α radiation (λ = 1.54178 Å). A small portion of the HDPE sample was cut out and attached to a custom mount with double-sided tape. Transmission X-ray diffraction patterns were collected and viewed using the Bruker APEX3 analysis suite.

5.2.4.3: VSFG System

Our broadband VSFG system is based on an amplified ultrafast laser system (Integra C, Quantronix) and broadband infrared optical parametric amplifier (OPA) (TOPAS-C, Light Conversion via Quantronix). Full details of the system have been published previously.[24] Briefly, a pair of Fabry-Perot étalons selected a narrow band visible wavelength of 786 nm, and the broadband IR output of the OPA was centered around 2900 cm^{-1}. All VSFG spectra were acquired in the *ssp* polarization combination: *s* polarized SFG produced by *s* polarized visible and *p* polarized IR probe beams.

A key modification for this work was the addition of a rotational sample mount that allows for 360° of rotation in the plane of the sample surface. Using this rotational mount, samples were scanned at two different orientations, with the direction of the pull oriented either parallel or perpendicular to the plane of incidence of the VSFG beams. The sample orientations are shown in Figure 5.4.

5.2.5: Results and Discussion

5.2.5.1 Characterization of Unpulled Samples

Melted and smoothed HDPE samples were characterized with both XRD and VSFG prior to any mechanical deformation. Figure 5.5 shows an XRD pattern taken from an unpulled HDPE sample. Each bright ring corresponds to diffraction from one set of ordered planes in the material. The presence of rings instead of discrete points of diffraction indicates that the sample is polycrystalline, and that the crystalline domains are randomly oriented throughout the material, i.e. the bulk sample is mostly isotropic. This diffraction pattern is consistent with prior results from isotropic semicrystalline polymer,[4] and indicates that there is no preferential direction to the ordering of the crystalline domains in the bulk of the polymer sample prior to deformation.

In contrast to the highly isotropic character of the bulk polymer indicated by the XRD data, VSFG spectra of unstressed samples show some variation with sample orientation. Figure 5.6 shows VSFG spectra from an unpulled HDPE sample at different orientations relative to the plane of incidence of the probe beams. (The orientations are depicted in Figure 5.4.) The spectrum from the perpendicular orientation is shown in blue, and the spectrum from the parallel orientation is in red. The difference in relative intensity of the two main peaks (symmetric and antisymmetric methylene stretches) indicates a variation in the average tilt angle of the methylene groups with sample orientation. This is an indication that the surface of the sample is not completely isotropic. The fact that intensity is measured for both the symmetric and antisymmetric C-H stretch modes indicates that there is some tilt of the methylene C_{2v} axis from the surface normal. There was also some variation between samples, with some samples showing

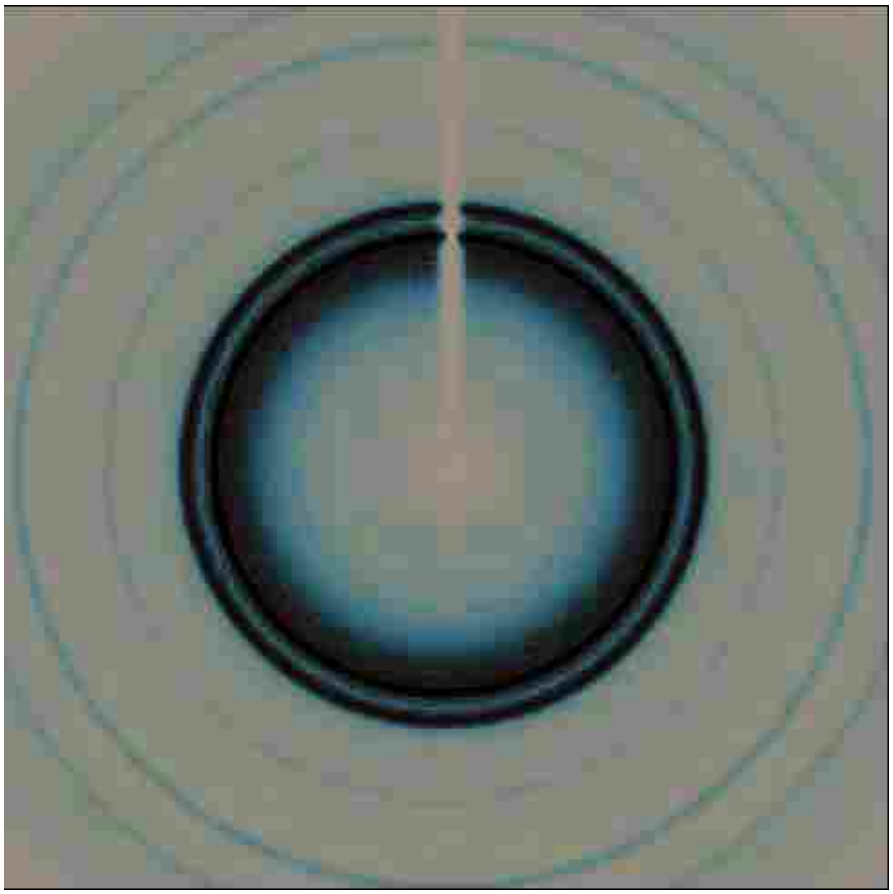

Figure 5.5. Representative XRD pattern from an unpulled HDPE sample. The presence of rings indicates that the polymer crystallites in this sample are randomly oriented.

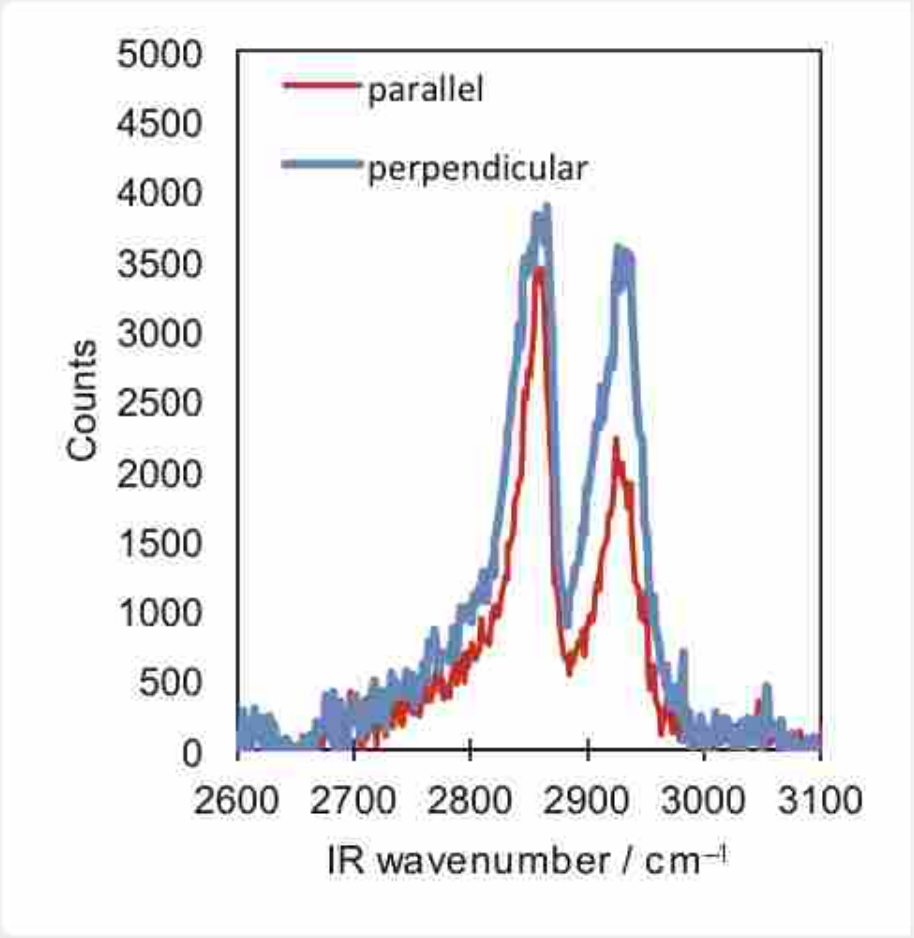

Figure 5.6. VSFG spectra of the unpulled HDPE sample from Figure 5.5 at two different orientations relative to the plane of incidence. The difference in the relative peak heights between the two orientations means that, in contrast to the bulk crystallites, there is some anisotropy in the orientation of the methylene groups on the sample surface.

a greater degree of azimuthal symmetry than others. These variations between samples may be a result of inconsistent shear stresses introduced during the smoothing process.

5.2.5.2: Response of HDPE to Mechanical Deformation

Four samples were subjected to tensile loading and deformed to different degrees of extension: 3, 4, 6, and 8 mm. At 3 mm extension, the sample showed no visible signs of necking. The sample pulled to 4 mm extension had begun to develop the opaque white appearance at the waist of the hourglass shape that is associated with necking. Necking became more pronounced as the extension increased and was fully present in the sample that was extended to 6 mm. Pulling to 8 mm only extended the width of the necked region.

Figure 5.7 shows the XRD pattern from the necked region of the sample pulled to 8 mm extension. Unlike the isotropic patterns for the unpulled material (Figure 5.5), diffracted intensity is only observed along a single axis for the pulled material. This indicates that the crystalline regions of the sample have adopted a preferred orientation in which the ordered planes are parallel to the direction of the tensile load. This matches what has been seen before with stress-induced alignment of semicrystalline polymers.[4] Another noteworthy observation is that diffracted intensity from the two bright innermost rings overlaps, or in other words, these diffraction peaks are broader than those in the unpulled XRD pattern. Peak broadening in XRD patterns is typically caused by a decrease in the size of the crystalline domains and/or an increase in microstrain in the lattice, thus this peak broadening could be a manifestation of the lamellae being broken into smaller and more strained pieces.

Figure 5.8 shows VSFG spectra for the four extended samples (pulled to 3, 4, 6, and 8 mm), all taken in the necked region, or the region where necking would take place, i.e. the waist of the hourglass shape. The representative unpulled spectra were from the same sample that was pulled

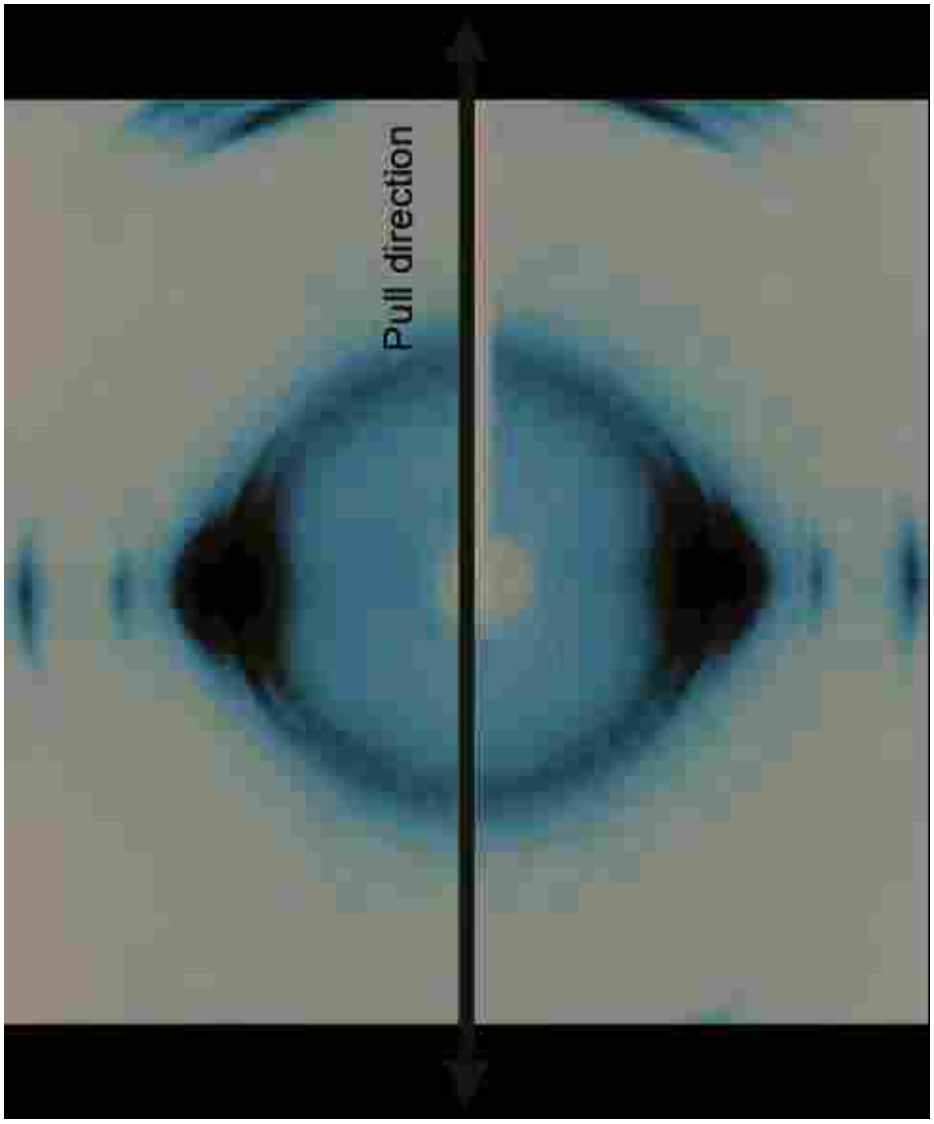

Figure 5.7. XRD pattern of the necked region of an HDPE sample pulled to 8mm. The anisotropic pattern indicates stress-induced ordering of the crystalline domains into a preferred orientation that is parallel to the direction of the tensile load.

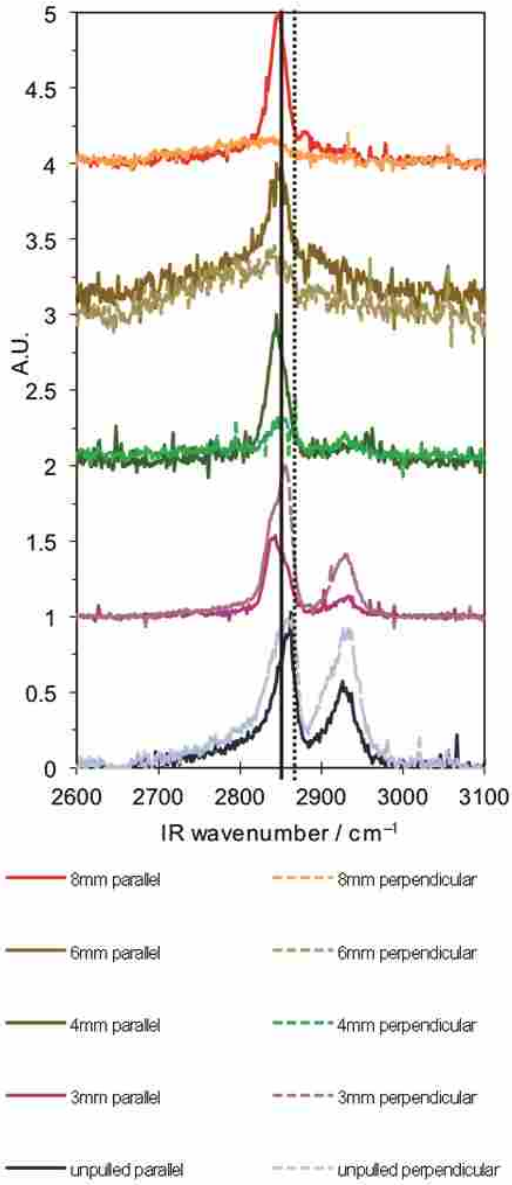

Figure 5.8. VSFG spectra in the parallel and perpendicular orientations for an unpulled HDPE sample and samples pulled to 3, 4, 6, and 8 mm. Necking was first observed in the sample pulled to 4 mm. Spectra are offset for clarity. Each spectrum is normalized to the highest signal level for that extension, regardless of sample orientation. Vertical lines indicate the frequency in cm^{-1} of the symmetric methylene stretch before (dashed) and after (solid) necking has occurred.

to 4 mm extension, and were acquired prior to the deformation. As can be seen in Figure 5.8, there are similar spectral features for each sample where whitening occurred (4 mm extension and beyond). These features include the disappearance of the antisymmetric stretch in both sample orientations, the disappearance of the symmetric stretch in the perpendicular orientation, and a redshift of the symmetric stretch in the parallel orientation relative to the unpulled sample. All these spectral changes give us insight into the changes in the average orientation of the methylene groups and the polymer backbone at the polymer free surface, as we now discuss.

5.2.5.3: Methylene Orientation in Necked HDPE

The most significant clue to the orientation of the methylene groups at the surface of mechanically deformed HDPE is the disappearance of the antisymmetric stretch signal from the VSFG spectrum in the necked region. As discussed earlier, if this high frequency peak were due to a Fermi resonance between the symmetric stretch and bend, we would expect the two peaks to behave similarly because they would be of the same symmetry. The fact that they behave differently following deformation is the basis for our assignment of the high frequency peak as the antisymmetric stretch. To aid in our interpretation of the spectral changes, we define a coordinate system for the methylene group as shown in Figure 5.9, with the H-C-H structure located in the *ac* plane. The C_{2v} symmetry axis and the transition dipole moment of the symmetric methylene stretch are both pointed along the *c* axis, and the transition dipole moment of the antisymmetric stretch is pointed along the *a* axis. The *b* axis is orthogonal to the plane defined by the H-C-H structure, and is therefore along the C-C-C backbone of the polymer.

The *p* polarized IR probe beam had a 60° angle of incidence. If the methylene groups are oriented such that the *c* axis points along the surface normal, then the IR probe beam will

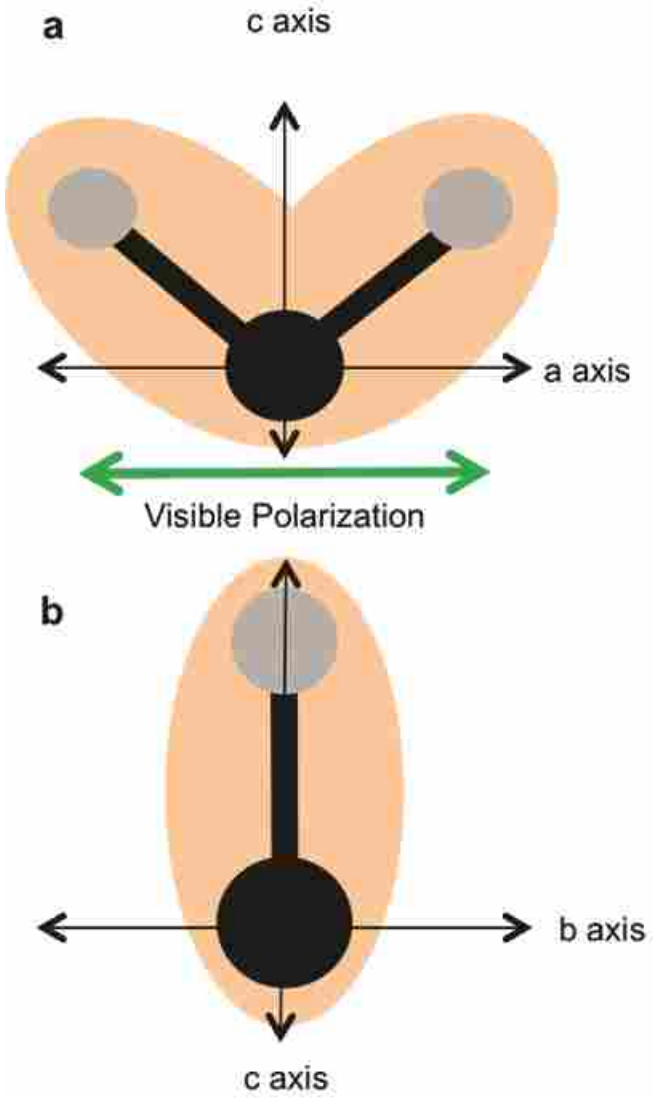

Figure 5.9. Illustration of the position of a methylene group in the internal *abc* coordinate system and its relation to the polarization of the visible probe beam. a) When the visible polarization is along the molecular *a* axis, there is significant electron density with which to interact. b) There is less electron density available for interaction when the visible beam polarization is along the *b* axis.

primarily overlap with the symmetric stretch, driving that motion resonantly. In this orientation, the IR probe beam will not couple as well to the antisymmetric stretch, as is seen in the measured spectra of the necked region. The average methylene orientation in the unpulled material is clearly more tilted than what we see in the necked region, as shown by the increased intensity of the antisymmetric methylene stretch for the unpulled sample. Thus, the mechanical deformation leads to a decrease in the tilt of the methylene groups with respect to the surface normal; the methylene groups are more upright after tensile loading.

Insights into the orientation of the polymer chains themselves can be gained by considering the interaction of the *s* polarized visible probe beam with the methylene groups. With this polarization, the visible electric field is oriented parallel to the surface and orthogonal to the plane of incidence. If the polymer chains are aligned with the direction of the pull, then with the sample positioned in the parallel orientation, the visible electric field is pointing along the molecular *a* axis. As seen in Figure 5.9a, this orientation provides a large cross section for interaction of the optical field with the electron density, increasing the VSFG signal. When the sample is in the perpendicular orientation, the visible electric field is pointed along the molecular *b* axis, where the cross section for interaction is much smaller, as shown in Figure 5.9b. This small interaction cross section will lead to very little upconversion, and therefore very weak VSFG signal. Thus, the disappearance of the symmetric stretch response from necked samples in the perpendicular orientation is consistent with an alignment of the polymer chains along the direction of the pull.

The redshift of the symmetric stretch peak in the VSFG spectrum of the necked samples is similar to what was seen by Zhang, et al.[25] in their work with ultra high molecular weight polyethylene (UHMWPE) and low-density polyethylene (LDPE). They found that the symmetric

stretch in the VSFG spectrum was 11 cm^{-1} lower in frequency for LDPE than for UHMWPE. This difference was attributed to differences in the degree of crystallinity in the two types of polyethylene, with UHMWPE being much more crystalline than LDPE. The gauche conformations imposed by bends in the polymer chains at the lamella surfaces in the crystalline domains increase the frequency of the symmetric methylene stretch. Zhang et al.[25] suggested that much of the VSFG signal from UHMWPE was produced by these gauche groups, resulting in a higher vibrational frequency in the VSFG spectrum for this material. The necking process is likely to lead to a reduction in the number of gauche methylene groups as the lamellae are broken up, leading to the observed red shift in the necked samples. The increased breadth of the diffraction intensity in the portion of the rings visible in the XRD pattern of the pulled sample is also consistent with the idea that the lamellae are being broken up.

In addition to reducing the concentration of gauche groups, necking is known to induce the formation of shish-kebab structures. In these structures, the polymer backbones within the lamellae are aligned parallel to the direction of the mechanical load, which is also parallel to the surface plane. This means that the methylene C_{2v} axis of the gauche groups in the bends of the lamellae are also oriented parallel to the surface plane. In this orientation, the gauche methylene groups are effectively invisible to VSFG.[21] The VSFG signal of the necked samples is therefore dominated by the aligned methylene groups within the polymer backbone and lamellae, which are primarily in the *trans* configuration and are oriented with the C_{2v} axis parallel to the surface normal. The VSFG response is also consistent with the polymer backbone in pulled HDPE being aligned with the direction of the mechanical load.

5.2.5.4: Other Aspects of the Necking Process

Additional insights into the surface structure of necked HDPE, and into the necking process, can be gained by further investigation of the VSFG spectra. Figure 5.10 shows VSFG spectra in the perpendicular orientation of the sample that was pulled to 4 mm extension both before and after the application of the tensile load. The spectrum of the unpulled material is shown in red and scaled on the left vertical axis, while the spectrum of the pulled material is shown in blue and scaled on the right axis. The overall signal from the pulled material is very weak compared to that of the material before loading, but a strong antisymmetric stretch response is still present. This comparison shows that the signal that does remain after pulling is more similar to the unstressed material than to the necked material of samples pulled to greater lengths. (For comparison, see the 8 mm parallel spectrum in Figure 5.8.) This may suggest that small pockets of unstressed material remain at the surface during the early stages of the necking process.

Figure 5.11 compares the VSFG spectra from the perpendicular orientation of the necked regions of the samples pulled to 4 and 8 mm. (The 4 mm spectrum is the same as in Figure 5.10.) In the sample pulled to 8 mm extension, some VSFG signal can be seen, although it looks significantly different than the sample pulled to 4 mm extension. In particular, the spectrum in the 8 mm sample is much broader than in the other spectra shown to this point. Figure 5.12 shows a VSFG spectrum acquired from the edge of the necked region of the sample pulled to 6 mm extension with the sample placed in the perpendicular orientation. This VSFG spectrum also appears very different from those in Figures 5.6, 5.8 and 5.10, which were taken well into the necked region; the spectrum is very broad and there appear to be dip-like features present at about the same frequencies where peaks were seen previously. In fact, the spectrum from the 8 mm

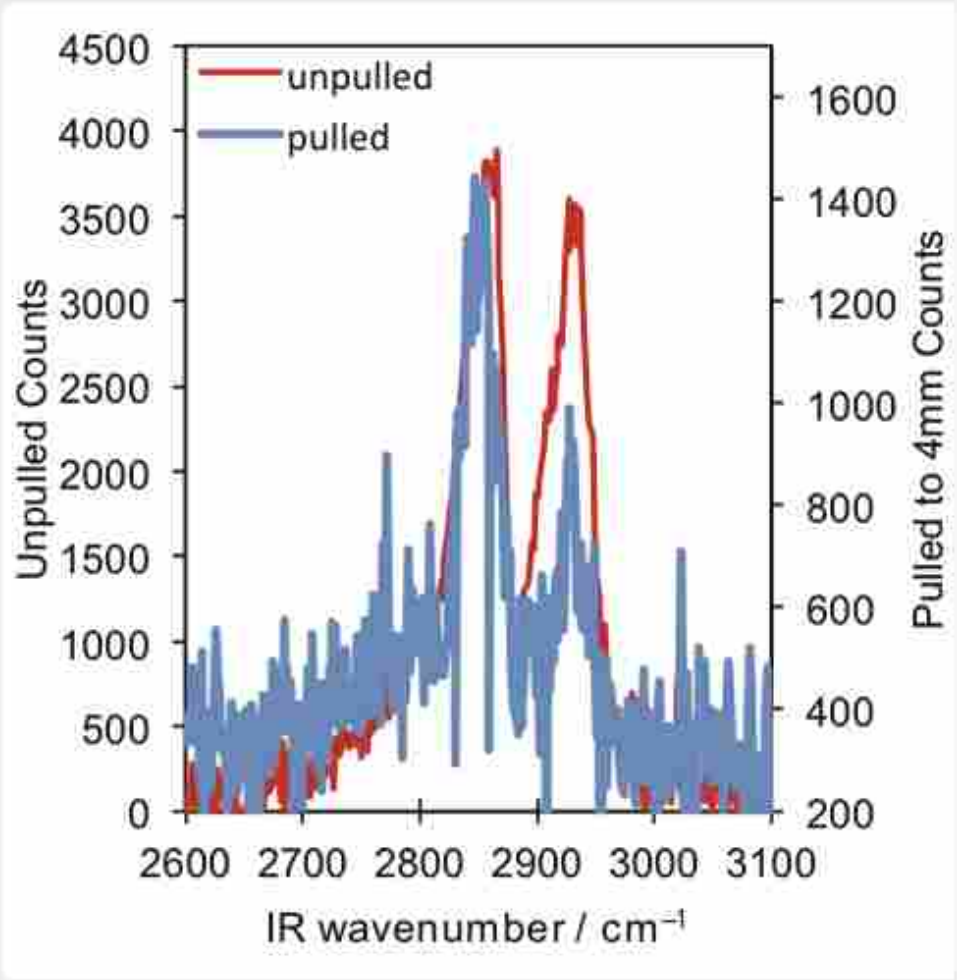

Figure 5.10. VSFG spectra taken in the perpendicular orientation from a sample pulled to 4mm before and after the pull.

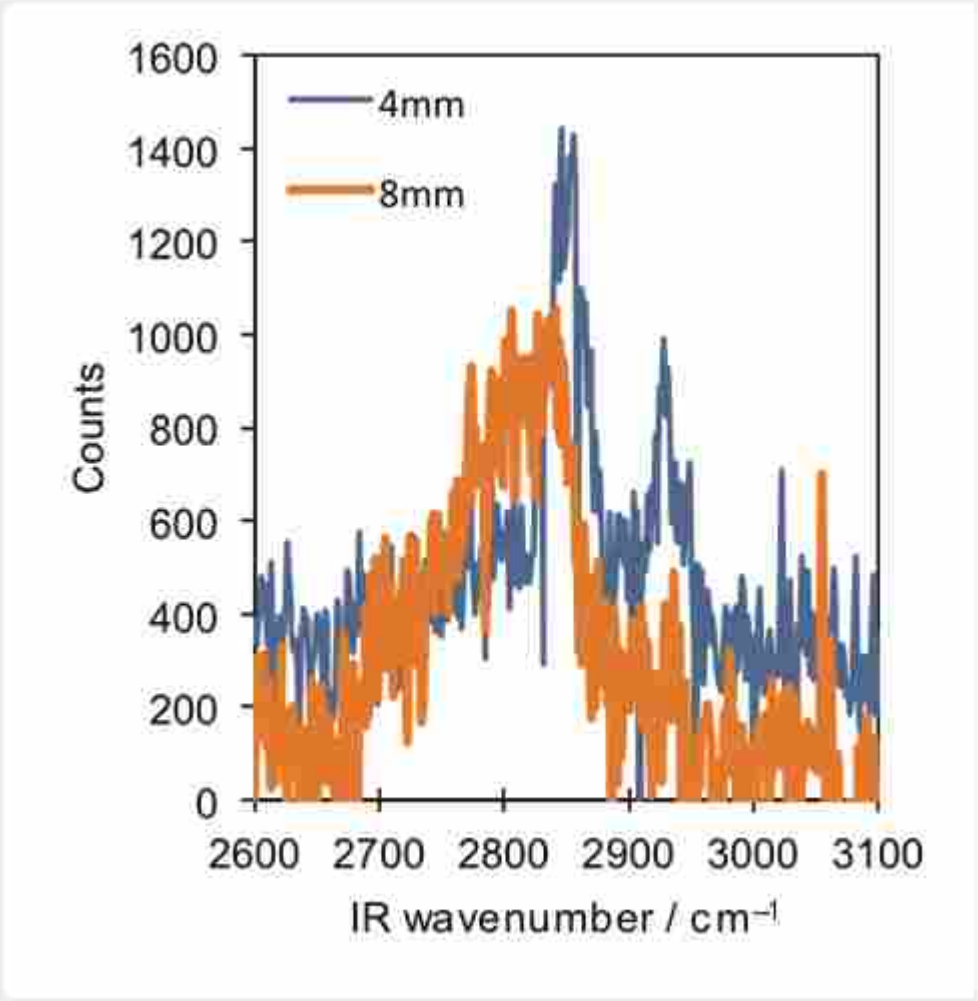

Figure 5.11. VSFG spectra taken in the perpendicular orientation from the necked region of HDPE samples pulled to 4 mm and 8 mm.

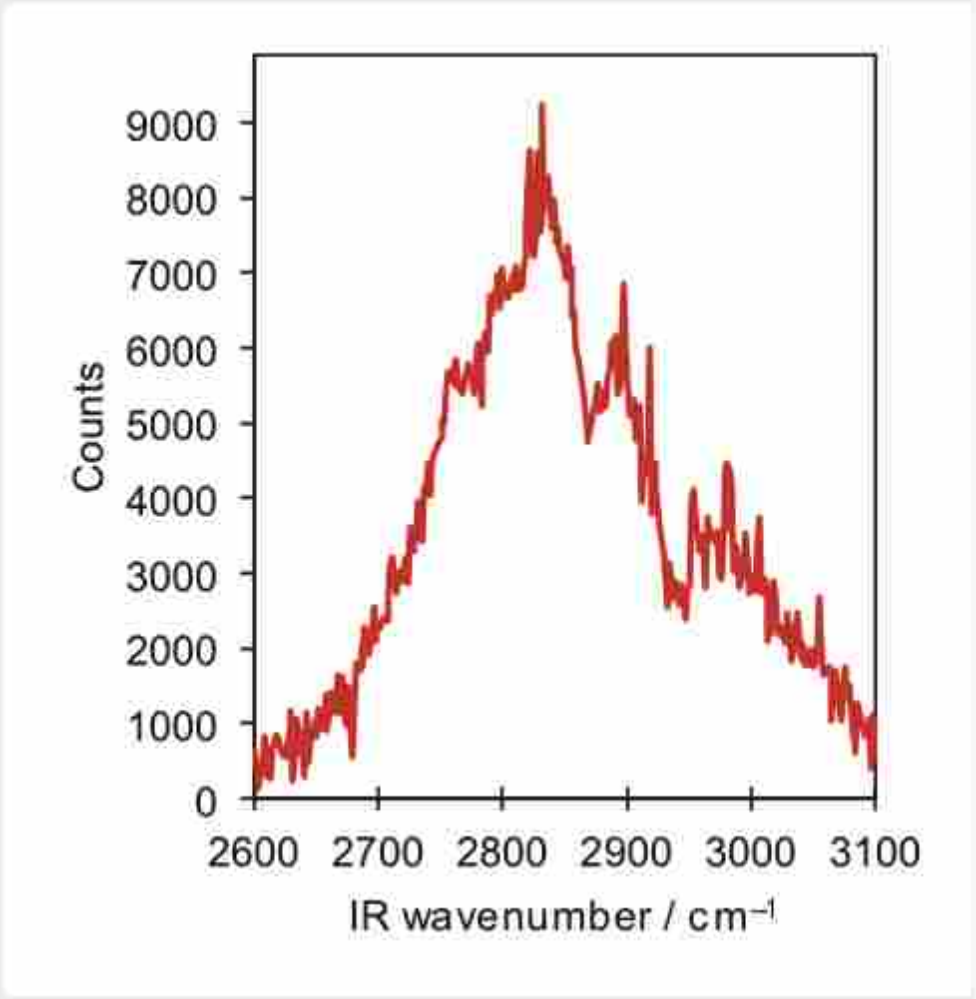

Figure 5.12. VSFG spectrum, with the sample in the perpendicular orientation, taken at the boundary between the necked and un-necked material of an HDPE sample that had been pulled to 6 mm.

sample in Figure 11 bears more resemblance to the spectrum in Figure 5.12 than to the other spectra in Figures 5.6, 5.8 and 5.10.

To better understand the spectra in Figures 5.11 and 5.12, it is necessary to briefly review an important aspect of VSFG spectroscopy. The main features of interest in a VSFG spectrum are the resonant vibrational peaks. These are seen when the frequency of the IR probe beam is resonant with molecular vibrations. In broadband VSFG systems, such as we use, the OPA produces a pulse that covers a broad range of IR frequencies and simultaneously excites multiple vibrations, thus no scanning of the IR frequency is required. The second type of signal in a VSFG measurement is known as a nonresonant response. Resonant features can interfere with the nonresonant signal either constructively, appearing as peaks, or destructively, appearing as dips, on this nonresonant response.[26] To a first approximation, this nonresonant signal does not depend on the IR frequency, therefore in scanning VSFG systems the nonresonant response simply affects the baseline signal. In broadband systems, however, where the IR spectrum of the OPA has a quasi-Gaussian profile, the nonresonant response will also have this same broad profile. The spectrum in Figure 5.12, and the spectrum in Figure 5.11 from the sample pulled to 8 mm extension, both appear to have a significant nonresonant response, as seen by the broad profile. In Figure 5.12, the resonant features clearly appear as dips on this nonresonant pedestal. The spectrum in Figure 5.11 is qualitatively similar to that of Figure 5.12, although the signal is much weaker, making it hard to directly compare them.

The origin of the nonresonant SFG response in polymeric materials is not completely understood, although some ideas have been put forward. Nonresonant SFG signal is generally thought to arise from an electronic response, and is often very strong from metals and semiconductors. A strong nonresonant response has also been seen in aged and annealed

polystyrene films,[24] and there it is thought to come from the high concentration of phenyl rings in the material, which have delocalized electrons. The structure of polyethylene, however, does not have an obvious source of readily polarizable electrons that could give rise to this type of response. One possible source is vinyl impurities where dehydrogenation has occurred and C=C bonds have formed.[27] The highly stressed state of the polymer chains in the transition area may facilitate the exposure of previously existing vinyl impurities.

Another possible origin of the nonresonant response is the presence of trapped electrons, which are expected to gather at low-density areas such as the surface or interfaces between crystalline and amorphous regions.[28-31] It has been proposed that nonresonant SFG signal may come from "interfacial potentials, generated by interfacial charges",[32] which adds weight to this possibility. Additional studies, using techniques such as small angle X-ray scattering (SAXS) that are sensitive to these internal interfaces, are therefore recommended. Another possibility is suggested by the work of Yamaguchi, et al.[33] They found that the liquid-air interface of hexane produced almost as much nonresonant signal as the liquid-air interface of benzene. They attributed this surprisingly large nonresonant response from hexane to electric quadrupole contributions, which are always allowed and are not restricted to a surface or interface.[34] These quadrupolar contributions may play a role in the stress-aligned HDPE chains, although it is not quite clear why this effect would be stronger in the transition region than it is in either the native, unstressed material or in the necked region.

When the sample from Figure 5.12 was scanned well inside the necked region, a much weaker nonresonant response was detected. Figure 5.13 shows VSFG spectra from this sample (pulled to 6 mm extension) from both the transition zone and in the center of the necked region; the sample was in the perpendicular orientation for both measurements, and the spectrum shown

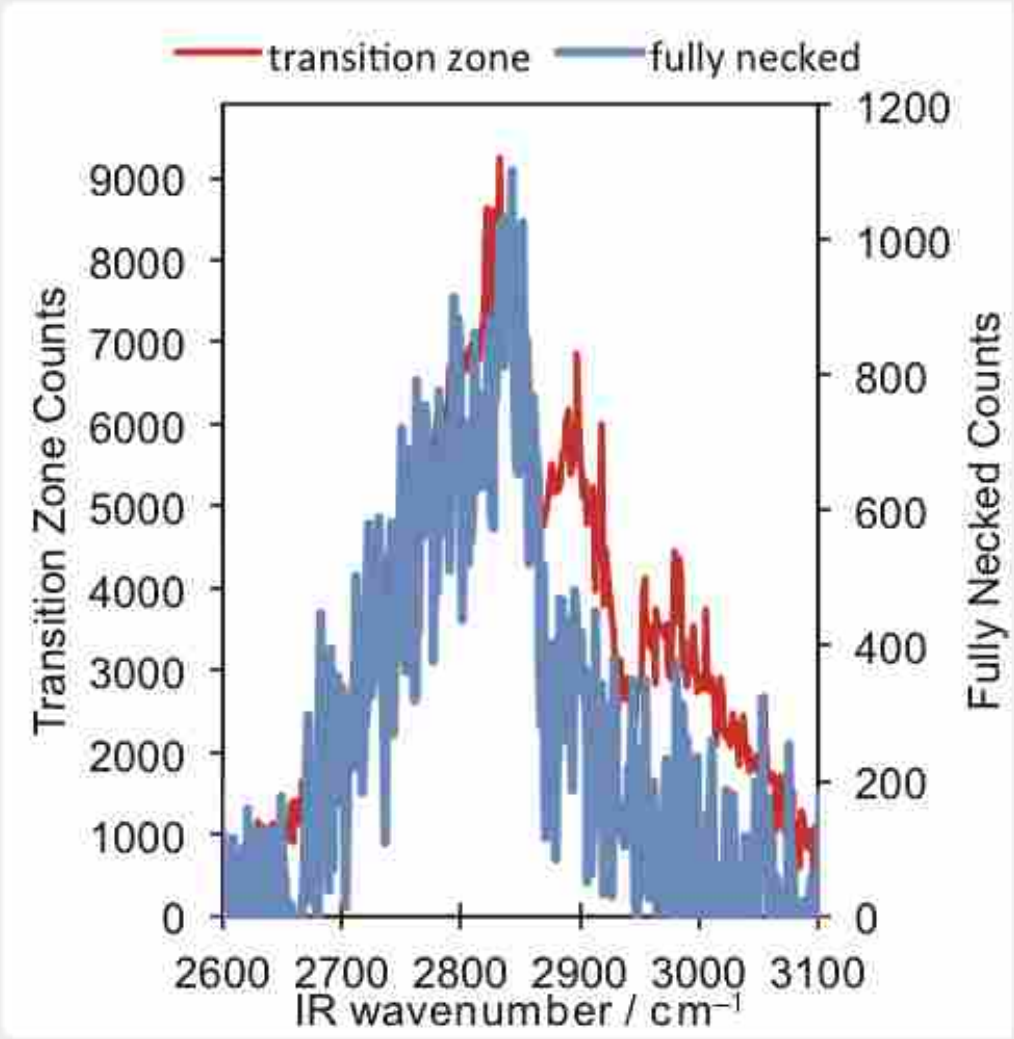

Figure 5.13. VSFG spectra from the sample pulled to 6 mm taken in the perpendicular orientation. The red spectrum is the same as that shown in Figure 12, taken from the transition zone between necked and un-necked regions. The blue spectrum is from the fully necked region of the same sample.

in red is the same from Figure 5.12. The broad nonresonant profile is clear in both spectra, however the overall signal is much weaker in the fully necked region than in the transition zone. The sharp dip in intensity at ~2870 cm^{-1} from the fully necked region is likely due to the interference of a resonant signal from the symmetric stretch with the nonresonant response. (When there is interference between resonant and nonresonant signals, the positions of the resonant features often appears slightly shifted.) Note that, unlike the spectrum from the transition region, there is very little evidence of the antisymmetric stretch in the spectrum from the fully necked region. This matches what is seen in the resonant response from the parallel orientation: a strong symmetric stretch response with a very weak antisymmetric stretch. Thus, there appears to be more that we can learn about the deformation process by paying closer attention to the nonresonant SFG response.

5.2.6: Additional Considerations

5.2.6.1 Orientation Analysis With Matlab Modeling

In addition to the analysis used in section 5.2.5.3, the orientation of methylene groups relative to the surface can also be determined by considering the Cartesian transform coefficients for a system with C_{2v} symmetry published by Hirose et al.[23] These coefficients transform the VSFG susceptibility tensor from the abc molecular reference frame, discussed in section 5.2.5.3, to an external xyz referenced frame. The transforms are performed using the Euler angles (θ,χ,ϕ) to relate the molecular reference frame (a,b,c) to the lab frame (x,y,z). Here θ represents the angle between the c and z axis, χ represents a rotation around the z axis, and ϕ represents a rotation around the c axis.

Because a methylene group has C_{2v} symmetry, the yyz transform of the aca tensor element is the only tensor element needed to model the antisymmetric stretch, when the SSP polarization combination is used. This transform coefficient is given by Hirose et al.[23] as:

$$-[(cos\theta - cos3\theta)/16](1 - cos2\chi)(1 + cos2\phi) - \left[\frac{1 - cos2\theta}{8}\right] sin2\chi sin2\phi \tag{1}$$

In this formalism, a perpendicular methylene orientation corresponds to a θ value of zero. A θ value of zero makes the relevant transform coefficient zero, leading to no antisymmetric stretch, as observed in necked HDPE samples. At other θ values, the antisymmetric stretch tends to oscillate with changing χ values.

For the symmetric stretch, the aac and ccc tensor elements are the elements of interest. When the SSP polarization combination is used, the yyz, xxz, xyz, and yxz components of the aac and ccc tensor elements are the relevant transform coefficients. Hirose defines these transforms as:

aacyyz

$$cos\left(\frac{\theta}{2}\right)[1 - cos(2\chi)cos(2\phi)] - \left[\frac{cos(\theta) - cos(3\theta)}{16}\right][1 - cos(2\chi)][1 + cos(2\phi)] + \left[\frac{1 + cos(2\theta)}{4}\right] sin(2\chi)sin(2\phi) \tag{2}$$

aacxxz

$$cos\left(\frac{\theta}{2}\right)[1 + cos(2\chi)cos(2\phi)] - \left[\frac{cos(\theta) - cos(3\theta)}{16}\right][1 + cos(2\chi)][1 + cos(2\phi)] - \left[\frac{1 + cos(2\theta)}{4}\right] sin(2\chi)sin(2\phi) \tag{3}$$

aacxyz

$$-cos\left(\frac{\theta}{2}\right) sin(2\chi)cos(2\phi) + \left[\frac{cos(\theta) - cos(3\theta)}{16}\right] sin(2\chi)[1 + cos(2\phi)] - \left[\frac{1 + cos(2\theta)}{4}\right] cos(2\chi)sin(2\phi) \tag{4}$$

$$-cos\left(\frac{\theta}{2}\right)sin(2\chi)cos(2\phi)+\left[\frac{cos(\theta)-cos(3\theta)}{16}\right]sin(2\chi)[1+cos(2\phi)]$$

aacyxz
$$-\left[\frac{1+cos(2\theta)}{4}\right]cos(2\chi)sin(2\phi) \quad (5)$$

cccyyz
$$\left[\frac{cos(\theta)-cos(3\theta)}{8}\right][1-cos(2\chi)] \quad (6)$$

cccxxz
$$\left[\frac{cos(\theta)-cos(3\theta)}{8}\right][1+cos(2\chi)] \quad (7)$$

cccxyz
$$\left[\frac{cos(\theta)-cos(3\theta)}{8}\right]sin(2\chi) \quad (8)$$

cccyxz
$$\left[\frac{cos(\theta)-cos(3\theta)}{8}\right]sin(2\chi) \quad (9)$$

Changing the azimuthal angle of the sample corresponds to rotating the methylene groups about the z axis. Because the methylene groups at the surface of the necked region of an HDPE sample all have a similar orientation, changing the azimuthal angle of the sample also effectively changes the Euler angle χ. The transforms in Equations 2-9 can be used to model the VSFG signal intensity produced by a methylene group at different values of θ, as χ. Because θ is the angle between the c and z axis, finding a modeled θ value that gives the experimentally observed response to changing χ will indicate the average tilt angle.

Making the assumption that the polymer backbone prevents the methylene group from rotating about the c axis allows the Euler angle ϕ to be set to 0. Setting ϕ equal to 0 means that there are now only three variables of interest in the transform coefficients: χ, ϕ, and the signal intensity, which is proportional to the sum of the transform elements. Figure 5.14 shows a graph made with ϕ set to 0, and the signal intensity modeled as the sum of the transform elements. Experimentally it was found that no symmetric stretch signal was produced at a χ value which is 90° away from the χ value where the most signal was produced. From the graph in Figure 5.14 it can be seen that this experimentally observed behavior is best theoretically fit at θ values of 0°

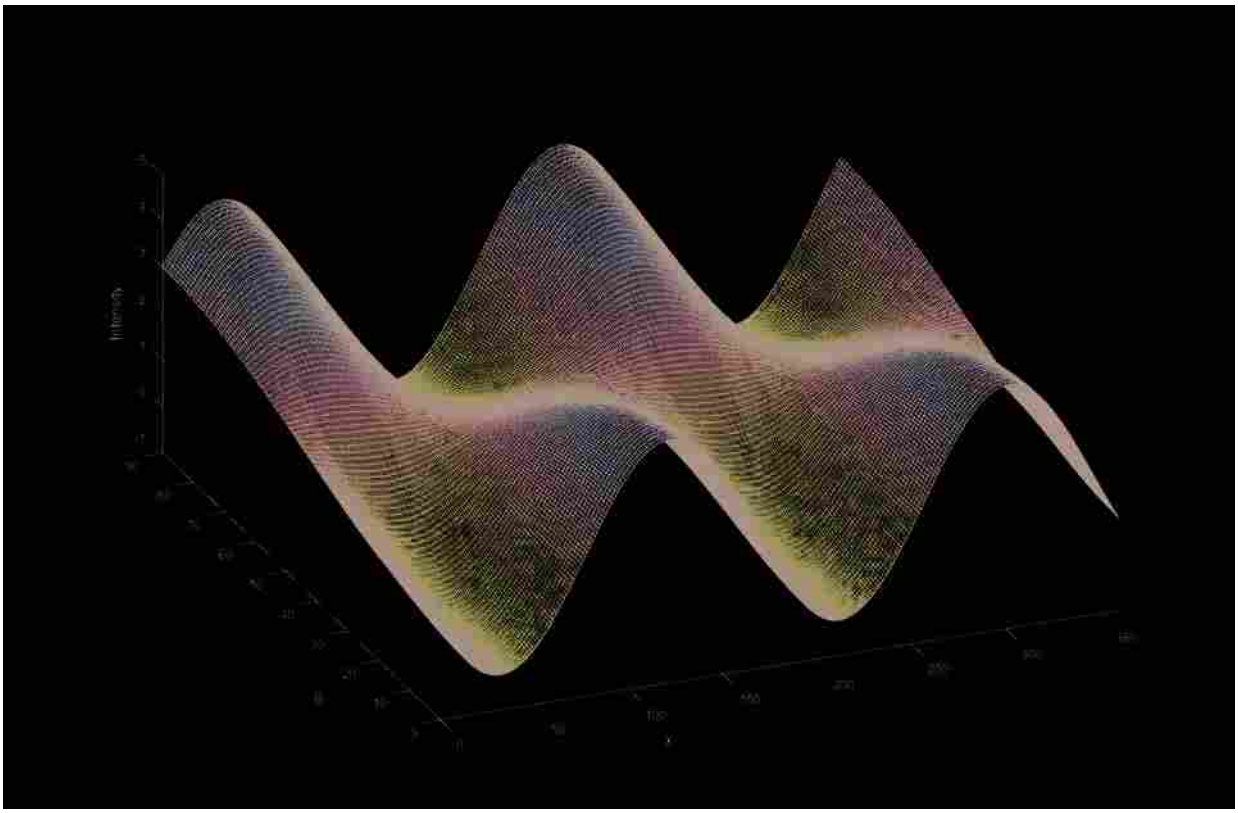

Figure 5.14. Graphical representation of how the VSFG signal intensity, from a methylene group symmetric stretch, is expected to vary at different tilt (θ) and azimuthal (χ) angles. The mathematical model this graph is based on was constructed using VSFG tensor element transforms from reference 23.

and 90°. Because a θ value of 0° also predicts the observed behavior of the antisymmetric stretch, the most likely tilt angle of the methylene groups in necked HDPE is 0°. This analysis was not performed on sample regions that had not necked because the response from these regions was not consistent from sample to sample, indicating that prior to necking each sample surface was unique, with no obvious patterns in the surface morphology.

5.2.6.2 Effects of Strain Rate and Aging in the Necked Region

The work discussed in this chapter opens the door for a wide range of new research. Two of the most obvious questions are how the rate of strain during deformation affects the final conformation of the material surface after loading and what happens to the deformed surface over time. The rate of strain is known to affect how a polymer deforms.[35-39] Preliminary evidence, however, suggests that the orientation of methylene groups and polymer chains at the surface of mechanically deformed HDPE is unaffected by the rate of strain. Figure 5.15 shows spectra from the necked regions of two different high density polyethylene (HDPE) samples. The sample in panel **a** was pulled to 20 mm of extension at a strain rate of 0.003 mm/s, which is the same rate as that used for samples in the submitted paper. The sample in panel **b** was pulled to 20 mm of extension at a strain rate of 0.03 mm/s. There is little difference in the spectra from these samples, which suggests that a different strain rate did not affect the molecular level, surface morphology. Replication of this data, and a wider range of strain rates, would be required to confirm that the molecular level surface morphology is truly independent of strain rate. Given that strain rate is known to affect polymer deformation, it would be wise to collect XRD data and SEM images of the samples before and after deformation to demonstrate that the polymer is behaving as expected.

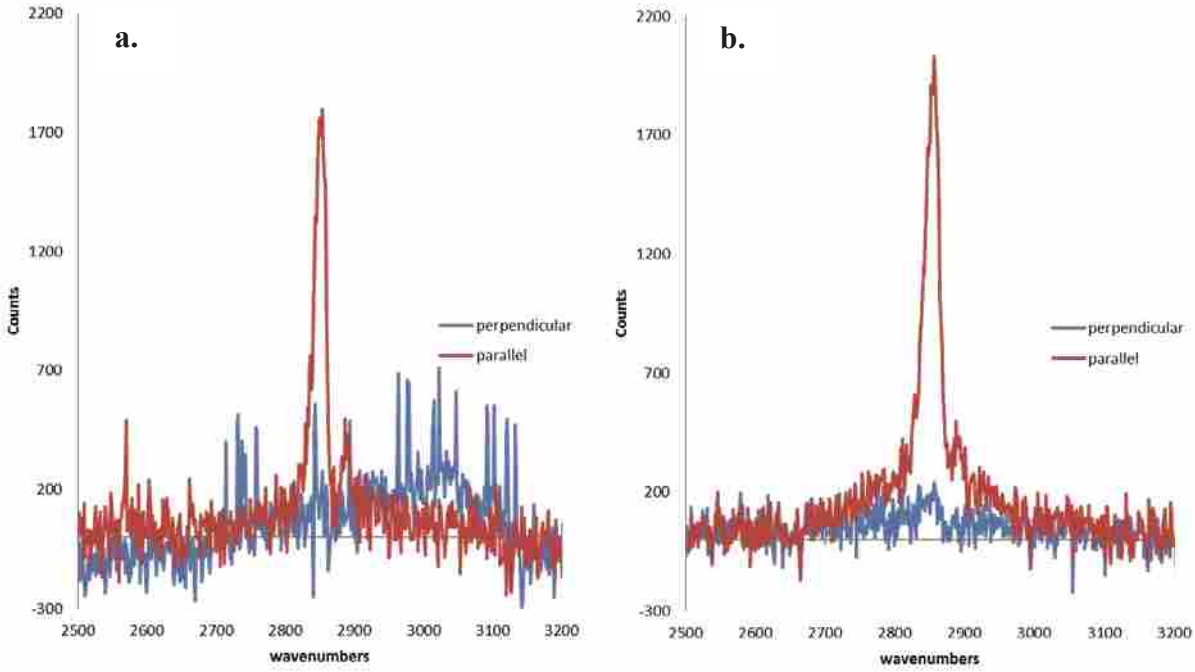

Figure 5.15. VSFG spectra from the necked region of two different HDPE samples. The sample shown in panel (a) was pulled to 20mm of deformation at a rate of 0.003mm/s. The sample shown in panel (b) was pulled to the same length of deformation at a rate of 0.03mm/s.

Aging in the necked region of HDPE samples is also of interest. Figure 5.16 shows VSFG spectra of the sample in panel **b** of Figure 5.15 in the perpendicular orientation. The blue spectrum was taken when the sample was 8 months old, and the red spectrum was taken when the sample was 9 months old. The reappearance of the symmetric stretch in the aged sample suggests that the chain alignment imposed by mechanical deformation has begun to relax at the polymer surface. It should be noted that although the symmetric stretch is again visible in the parallel orientation after 9 months of aging, the signal intensity is a fifth of the symmetric stretch when the sample is in the parallel orientation. This suggests that the majority of the detected polymer chains are still in the aligned position.

5.2.7: Conclusions

Bulk samples of HDPE were investigated with both VSFG and XRD prior to and after cold drawing. Prior to the mechanical deformation, the samples exhibited XRD patterns consistent with a mostly isotropic semicrystalline material. The VSFG spectra from the surface of unstressed material showed variability in the surface orientation of the methylene groups and significant tilt from the surface normal of the methylene C_{2v} axis. Mechanical deformation sufficient to cause necking of the polymer resulted in dramatic changes to both the XRD patterns and VSFG spectra. The XRD results indicate a stress-induced preference in the orientation of the crystalline regions of the polymer, and the VSFG results are consistent with the polymer chains being aligned with the pull direction. The VSFG results also show that surface methylene groups adopt an orientation where the local C_{2v} symmetry axis of a methylene group is along the surface normal. For samples that did not completely neck, the VSFG spectra did not exhibit all these changes, suggesting that the polymer strands are in an intermediate configuration. Increases in the nonresonant SFG response in the transition region of necked samples were also observed,

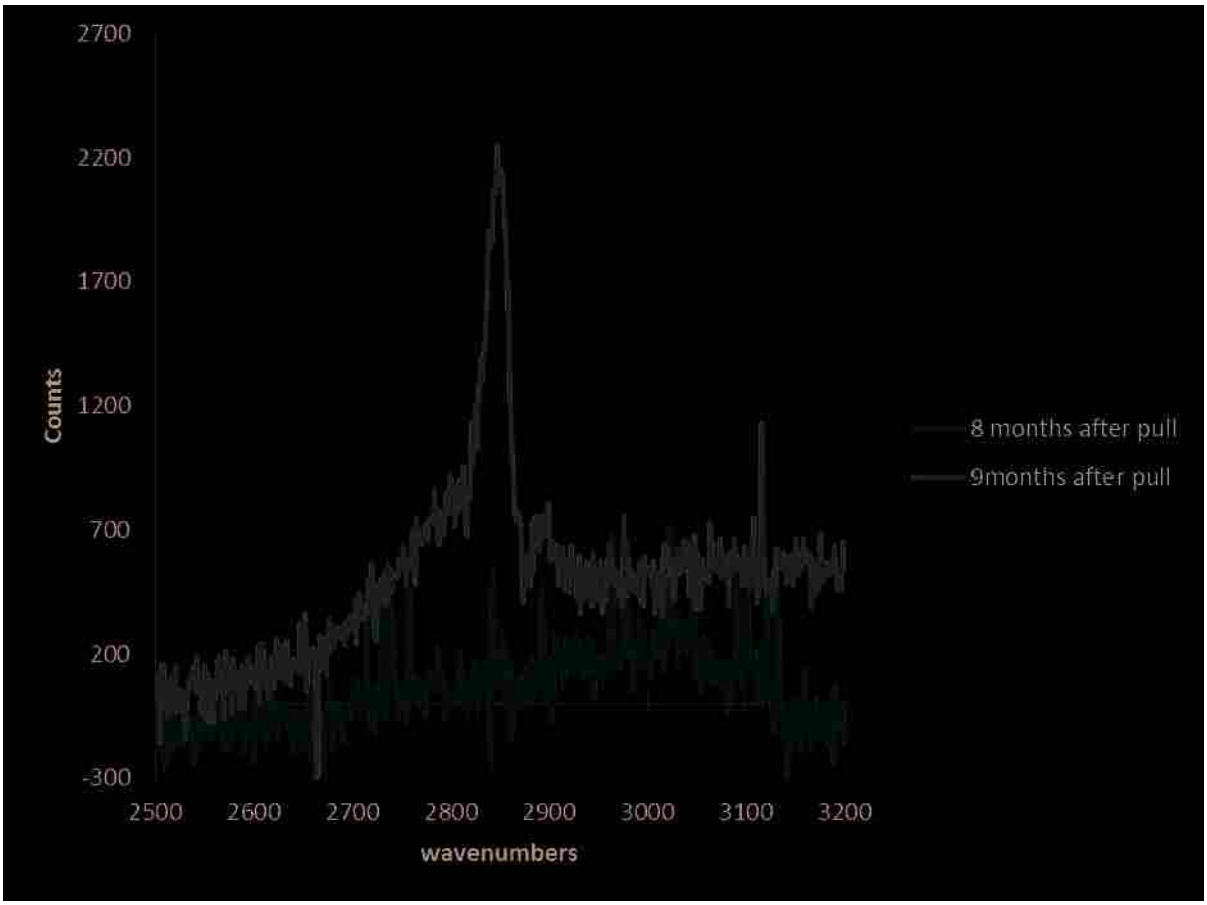

Figure 5.16. VSFG spectra of the sample in panel (b) of Figure 6.15 in the perpendicular orientation. The blue and red spectra were taken 8 and 9 months after mechanical deformation.

which may provide further insight into the dynamics of reorganization in response to the mechanical deformation.

Much of the prior work on polymeric systems with VSFG has focused on thin films, and our work demonstrates the potential for VSFG to identify the molecular-level changes due to mechanical deformation of bulk polymer samples. We have identified important spectroscopic signatures, namely changes in relative intensity of key vibrational modes and the amount of nonresonant signal that can be correlated to mechanical deformation. We are working to further develop methods to use these techniques to identify signs of deformation and fatigue in other polymeric materials. These spectroscopic signatures will then enable us to determine aspects of the stress history of a given sample in a noninvasive, nondestructive fashion. Because polymers are widely used throughout modern society in applications ranging from food storage to artificial joints, the ability to identify signs of mechanical weakness in this fashion has great value.

We will also extend our efforts to better understand the molecular-level dynamics of how a polymeric material responds to mechanical deformation. One way we will do this is by using unpulled samples with different degrees of crystallinity. We are particularly interested in looking for the changes in the nonresonant response at the transition zone of the necked region and how that response changes with the degree of crystallinity. If this response is due to the presence of trapped charges at the boundary of amorphous and crystalline regions, then we should see a correlation between the degree of crystallinity and the nonresonant response.

We will also expand our efforts to investigate the effects of strain rate, aging, and load cycling on the surface and bulk structure of polymeric materials. Preliminary data suggest that the amount of material in the necked region that does not adopt the aligned orientation may depend on strain rate, but this needs to be investigated more fully. Long-term (week to month)

relaxation effects will also be investigated. We also plan to probe polymeric samples while they are being held under tensile load, which will allow us to further investigate how this important class of materials responds to mechanical stress in real time.

AUTHOR INFORMATION

Corresponding Author

*jepatterson@chem.byu.edu.

Present Addresses

† McKetta Department of Chemical Engineering, University of Texas, Austin.

‡ IM Flash Technologies, Lehi, UT.

Author Contributions

The manuscript was written through contributions of all authors. All authors have given approval to the final version of the manuscript.

ACKNOWLEDGMENTS: The authors acknowledge the assistance of Elissa Nysetvold and Seth Babcock in helping develop the early stages of our sample preparation process, and Kaylee Rellaford for assistance in collecting the XRD patterns.

5.3: REFERENCES

(1) Anuar Sharuddin, S. D.; Abnisa, F.; Wan Daud, W. M. A.; Aroua, M. K. A review on pyrolysis of plastic wastes. **2016**, *115*, 308-326.

(2) Shen, Y. R. Phase-Sensitive Sum-Frequency Spectroscopy. *Annual Review of Physical Chemistry* **2013**, *64*, 129-150.

(3) Global Demand for Polyethylene

to Reach 99.6 Million Tons in 2018. *Pipeline Gas Journal* **2014**, *241*.

(4) Addiego, F.; Dahoun, A.; G'Sell, C.; Hiver, J.-M. Characterization of volume strain at large deformation under uniaxial tension in high-density polyethylene. **2006**, *47*, 4387-4399.

(5) Bartczak, Z.; Galeski, A.; Argon, A. S.; Cohen, R. E. On the plastic deformation of the amorphous component in semicrystalline polymers. **1996**, *37*, 2113-2123.

(6) Hiss, R.; Hobeika, S.; Lynn, C.; Strobl, G. Network Stretching, Slip Processes, and Fragmentation of Crystallites during Uniaxial Drawing of Polyethylene and Related Copolymers. A Comparative Study. *Macromolecules* **1999**, *32*, 4390-4403.

(7) Jiang, Z.; Tang, Y.; Men, Y.; Enderle, H.-F.; Lilge, D.; Roth, S. V.; Gehrke, R.; Rieger, J. Structural Evolution of Tensile-Deformed High-Density Polyethylene during Annealing: Scanning Synchrotron Small-Angle X-ray Scattering Study. *Macromolecules* **2007**, *40*, 7263-7269.

(8) Lagaron, J. M.; Dixon, N. M.; Reed, W.; Pastor, J. M.; Kip, B. J. Morphological characterisation of the crystalline structure of cold-drawn HDPE used as a model material for the environmental stress cracking (ESC) phenomenon. **1999**, *40*, 2569-2586.

(9) Lindenmeyer, P. H.; Lustig, S. Crystallite orientation in extruded polyethylene film. **1965**, *9*, 227-240.

(10) Pawlak, A.; Galeski, A. Plastic Deformation of Crystalline Polymers: The Role of Cavitation and Crystal Plasticity. *Macromolecules* **2005**, *38*, 9688-9697.

(11) Peterlin, A.; Meinel, G. Thermodynamic Properties of Drawn Linear Polyethylene. *Journal of Applied Physics* **1965**, *36*, 3028-3033.

(12) Aggarwal, S. L.; Tilley, G. P.; Sweeting, O. J. Orientation in extruded polyethylene films. **1959**, *1*, 91-100.

(13) Wing-Fu, L. Study on Modification of Polymer Properties by the Cold Drawing Process. *Soft* **2015**, *4*.

(14) Opdahl, A.; Somorjai, G. A. Stretched polymer surfaces: Atomic force microscopy measurement of the surface deformation and surface elastic properties of stretched polyethylene. **2001**, *39*, 2263-2274.

(15) Ben Jar, P. Y. Transition of neck appearance in polyethylene and effect of the associated strain rate on the damage generation. **2014**, *54*, 1871-1878.

(16) Rodriguez, F.; Cohen, C.; Ober; K., C.; Lynden, A.: *Principles of Polymer Systems*; 6 ed.; CRC Press Taylor and Francis

Group: New York, 2015.

(17) Shen, Y. R. Surface properties probed by second-harmonic and sum-frequency generation. **1989**, *337*, 519-525.

(18) Bunn, C. W. The crystal structure of long-chain normal paraffin hydrocarbons. The "shape" of the <CH2 group. *Transactions of the Faraday Society* **1939**, *35*, 482-491.

(19) Lu, R.; Gan, W.; Wu, B.-h.; Chen, H.; Wang, H.-f. Vibrational polarization spectroscopy of CH stretching modes of the methylene group at the vapor/liquid interfaces with sum frequency generation. *The journal of physical chemistry. B* **2004**, *108*, 7297-7306.

(20) Zhang, D.; Shen, Y. R.; Somorjai, G. A. Studies of surface structures and compositions of polyethylene and polypropylene by IR + visible sum frequency vibrational spectroscopy. *Chem. Phys. Lett.* **1997**, *281*, 394-400.

(21) Hirose, C.; Akamatsu, N.; Domen, K. Formulas for the analysis of surface sum-frequency generation spectrum by CH stretching modes of methyl and methylene groups. *The Journal of Chemical Physics* **1992**, *96*, 997-1004.

(22) Guyot-Sionnest, P.; Hunt, J. H.; Shen, Y. R. Sum-frequency vibrational spectroscopy of a Langmuir film: Study of molecular orientation of a two-dimensional system. *Physical Review Letters* **1987**, *59*, 1597-1600.

(23) Hirose, C.; Akamatsu, N.; Domen, K. Formulas for the Analysis of the Surface SFG Spectrum and Transformation Coefficients of Cartesian SFG Tensor Components. *Applied Spectroscopy* **1992**, *46*, 1051-1072.

(24) Curtis, A. D.; Reynolds, S. B.; Calchera, A. R.; Patterson, J. E. Understanding the Role of Nonresonant Sum-Frequency Generation from Polystyrene Thin Films. *The Journal of Physical Chemistry Letters* **2010**, *1*, 2435-2439.

(25) Zhang, D.; Shen, Y. R.; Somorjai, G. A. Studies of surface structures and compositions of polyethylene and polypropylene by IR+visible sum frequency vibrational spectroscopy. **1997**, *281*, 394-400.

(26) Bain, C. D. Sum-frequency vibrational spectroscopy of the solid/liquid interface. *Journal of the Chemical Society, Faraday Transactions* **1995**, *91*, 1281-1296.

(27) Ceresoli, D.; Tosatti, E.; Scandolo, S.; Santoro, G.; Serra, S. Trapping of excitons at chemical defects in polyethylene. *The Journal of Chemical Physics* **2004**, *121*, 6478-6484.

(28) Serra, D. C. a. M. C. R. a. E. T. a. S. S. a. G. S. a. S. Exciton self-trapping in bulk polyethylene. *Journal of Physics: Condensed Matter* **2005**, *17*, 4621.

(29) Serra, S.; Tosatti, E.; Iarlori, S.; Scandolo, S.; Santoro, G. Interchain electron states in polyethylene. *Physical Review B* **2000**, *62*, 4389-4393.

(30) Serra, S.; Iarlori, S.; Tosatti, E.; Scandolo, S.; Righi, M. C.; Santoro, G. E. Self-trapping vs. non-trapping of electrons and holes in organic insulators: polyethylene. **2002**, *360*, 487-493.

(31) Righi, M. C.; Scandolo, S.; Serra, S.; Iarlori, S.; Tosatti, E.; Santoro, G. Surface States and Negative Electron Affinity in Polyethylene. *Physical Review Letters* **2001**, *87*, 076802.

(32) Geiger, F. M. Second Harmonic Generation, Sum Frequency Generation, and $\chi(3)$: Dissecting Environmental Interfaces with a Nonlinear Optical Swiss Army Knife. *Annual Review of Physical Chemistry* **2009**, *60*, 61-83.

(33) Electric quadrupole contribution to the nonresonant background of sum frequency generation at air/liquid interfaces. *The Journal of Chemical Physics* **2011**, *134*, 184705.

(34) Shen, Y. R. Basic Theory of Surface Sum-Frequency Generation. *The Journal of Physical Chemistry C* **2012**, *116*, 15505-15509.

(35) Hobeika, S.; Men, Y.; Strobl, G. Temperature and Strain Rate Independence of Critical Strains in Polyethylene and Poly(ethylene-co-vinyl acetate). *Macromolecules* **2000**, *33*, 1827-1833.

(36) Jacob, G. C.; Starbuck, J. M.; Fellers, J. F.; Simunovic, S.; Boeman, R. G. Strain rate effects on the mechanical properties of polymer composite materials. **2004**, *94*, 296-301.

(37) Parsons, M.; Stepanov, E. V.; Hiltner, A.; Baer, E. Effect of strain rate on stepwise fatigue and creep slow crack growth in high density polyethylene. **2000**, *35*, 1857-1866.

(38) Ching, E. C. Y.; Poon, W. K. Y.; Li, R. K. Y.; Mai, Y.-W. Effect of strain rate on the fracture toughness of some ductile polymers using the essential work of fracture (EWF) approach. **2000**, *40*, 2558-2568.

(39) Dusunceli, N.; Colak, O. U. The effects of manufacturing techniques on viscoelastic and viscoplastic behavior of high density polyethylene (HDPE). **2008**, *29*, 1117-1124.

Chapter 6: Paused Research Projects

6.1: Introduction

This chapter discusses research projects that have shown potential but are not far enough along to publish and are not currently being worked on. The hope is that this chapter might serve as a reference for researchers looking to renew these investigations.

6.2: Scanning Samples While Under Load

The redesigned rotational sample mount, discussed in section 2.3.5, was developed to allow VSFG spectra to be taken from samples while they are under a controlled load provided by the Instron 3345 material testing machine. The mount is designed to handle any sample that has a flat surface and is small enough to fit inside the mount. This flexibility presents a wide range of experimental possibilities. Investigating several HDPE behaviors that were observed during the work discussed in Chapter 5, and returning to Dr. James Patterson's initial research focus of studying buried adhesive interfaces as they are under load, are among the most promising avenues of investigation.

6.2.1: Adhesives

Chapter 6 of Dr. Angela Calchera's dissertation discusses progress the lab group made in studying adhesives under load.[1] Figure 6.1 is a diagram of a common sample configuration for that earlier work. The samples were generally constructed with a fused silica window that had a thin polymer film on the adhesive side. The polymer film was then glued to a metal post that was connected to the Instron via a cable. The VSFG excitation and signal beams passed through the fused silica window. A major obstacle in the original adhesives work was that the polymer thin

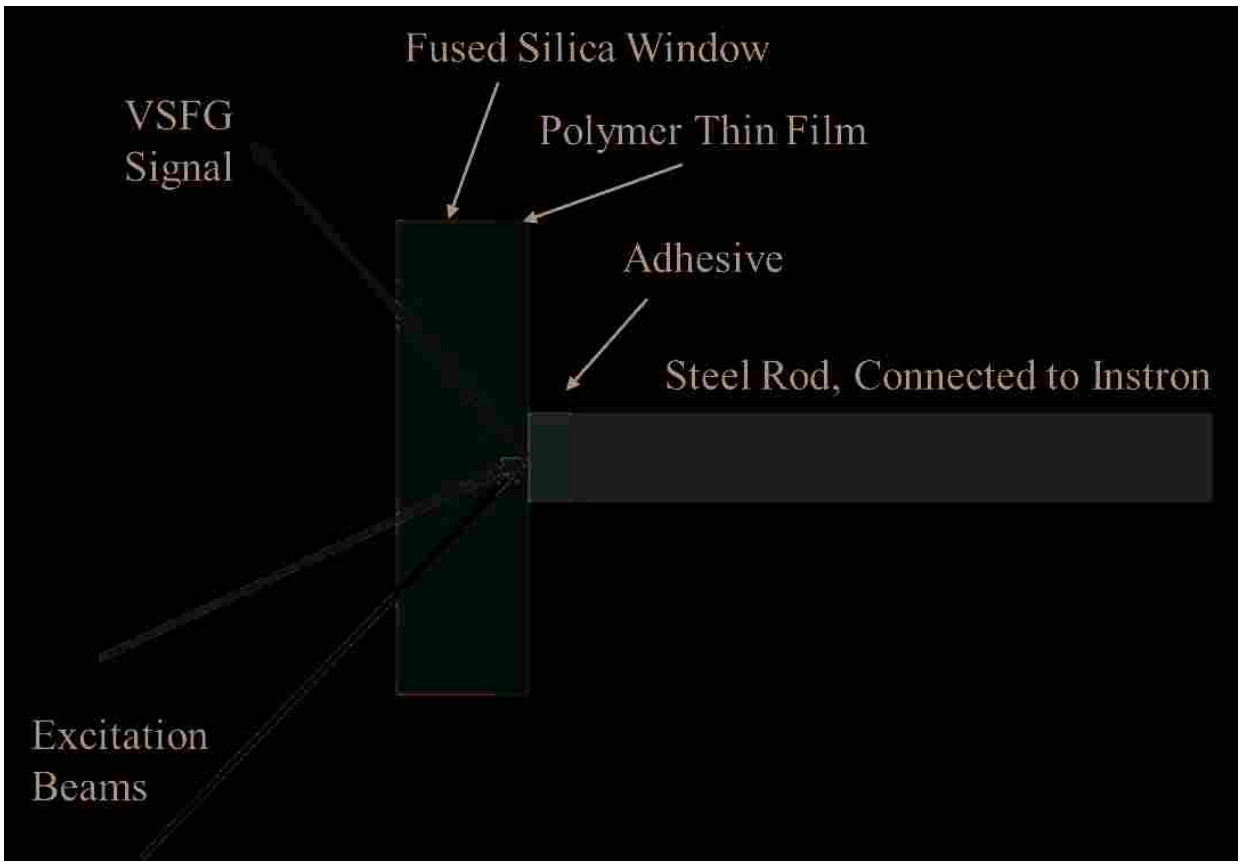

Figure 6.1. Diagram of the adhesives testing setup with the original sample mount.

film, to which the metal posts were glued, tended to delaminate from the fused silica. Even without the polymer thin film, the adhesive tended to fail before VSFG spectra could be obtained. This early failure was probably because the older experimental setup had the adhesive placed on the end of a metal post that had an area of less than 0.5 cm^2.

The problem of early breakage in adhesive samples may have been solved by the new sample mount. A diagram of a suggested adhesive sample for use with the new mount is shown in Figure 6.2. This design removes the polymer thin film as a failure point and allows for roughly 4 cm^2 of adhesive surface contact. Both of these changes should significantly increase the amount of load an adhesive sample can take while being scanned.

It should be noted that the old adhesive sample mount and new live pull mount are configured to perform two different types of material tests. The original mount, shown in Figure 6.1, was constructed to perform a tensile test, where the adhesive is pulled in opposite directions by uniaxial forces. The current mount, shown in Figure 6.2, is designed to perform a lap shear test, where forces are applied to pull the sample apart along the plane of adhesion. Both are standard methods of testing adhesives. The lap sheer method was chosen for the new mount because this design also allows polymer and composite samples to be scanned while under load without reconfiguring the sample mount.

6.2.2: Extruded Polymers

Taking VSFG spectra of HDPE samples, like those used in Chapter 5, while they are under load may help explain the large amount of nonresonant SFG signal produced at the edge of the necked region of the samples. This behavior is discussed in Chapter 5 of this text, and the relevant figure has been reproduced in Figure 6.3. Drs. Calchera and Curtis observed a similar

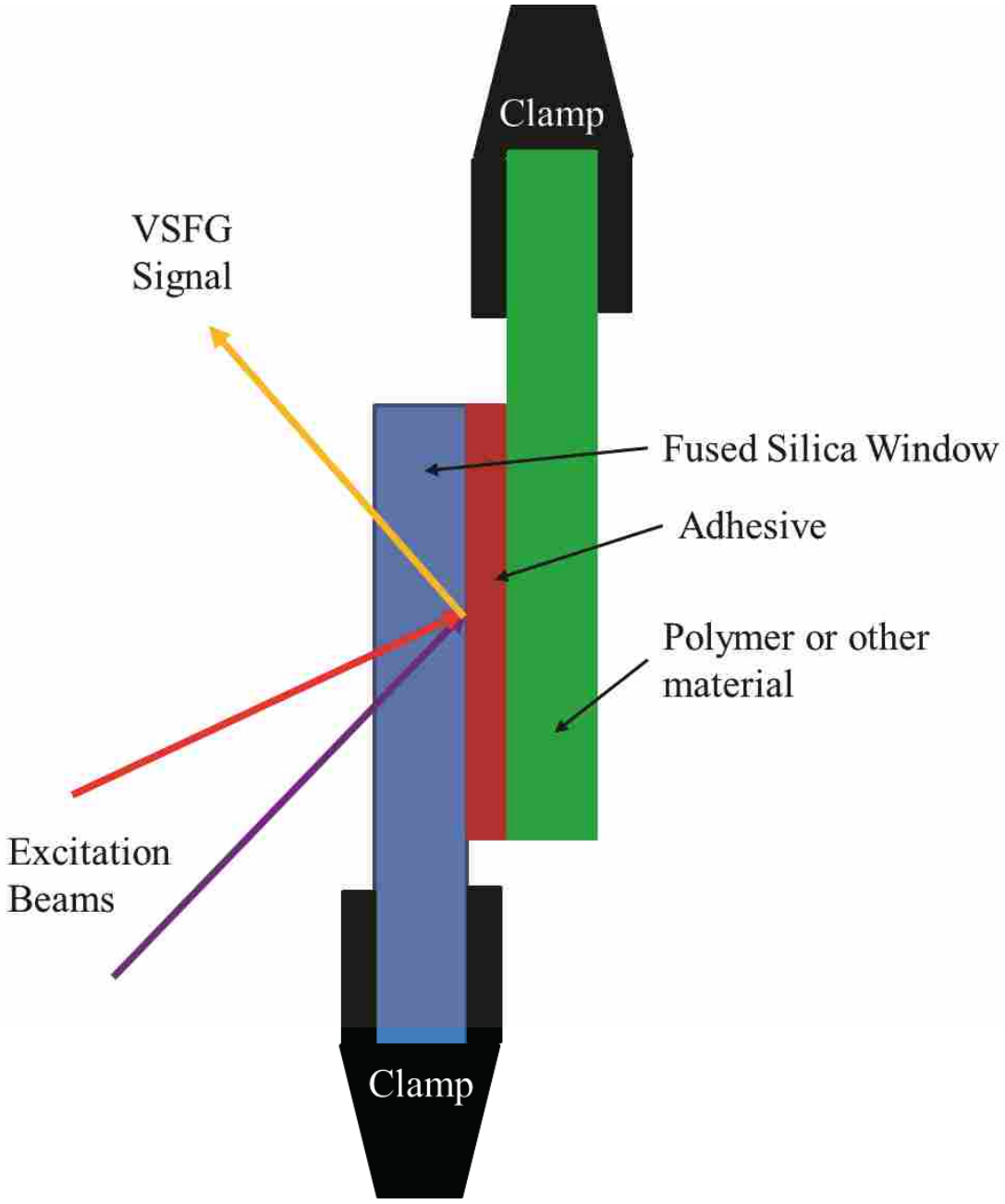

Figure 6.2. Diagram of the adhesive testing setup with the new sample mount.

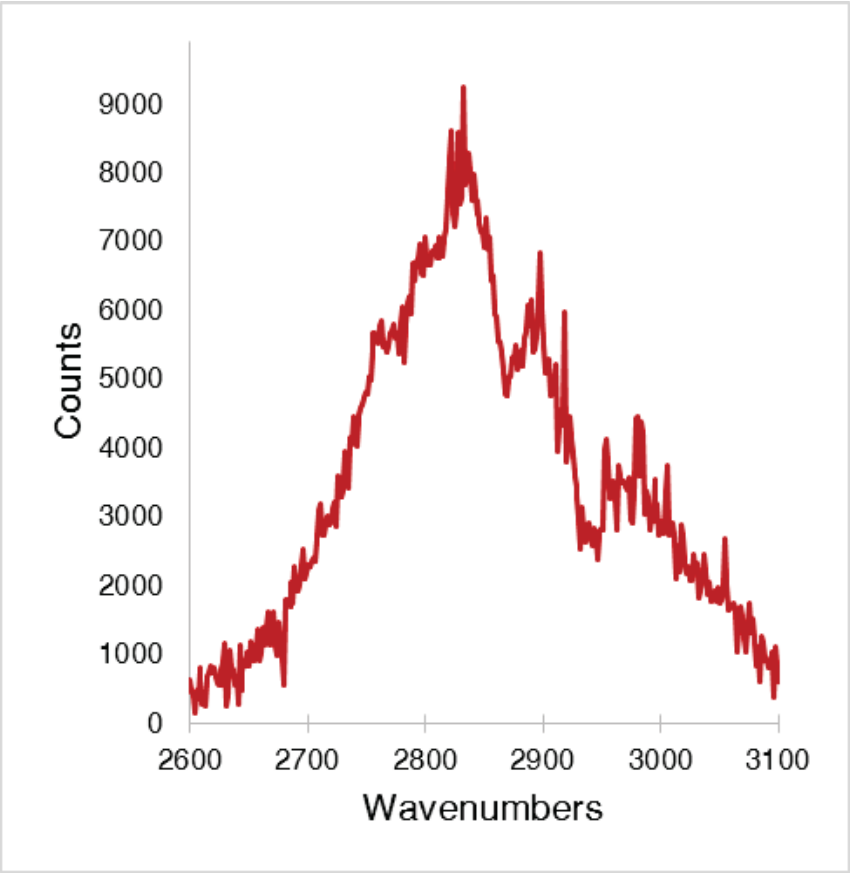

Figure 6.3. Reproduction of Figure 5.12. VSFG spectrum, with the sample in the perpendicular orientation, taken at the boundary between the necked and un-necked material of an HDPE sample that had been pulled to 6 mm.

increase in nonresonant signal from polymer thin films under load, which is shown in Figure 6.4.[1] One of the possible explanations for the large nonresonant signal from HDPE is that polymer chains at the boundary between necked and unnecked material are locked into a stressed position. This explanation would be supported if the nonresonant signal intensity increased as the HDPE samples were stressed, as Drs. Calchera and Curtis observed with their adhesive samplesw. Long term, this work may allow for nonresonant SHG to provide real time stress analysis of polymers and composites.

Sample relaxation under load is also an intriguing area of investigation. Our stressed HDPE samples were pulled to a set extension and then held at that point for several hours. Soon after the initial pull, the force needed to keep the samples at a given extension began to go down, and continued to do so for as long as the Instron tracked it. It would be very interesting to see if/how the HDPE sample surface changed during this process. VSFG signal tends to be much stronger from necked HDPE sample regions, so for better time resolution, I would suggest focusing on that portion of a sample.

Another interesting behavior of necked HDPE under load was observed by Wing-Fu. [2] They observed that "When the necking region was touched by fingers, there was an increase in the load experienced by the specimen. Such an increase in load disappeared once the fingers were removed, and the load experienced by the specimen returned to the original level…" Samples could be heated with a thermocouple or heat gun while being scanned and under load. This would allow for a more controlled, and in depth, investigation into how temperature affects the behavior of a polymer while it is under load.

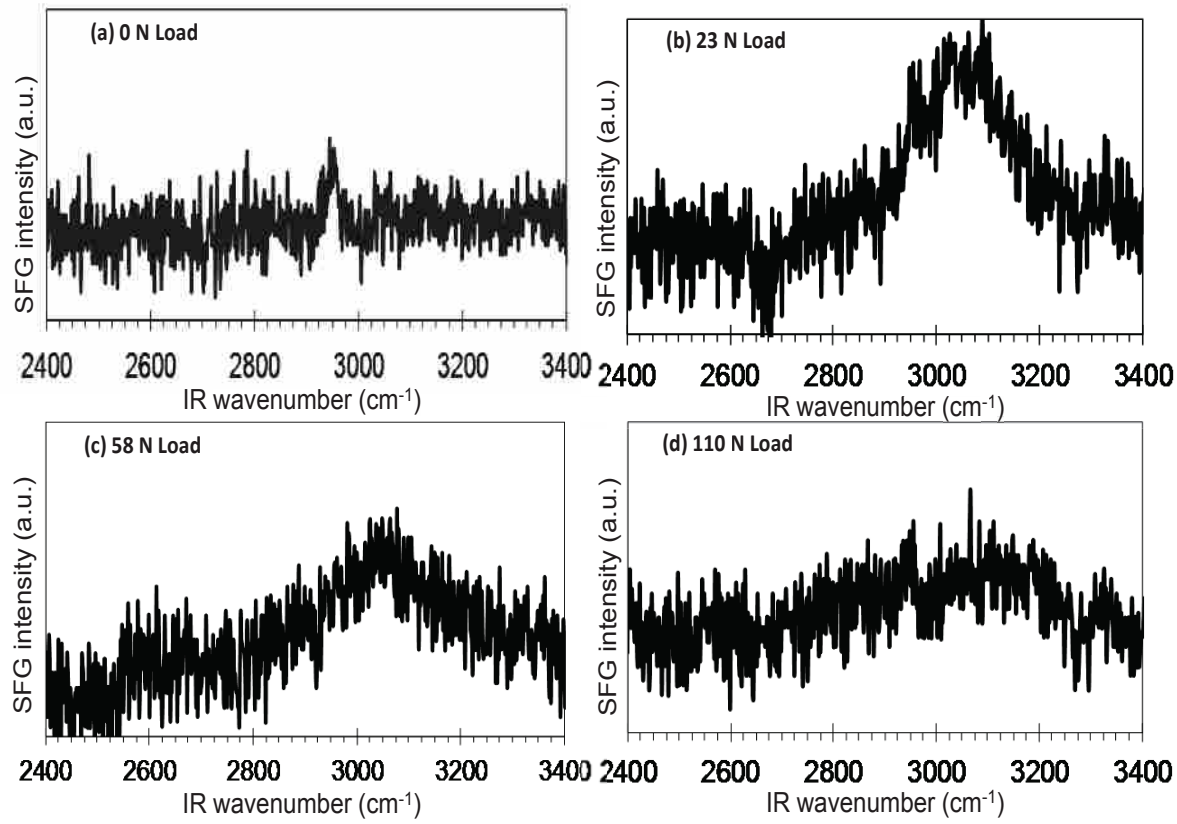

Figure 6.4. VSFG spectra of a PMMA thin film attached to a metal post with rubber cement. Each spectra was taken with a different amount of load on the adhesive bond. From reference 1.

6.3: Polycarbonate Lexan Thin Film Aging

6.3.1: Background

In 2010, Curtis et al.[3] published findings that challenged the conventional treatment of nonresonant sum-frequency generation (NR-SFG) signal. Prior to that publication, the nonresonant SFG component had been treated as a background. Curtis et al.[3-5] demonstrated that the NR-SFG signal was sensitive to differences between materials, as well as changes in a material, and thus could not be treated largely as a consistent background.

SFG spectra of polystyrene thin films on different substrates, seen in Figure 6.5, were used to show differences in the NR-SFG response from different materials. Panel **b** shows normalized spectra taken from a polystyrene thin film on silicon, sapphire, and fused silica substrates. The visible pulse delay time for these spectra was such that the NR-SFG signal was completely suppressed. With the NR-SFG signal suppressed, the resonant VSFG spectra for each of these sample types was the same. Spectra shown in Figure 6.5 **a** were taken from polystyrene thin films of different substrates with the time delay shortened to allow 10 percent of the nonresonant signal from a gold mirror to persist. These spectra are noticeably different which means that although the polystyrene surface was the same for each sample type, the nonresonant signals, and the detected spectra, were different. These differences could lead to the false conclusion that the polymer surfaces of the three samples were different, even though they were not.

Changes in the nonresonant response as a result of aging and annealing polystyrene thin film on a silicon wafer were even more problematic for VSFG systems that could not suppress NR-SFG signal contributions. Normalized spectra, seen in Figure 6.6 **b**, show that average tilt angle of the interrogated phenyl groups was unchanged by either annealing or age. Spectra shown in

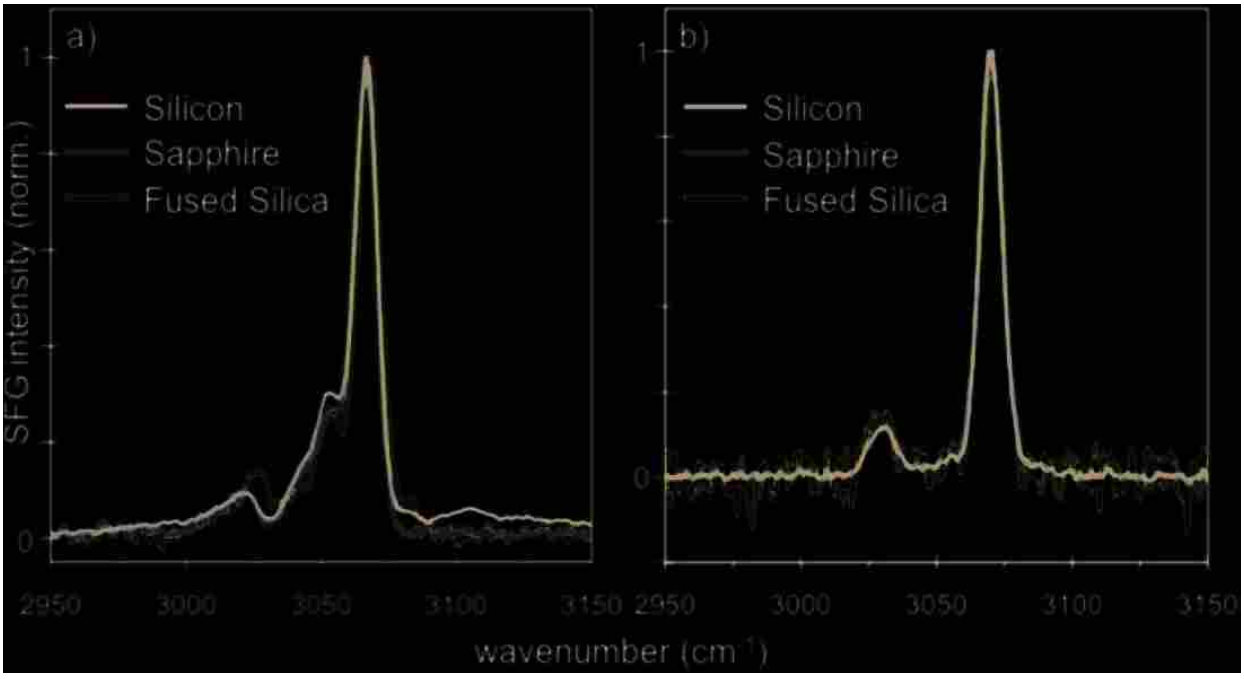

Figure 6.5. Normalized VSFG spectra of a polystyrene thin film on a silicon wafer, sapphire, and fused silica substrate with (a) 10% of the maximum nonresonant signal present, and (b) the nonresonant signal fully suppressed. From reference 3.

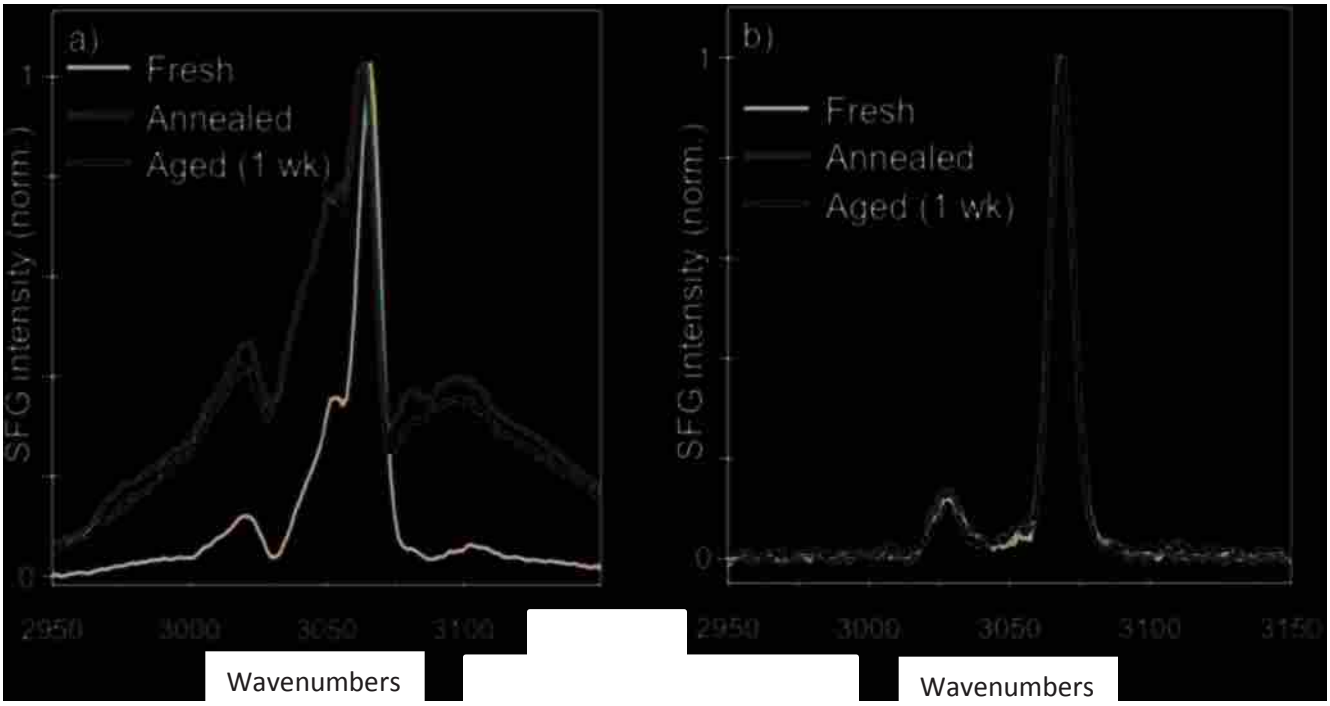

Figure 6.6. Normalized VSFG spectra of a polystyrene thin films on a silicon wafer with (a) 10% of the maximum nonresonant signal present, and (b) the nonresonant signal fully suppressed. From reference 3.

figure 6.6 **a** are of the same samples taken with 10 percent of the nonresonant signal present. Unlike the purely resonant spectra, these showed significant differences, especially between fresh and treated samples. This means that changes in SFG spectra that contain nonresonant signal can come from either the intended and interpretable resonant response, or from the less well understood nonresonant response. This behavior makes precise analysis difficult, and conclusions drawn from these spectra are suspect.

Having shown that unsuppressed SFG spectra could be misleading for polymer thin films on different substrates and for treated materials, Curtis et al. went on to show that, even for fresh samples on identical substrates, the nonresonant response could not be treated as a background.[4] Figure 6.7 **a** shows VSFG spectra, taken off resonance, of a bare silicon wafer and one coated with a polystyrene thin film. The increase in the nonresonant signal with the addition of the polystyrene thin film means that the nonresonant signal from the substrate cannot be assumed to be the same once a coating has been applied. Literature discussed in section 1.3.4 suggests that this caution applies to a wide range of systems. Figure 6.7 **b** showed that not only did the amount of nonresonant signal change with the addition of a polymer coat, but that the thickness of the coating also affected the nonresonant signal. The final and most telling blow to the practice of treating the nonresonant signal as a background came from work shown in Figure 6.7 **c,** which showed that absorption from a material, such as a thin film coating, shaped the corresponding nonresonant profile. In other words, the presence of a resonant signal shaped the corresponding nonresonant signal so that it was no longer the same as that measured off resonance.

Curtis et al. theorized that the increase in the nonresonant signal from a silicon wafer with the addition of a polystyrene thin film may be caused by interactions between the substrate and polymer.[4] This proposal is supported by some of my work, discussed in more detail in Chapter 3.

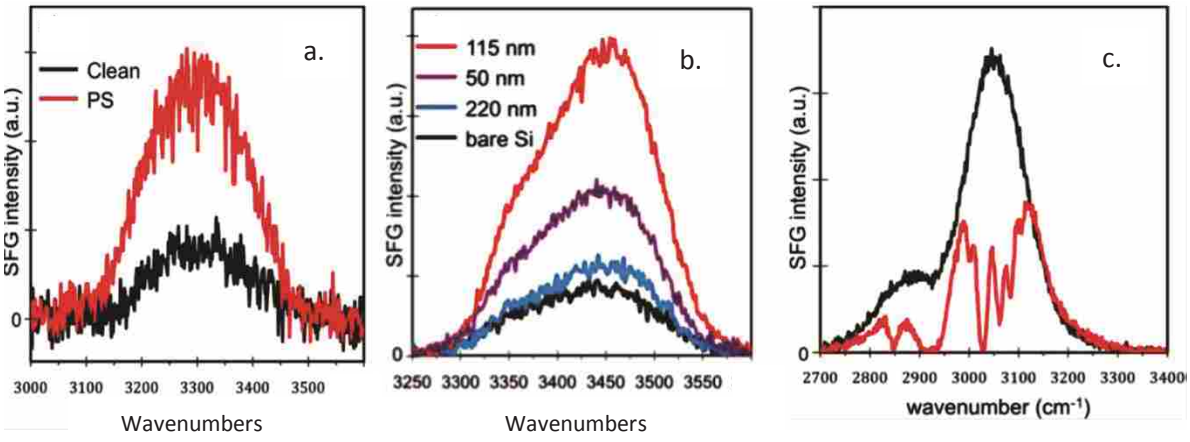

Figure 6.7. (a) NR-SFG spectra of a silicon wafer with and without a polystyrene thin film. (b) NR-SFG spectra of different thicknesses of polystyrene on a silicon wafer. (c) NR-SFG spectra from gold with (red) and without (black) a polystyrene film placed in the IR beam path. From reference 4.

It was found that the polarization of the nonresonant signal produced by a Si(111) substrate changed from P to S with 60° periodicity as the wafer was rotated in the plane of the sample face. This same pattern was observed in the nonresonant signal produced from a Si(111) wafer coated with a polystyrene thin film, which suggests that the majority of the detected NR-SFG signal was produced from the silicon substrate.[6] The dielectric permittivity of polystyrene thin films is known to decrease with age.[7] This decreased ability to dampen electric fields may allow the substrate, and the polymer's electrons near the substrate, to interact more strongly with the excitation beams, producing a stronger nonresonant signal.

6.3.2: Project Motivation

In an effort to better understand the material changes that were responsible for the nonresonant signal behavior observed by Curtis et al.[3,4] in aged and annealed polymer thin films; we decided to study the nonresonant response from polycarbonate thin films as they aged. Polycarbonate was chosen for study because, like polystyrene, it has six member aromatic rings, but unlike polystyrene, the aromatic rings in polycarbonate are part of the polymer backbone, which should make them much less mobile.

6.3.3: Results and Discussion

The first difference observed between polystyrene and polycarbonate thin films was the amount of nonresonant signal relative to resonant signal. This difference can be seen in Figure 6.8. Both samples have a Si wafer substrate, and the spectra were taken with a time delay that allowed 10% of the full nonresonant signal from gold to remain. The polystyrene film is approximately 90 nm thick, while the polycarbonate film was estimated to be roughly 400 nm thick.

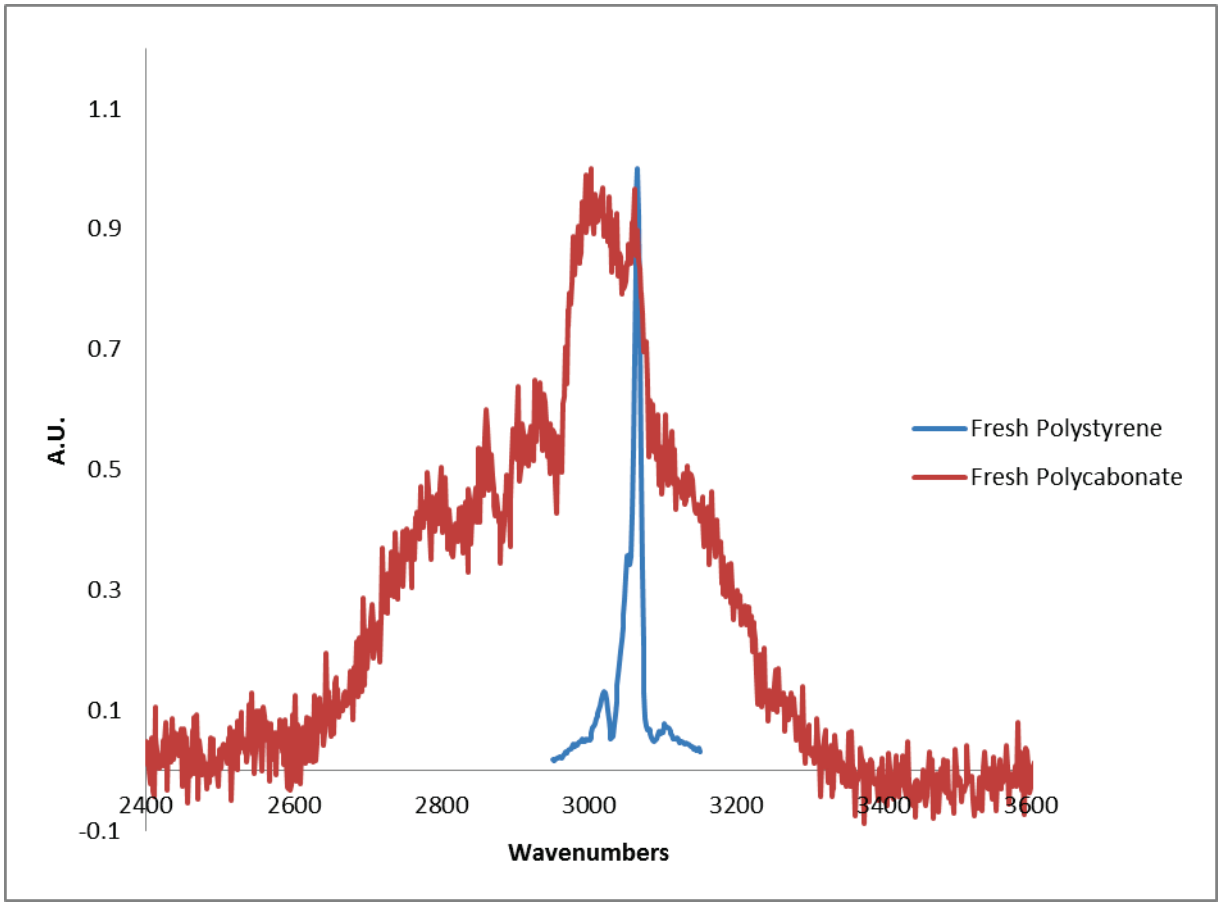

Figure 6.8. VSFG spectra of fresh polystyrene (blue) and polycarbonate (red) with 10% of the maximum nonresonant signal present.

The differences in film thickness may account for a larger proportion of nonresonant signal from the polycarbonate sample, but panel **b** of Figure 6.7 suggests that increasing the depth of the polymer film may suppress the nonresonant signal strength rather than enhance it. Ruling out this possibility experimentally could be done fairly easily by scanning samples of both polymers with the same film thickness.

The differences in the structure of the polymers may also explain the much higher percentage of nonresonant signal observed from fresh polycarbonate. The aromatic rings of polystyrene are attached to the polymer backbone through a carbon-carbon bond. At the free surface, this gives the phenyl groups a relatively large degree of freedom, and allows them to stand out from the polymer surface. The aromatic rings in polycarbonate, however, are part of the polymer backbone. This means that if the polymer chain is lying relatively flat on the polymer surface, the aromatic ring is likely to also be lying flat on the surface. Since functional groups lying in the surface plane cannot produce resonant SFG signal, a polycarbonate surface may produce much less resonant signal from the aromatic rings than a comparable polystyrene surface. Thus, the larger amount of nonresonant signal, relative to resonant signal, from polycarbonate may actually be caused be a weaker resonant signal, not a stronger nonresonant signal.

The larger proportion of nonresonant signal from fresh polycarbonate thin films may also be because polycarbonate is more transparent to the excitation or signal beams, allowing more NR-SFG to be generated, or transmitted from, the substrate surface. The different amount of nonresonant signal observed at different azimuthal angles, shown in Figure 6.9 suggest that the observed NR-SFG signal was either produced at the substrate, or by textured portions of the polycarbonate thin film.

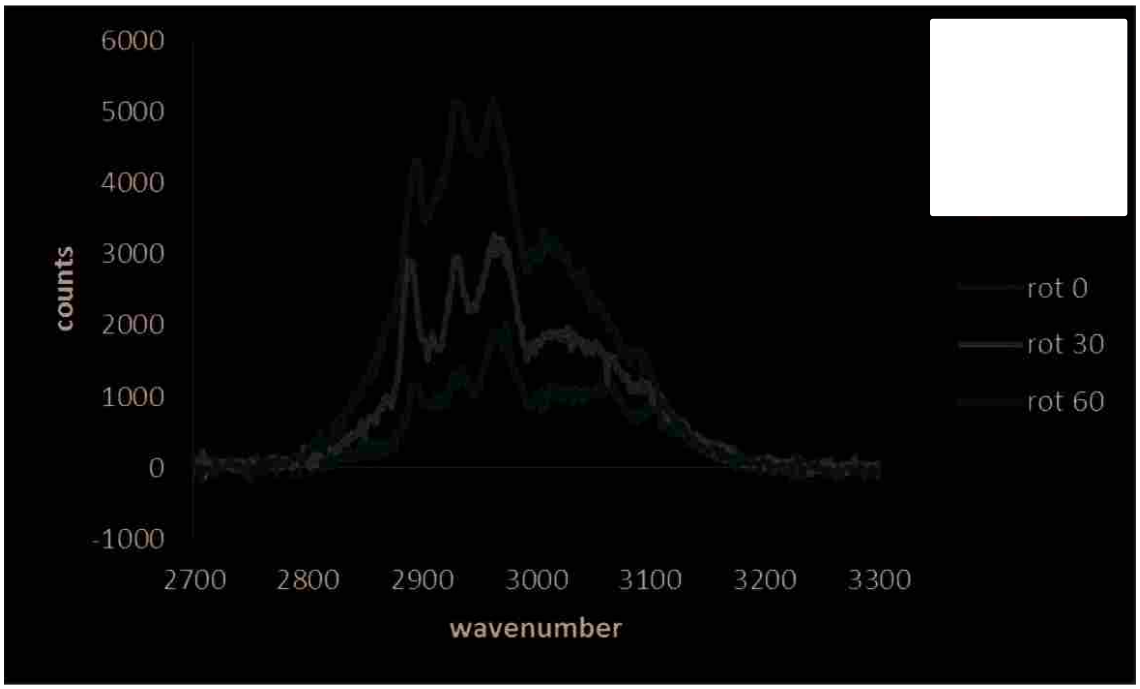

Figure 6.9. VSFG spectra of a fresh polycarbonate Lexan thin film on a silicon wafer. Spectra were taken at azimuthal angles of 0°, 30°, and 60° with 10% of the maximum nonresonant signal present.

As discussed in section 5.2.5.4 of this test, the alignment of polymer chains is suspected as the source of a large nonresonant response at the boundary of the necked regions of mechanically deformed high density polyethylene (HDPE) samples, and in polystyrene/PMMA thin films under load. A similar chain alignment in the polycarbonate thin films, created during the spin coating process, may be responsible for the relatively large nonresonant response from fresh polycarbonate thin films, and for the observed differences in signal levels at different azimuthal angles. This is supported by the fact that the azimuthal angle has much less effect on the NR-SFG signal level as the sample ages, as can be seen in Figure 6.10.

The observed drop in the angular dependence of the nonresonant signal level was accompanied by an overall drop in nonresonant signal level at all measured angles. These changes are shown in Figure 6.11, where panel **a** is the sample at an arbitrary initial position, panel **b** is the sample rotated 30° from the initial position, panel **c** is the sample rotated 60° from the initial position, and panel **d** shows a different sample which also had a drop in nonresonant signal level over time. All of these spectra were taken with the visible pulse delayed in time to the point where 10% of the maximum nonresonant signal was produced from gold. In addition to the overall drop in signal level, there is also a shift to the left in the nonresonant profile of each sample and azimuthal angle. Also of interest is the increase in nonresonant signal shown in panel **d,** which is followed by a significant decrease in nonresonant signal intensity.

Given that polycarbonate thin films are known to retain some solvent over time[8] and polystyrene thin films do not,[9] it was possible that solvent retention was responsible for the observed difference in nonresonant response to aging from polycarbonate and polystyrene thin films. To test this, two polycarbonate thin film samples, labeled 11 and 12, were scanned soon after spin coating, and then placed under vacuum for two days. Samples 13 and 14 were created

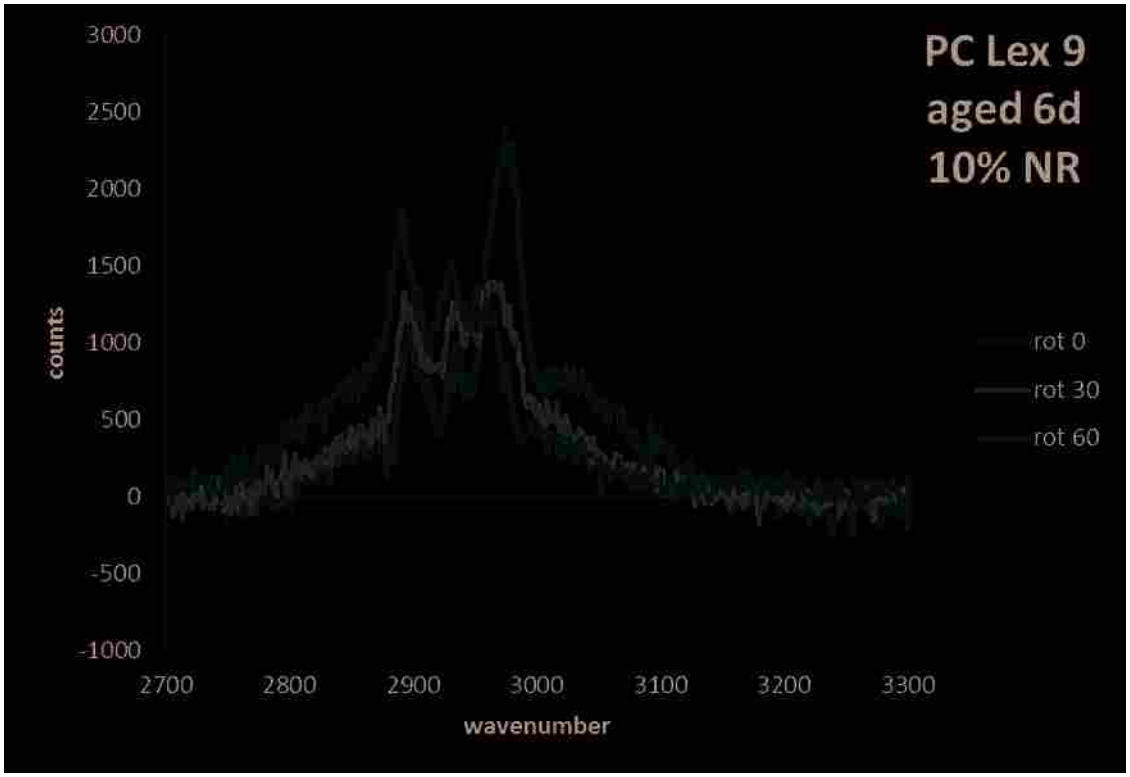

Figure 6.10. VSFG spectra of the sample in Figure 6.9. after ageing six days. Spectra were taken at azimuthal angles of 0°, 30°, and 60° with 10% of the maximum nonresonant signal present.

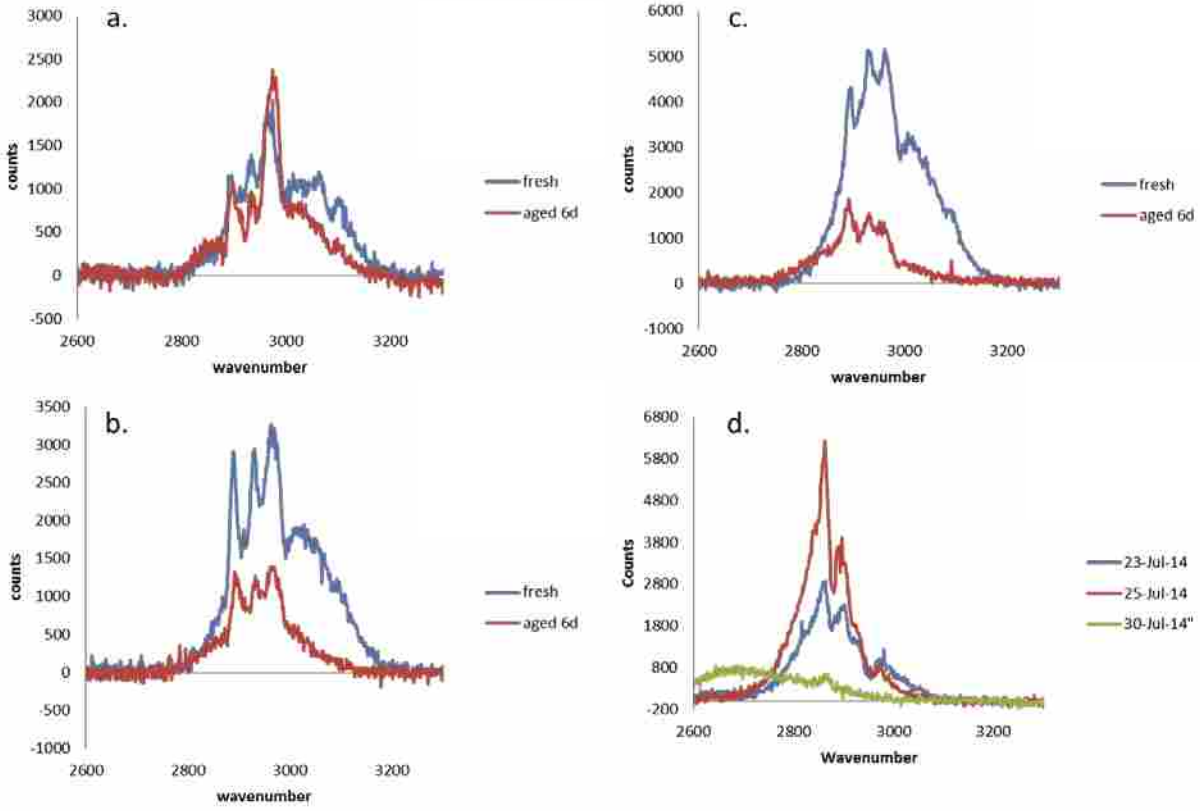

Figure 6.11. VSFG spectra of a polycarbonate Lexan thin films on a silicon substrate. (a,b,c) are of from the same sample with spectra taken at azimuthal angles of (a) 0°, (b) 30°, and (c) 60°. The blue spectra were taken from the fresh sample while the red spectra were taken after six days of aging. (d) shows a different polycarbonate Lexan thin film on a silicon wafer aged two days (blue), four days (red), and nine days (green). All spectra were taken with 10% of the maximum nonresonant signal present.

at the same time, and from the same polycarbonate solution, as samples 11 and 12. Samples 13 and 14 were allowed to age in a covered petri dish. The results of this study are shown in Figure 6.12, where spectra from samples 11 and 12 are shown in panels **a** and **b** respectively, and spectra from samples 13 and 14 are shown in panels **c** and **d**. To give a more accurate day to day signal comparison, each spectrum has been normalized to the amount of nonresonant signal produced by a gold mirror that day. Although the samples were each quite different, they all followed the pattern seen in Figure 6.11 **d,** with the signal strength first going up then back down over time. The observed rise and fall of nonresonant signal intensity from polycarbonate Lexan thin films may be a result of either changes in nonresonant signal produced from the polymer, or from changes in the polymer which allow different amount of signal to be generated on the silicon substrate. Taking absorption readings of polycarbonate thin films as they age may help determine which of these possibilities is truly responsible.

6.3.4: Suggested Next Steps

This work makes clear that polycarbonate Lexan thin films undergo interesting changes as they age. These changes do not appear to be related to solvent retention, and may be caused by changes in the optical absorption properties of the film over time. The observed behavior may also be caused by changes to the film's own nonresonant response, or to the interaction between the film and the substrate.

Changes in the optical absorption behavior of a polycarbonate film should by the easiest possibility to investigate. This can be done by coating a transparent substrate, like fused silica, and tracking the absorption profile over time. Both sample preparation and taking the absorption profile are pretty simple, so this should make a good project for an inexperienced researcher.

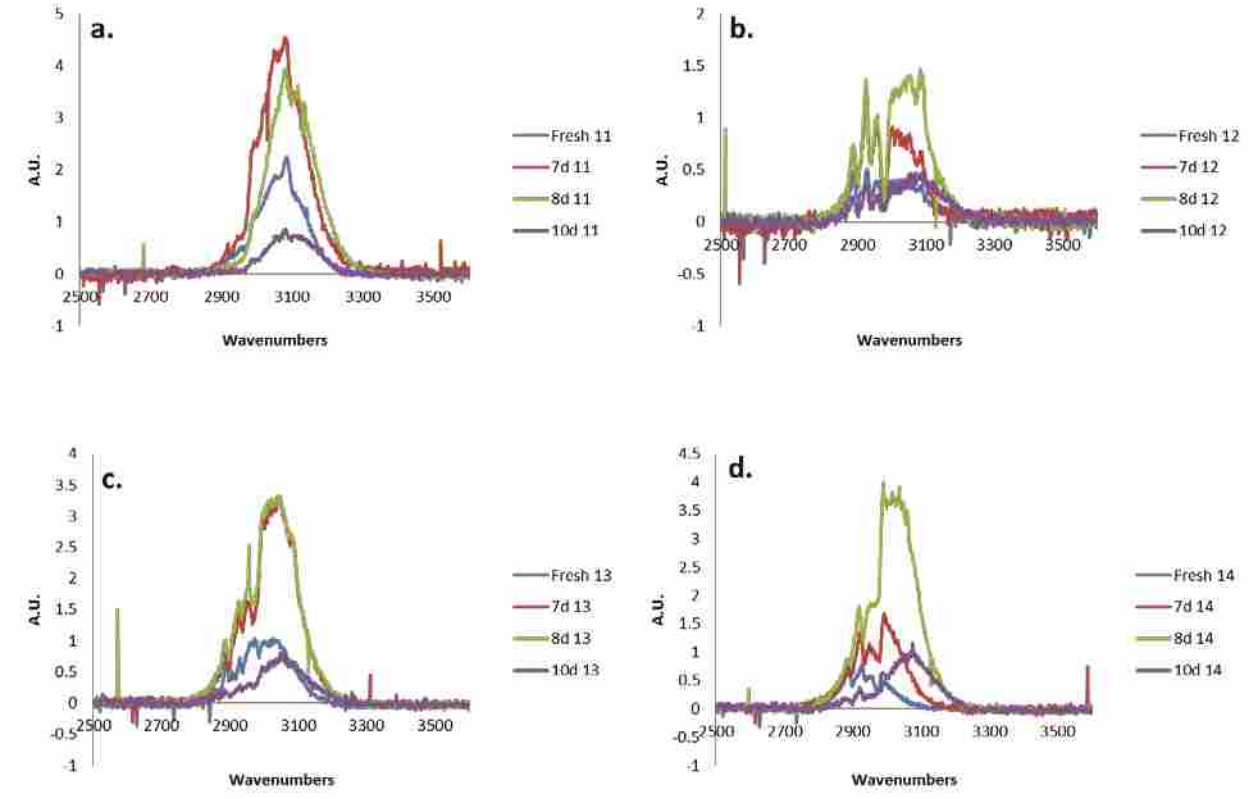

Figure 6.12. VSFG spectra of four differnet polycarbonate Lexan thin films on Si substrates taken from fresh (blue), seven days old (red), eight days old (green) and ten days old (purple). The samples in (a) and (b) were held under vacuum for two days. All spectra were taken with 10% of the maximum nonresonant signal present.

Tracking the nonresonant response over time from polycarbonate thin films on different substrates would also yield interesting information. If NR-SFG changes were consistent between substrate types, then changes in the polymer are probably the cause. If the NR-SFG response behaves differently over time for samples with different substrates, then either optical absorption or polymer-substrate interactions are probably the cause. Absorption data taken over time would give information as to which of these causes was most likely.

6.4: Plasma Treatment

6.4.1: Polymer Sheets

At one time, the VSFG system was down for several months, so Joshua Hanson and I spent some time studying polymers with x-ray diffraction (XRD). One particularly interesting result of this work was the discovery that surface modification in a plasma cleaner can change the XRD pattern for semicrystalline polymers. This was exploratory work with polypropylene and polyethylene samples that were cut from scraps of commercial sheets, obtained from the chemistry central stockroom, who didn't know where they got them from.

XRD data were collected using a PANalytical X'Pert Pro diffractometer with a Cu X-ray source, a Ge-111 monochromator that provides Cu-$K_{\alpha 1}$ (λ = 1.5406 Å) radiation, and an X'Celerator detector. Samples were mounted using a custom mount developed by Dr. Stacey Smith, and scanned from 10° to 90° 2theta.

The polypropylene sample was treated with plasma generated from atmospheric gasses for 4s. XRD patterns taken before and after plasma treatment are shown in Figure 6.13. Treatment in the plasma cleaner appears to have removed some of the ordered planes detected by the XRD instrument. A polyethylene sample treated for 1s in the plasma cleaner did not lose ordered

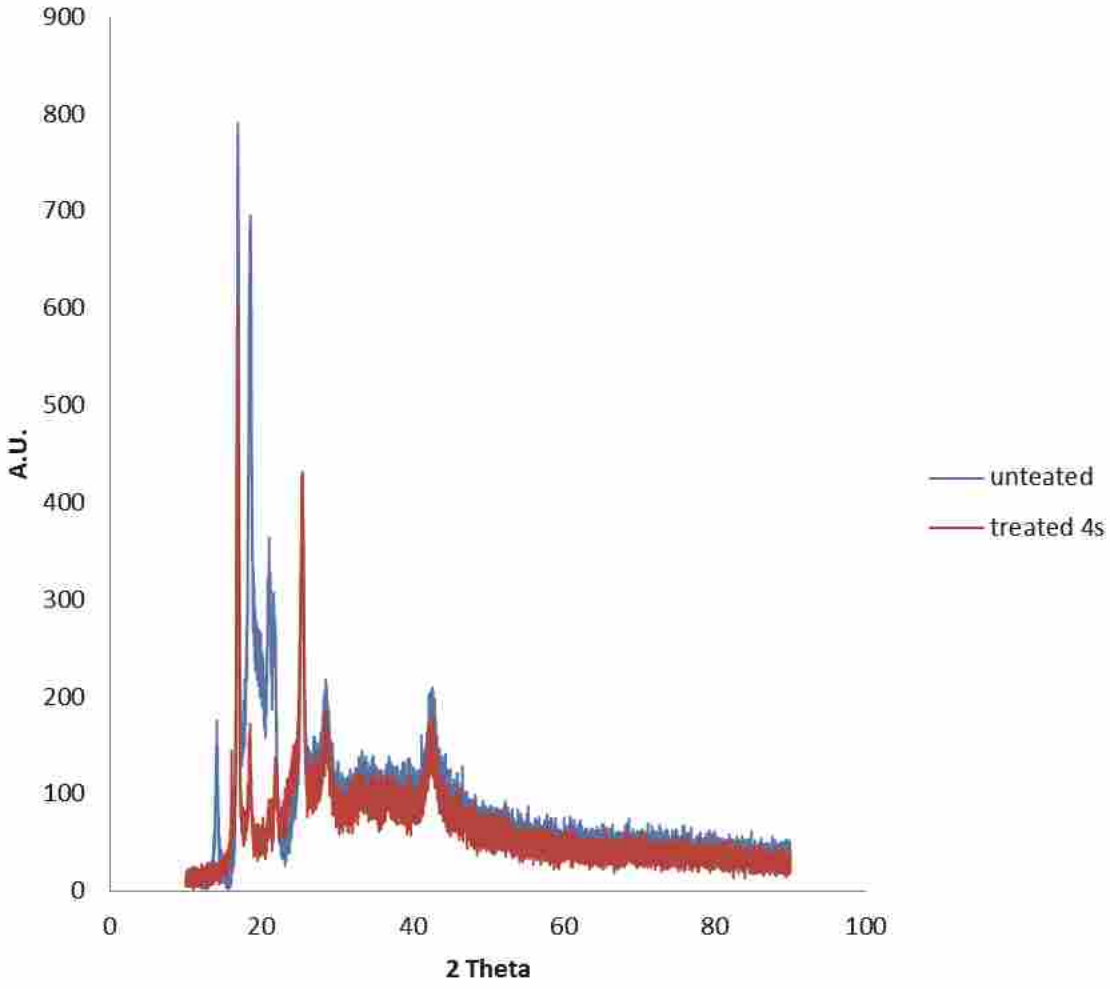

Figure 6.13. XRD diffraction patterns from a polypropylene sample before (blue) and after (red) four seconds of treatment in a plasma cleaner.

planes altogether; however, as shown in Figure 6.14, the detected intensity for both of the largest responses was significantly diminished. Interestingly, the peaks had returned after 6 days, but a large amorphous halo also appeared. Retreatment with plasma had little to no effect on the aged polyethylene sample.

6.4.2: Polymer Thin Films

Dr. Calchera observed interesting changes in the resonant response of polystyrene thin films after treatment in a plasma cleaner.[10] I spent some time investigating how plasma treatment affected the nonresonant response from polymer thin films. The observed nonresonant behavior was quite confusing at the time. Figure 6.15 shows VSFG spectra from two polystyrene thin film samples on polycrystalline stainless steel substrates. Both films were treated in the same part of the plasma cleaner for 1.23 s each. Both display the increase in resonant SFG signal that Dr. Calchera observed, but the nonresonant response from the sample in panel **a** went down, while the nonresonant response from the sample in panel **b** had a large increase in signal intensity.

The data shown in Figure 6.16 may help explain this behavior. This was a polycarbonate thin film on a Si wafer substrate that was treated for 0.89 s. The nonresonant signal went down with the sample in one orientation, but up when the sample was rotated 90°. At this time we didn't know that the azimuthal angle for Si(111) wafers affected nonresonant SFG signal, and didn't distinguish between which cut of Si wafers were used for substrates. I suspect that the sample in Figure 6.16 may have been on a Si(111) wafer, which could account for the different responses to plasma treatment at the two azimuthal angles. Although the nonresonant response from polycrystalline stainless steel plates, such as those used for substrates in Figure 6.15, does not vary with azimuthal angle, currents induced in the substrate by the cleaner's RF field might be affected by the material texture, and thus be directionally dependent. With this in mind, looking

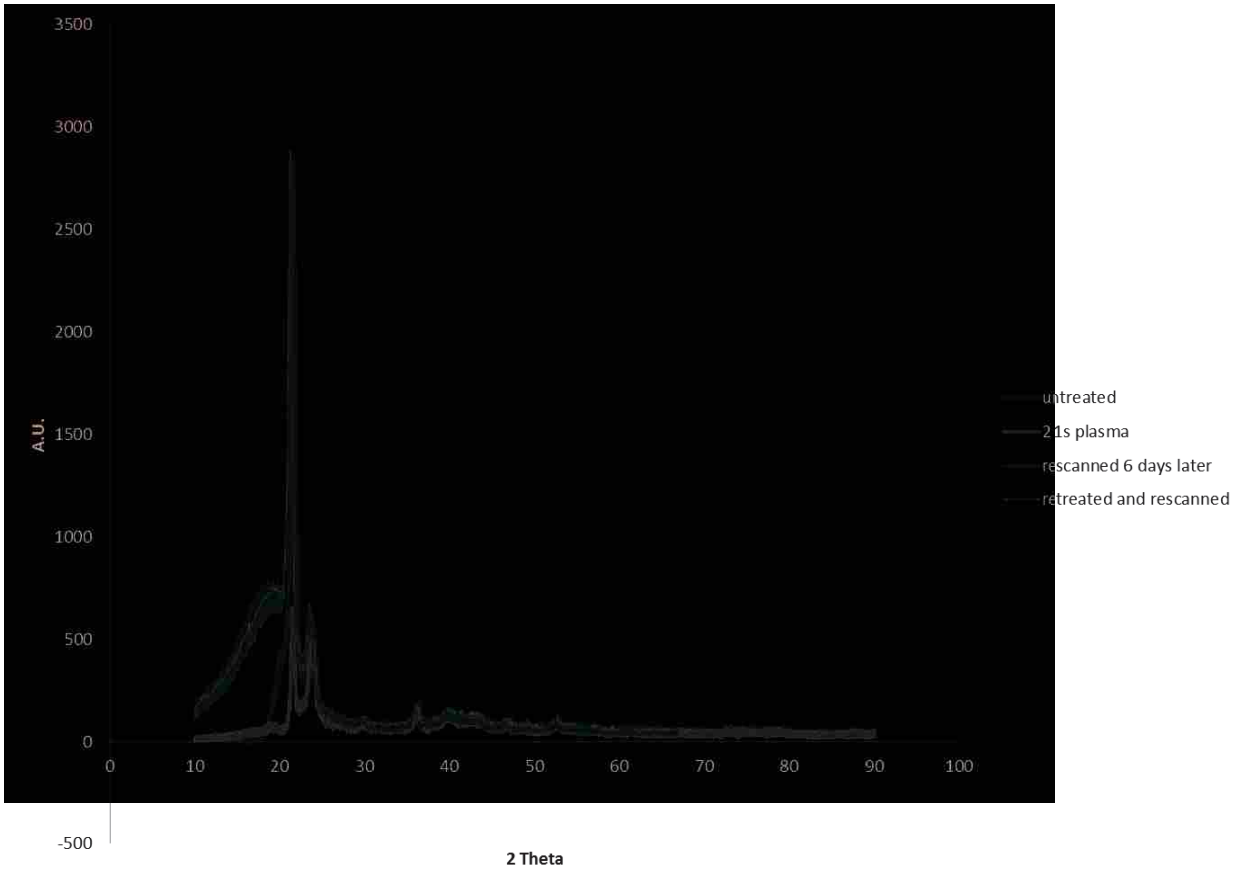

Figure 6.14. XRD diffraction patterns from a polyethylene sample before (blue) and after (red) one second of treatment in a plasma cleaner. The sample was then rescanned six days later before (green) and after (purple) being retreated in the plasma cleaner for one second. Note: small variations in peak locations and intensities may be due to inconsistencies in loading the samples.

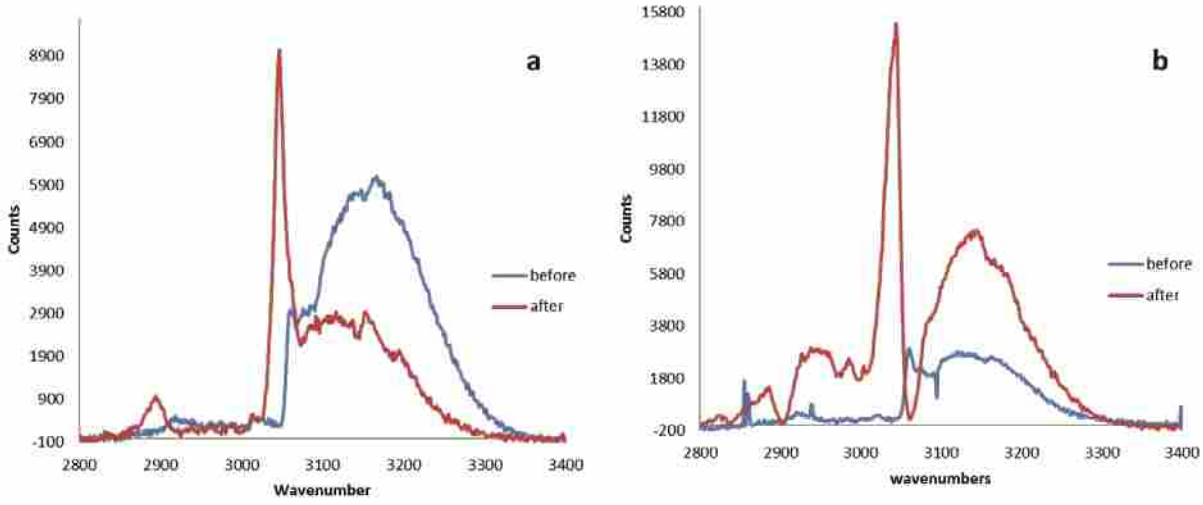

Figure 6.15. VSFG spectra of two different polystyrene thin film samples on stainless steel substrates before (blue) and after (red) 1.23s of treatment in a plasma cleaner. All spectra were taken with 10% of the maximum nonresonant signal present.

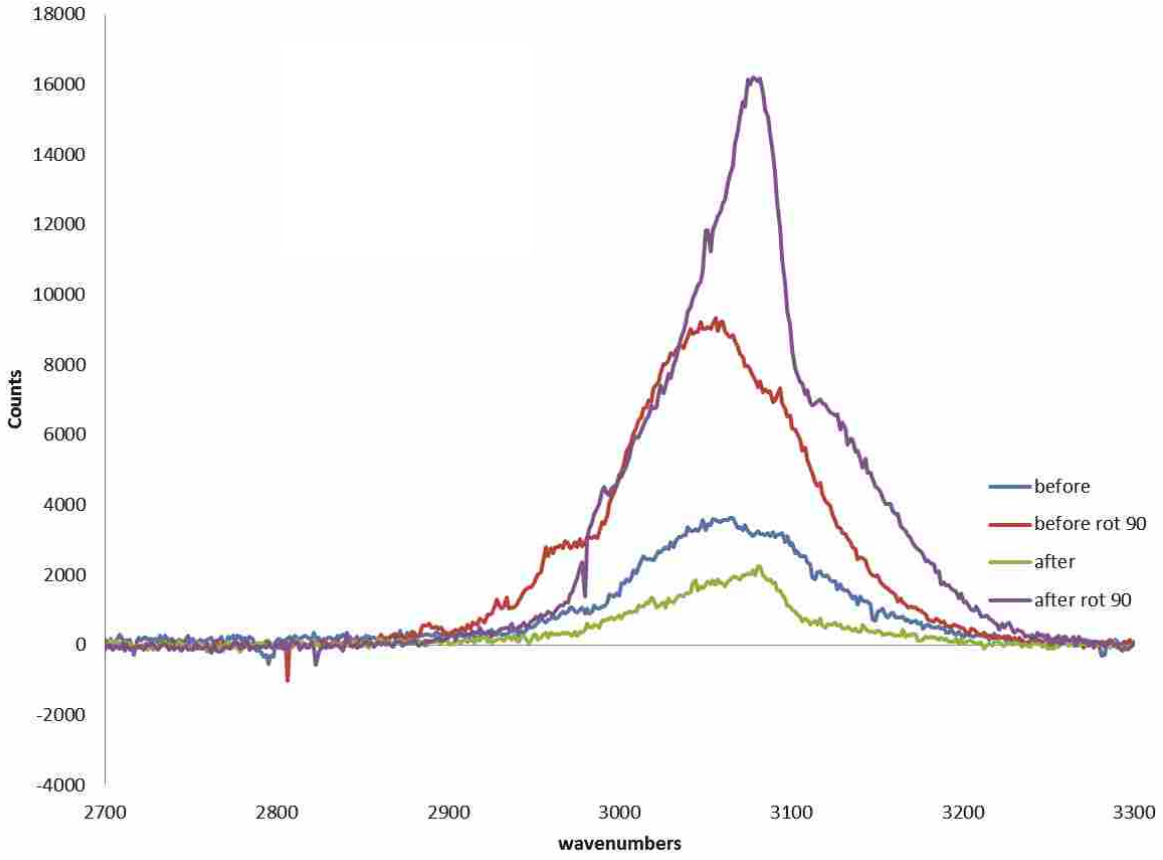

Figure 6.16. VSFG spectra of a polycarbonate Lexan thin film on a silicon wafer substrate before (blue, red) and after (green, purple) 0.89s of treatment in a plasma cleaner. The red and purple spectra were taken with a 90° azimuthal angle difference from the blue and green spectra. All spectra were taken with 10% of the maximum nonresonant signal present.

into how polymer thin films respond to plasma cleaning, while noting the substrate type and orientation may be worthwhile.

6.5: Conclusion

All of these projects have potential; however, I would like to highlight a few that seem particularly promising. Scanning samples while under load (section 6.2) has immense potential for a researcher that can make a substantial time commitment. So far as I am aware, this project is unique, and should generate a great deal of interest in materials communities. Also, once you have the system working for one type of material, scanning others should be relatively easy. This means that developing this one method should lead to several publications.

For researchers looking for a 10-20 h/week project, I would recommend looking into how polycarbonate thin film absorption spectra change over time (section 6.3), and how plasma treatment changes the XRD patterns for bulk polymers (section 6.4.1). Both projects appear to be in areas where little work has been done and have the potential to generate publications. The polycarbonate aging project will need someone who can commit an hour or so a day, while the plasma project requires time blocks of 2-5 h.

6.6: References

(1) Calchera, A. R. Obstacles And Solutions To Studying Functional Adhesives Using Vibrational Sum-Frequency Generation Spectroscopy. Brigham Young University, 2013.

(2) Wing-Fu, L. Study on Modification of Polymer Properties by the Cold Drawing Process. *Soft* **2015**, *4*.

(3) Curtis, A. D.; Reynolds, S. B.; Calchera, A. R.; Patterson, J. E. Understanding the Role of Nonresonant Sum-Frequency Generation from Polystyrene Thin Films. *The Journal of Physical Chemistry Letters* **2010**, *1*, 2435-2439.

(4) Curtis, A. D.; Burt, S. R.; Calchera, A. R.; Patterson, J. E. Limitations in the Analysis of Vibrational Sum-Frequency Spectra Arising from the Nonresonant Contribution. *The Journal of Physical Chemistry C* **2011**, *115*, 11550-11559.

(5) Quast, A. D.; Curtis, A. D.; Horn, B. A.; Goates, S. R.; Patterson, J. E. Role of Nonresonant Sum-Frequency Generation in the Investigation of Model Liquid Chromatography Systems. *Analytical Chemistry* **2012**, *84*, 1862-1870.

(6) Averett, S. C.; Calchera, A. R.; Patterson, J. E. Polarization and phase characteristics of nonresonant sum-frequency generation response from a silicon (111) surface. *Optics Letters* **2015**, *40*, 4879-4882.

(7) Fukao, K.; Koizumi, H. Glassy dynamics in thin films of polystyrene. *Physical Review E* **2008**, *77*, 021503.

(8) Siegmann, A.; Geil, P. H. Crystallization of polycarbonate from the glassy state. part I. Thin films cast from solution. *Journal of Macromolecular Science, Part B* **1970**, *4*, 239-271.

(9) Zhang, X.; Yager, K. G.; Kang, S.; Fredin, N. J.; Akgun, B.; Satija, S.; Douglas, J. F.; Karim, A.; Jones, R. L. Solvent Retention in Thin Spin-Coated Polystyrene and Poly(methyl methacrylate) Homopolymer Films Studied By Neutron Reflectometry. *Macromolecules* **2010**, *43*, 1117-1123.

(10) Calchera, A. R.; Curtis, A. D.; Patterson, J. E. Plasma Treatment of Polystyrene Thin Films Affects More Than the Surface. *ACS Applied Materials & Interfaces* **2012**, *4*, 3493-3499.

Appendices

A.1: Live-Pull Rotational Sample Mount Blueprints

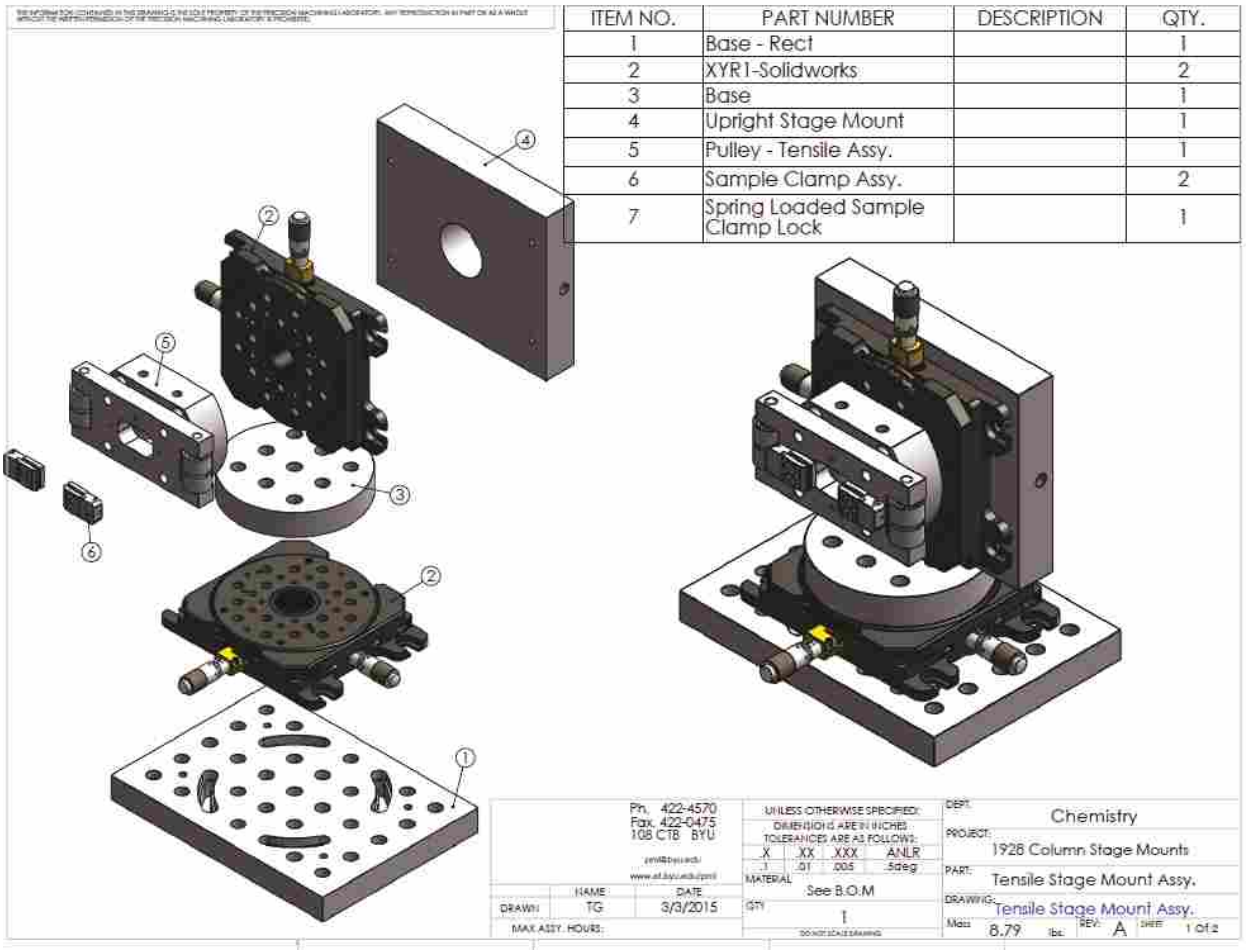

ITEM NO.	PART NUMBER	DESCRIPTION	QTY.
1	Base - Rect		1
2	XYR1-Solidworks		2
3	Base		1
4	Upright Stage Mount		1
5	Pulley - Tensile Assy.		1
6	Sample Clamp Assy.		2
7	Spring Loaded Sample Clamp Lock		1

ITEM NO.	PART NUMBER	QTY.
1	Rotational Plate	1
2	Roller Assy.	4
3	Tensile Bar	1
4	ASME B18.8.2 - 0.2502x2	4
5	Sample Clamp Assy.	2
6	Containment Bridge	2
7	Sample	1
8	HX-SHCS 0.164-32x1x1-S	4

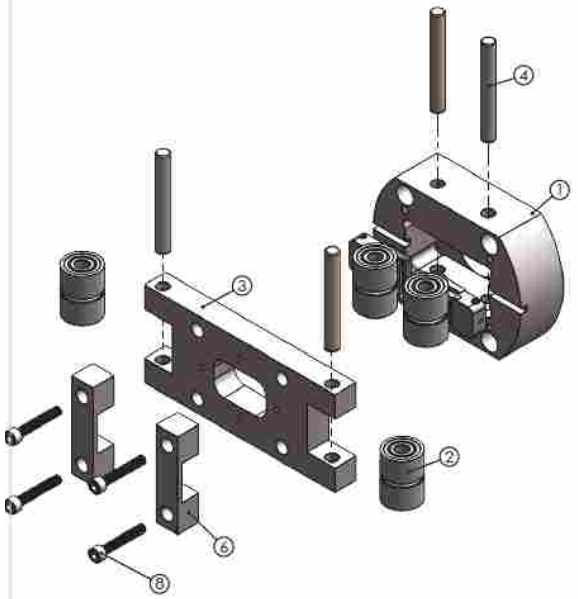

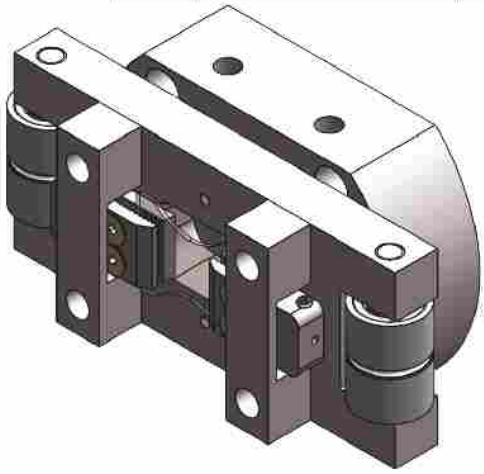

PML
Ph. 422-4570
Fax 422-0475
108 CTB BYU
pml@byu.edu
www.et.byu.edu/pml

	NAME	DATE
DRAWN	TG	4/14/2016
MAX ASSY. HOURS:		

UNLESS OTHERWISE SPECIFIED:
DIMENSIONS ARE IN INCHES
TOLERANCES ARE AS FOLLOWS:

X	XX	XXX	ANLR
.1	.01	.005	.5deg

MATERIAL: See B.O.M
QTY: 1
DO NOT SCALE DRAWING

DEPT: Chemistry
PROJECT: 2447 Mods of Polymer Line Pull
PART: Pulley - Tensile Assy.
DRAWING: Pulley - Tensile Assy.
Mass: 1.32 lbs. REV: B SHEET: 1 OF 1

ITEM NO.	PART NUMBER	QTY.
1	Sample Clamp	1
2	Sample Clamp Jaw	1
3	Cable Connector	1
4	SCHCSCREW 0.138-32x0.25x0.25-HX-S	2
5	SSCUPSKT 0.138-32x0.25-HX-S	2

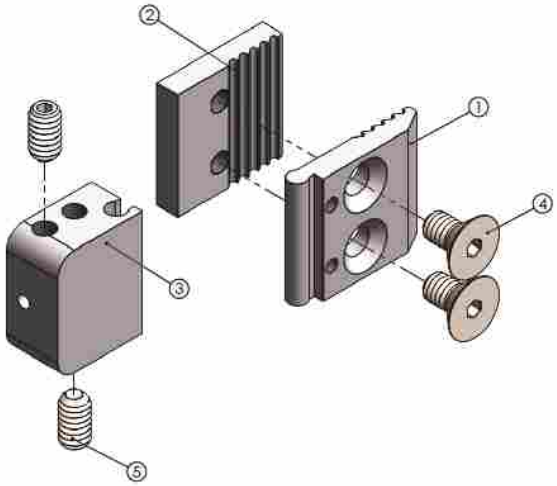

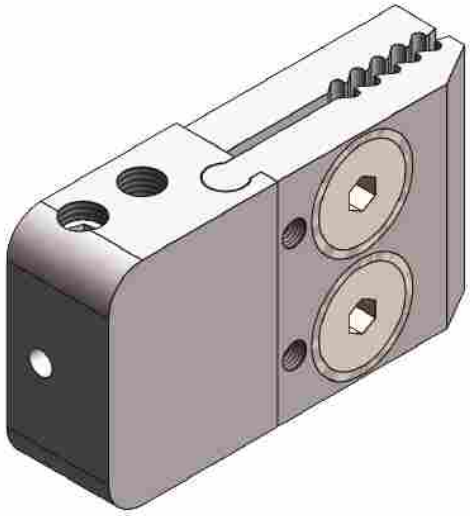

Assemble and supply fasteners.

PML
Precision Machining Laboratory
Ph. 422-4570
Fax. 422-0475
108 CTB BYU
pml@byu.edu
www.et.byu.edu/pml

	NAME	DATE
DRAWN	TG	5/23/2016
MAX ASSY. HOURS:	1	

UNLESS OTHERWISE SPECIFIED:
DIMENSIONS ARE IN INCHES
TOLERANCES ARE AS FOLLOWS:

X	XX	XXX	ANLR
.1	.01	.005	.5deg

MATERIAL: See B.O.M
QTY: 2
DO NOT SCALE DRAWING

DEPT: Chemistry
PROJECT: 2475 New Grip Design
PART: Sample Clamp Assy.
DRAWING: Sample Clamp Assy.
Mass: 0.05 lbs. REV: B SHEET 1 OF 1

ITEM NO.	PART NUMBER	DESCRIPTION	QTY.
1	Base - Rect		1
2	XYR1-Solidworks		1
3	Base		1
4	Slotted Upright Mount		1

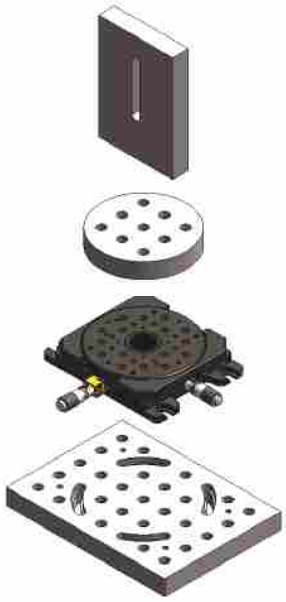

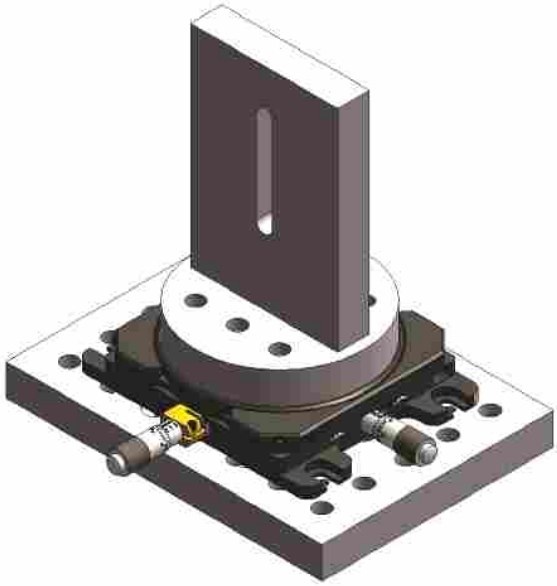

PML Precision Machining Laboratory

Ph. 422-4570
Fax. 422-0475
108 CTB BYU

	NAME	DATE
DRAWN	TG	11/21/2014
MAX ASSY. HOURS:		

UNLESS OTHERWISE SPECIFIED:
DIMENSIONS ARE IN INCHES
TOLERANCES ARE AS FOLLOWS:

X	XX	XXX	ANLR
.1	.01	.005	.5deg

MATERIAL: See B.O.M
QTY: 1
DO NOT SCALE DRAWING

DEPT: Chemistry
PROJECT: 1928 3 Axis Column Stage & Mounts
PART: Column Stage Mount Assy.
DRAWING: Column Stage Mount Assy.
Mass: 5.32 lbs. REV: A SHEET: 1 OF 1

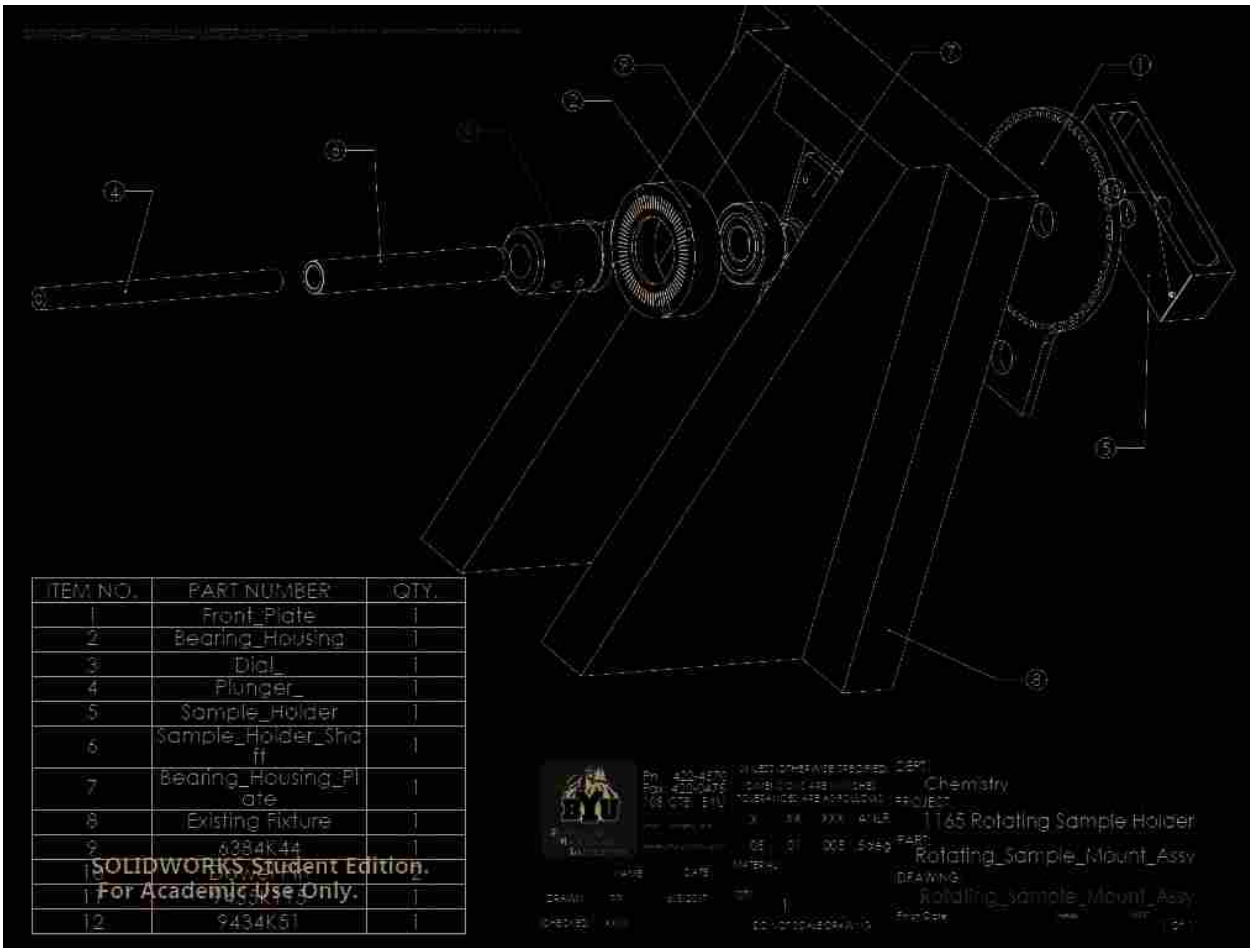

ITEM NO.	PART NUMBER	QTY.
1	Front_Plate	1
2	Bearing_Housing	1
3	Dial_	1
4	Plunger_	1
5	Sample_Holder	1
6	Sample_Holder_Shaft	1
7	Bearing_Housing_Plate	1
8	Existing Fixture	1
9	6384K44	1
10	[illegible]	1
11	[illegible]	1
12	9434K51	1

Chemistry

1165 Rotating Sample Holder

Rotating_Sample_Mount_Assy

Rotating_Sample_Mount_Assy

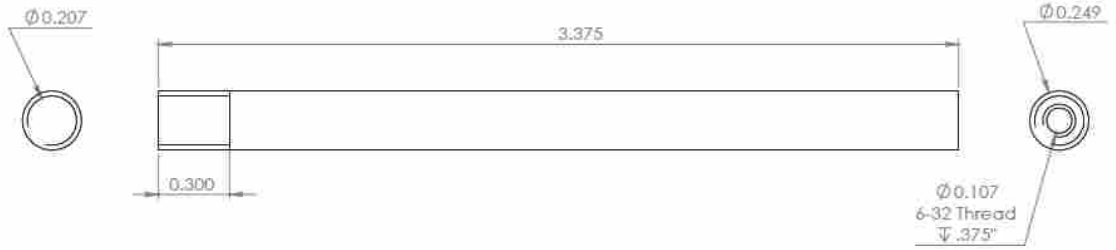

Ph. 422-4570
Fax. 422-0475
108 CTB BYU
www.et.byu.edu/pmi

	NAME	DATE
DRAWN	TG	6/8/2017
CHECKED	XXXX	

UNLESS OTHERWISE SPECIFIED:
DIMENSIONS ARE IN INCHES
TOLERANCES ARE AS FOLLOWS:

.X	.XX	.XXX	ANLR
.05	.01	.005	.5deg

MATERIAL: 6061 Alloy
QTY: 1
DO NOT SCALE DRAWING

DEPT: Chemistry
PROJECT: 1165 Rotating Sample Holder
PART: Plunger_
DRAWING: Plunger_
Finish Date:
SHEET: 1 Of 1

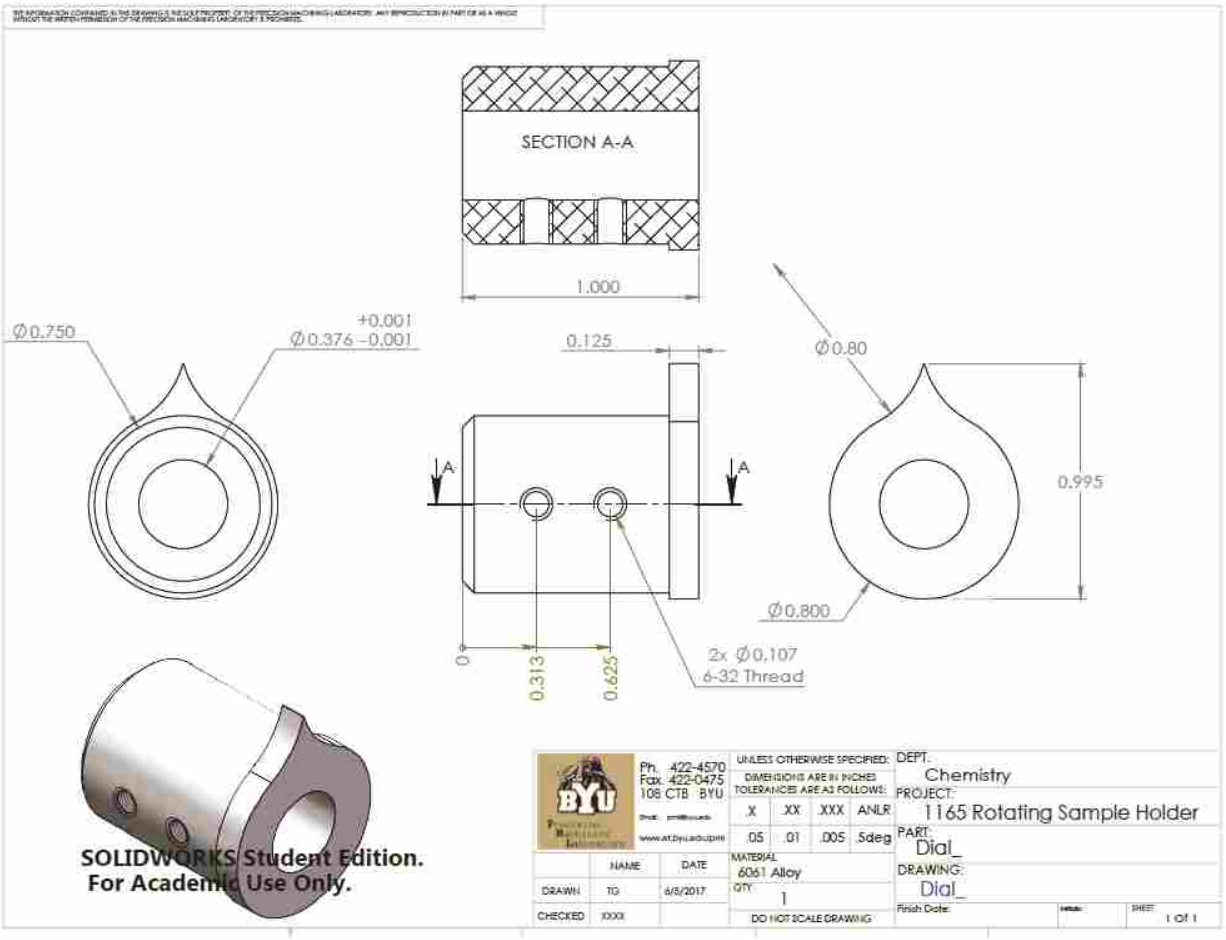
SECTION A-A
1.000
Ø0.750
+0.001
Ø0.376 -0.001
0.125
Ø0.80
A
A
0.995
Ø0.800
0
0.313
0.625
2x Ø0.107
6-32 Thread
SOLIDWORKS Student Edition.
For Academic Use Only.
Ph. 422-4570
Fax. 422-0475
108 CTB BYU
UNLESS OTHERWISE SPECIFIED:
DIMENSIONS ARE IN INCHES
TOLERANCES ARE AS FOLLOWS:
X XX .XXX ANLR
.05 .01 .005 .5deg
NAME DATE
DRAWN TG 6/8/2017
CHECKED XXXX
MATERIAL
6061 Alloy
QTY
1
DO NOT SCALE DRAWING
DEPT.
Chemistry
PROJECT:
1165 Rotating Sample Holder
PART:
Dial_
DRAWING:
Dial_
Finish Date:
SHEET
1 Of 1

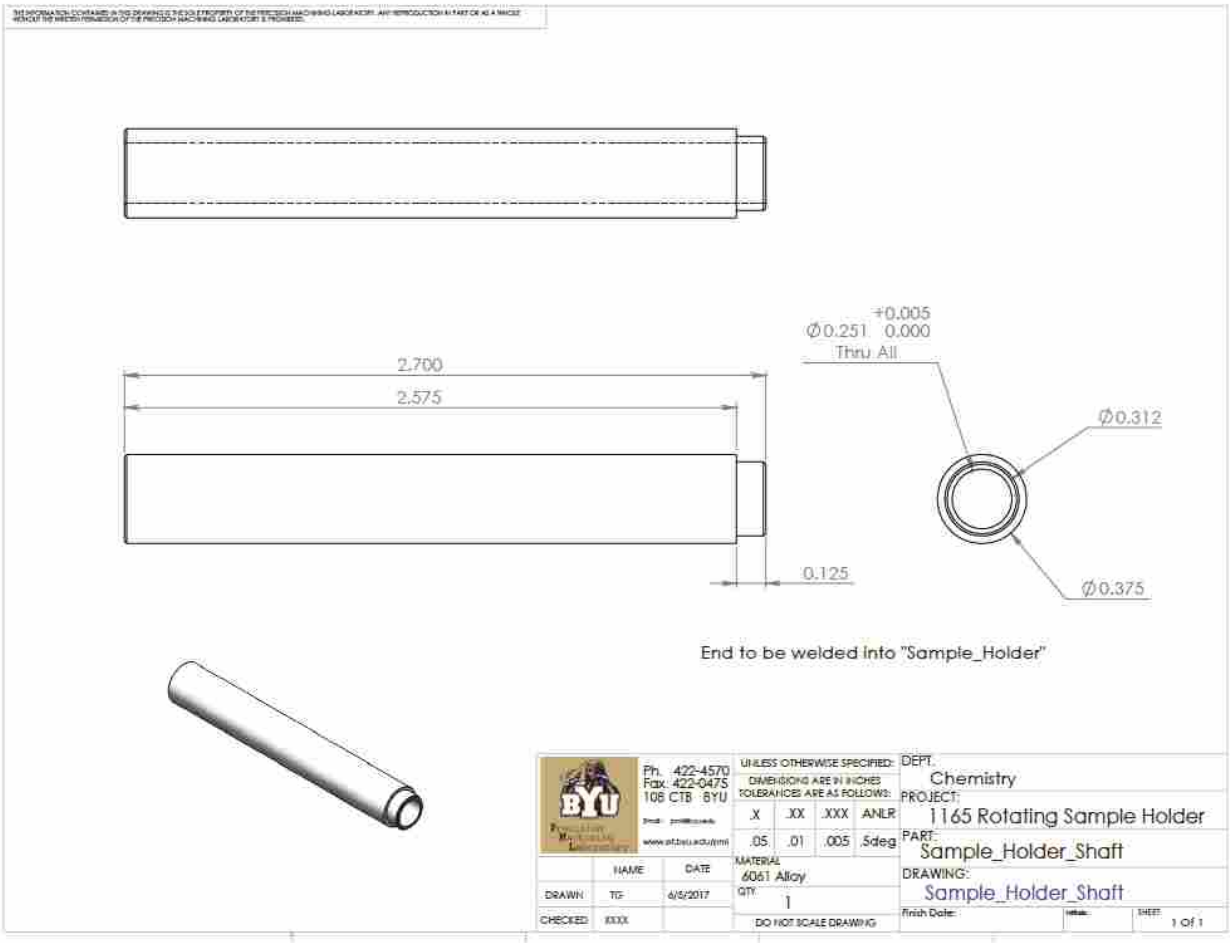
+0.005
Ø0.251 0.000
Thru All
2.700
2.575
Ø0.312
0.125
Ø0.375
End to be welded into "Sample_Holder"
Ph. 422-4570
Fax. 422-0475
106 CTB BYU
UNLESS OTHERWISE SPECIFIED:
DIMENSIONS ARE IN INCHES
TOLERANCES ARE AS FOLLOWS:
.X .XX .XXX ANLR
.05 .01 .005 .5deg
NAME DATE
DRAWN TG 6/5/2017
CHECKED XXX
MATERIAL
6061 Alloy
QTY
1
DO NOT SCALE DRAWING
DEPT.
Chemistry
PROJECT:
1165 Rotating Sample Holder
PART:
Sample_Holder_Shaft
DRAWING:
Sample_Holder_Shaft
Finish Date:
SHEET
1 Of 1


http://www.mclabs.us/thorproduct.cfm?partnumber=XYR1
Chemistry
1928 Column Stage Mounts
XYR1-Solidworks
XYR1-A Assembly

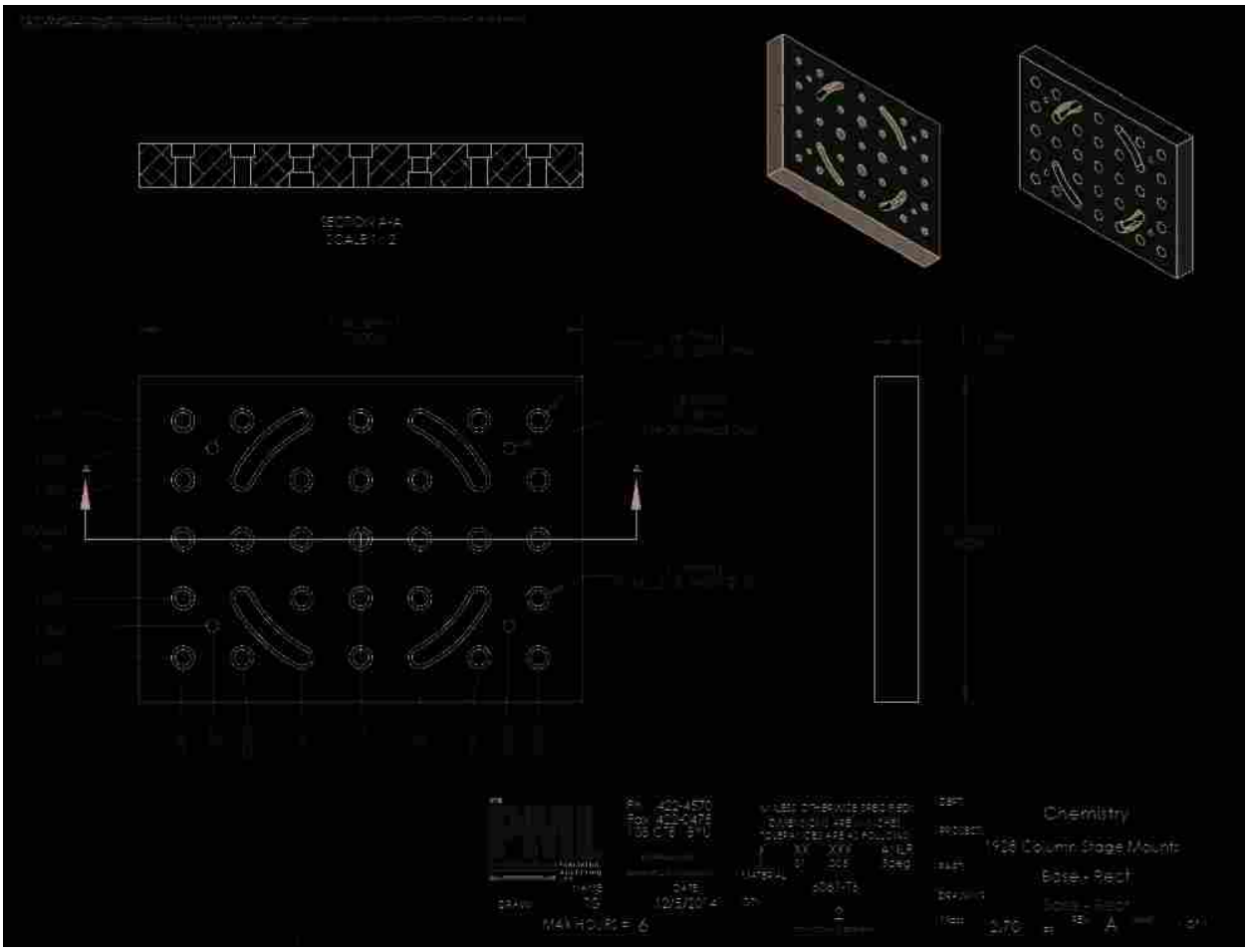
SECTION A-A
SCALE 1 : 2
Chemistry
1928 Column Stage Mount
Base - Rect
MAX HOLE = 6


Chemistry
1928 Column Stage Mounts
Base
See BOM
12/8/2014
4
0.86
A

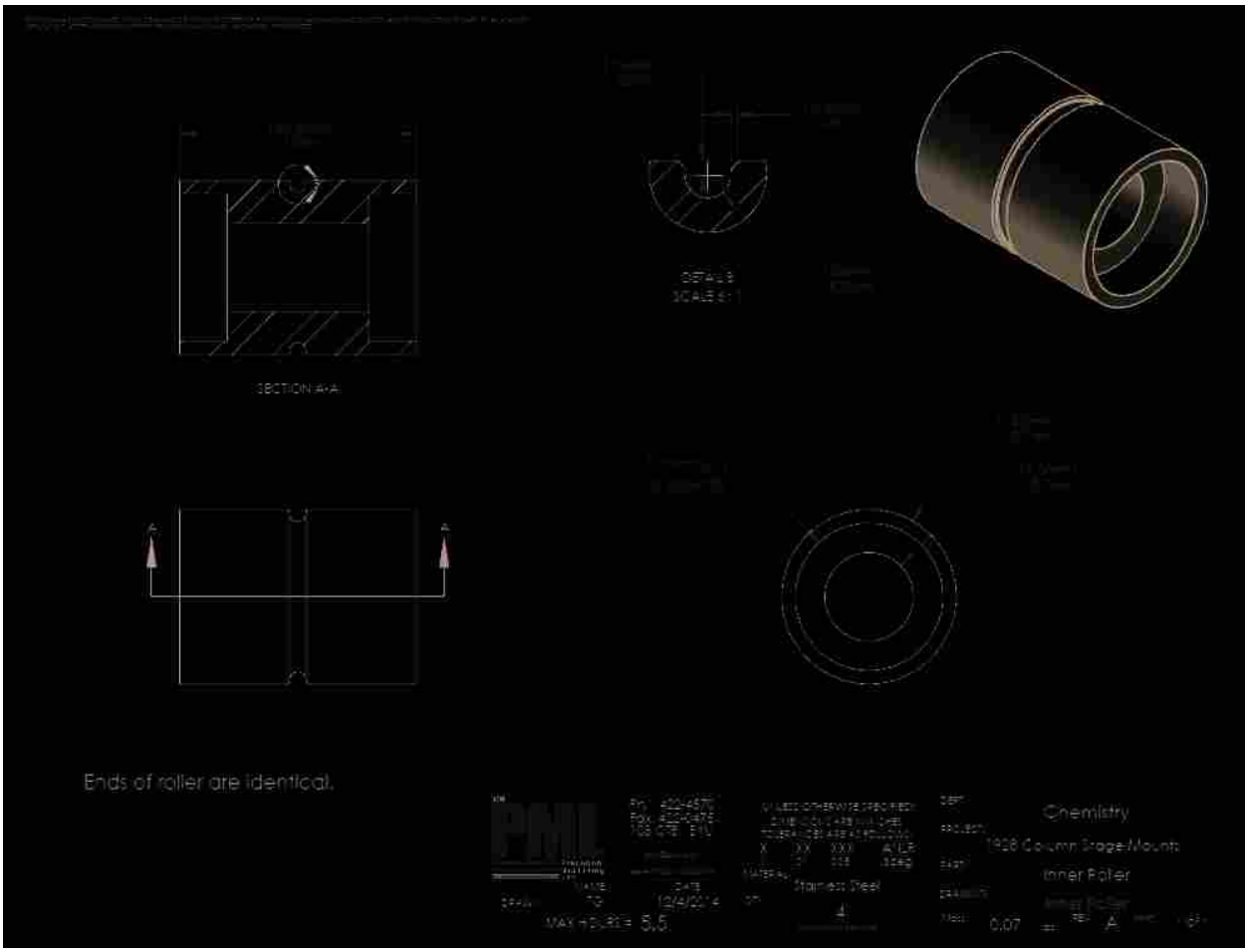
SECTION A-A
Ends of roller are identical.
Stainless Steel
Chemistry
1908 Column Stage Mounts
Inner Roller

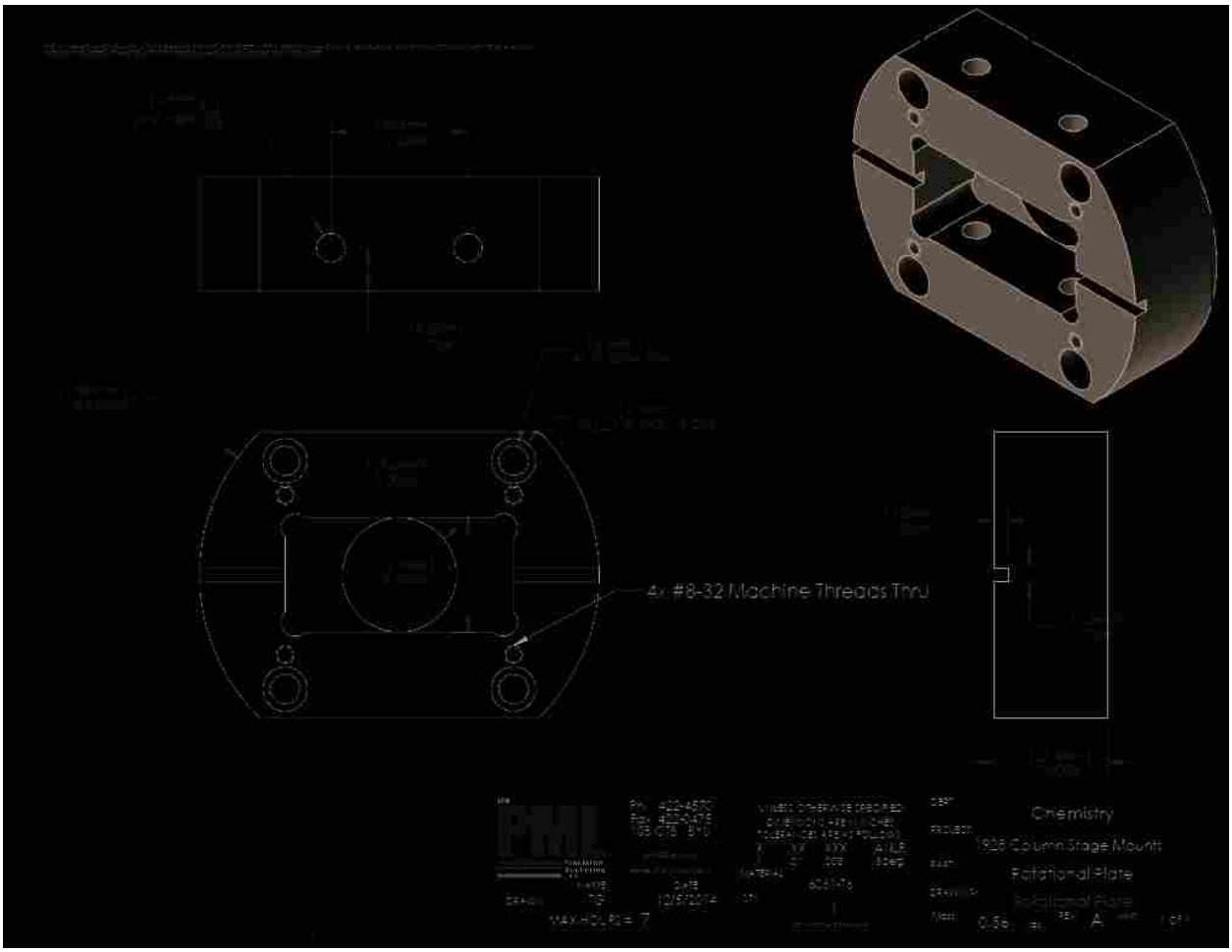
4x #8-32 Machine Threads Thru
Chemistry
1926 Column Stage Mounti
Rotational Plate

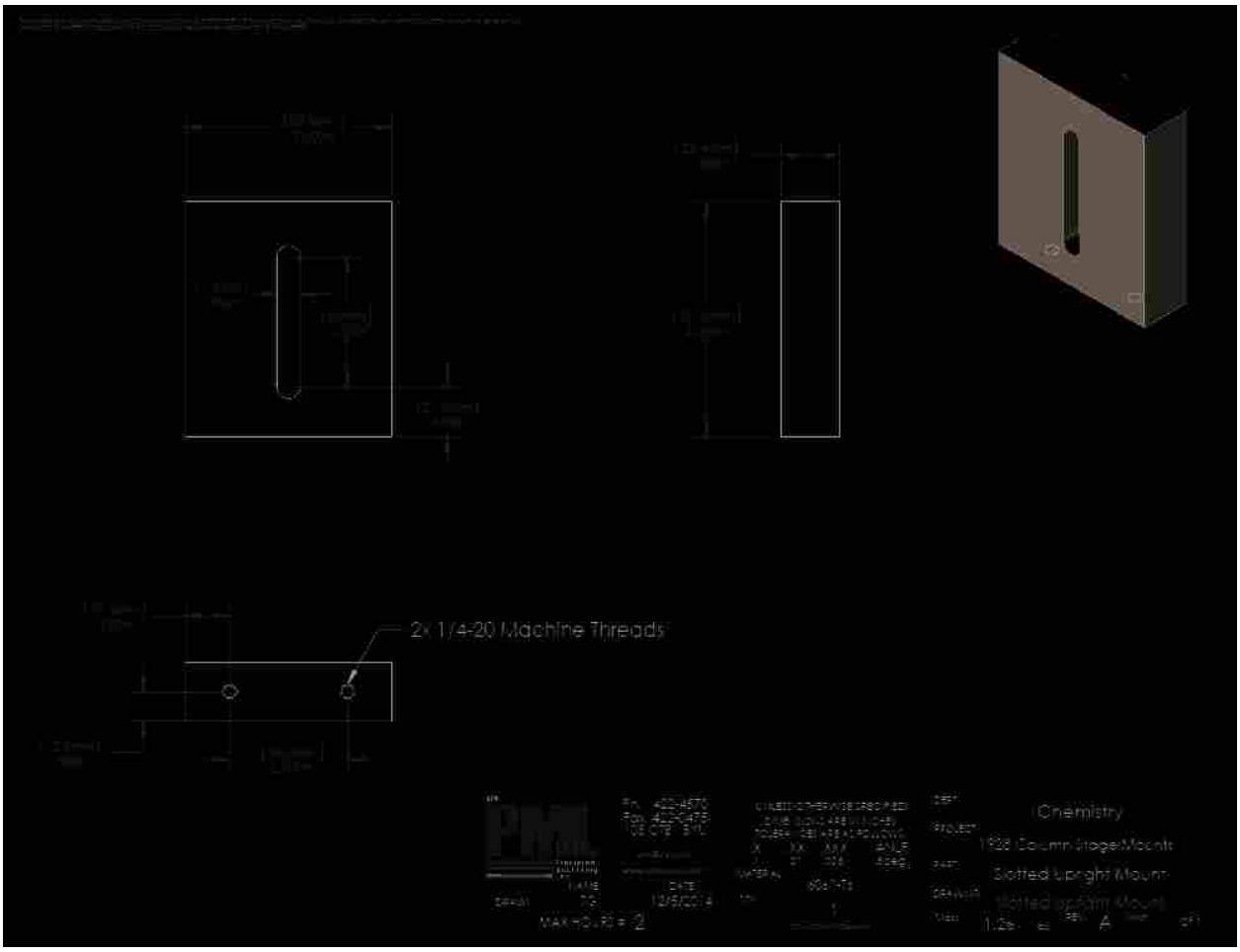
2x 1/4-20 Machine Threads
Chemistry
1938 Column Stage Mounts
Slotted Upright Mount

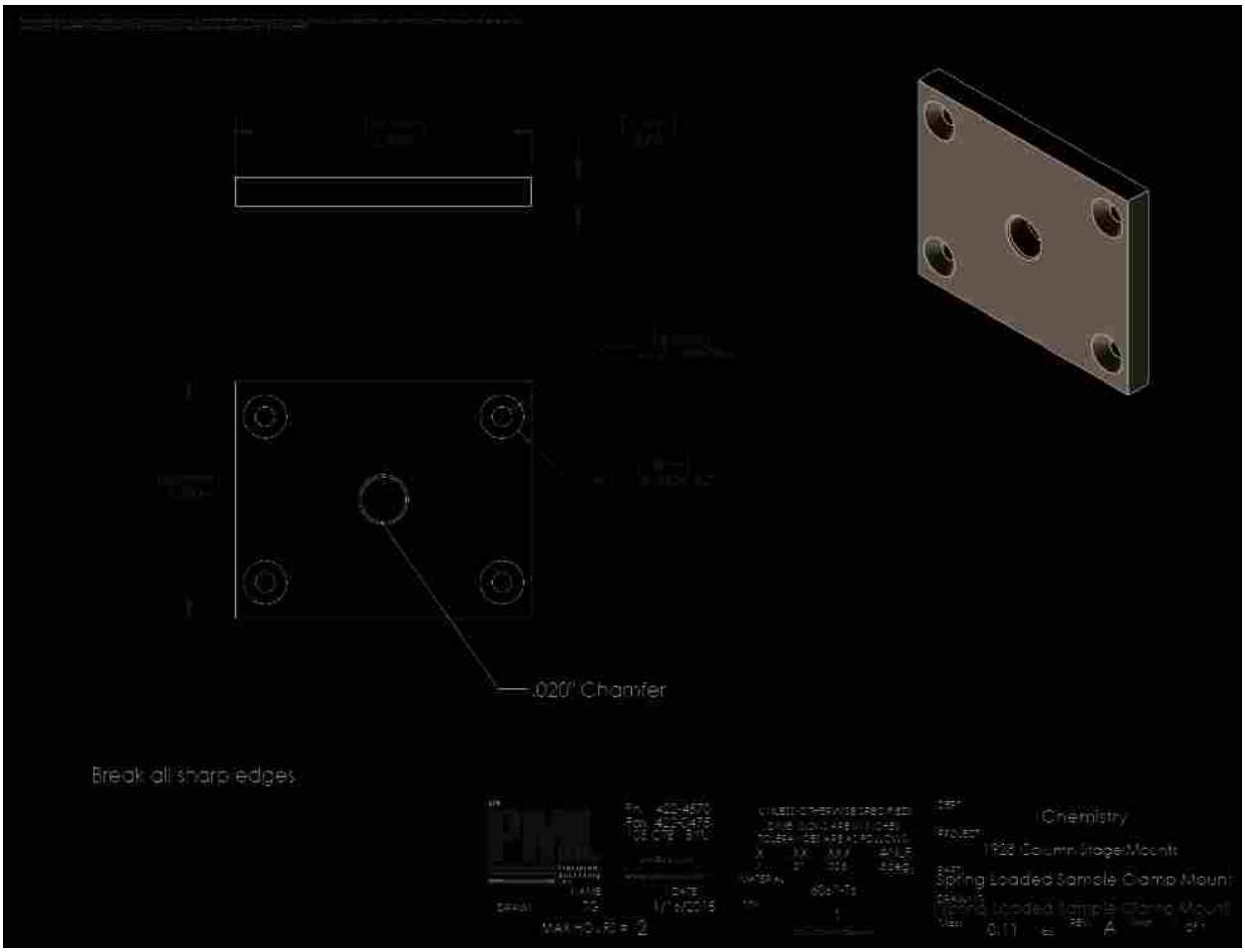
.020" Chamfer
Break all sharp edges
Chemistry
1938 Column Stage Mounts
Spring Loaded Sample Clamp Mount
Spring Loaded Sample Clamp Mount
0.11
A

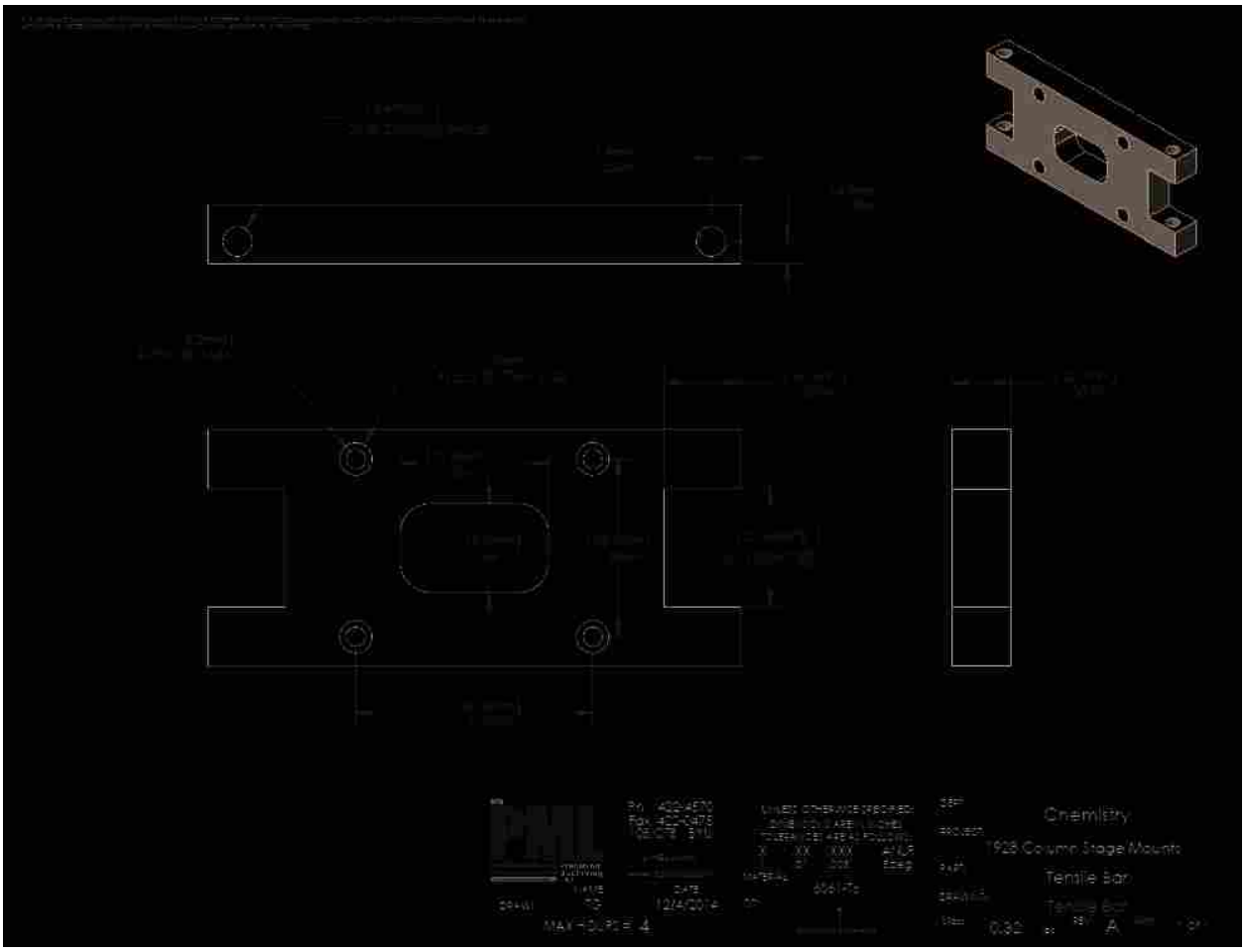
Chemistry
1928 Column Stage Mounts
Tensile Bar
Tensile Bar
0.30
A

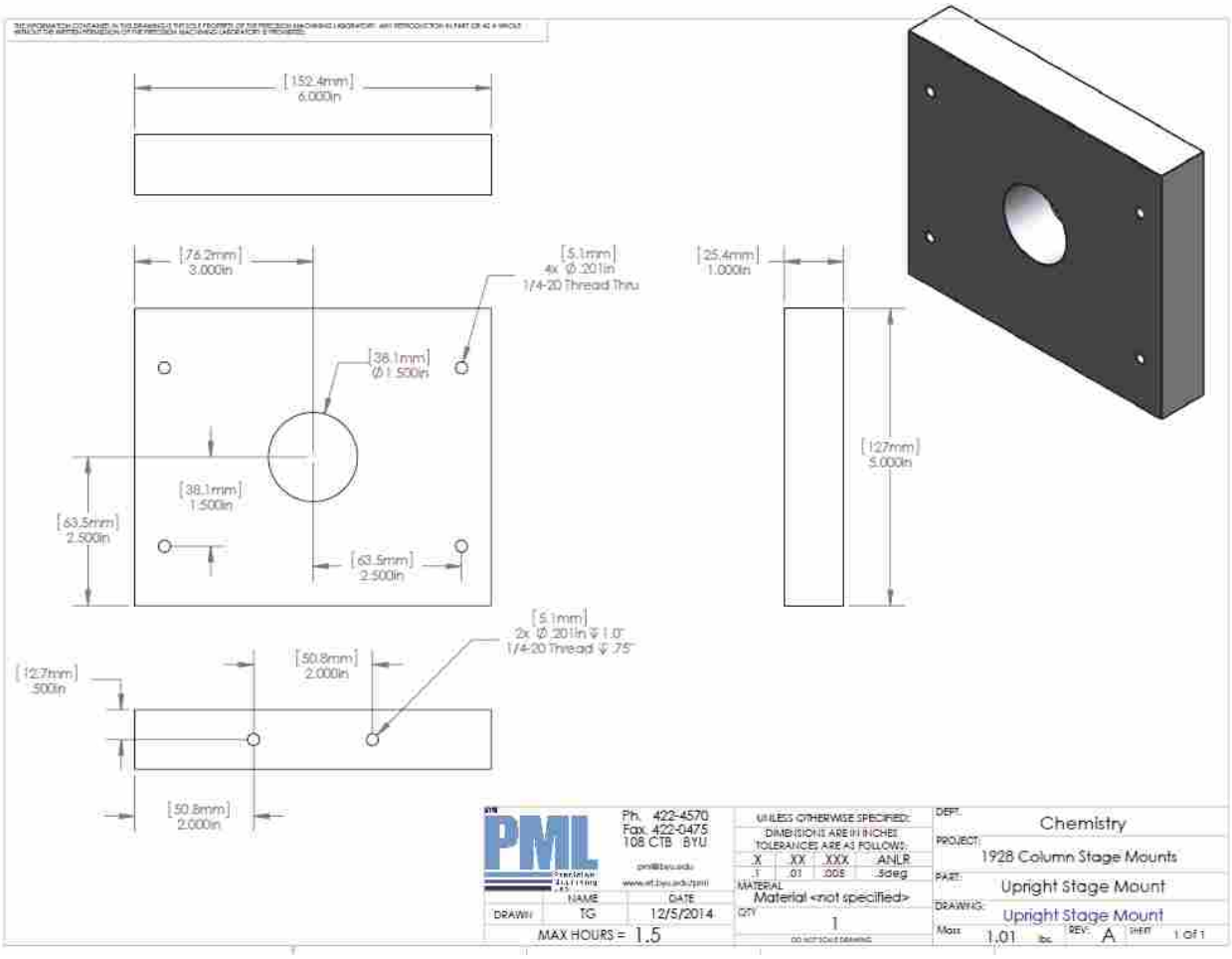
[152.4mm]
6.000in
[76.2mm]
3.000in
[5.1mm]
4x Ø.201in
1/4-20 Thread Thru
[38.1mm]
Ø1.500in
[38.1mm]
1.500in
[63.5mm]
2.500in
[63.5mm]
2.500in
[25.4mm]
1.000in
[127mm]
5.000in
[5.1mm]
2x Ø.201in ↧1.0"
1/4-20 Thread ↧.75"
[12.7mm]
.500in
[50.8mm]
2.000in
[50.8mm]
2.000in
PML
Precision Machining Lab
Ph. 422-4570
Fax. 422-0475
108 CTB BYU
pml@byu.edu
www.et.byu.edu/~pml
NAME
DATE
DRAWN
TG
12/5/2014
MAX HOURS = 1.5
UNLESS OTHERWISE SPECIFIED:
DIMENSIONS ARE IN INCHES
TOLERANCES ARE AS FOLLOWS:
X XX .XXX ANLR
1 .01 .005 .5deg
MATERIAL
Material <not specified>
QTY
1
DO NOT SCALE DRAWING
DEPT.
Chemistry
PROJECT:
1928 Column Stage Mounts
PART:
Upright Stage Mount
DRAWING:
Upright Stage Mount
Mass
1.01
lbs
REV:
A
SHEET
1 OF 1

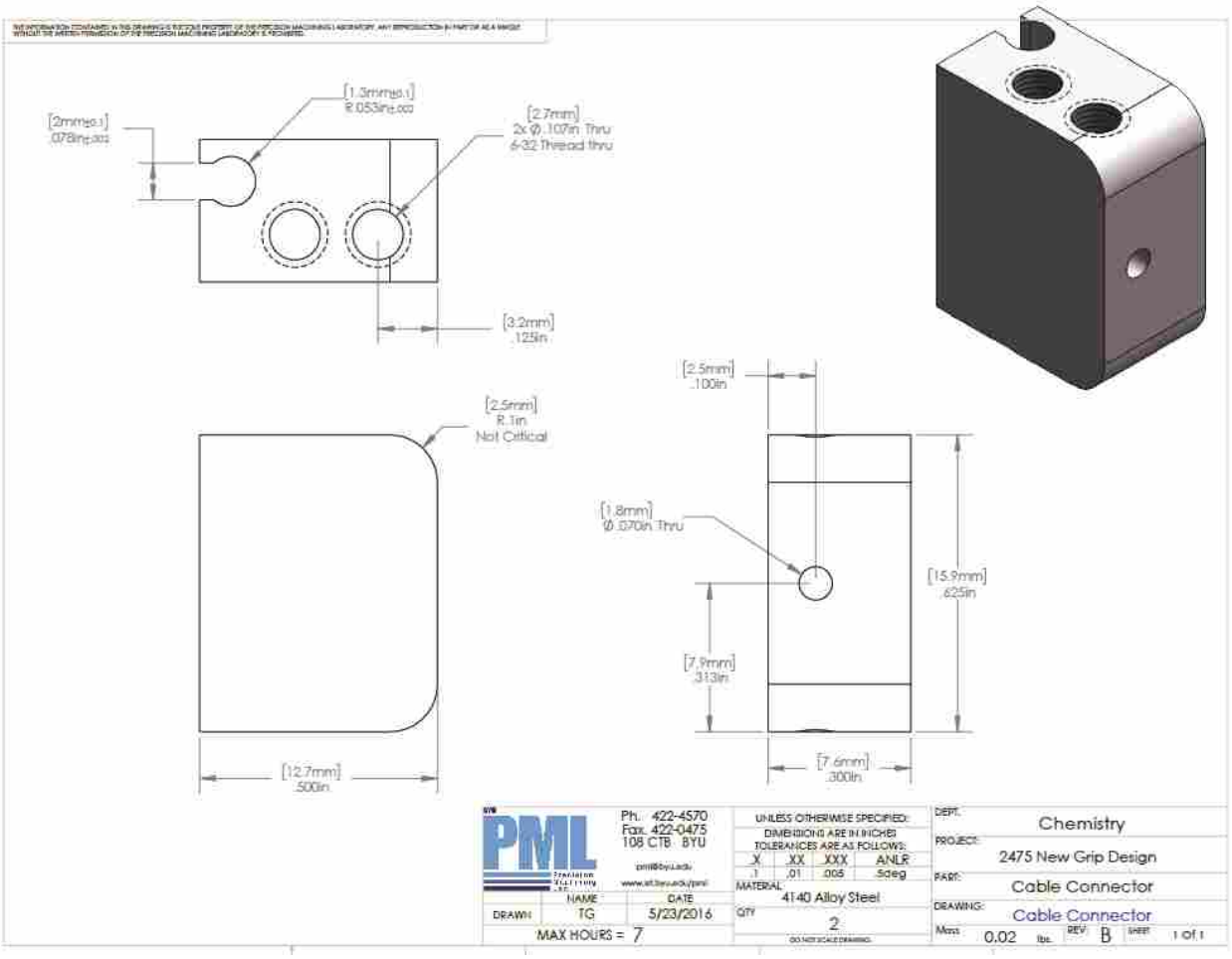
[1.3mm±0.1]
R.053in±.002
[2mm±0.1]
.078in±.002
[2.7mm]
2x Ø .107in Thru
6-32 Thread thru
[3.2mm]
.125in
[2.5mm]
R.1in
Not Critical
[12.7mm]
.500in
[2.5mm]
.100in
[1.8mm]
Ø .070in Thru
[15.9mm]
.625in
[7.9mm]
.313in
[7.6mm]
.300in
PML
Precision Machining Laboratory
Ph. 422-4570
Fax. 422-0475
108 CTB BYU
pml@byu.edu
www.et.byu.edu/pml
NAME
DATE
DRAWN
TG
5/23/2016
MAX HOURS = 7
UNLESS OTHERWISE SPECIFIED:
DIMENSIONS ARE IN INCHES
TOLERANCES ARE AS FOLLOWS:
X XX XXX ANLR
.1 .01 .005 .5deg
MATERIAL
4140 Alloy Steel
QTY
2
DO NOT SCALE DRAWING
DEPT.
Chemistry
PROJECT:
2475 New Grip Design
PART:
Cable Connector
DRAWING:
Cable Connector
Mass
0.02
lbs.
REV
B
SHEET
1 of 1

A.2: Matlab code for modeling in section 5.2.6.1

```
>> [x,z]= meshgrid(0:1:360, 0:1:360);

>> y=0

>> cccyxz = -((cosd(z)-cosd(3.*z))./8).*sind(2.*x);

>> ccc = cccxxz + cccyyz + cccxyz +cccyxz;

>> sym = ccc + aac;

>> surf(x,y,sym)

>> xlabel('Chi')

>> ylabel('Phi')

>> cccyyz = ((cosd(z)-cosd(3.*z))./8).*(1-cosd(2.*x));

>> cccxxz = ((cosd(z)-cosd(3.*z))./8).*(1+cosd(2.*x));

>> cccxyz = -((cosd(z)-cosd(3.*z))./8).*sind(2.*x);

>> cccyxz = -((cosd(z)-cosd(3.*z))./8).*sind(2.*x);

>> ccc = cccxxz + cccyyz + cccxyz +cccyxz;

>> aacyyz = cosd(z./2).*(1-cosd(2.*x).*cosd(2.*y))- ((cosd(z) - cosd(3.*z))./16).*(1-
cosd(2.*x)).*(1+cosd(2.*y))+ ((1+cosd(2.*z))./4).*sind(2.*x).*sind(2.*y);

>> aacxxz = cosd(z./2).*(1+cosd(2.*x).*cosd(2.*y))- ((cosd(z) -
cosd(3.*z))./16).*(1+cosd(2.*x)).*(1+cosd(2.*y))- ((1+cosd(2.*z))./4).*sind(2.*x).*sind(2.*y);

>> aacxyz = -cosd(z./2).*sind(2.*x).*cosd(2.*y)+((cosd(z)-cosd(3.*z))./16).*sind(2.*x).*(1+cosd(2.*y))-
((1+cosd(2.*z))./4).*cosd(2.*x).*cosd(2.*y);

>> aacyxz = aacxyz;

>> aac = aacyyz + aacxxz + aacyxz + aacxyz;

>> sym = ccc + aac;

>> surf(x,z,sym)
```